Advanced Porous Materials (APMs) as Host to Develop Composite Materials: Stability and Functional Studies

A Thesis

Submitted in Partial Fulfillment of the Requirements for the

Degree of

Doctor of Philosophy

by

Samraj Mollick
Reg. ID: 20153362

Indian Institute of Science Education and Research (IISER), Pune

2020

Dedicated to

Maa, Abba and Dada (Sabraj)

Indian Institute of Science Education and Research (IISER), Pune

Certificate

It is hereby certified that the work described in this thesis entitled *"Advanced Porous Materials (APMs) as Host to Develop Composite Materials: Stability and Functional Studies"* submitted by *Mr. Samraj Mollick* was carried out by the candidate, under my supervision. The work presented here or any part of it has not been included in any other thesis submitted previously for the award of any degree or diploma from any other university or institution.

Date: 29.10.2020

Dr. Sujit K. Ghosh
Research Supervisor
Email: sghosh@iiserpune.ac.in
Contact No.:+91(20)25908076

Declaration

I declare that this written submission represents my ideas in my own words and wherever other's ideas have been included; I have adequately cited and referenced the original sources. I also declare that I have adhered to all principles of academic honesty and integrity and have not misrepresented or fabricated or falsified any idea/ data/ fact/ source in my submission. I understand that violation of the above will cause for disciplinary action by the Institute and can also evoke penal action from the sources which have thus not been properly cited or from whom proper permission has not been taken when needed.

Date: 29.10.2020

Samraj Mollick

Reg. Id: 20153362

Acknowledgement

At the very outset, I would like to take the opportunity to convey my deepest gratitude to my research supervisor **Dr. Sujit K. Ghosh** for his continuous support and motivation throughout my PhD tenure. I feel his illimitable encouragement has propelled my research in forward direction. It has been an immense privilege for me to work under his supervision. I believe that his inspiring guidance has helped me to design and execute different research projects successfully. Thank you very much Sir for all your diligent efforts, trust in me and most importantly for being such a wonderful guide.

I sincerely acknowledge the former director of Indian Institute of Science Education and Research (IISER) Pune Prof. K. N. Ganesh and the current director Prof. J. B. Udgaonkar for providing world class facilities and having a vibrant research environment. I am also extremely thankful to my research advisory committee (RAC) members, Prof. Avinash kumbhar (Pune University) and Dr. Shabana Khan(IISER, Pune) for their valuable suggestions, advices and support during the annual RAC meetings. I am also grateful to former chair Prof. M. Jayakannan and present chair Prof. H. N. Gopi and all other faculty members of the department of chemistry for being approachable for any help and maintaining such research friendly healthy environment in the department. I sincerely thank all the collaborators - especially Prof. Myoung Soo Lah (Ulsan National Institute of Science and Technology, South Korea), Prof. Jianwen Jiang (National University of Singapore, Singapore), Dr. Rajat Saha (Kazi Nazrul University, India), Dr. Atanu Jana (Ulsan National Institu te of Science and Technology, South Korea, who assisted me in completion of different projects. It has been a great privilege for me to be a part of the 'Microporous Materials Lab' and I am extremely grateful to all the past and present members of the team. I would like to thank all of them (Dr. Sanjog Nagarkar, Dr. Biplab Joarder, Dr. Biplab Manna, Dr. Soumya Mukherjee, Dr. Avishek Karmakar, Arif Inamdar, Dr. Tarak Nath Mandal, Dr. Sreenu Bhanoth, Shilpa Sonar, Dr. Aamod V. Desai, Dr. Partha Samanta, Shivani Sharma, Yogeshwar More, Prateek Agrawal, Arunabha Sen, Subhajit Dutta, Sumanta Let, Writakshi Mandal, Sahel Fajal, Debanjan Mahato, Satyam Saurabh, Naveen Kumar, Priyanshu Chandra, Govind, Kriti Gupta). Thank you very much all for your significant contribution, help and providing

friendly environment in the lab. My sincere thanks go out for all my seniors: Sanjog, Biplab da, Manna da, Soumya da and Avishek da, Tarak da, Aamod and Partha da for their guidance, support and valuable suggestions. I would to mention that it was an immense pleasure to work with all of you and I feel I have learnt a lot of things from you guys. Of them, I have worked most of the time with Tarak da and Soumya da; thank you all for teaching me a lot of lessons. Apart from my seniors, I would like to express my special appreciation to all my current lab members, because without them this journey would not have been as exciting and memorable as it has been. I would consider myself lucky to have a batch-mate and friend like Yogesh, with whom I had maximum overlap in time and spent most of the time in lab. I would like to acknowledge the prompt and unconditional assistance from Sahel, Subhajit, Sumanta, Shivani, Arunabha, Writakshi and Debanjan whenever required. I am thankful to Tarak da and Sreenu for providing a timely advice and perspective. I would like to specially mention about undergraduate student Satyam who worked with me over a long period - for his enthusiastic involvement and optimistic ideas. I am especially thankful to Tarak da, Sahel and Satyam for their invaluable support during the last phase of my PhD.

I would like to convey my deepest regards towards my old school and university teachers who have encouraged me throughout different stages of life. I am also very much thankful to Dr. Mahadeb Maity and Dr. Kanchan Bag (Garhbeta College) for inspired me to pursue a PhD degree. I would like to express my sincere regards towards all the faculty members of Banaras Hindu University (BHU), Varanasi, for their lessons and support during my Masters study. I am also thankful to Prof. K. K. Upadhyay (BHU, Varanasi) for providing me the opportunity to carry out my Masters project for one year in his lab.

I acknowledge University Grant Commission (UGC), India for providing me fellowship. I would also like to thank American Chemical Society (ACS), Royal Society of Chemistry (RSC), John Wiley & Sons (Wiley-VCH),Cell Press, Nature Publishing Group (NPG), Elsevier for the various research articles and review that I managed to publish in my PhD tenure. For the smooth progress in a long course, the support of technical and administrative staff is equally important. I thank Dr. Umesha reddy Kacherki and Anuradha for library support, technical staff of the institute - Parveen Nasa, Archana, Mahesh Jadhav, Nilesh Dumbre, Swati, Anil, Yatish, Ganesh Dimbar, Suresh Prajapat, Sandeep, Nitin, Megha,

Deepali and administrative staff - Mayuresh, Nayana, Tushar, Vrushali, Suresh, Prabhas, Priyadarshani for their prompt assistance at multiple occasions. During my PhD tenure, I had the opportunity to attend national (MTIC-2017) and international conferences (EuroMOF-2017), for which I thank SERB and UGC for funding. I wish to thank all my friends for their support and help at different stages of my life, especially, Rahul, Rahi, Rishav, Debanjan, Soumendu, Rajarshi, Javid, Naveen, Danish, Samrat, Bappa, Saheb, Jahurul, Aloke, Sumit, Avishek, Gurudas, Chiranjit, Ashu, Kuldeep, Vishal, Ali, Animesh, Souvik, Arup, Nayim, Shiba. I thank all my batch-mates (January-2015) and Chemphilic team-2018-19. I would like to acknowledge Reja da, Barun da, Maidul da, Shyama da, Abhik da, Chandramouli da, Soumendu, Sudeb da, Bijoy da, Kingshuk, Indra, Sumit, Swattik, Rinku. I apologize in advance for not being able to take all of your names, but am sure, it would not offend you to a great extent. Also, I would like to mention about our Bengali football and cricket team, of which I was a part for the last five years and I wish the members all the success in the forthcoming years. Lastly, I am really grateful to my whole family members (my parents, dada, chacha, chachi, Fufu, jamai). Especially, I would like to thank my parents and my elder brother Sabraj, who stood beside me at every moment of my life so far. Without their scarifies, motivation and support, I would not have reached here.

- Samraj Mollick

Contents

Synopsis

The primary motivation of this thesis is based on the stability and functional studies of composite materials where advanced porous materials (APMs) are used as a host matrix while unstable functional materials were used as a guest. Although traditional porous solids are essential for our daily life, on-demand targeted application is almost impossible with these materials. The advantageous of structure-property correlation feature along with numerous possibilities of structural as well as compositional variation put APMs as a unique class of polymeric materials making them a frontrunner in the domain of material science. The features offered by APMs are suitable in a variety of applications ranging from energy, environment to bio-medical. But APMs have not been profoundly studied for stabilization of unstable functional materials. In this context, the instability and aggregation issues of metal-organic polyhedra (MOP) have been resolved and were utilized for water purification. Further, the extremely unstable hybrid perovskite materials are protected inside different APM matrices and were further utilized in photocatalysis of toxic organic pollutants or light-emitting diode applications respectively.

Chapter 1. Introduction

At the outset, a brief discussion about traditional porous solids and distinction between APMs are included. Different types of APMs and their properties have been briefly discussed, and the scope of APMs toward hosting different functional materials is provided. In addition, another discussion regarding composite materials is also included in the later part of this section. The advantages of APMs as host matrix and various synthesis approach of composite materials have been discussed thoroughly in this chapter. The whole research works are divided into two parts and each part further separated by two chapters respectively . In Part-I, stability and functional studies of MOP are discussed while extremely unstable hybrid perovskite materials are stabilized by loading into different APMs matrix, and their functional studies are included in the part-II.

Part-I: Stabilization and Functional Studies of Metal-Organic Polyhedra (MOP)

The issues and stabilization strategies of MOP have been thoroughly discussed here. This section of the thesis is divided into two chapters i.e. chapter-2 and chapter-3. In chapter-2, one of the unstable APM, i.e. carboxylate MOP is stabilized by the strategic decoration of hydrophobic alkyl functional groups on the outer-surface of the cages. While in chapter-3, the aggregation issue of MOP is resolved by covalent grafting into another APM matrix i.e. crystalline COF matrix and utilized for water prification.

Chapter 2. Outer Surface Hydrophobic Shielding Strategy to Enhance the Chemical Stability of Metal-Organic Polyhedra

In this chapter, a series of neutral, spherical shaped based chemically robust carboxylate MOPs are design and synthesized. The prototype outer-surface hydrophobic shielding strategy is used to stabilize the MOPs system where the metal-ligand bond is not so strong. Fine-tuning of hydrophobic shielding is key to attaining chemical inertness with retention of the framework integrity over a wide range of pH values, in strongly acidic conditions, and oxidizing and reducing media. The ultra stability of such materials is further corroborated by molecular modelling studies.

Reference: Samraj Mollick, Soumya Mukherjee, Dongwook Kim, Zhiwei Qiao, Aamod V. Desai, Rajat Saha, Yogeshwar D. More, Jianwen Jiang, Myoung Soo Lah and Sujit K. Ghosh. Angew. *Chem. Int. Ed.* **2019**, *58*, 1041-1045.

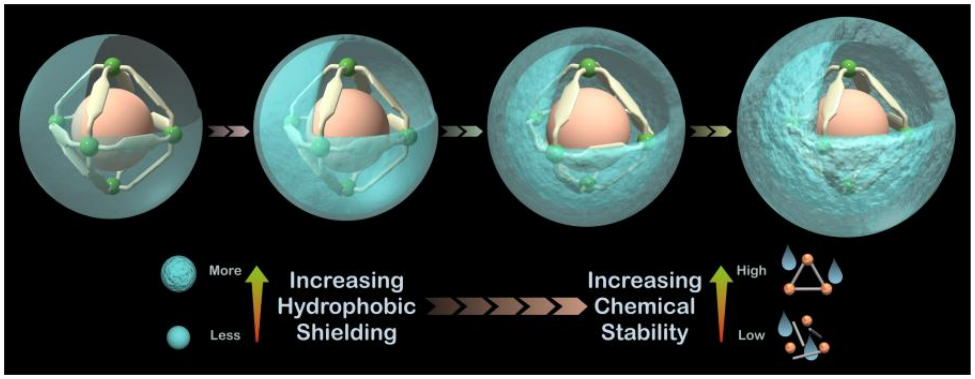

Chapter 3. Hybridization of Cage and COF: A New Type of Hybrid Materials for Sequestration of oxo-anions from Water

In this chapter, an amino-functionalized, cationic metal-organic cage molecule is covalently linked with another APM matrix i.e. crystalline porous COF. After covalent tethering into the COF matrix, the aggregation issue of cage molecule is resolved as the COF matrix tightly anchor and separate them from each other. The resulting anion exchangeable hybrid composite material exhibits very fast and selective sequestration of high as well as a very trace amount of a wide range of metal-based toxic oxoanions ($HAsO_4^{2-}$, SeO_4^{2-}, CrO_4^{2-}, ReO_4^- and MnO_4^-) from the mixture of excessive (~1000 folds) other interfering anions to well below the permissible drinking water limit. Moreover, the hybrid cationic nanotrap material can efficiently reduce the As(V) level from a highly contaminated groundwater sample to below the WHO permitted level.

Reference: Samraj Mollick, Sahel Fajal, Satyam Saurabh, Debanjan Mahata and Sujit K. Ghosh. *ACS Cent. Sci.* **2020,** *6*, 1534-1541.

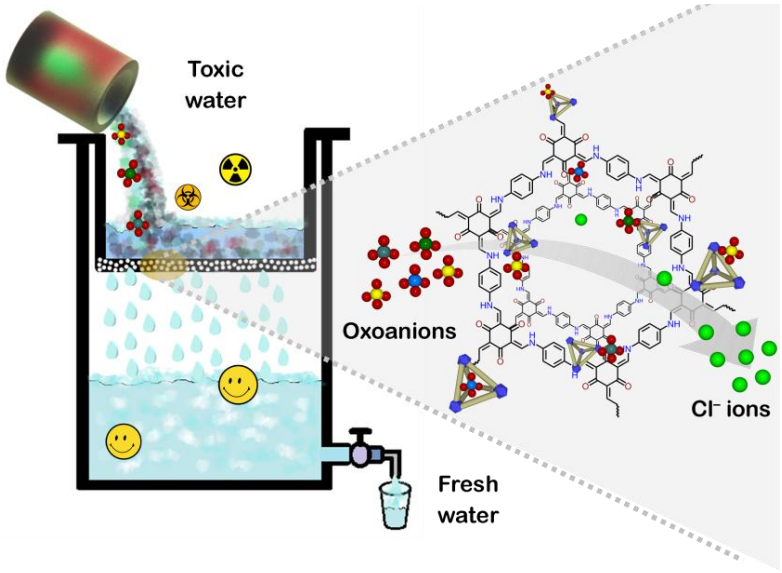

Toxic oxoanions capture by IPcom-3(200) hybrid material

Part-II: Stabilization and Functional Studies of Hybrid Halide Perovskite@APM Composite

In this section, the long standing stability issue of hybrid perovskite materials have been resolved by embedding them into different APMs matrices, and the final composite materials are then utilized in various applications. This section is also further divided into two chapters, i.e. chapter-4 and chapter-5. HBP NCs are stabilized and were used in various functional studies through embedding them into MOF and porous MOG matrices in chapter-4 and chapter-5 respectively.

Chapter 4. Ultrastable Luminescent Hybrid Bromide Perovskite@MOF Nanocomposites for the Degradation of Organic Pollutants in Water

In this chapter, HBP nanocrystals (NCs) have been stabilised within a well-known chemically stable metal-organic framework (MOF) viz. zeolitic imidazolate framework (ZIF-8) via pore-encapsulated solvent directed (PSD) approach. The composites maintain their structural integrity as well as photoluminescence (PL) properties upon exposure to a wide range of polar solvents including water (even in boiling conditions), prolonged exposure to UV irradiation and elevated temperature for a longer period of time. Further on the basis of high stability, HBP@MOF composites they have been employed as heterogeneous photocatalyst to degrade toxic organic pollutants directly in water.

Reference: Samraj Mollick,[†] Tarak Nath Mandal,[†] Atanu Jana, Sahel Fajal, Aamod V. Desai and Sujit K. Ghosh. *ACS Appl. Nano Mater*. **2019**, *2*, 1333-1340.

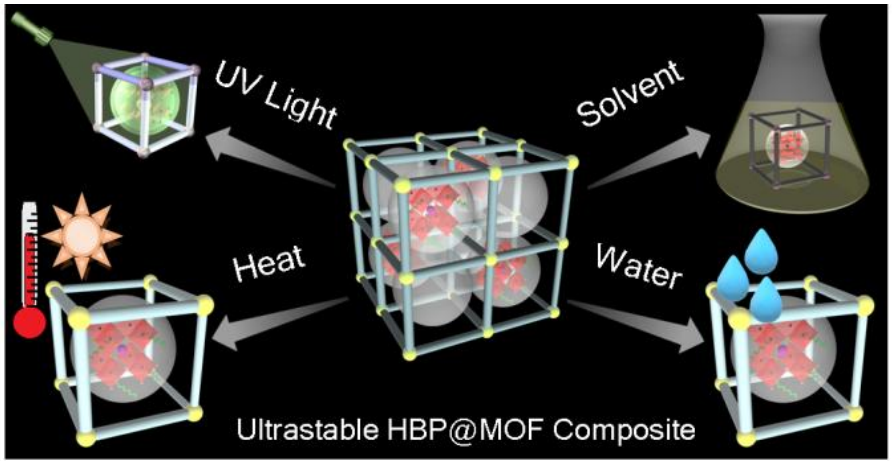

Chapter 5. Hybrid Blue Perovskite@Metal-Organic Gel (MOG) Nanocomposite: Simultaneous Improvement of Luminescence Property and Stability

In this chapter, an extremely unstable blue-emitting hybrid perovskite materials is embedded inside by taking a porous MOG as an APM host matrix. The resulting composite ($EAPbBr_3$@MOG, EA: ethylammonium) shows sharp emission in the intense blue region (λ_{max}<440 nm) with substantial 10-fold enhancement in the PLQY (~53%) as compared to $EAPbBr_3$ NCs (~5%). The porous MOG matrix offers dual benefits to the perovskite NCs i.e. simultaneous dramatic improvement of both luminescence property as well as stability. Incorporation of perovskite NCs into soft MOG matrix provides the additional benefits of flexibility. Combination of high brightness, stability and flexibility of these composites allow to fabricate white-light-emitting diode as an application study.

Reference: Samraj Mollick,[†] Tarak Nath Mandal,[†] Atanu Jana, Sahel Fajal and Sujit K. Ghosh. *Chem. Sci*. **2019**, *10*, 10524-10530.

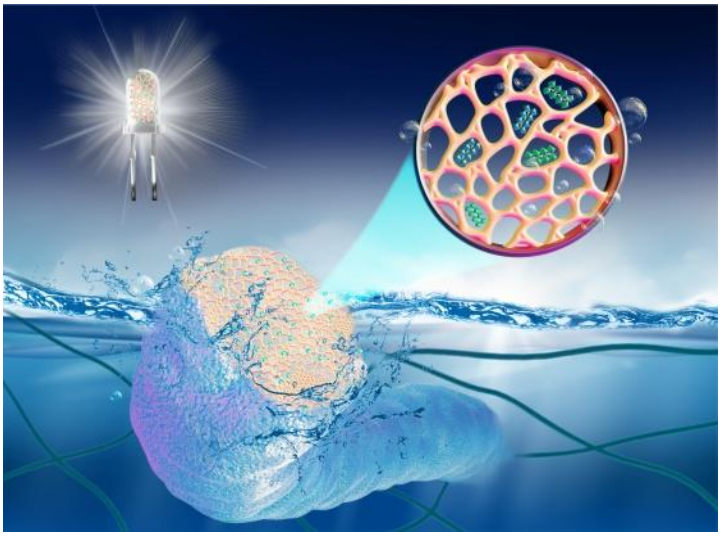

Abbreviations

Anal.	Analysis
Calc.	Calculated
DMF	N,N'-dimethylformamide
MeOH	Methanol
EtOH	Ethanol
FT-IR	Fourier transform infra-red spectroscopy
mg	Miligram
g	Gram
SCXRD	Single-Crystal X-Ray Diffraction
RT	Room Temperature
min	Minutes
mL	Milliliter
mmol	Milli moles
MOF	Metal-Organic Framework
MOP	Metal-Organic Polyhedra
COF	Covalent-Organic Framework
MOG	Metal-Organic Gel
HCP	Hyper-cross-linked polymer
HBP	Hybrid Bromide Perovskite
PXRD	Powder X-Ray Diffraction
RT	Room Temperature
TGA	Thermo-gravimetric Analysis
UV	Ultraviolet
FE-SEM	Field Emission Scanning Electron Microscopy
NMR	Nuclear Magnetic Resonance
EDX	Energy Dispersive X-ray Analysis
ICP-AES	Inductively Coupled Plasma Atomic Emission Spectroscopy
ICP-MS	Inductively Coupled Plasma Mass Spectroscopy

Rights and Permissions

Part-I:

Reprinted (adapted) with permission from *Chem. Asian J.* **2019**, *14*, 3096-3108, Copyright 2019: John Wiley and Sons. Licence number 4865211327871 dated 10th July 2020.

Chapter 2:

Reprinted (adapted) with permission from *Angew. Chem. Int. Ed.* **2019**, *58*, 1041-1045, Copyright 2019: John Wiley and Sons. Licence number 4865211425858 dated 10th July 2020.

Chapter 3:

Reprinted (adapted) with permission from *ACS Cent. Sci.* **2020**, *6*, 1534-1541 (https://pubs.acs.org/doi/10.1021/acscentsci.0c00533). Further permissions related to the material excerpted should be directed to the ACS.

Chapter 4:

Reprinted (adapted) with permission from *ACS Appl. Nano Mater.* **2019**, *2*, 1333-1340. Copyright 2019: American Chemical Society.

Chapter 5:

Reprinted (adapted) with permission from *Chem. Sci.* **2019**, *10*, 10524-10 530. Copyright 2019: Royal Society of Chemistry. This article is licensed under a Creative Commons Attribution-NonCommercial 3.0 Unported Licence.

Research Publications

(† - indicates equal contribution)

Included in Thesis:

1. Hydrophobic Shielding of Outer Surface: Enhancing the Chemical Stability of Metal-Organic Polyhedra.

   Samraj Mollick, Soumya Mukherjee, Dongwook Kim, Zhiwei Qiao, Aamod V. Desai, Rajat Saha, Yogeshwar D. More, Jianwen Jiang, Myoung Soo Lah and Sujit K. Ghosh.

   Angew. Chem. Int. Ed. **2019**, *58*,1041-1045.

2. Nanotrap Grafted Anion Exchangeable Hybrid Materials for Efficient Removal of Toxic Oxoanions from Water.
Samraj Mollick, Sahel Fajal, Satyam Saurabh, Debanjan Mahata and Sujit K. Ghosh.

ACS Cent. Sci. **2020** (under minor Revision).

3. Ultrastable Luminescent Hybrid Bromide Perovskite@MOF Nanocomposites for the Degradation of Organic Pollutants in Water.
Samraj Mollick,† Tarak Nath Mandal,† Atanu Jana, Sahel Fajal, Aamod V. Desai and Sujit K. Ghosh. .
ACS Appl. Nano Mater. **2019**, *2*, 1333-1340.

4. A Hybrid Blue Perovskite@Metal-Organic Gel (MOG) Nanocomposite: Simultaneous Improvement of Luminescence and Stability.
Samraj Mollick,† Tarak Nath Mandal,† Atanu Jana, Sahel Fajal and Sujit K. Ghosh.
Chem. Sci. **2019**, *10*, 10524-10530.

5. Stabilizing Metal-Organic Polyhedra (MOP): Issues and Strategies.
Samraj Mollick, Sahel Fajal, Soumya Mukherjee and Sujit K. Ghosh.
Chem. Asian J. **2019**, *14*,3096-3108. (Selected as Front Cover)

Not Included in Thesis:

6. Turning Disadvantage into Advantage: Unprecedented Improvement of Luminescence Property of Hybrid Blue Perovskite via Loading into Metal-Organic Cage Matrix.
Samraj Mollick, Writakshi Mandal, Tarak Nath Mandal, Satyam Saurabh, Sahel Fajal, Debanjan Mahato, Atanu Jana, and Sujit K. Ghosh..
Manuscript under preparation.

7. Enhanced Acetylene Separation by Integration of Metal-Organic Polyhedra (MOP) into Metal-Organic Frameworks (MOFs).
Samraj Mollick, Subhajit Dutta, Satyam Saurabh, Sumanta Let, Sahel Fajal**,** Gourab Kumar Dam, and Sujit K. Ghosh.
Manuscript under preparation.

8. Functionalized Macroporous MOFs for Record Uranyl Capture from Water.
Samraj Mollick, Satyam Saurabh, Sahel Fajal, Debanjan Mahato, Writakshi Mandal and Sujit K. Ghosh.
Manuscript under preparation.

Chapter 1

Introduction

1.1 Porous Materials

Porosity is an important feature of a material. In a conventional sense, porous materials must have permanent, interconnected voids that are permeable to gases or liquids. Generally, Porosity can be observed in rocks, ceramics, soils, biological tissue, charcoal, dried plant husks, and have been utilized for filtration, purification, petrochemicals, cooling, etc.[1-4] In modern times, there is a growing demand for utilization of porous solids not only limited to adsorption and catalysis, but they are also deployed in different sectors including energy, environmental, and health department. The porous solids have ubiquitous influence on our society and are indispensable in our daily life for a long time. However, the target-specific applications are almost impossible with such traditional porous solids as the structure-property relationship remains unknown. Therefore, the search for a new class of porous materials is essential where fine-tuning of order and functionalities at the atomic level could be easily attained. Such exquisite control over the entire structures of the porous materials permits the tailoring of materials for challenging and appealing applications that are still not realized by such traditional porous solids. This newly developed special class of porous materials have been termed as advanced porous materials (APMs).[5,6] The discovery of APMs at the end of eighties has brought a revolution in chemistry and material engineering. The participation of the ever-escalating number of researchers in this newly developed field owing to the possibilities of unlimited chemical and structural features in this class of materials present scope for imaginative chemists. The unique arrangement of organic, inorganic or combination of both moieties affords a new class of porous materials, potentially complementary and even much more attractive compared to traditional porous solids.[7-11]

1.2 Advanced Porous Materials (APMs)

APMs encompass a wide range of materials i.e., metal-organic frameworks (MOFs), porous organic materials (POMs), metal-organic polyhedra (MOPs), metal-organic gel (MOG) etc (Figure 1.1).[6] The research interest in APMs have skyrocketed in various aspects pertaining to its several key features. Firstly, APMs can be designed to feature high surface area and well-defined functional pores. Secondly, some of them can be readily molded into monolithic forms or thin films which provide substantial advantages in many practical applications. Additionally, few of them can even be dissolved in a common solvent and processed into workable forms without compromising their inherent porosity, which is almost impossible to imagine with conventional porous solids. Furthermore, stimuli-responsive APMs can also be designed that are capable of reversibly switching between the open and closed porous state after applying an external stimuli. Last but not least, myriad choice of easy synthetic routes render them

superiority over other traditional porous solids. Such unique features are generally not observed in classical porous solids.

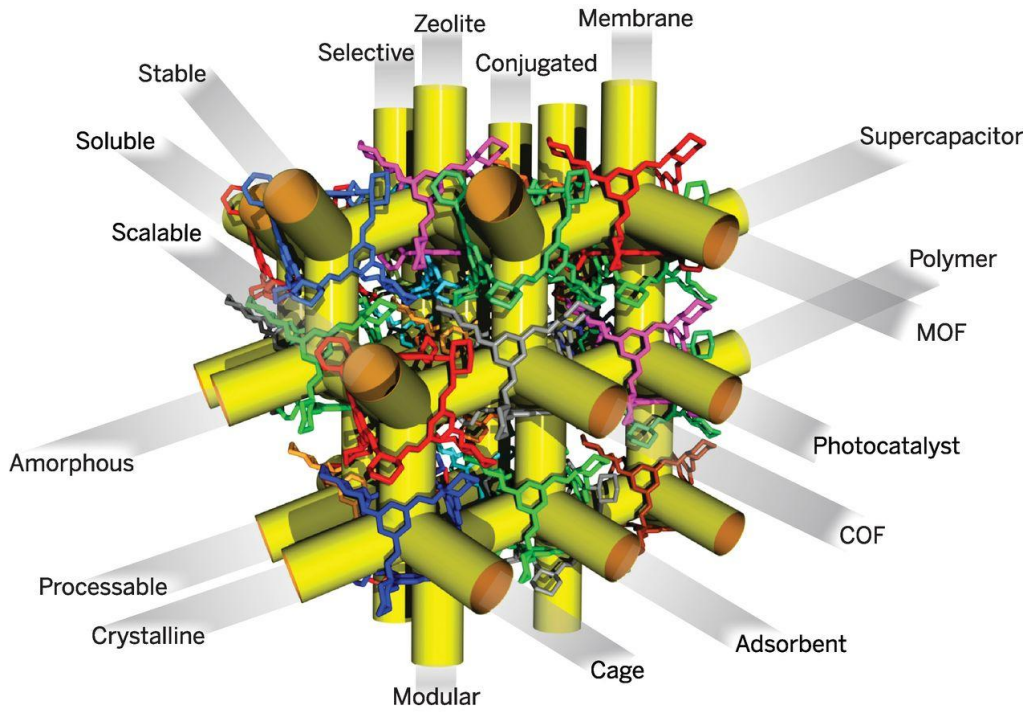

Figure 1.1: Schematic representation of different types of porous materials with their potential properties and applications. Reproduced with permission from reference 8.

Metal-Organic Frameworks (MOFs): MOFs are known as coordination polymers, ingeniously constructed through metal ions/nodes (sometimes called as secondary building units, SBUs) and organic struts, having potential voids.[12-14] It can be synthesized by conventional solvothermal as well as room temperature methods and their structures are regularly characterized in the laboratory by X-ray, synchrotron or neutron diffraction studies. The unprecedented surge in MOF research has been observed owing to its limitless possibility of tailored properties on account of enormous structural and functional variations.[15,16] Prior to this, no other materials offered accurate fine-tuning of structure and composition simultaneously. MOFs have been exclusively studied in a wide range of applications viz. gas storage, sensing, chemical separation, catalysis, drug delivery, biomedical imaging, template for carbon and metal oxides and many more.[13, 17-18] One of the unique features demonstrated by MOFs is the straightforward achievement of target-specific applications owing to its structure-property correlation, which led them

one step ahead compared to other porous solids. Although a limited number of MOFs have been entered into the commercial sectors, these materials surely will rule in various fields in the near future.

Porous Organic materials (POMs): In contrast to other APMs, porous organic materials (POMs) are solely built from organic components connected through covalent linkages. Recently POMs have received a significant research interest due to their combined properties of both porous materials and polymers.[19] A plethora of synthetic methods are available to produce POMs with a variety of structures including covalent-organic frameworks (COFs), hypercrosslinked polymers (HCPs), conjugated micropourous polymers (CMPs), polymer of intrinsic microporosity (PIM), covalent triazine framewoks (CTFs) and porous aromatic frameworks (PAFs).[20-24] Combination of thermal and chemical stability along with a huge number of organic functionalities and extended pi-conjugated frameworks are frequently claimed as key advantages of POMs over other APMs materials. Among the variety of POMs, structure-property correlation feature of COFs help them to advance in the forefront making them a research hotspot in recent times. COFs represent an emerging class of crystalline porous organic materials, in which atoms are covalently linked together to form an open extended network. COFs also have several properties like well-defined ordered structures, exceptional thermal and chemical stabilities, tunable pore size, and high porosity. Combination of these features render COFs as a viable contender in a range of applications, i.e., catalysis, membrane separation, gas storage, drug delivery, and electronics.[20] A variety of COFs has been produced through the formation of B-O, C-N, B-N, and B-O-Si linkages. Depending on the dimensions of the materials, COFs can be categorized into either 2 or 3-dimensional architectures. In the 2D COFs, the layered frameworks are stacked through strong supramolecular Pi bonding in an ordered columnar manner which facilitates the transportation of charge carriers towards the stacking directions. Therefore, 2D COFs holds great potential toward pi-electronics and functional materials for optoelectronics and photovoltaics applications. In contrast, 3D COFs are extended network in all three dimensions through a sp^3 carbon or silane atoms. Hence, 3D COFs possess ultra high surface area, low densities, and huge open functional sites. These features of 3D COFs makes them suitable alternative for gas storage applications.

Metal-Organic Polyhedra (MOPs): The term metal-organic polyhedra (MOP) was first introduced in the early 21st century. Unlike MOFs, metal-organic polyhedra are discrete molecular entities constructed from coordination assisted self-assembly of metal ions or metal clusters and organic building blocks having symmetric well-defined structures and confined cavities with multiple pore apertures.[25] MOPs are also sometimes recognized as nanoballs, nanospheres, nanocapsules or nanocages. The research interest in MOPs has grown significantly in the last two decades due to their wide range of applications in catalysis, sensing, host-guest chemistry, separation and storage, drug delivery, ion channel and many more.[26]

Additionally, the solubility of MOPs offers several advantages over other APMs in easy fabrication of thin films, membranes, ion channels including various biological applications etc.[27] A variety of design strategies were developed by supramolecular chemists for the synthesis of MOPs that includes directional bonding, molecular library, symmetry interaction, molecular panelling, weak-link, reticular chemistry, supramolecular blueprint and bridging ligand substitution strategies.

Metal-Organic Gel (MOG): Another newly developed APMs are soft metal-organic gels (MOGs), assembled from metal centers with organic ligands through metal-ligand coordination and various intermolecular forces e.g., weak Van der Walls interactions, hydrogen bonds, π-π stacking, etc. MOGs have shown attractive potential applications in the field of adsorption, sensing, catalysis, magnetism, drug delivery, etc. Moreover, high crack resistance capability and good foldability make them potential candidates for various wearable optoelectronic devices.[28] Porous MOGs having dual characters of both MOFs and gel characteristics in terms of varying pore sizes, tunable porosity, high specific surface areas along with flexibility, can easily be fabricated into different feasible structures in a much more efficient way.[29] The sponges like soft MOGs are also well suited as supporting matrix for synthesizing different shape and size specific NPs in a simplistic way.

1.3 Composite Materials

A composite material can be defined as a combination of two or more substances which retain their inherent identity or sometimes exhibits better and unique properties than those individual substances used alone.[30,31] The properties of composite materials depend on several factors: (I) the properties of individual components; (II) the relative amount of the components; (III) size, shape and distribution of the components, and (IV) the degree of interactions between the parental components, etc. In general, composite materials consist of a host matrix and functional guest species, where the guests are used for their higher activity while the host matrix is often used as a support for the guests. A variety of porous materials are frequently used as a host matrix for support media (Figure 1.2). These porous matrixes immobilize the functional guest materials and restrict both leaching and aggregation tendencies accompanying remarkable enhancement in their reactivity.[32] Furthermore, the host matrices can offer additional active sites which work synergistically with the guest in the composite material. In this regard, the APMs are an ideal choice as a host matrix for the encapsulation of different functional guests due to its tunable pore environment, uniform pore structures, multiple functional sites, flexibility in frameworks.[33] The selection of an appropriate host matrix can be achieved by taking advantage of a huge library of APMs, although sometimes simulation techniques are also used as an efficient screening

method. APMs are an ideal choice for encasing different functional guest species because of its following features.

Tunable pore environments: The pore surfaces of APMs are functionalized before or after post-assembly modification method. The APMs with similar structures and distinctive functionalities can be

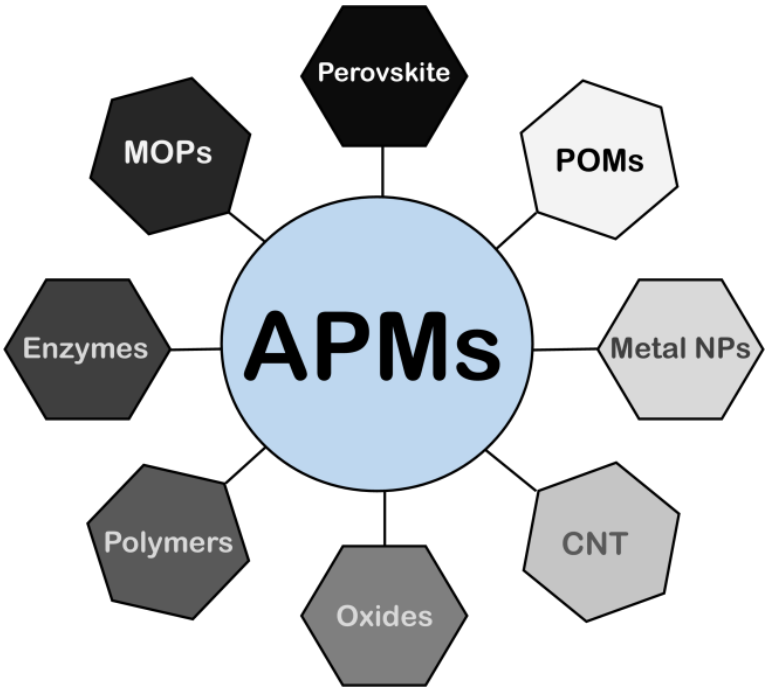

Figure 1.2: Composites of APMs and various functional materials.

synthesized by the utilization of isoreticular concept. Similar shape with large pore aperture can be easily achieved by increasing the length of the organic building block. The combination of identical structures and additional functional sites in the pore environment creates a huge impact on the performance efficiency of loaded guest materials. Furthermore, the tunability of the pore sizes of APMs influences the diffusivity of guest molecules, which has a fundamental importance in their potential applications.

Large pores with small windows: APMs having ordered pore cavities that are accessible through small apertures are suitable as a host matrix for accommodating functional guests. If APMs have unidirectional 1D channels, the loaded guest molecules can freely move through the channels and sometimes can aggregate or escape from the internal cavity. But, APMs with large cavity with small pore aperture prevents the leaching or aggregation propensity of the guests and also helps them to immobilize into the

host matrix. In this case, the size of the guest species should be in between the internal cavity and pore aperture of the host matrix, although flexible hosts provide some relaxation.

Uniform pore structure: Crystalline Porous materials are composed of uniform cavity distributed throughout their lattice with long-range order. Thus APMs featuring crystallinity enables the ordered arrangement of guest species in the host matrix and facilitate the examination of interactions between the host matrix and entrapped guest species.

Multiple functional sites: APMs can be functionalized by modifying either the organic struts or metal nodes or by modifying both at a time. The incorporation of various functional sites into a framework can allow them to work in a cooperative and synergistic manner, which is not possible in traditional porous solids. For instance, the photocatalytic performances of the guest species can be enhanced to a great extent by incorporating semiconducting metal nodes or light-sensitive organic building blocks in the porous frameworks.

Flexible frameworks: APMs have a unique feature of flexibility in frameworks which is also an essential requirement for hosting the functional guest species. The smaller pore cavity of APMs matrix can sometimes accommodate the larger size of the guest species due to the flexible character in the frameworks, which is unimaginable for conventional porous solids.

1.4 Synthesis Strategy of Composite Materials

The performance efficiency of composite materials strongly depends on the shape, size and distribution of guest species into the host matrix. The development of facile fabrication protocols control these important parameters and consequently influences the overall performance efficiency to a great extent of composite materials. Few strategies are well-documented for the immobilization of guest species into the host matrix.

Assembly of guest species inside the pre-synthesized host cavity: In this procedure, the functional guest species are formed through immobilization of the guest precursors inside the pre-synthesized host matrix (Figure 1.3 and 1.4).[34] This widely adopted technique known as ship-in-bottle strategy. In this approach, first, the guest precursors are impregnated into an APM matrix by various techniques such as vapour deposition, solid grinding and solution infiltration, followed by reduction of precursors to desired guest material. In this approach, the host pores limit the growth of the guest species, so that they remain confined inside the pores. However, some challenges still remain in this technique. (I) the host matrix should be stable under the synthetic condition of guest species. (II) Partial degradation of host framework

due to the formation of larger size guest species. (III) The precise control over internal location, composition, and structure of guest species into the host cavity is challenging. Several methods are available for the infiltration of guest precursors into the host matrix which are described as follows.

(I) Chemical vapour deposition (CVD): CVD is one of the oldest methods known for the loading of guest species into the host matrix. In this process, first precursor molecules are impregnated into the pores of a host matrix by a sublimation process and subsequently decomposition achieved by thermal or photochemical conditions. As this method avoids the use of any solvents, it allows maximum loading of the guest species into the host matrix. However, the major drawback in this process is the formation of bigger sized guest species compared to the pores of the host matrix, resulting in partial breakage of the frameworks. Moreover, the CVD process still not investigated completely due to its difficulty in controlling the deposition process in a reproducible manner.

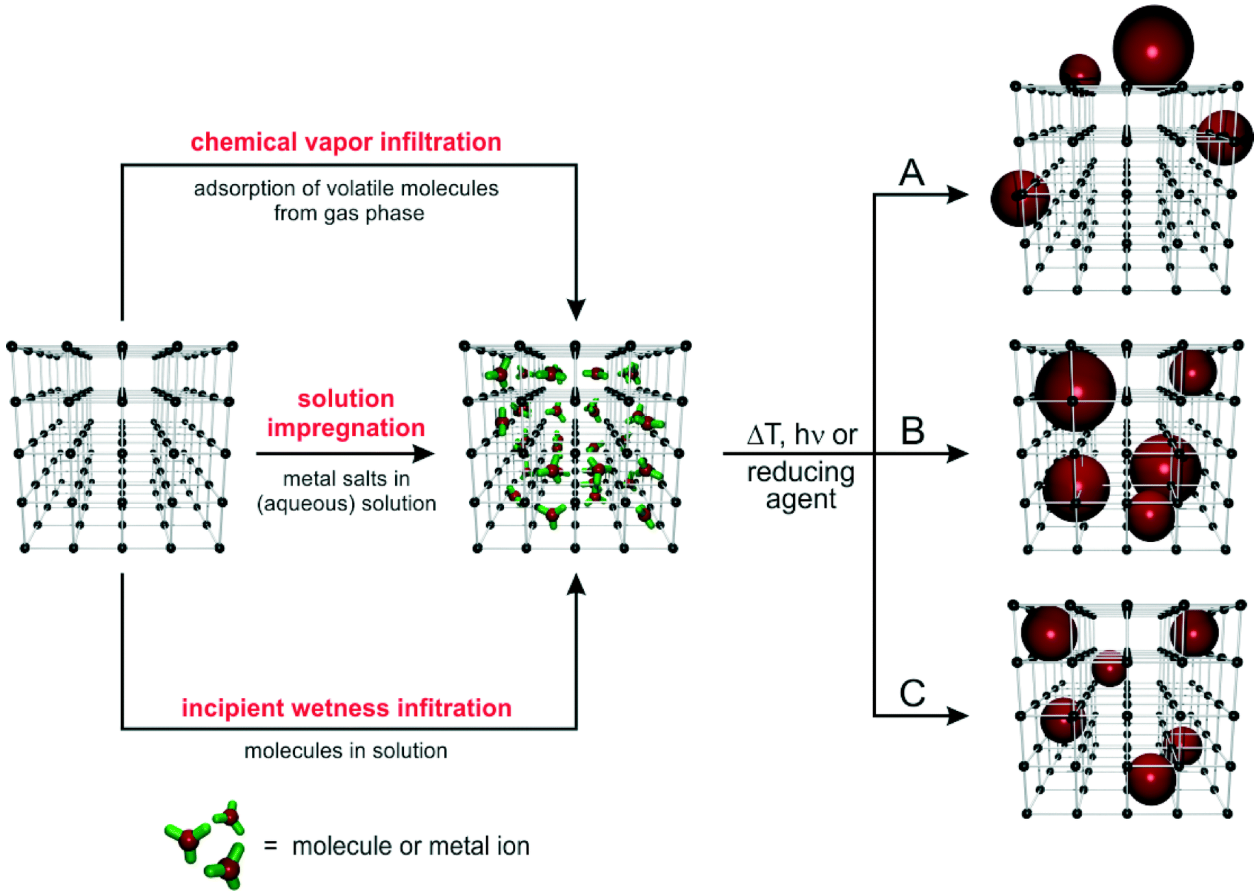

Figure 1.3: Schematic representation for the fabrication of functional guest species into a pre-synthesized host cavity Reproduced with permission from reference 31.

(II) Solution infiltration method: The following approach entails the use of the precursor solutions for the liquid phase impregnation. In this process, the solution of the guest precursors is immersed in an appropriate solution to infiltrate into the empty cavity of the host matrix. Subsequently, reduction of the precursors is carried out for the construction of desired guest species. The loading capacity depends on the solubility of the guest precursors in the solution. The distribution of the guest species throughout the host matrix depends on both guest precursors and the nature of the host matrix. The limitation of this method is the formation of a broad particle-size throughout the host matrix. Sometimes, the host matrix may collapse under the harsh condition of external reducing agents like $NaBH_4$ or hydrazine.

(III) Incipient wetness impregnation: This process is quite similar to the solution impregnation technique, the only difference is the precursor solution of guest is reduced to a minimum amount. Although, in this technique, the maximum loading of guest species is possible without decomposition of the framework, but it is limited by the solubility of guest precursors in suitable solvents.

(IV) Solid-state grinding: Infiltration of guest species inside the porous host matrix can also be achieved by solid-state grinding of volatile guest precursors without the addition of any solvents. During the grinding process, the volatile guest precursors sublimate to vapour and diffuse into the cavities of the host matrix, resulting well-distributed deposition of precursors molecules. Subsequently, the reduction of the embedded guest precursors is carried out to produce small-sized desired guest species throughout the host matrix. The grinding process is a relatively simple and effective way for producing the guest loaded host matrix without using any solvents and washing procedures after infiltration.

Assembly of host around the guest species: This approach is bottle-around-ship or template synthesis approach, where the desired composite is fabricated by the construction of a host matrix via self-assembly around the pre-synthesized functional guest species.[35] Generally, the pre-synthesized guest species are not present in the cavities of the host matrix but instead are covered by the host framework. In this process, not only the common problems, i.e., the aggregation of guest species on the external surface and partial damage of the host framework is overcome, but also composition, size, and morphology of the guest species can also be preserved. As the guest species are synthesized prior to the encapsulation, their particle size is not restricted to the aperture size of the host frameworks. However, in this strategy guest species are generally undergoing self-nucleation outside the host matrix. Additionally, in most of the cases, guest materials are unable to stand under the reaction condition of the host matrix.

Sandwich assembly strategy: Guest species are impregnated between the two shells of the porous host matrix in this method.[34] This unique approach involves the preparation of a host core followed by infiltration of desired guest species and subsequently overgrowth of a porous host shell onto the guest

deposited host core. The multi-layered composite materials can also be synthesized by repeating both the steps i.e. functional guest deposition and host overgrowth. This process provides good control over the position, shape, and composition of the guest species in the desired composite material. The major challenge in this method is the growth of fracture-free shell on the core. In addition, extra surfactant capping agents are needed to the formation of fracture-free shell on the guest deposited host core when a selected matrix is of mismatched topologies.

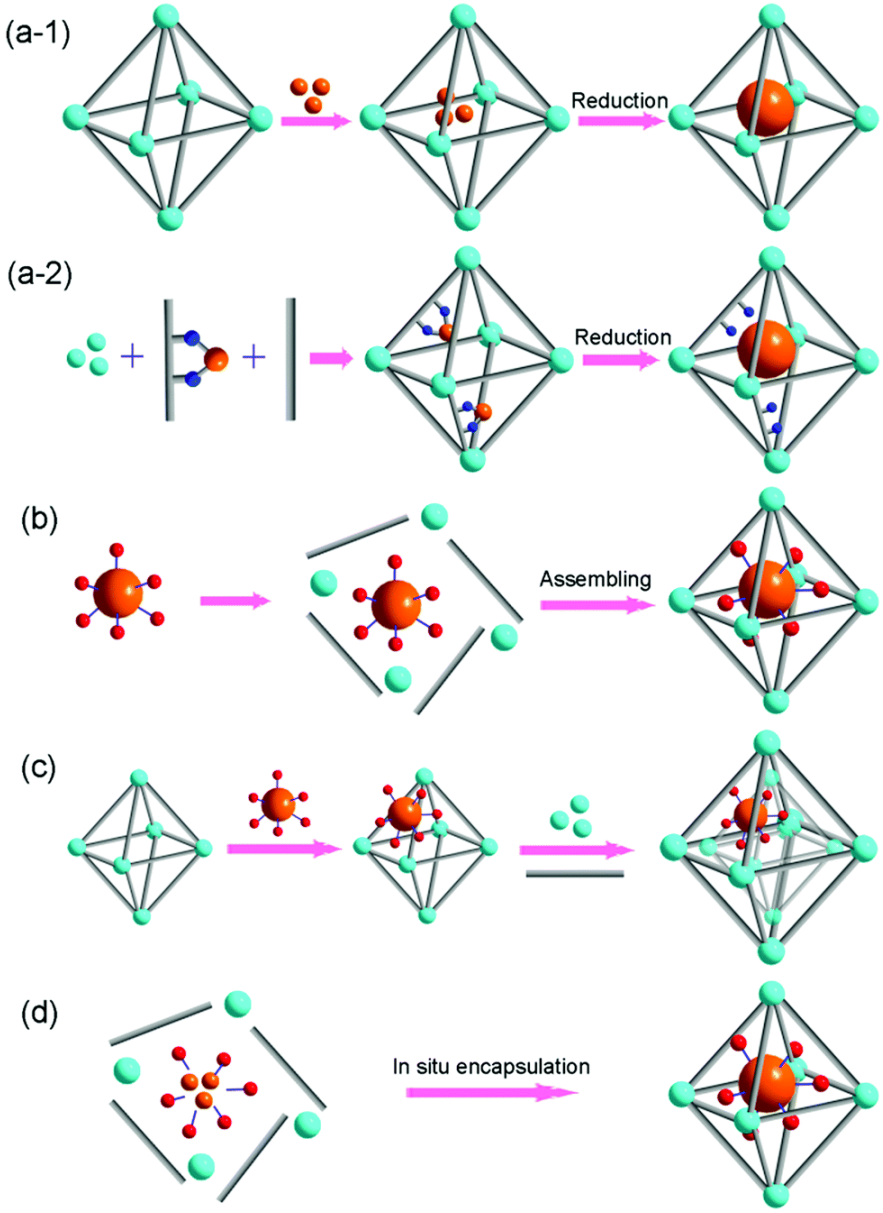

Figure 1.4: Schematic representation for the fabrication of composite materials. Reproduced with permission from reference 34.

***In situ* encapsulation strategy:** This strategy entails mixing of all the constituents of both the host matrix and functional guest precursors in a proper solution, where the guest species and host framework forms simultaneously.[36] The balance between the nucleation rates of both the materials are strongly dependent on several factors viz. precursors concentrations, solvents selection, reaction temperature and modulators. This recently developed one-pot synthesis method is suited for composite materials in practical applications due to its ease of operation, low production cost and reproducibility. Nevertheless, as both the guest species and host matrix synchronously form at the same reaction condition, control growth of these two distinct complexes is a challenging task.

1.5 Functional Applications of Composite Materials

Nano-sized functional guests entrapped inside a porous cavity possess noticeably different physicochemical properties as compared to their bulk forms on account of their large surface-to-volume ratio and quantum effects. While a great deal of research efforts have been devoted to produce new APMs aimed at various exciting applications, immobilization of a variety of functional guests into APM support has also been proposed simultaneously to combine their merits and alleviate the weakness of both the parental components. APM based composites has been extensively applied in a wide range of applications by taking advantages of growth restriction of nano-sized guests, large surface areas and size selectivity of APM matrices (Figure 1.5).

Sorption Studies: Adsorption properties of gases/liquids in APM matrix is crucial for many applications, such as storage, separation and transportation.[37,38] The inherent tunable voids and target-specific functional composition of APMs make them attractive for adsorption based applications. However, lack of flexibility/brittleness, durability, complicated fabrication and limited scalability have made pure APMs suboptimal contender towards commercialization. Recently, it has been shown that the loading of functional guests can tune the adsorption capacity of APMs. Selective and efficient adsorption of sorbate molecules could also be achieved by the infiltration of nano-sized guests with an optimal affinity towards specific molecules of interest.

Sensing: Few APMs have shown bright luminescence properties originating from its building blocks (either organic or combination of both organic and inorganic moieties) that provides a unique platform for utilization for attractive applications.[39] The multi-encapsulation of luminescent guests into the APM matrices is an effective approach for the fabrication of efficient light sources that include display, light-emitting diodes (LEDs), laser, etc. The APM matrices protect the unstable luminescent guests from various chemical decompositions as well as prevent them from aggregation.[40] Sometimes, APM matrix

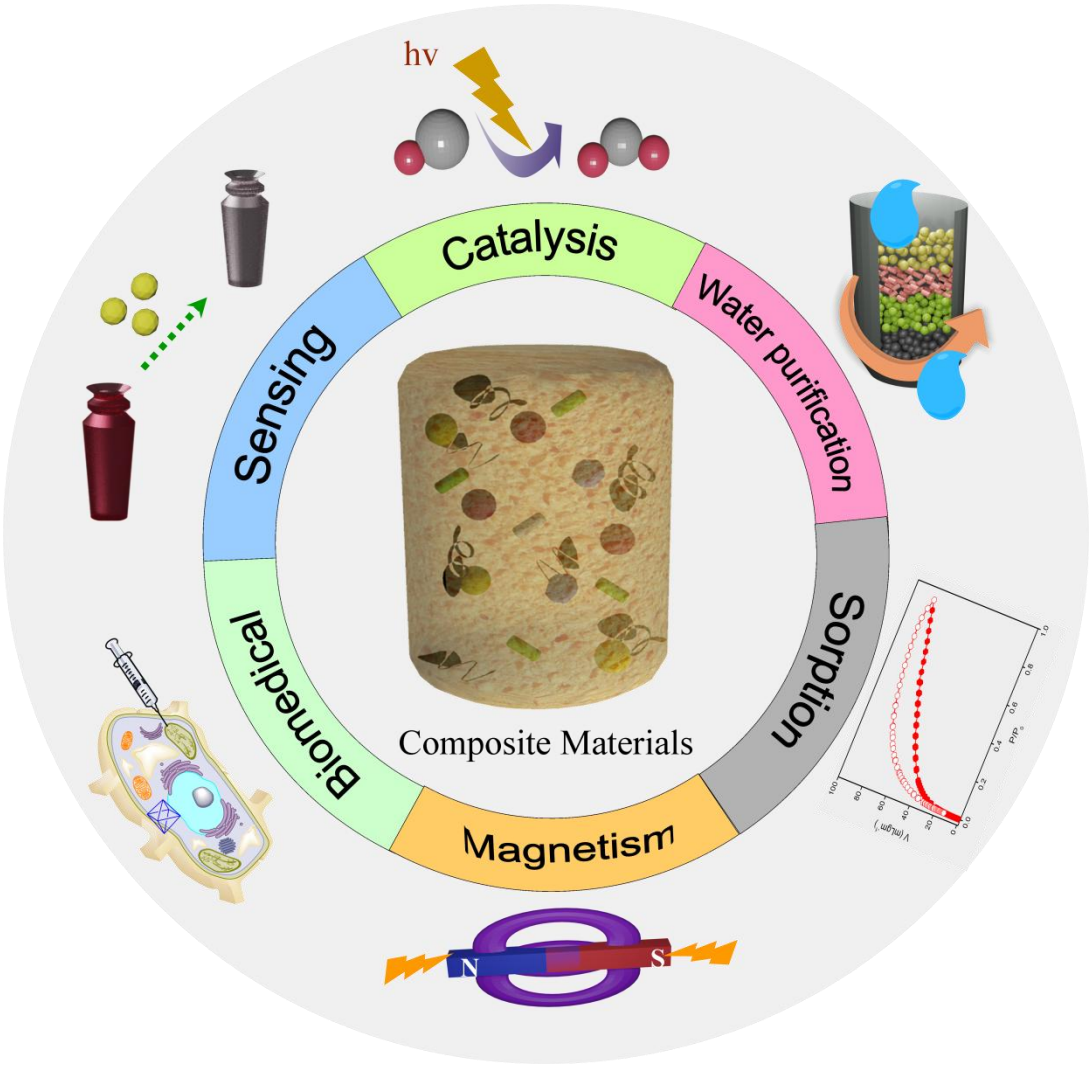

Figure 1.5: Schematic representation for the wide range of applications with composite materials.

also helps to improve the luminescence property significantly compared to its pristine guests due to its strong interactions with guests.

Catalytic Properties: Variety of nano-sized materials including enzymes are known for their catalytic activity due to their excellent abilities such as exceptional affinities towards the substrate and catalytic performance efficiency based on their high stereo-, chemo-, and regioselectivities.[41] However, even with these outstanding advantages, these functional materials exhibited low operational stability, difficult recovery and lack of reusability under operational conditions. Therefore, immobilization of such materials into porous materials are one of the most effective strategies to mitigate these challenges and also widen their applications.[42] APMs are most suited for this purposes due to their ultrahigh surface area including

tunable pores as well as adjustable surface functionalities, making them industrially and commercially viable.

Water Purification: Sequestration of toxic pollutants (both organic as well inorganic) from highly contaminated wastewater streams through adsorption process is an attractive alternative technique. However, conventional ion exchange resigns including porous materials, suffer from very slow kinetics, poor capturing efficiency and limited selectivity for toxic pollutants.[43] Very recently, APMs combined with other functional materials not only enhances their removal performance efficiencies but also render them practical utility.[44]

Biomedical Applications: Recent reports reveal that APMs has great potential for biomedical applications especially, carrier of drug molecules and contrast agents for medical imaging. The functionalized pore surface of APMs can provide exquisite control over the colloidal stability, biocompatibility, recognition capabilities and biodistribution of drug molecules.[45] These properties strongly affects the biomedical applications compared to the stand-alone drug molecules. Additionally, APMs offer control drug loading and release due to its tunable pore architecture and compositions. However, covalent grafting of drug molecules to the pore surfaces sometimes reduce the porosity of APMs due to inclusion of the drug molecules. To avoid this problem, the accessible aperture size of selected APMs should be smaller than the selected drug molecules.

Magnetic properties: Magnetic property is crucial for many applications viz. high-density information storage, quantum computing, magnetic resonance signal enhancer and many more.[46] Although a library of APMs exhibits magnetic behaviour, the construction of a porous APMs with excellent magnetism still remains a challenging task. Therefore, immobilization of magnetic guests into the cavity of APMs can partially allow to mitigate these issues as the porosity and magnetism are the two reverse features of a material.

1.6 Thesis Overview

Herein, all the works included in this thesis has focused on the stability and functional studies of unstable materials after loading into different advanced porous materials (APMs). Although APMs are utilized in a variety of applications, but they are rarely been used for stabilization of unstable materials as a host matrix. The whole thesis consists of two parts and each part is further separated into two chapters respectively. In part-I, the stabilities and functional studies of carboxylate MOPs are described, while in part-II stability issues of perovskite have been resolved after impregnation into diverse APM matrices and are further utilized in different applications.

Cu(II) based carboxylate MOP is one of the APMs that suffer from two major challenges namely, hydrolytic instability and aggregation after guest removal. Either or combination of both of these shortcomings restricts the realization of the full potential of these materials. In chapter-2, a series of chemically stable Cu(II) based carboxylate MOP has been synthesized by using the outer-surface hydrophobic shielding as a general strategy. The hydrolytic instability issue of MOPs is overcome in this chapter. Another shortcoming, i.e., aggregation issue also influences the performance efficiency to a great extent. Therefore in chapter-3, the aggregation issue is resolved by covalently grafting of cage molecules into a COF matrix. The overall composite material is transformed into cationic nature due to the existence of cationic cage molecules. The resulting hybrid material is then used for water purification as a functional study.

Hybrid bromide perovskites (HBPs) have emerged as a promising candidate in optoelectronic applications. However, the extreme instability of these materials under working conditions has retarded its progress towards commercialization. In part-II, extremely unstable hybrid perovskite is stabilized in different APM matrices. In chapter-4, hybrid perovskite NCs are impregnated inside a well-known chemically stable MOF matrix. The resulting composite materials have been employed as a heterogeneous photocatalyst to degrade lethal organic pollutants directly in water media. Although the materials showed exceptional stability in a variety of polar solvents including water for a longer period of time, these materials are not suitable for optoelectronic applications due to its heterogeneous nature. Therefore, for utilization in device technology, the HBP NCs should be embedded into soft porous materials. In chapter-5, blue-emitting HBP NCs are embedded inside a soft porous MOG matrix. Here, the host MOG matrix offers dual benefits to the perovskite NCs: namely, it serves as a protective barrier against the degradation under working conditions and also enhances the luminescence properties. Additionally, the as-synthesized flexible composite materials were coated on a UV LED for the construction of white light-emitting diode (WLEDs).

1.7 References

[1] D. Wu, F. Xu, B. Sun, R. Fu, H. He, K. Matyjaszewaski, *Chem. Rev.* **2012**, *112*, 3959-4015.

[2] A. I. Cooper, *ACS Cent. Sci.* **2017**, *3*, 544-553.

[3] A. Corma, *Chem. Rev.* **1997**, *97*, 2373-2419.

[4] M. E. Davis, R. F. Lobo, *Chem. Mater.* **1992**, *4*, 756-768.

[5] F. Fajula, A. Galarneau, F. Di Renzo, *Microporous Mesoporous Mater.* **2005**, *82*, 227-239.

[6] D. Zhao, P. K. Thallapally, C. Petit, J. Gascon, *ACS Sustainable Chem. Eng.* **2019**, *7*, 7997-7998.

[7] M. E. Davis, *Nature*, **2002**, *417*, 813-821.

[8] A. G. Slater, A. I. Cooper, *Science* **2015**, *348*, aaa8075.

[9] J. A. Evans, K. E. Jelfs, G. M. Day, C. Doonan, *Chem. Soc. Rev.* **2017**, *46*, 3286-3301.

[10] J. Zhang, J. Chen, S. Peng, S. Peng, Z. Zhang, Y. Tong, P. W. Miller, X.-P. Yan, *Chem. Soc. Rev.* **2019**, *48*, 2566-2595.

[11] X.Y. Yang, L.-H. Chen, Y. Li, J. C. Rooke, C, Sanchez, B.-L. Su, *Chem. Soc. Rev.* **2017**, *46*, 481-558.

[12] G. Maurin, C. Serre, A. Cooper, G. Ferey, *Chem. Soc. Rev.* **2017**, *46*, 3104-3107.

[13] H.-C. Zhou, S. Kitagawa, *Chem. Soc. Rev.* **2014**, *43*, 5415-5418.

[14] H. Furukawa, U. Muller, O. M. Yaghi, *Angew. Chem. Int. Ed.* **2015**, *54*, 2-16.

[15] L. Jiao, J. Y. R. Seaw, W. S. Skinner, Z. U. Wang, H.-L. Jiang, *Mater. Today* **2019**, *27*, 43-68.

[16] A. Carne, C. Carbonell, I. Imaz, D. Maspoch, *Chem. Soc. Rev.* **2011**, *40*, 291-305.

[17] X. Cao, C. Tan, M. Sindoro, H. Zhang, *Chem. Soc. Rev.* **2017**, *46*, 2660-2677.

[18] W. P. Lusting, S. Mukherjee, N. R. Rudd, A. V. Desai, J. Li, S. K. Ghosh, *Chem. Soc. Rev.* **2017**, *46*, 3242-3285.

[19] S. Das, P. Heasman, T. Ben, S. Qiu, *Chem. Rev.* **2017**, *117*, 1515-1563.

[20] S.-Y. Ding, W. Wang, *Chem. Soc. Rev.* **2013**, *42*, 548-568.

[21] L. Tan, B. Tan, *Chem. Soc. Rev.* **2017**, *46*, 3322-3356.

[22] N. Chaoui, M. Trunk, R. Dawson, H. Schmidt, A. Thomas, *Chem. Soc. Rev.* **2017**, *46*, 3302-3321.

[23] R. Dawson, A. I. Cooper, D. J. Adams, *Prog. Polym. Sci.* **2012**, *37*, 530-563.

[24] Y. Yuan, G. Zhu, *ACS Cent. Sci.* **2019**, *5*, 409-418.

[25] D. J. Tranchemontagne, Z. Ni, M. O'Keeffe, O. M. Yaghi, *Angew, Chem. Int. Ed.* **2008**, *47*, 2-14.

[26] N. Ahmad, A. H. Chughtai, H. A. Younus, F. Verpoort, *Coord. Chem. Rev.* **2014**, *280*, 1-27.

[27] N. Ahmad, H. A. Younus, A. H. Chughtai, F. Verpoort, *Chem. Soc. Rev.* **2015**, *44*, 9-25.

[28] J. Zhang, C.-Y. Su, *Coord. Chem. Rev.* **2013**, *257*, 1373-1408.

[29] J. H. Jung, J. H. Lee, J. R. Silverman, G. John, *Chem. Soc. Rev.* **2013**, *42*, 924-936.

[30] C. R. Kim, T. Uemura, S. Kitagawa, *Chem. Soc. Rev.* **2016**, *45*, 3828-3845.

[31] C. Rosler, R. A. Fischer, *CrystEngComm*, **2015**, *17*, 199-217.

[32] A. Aijaz, Q. Xu, *J. Phys. Chem. Lett.* **2014**, *5*, 1400-1411.

[33] S. Dang, Q. Zhu, Q. Xu, *Nat. Rev. Mater.* **2017**, *3*, 17075.

[34] L. Chen, R. Luque, Y. Li, *Chem. Soc. Rev.* **2017**, *46*, 4614-4630.

[35] J. Aguilera-Sigalat, D. Bradshaw, *Coord. Chem. Rev.* **2016**, *307*, 267-291.

[36] S. Wang, C. M. McGuirk, A. d'Aquino, J. A. Mason, C. A. Mirkin, *Adv. Mater.* **2018**, *30*, 1800202.

[37] Q.-L. Zhu, Q. Xu, *Chem. Soc. Rev.* **2014**, *43*, 5468-5512.

[38] B. Seoane, J. Coronas, I. Gascon, M. Etxeberria Benavides, O. Karvan, J. Caro, F. Kapteijn, J. Gascon, *Chem. Soc. Rev.* **2015**, *44*, 2421-2454.

[39] Y. Cui, J. Zhang, H. He, G. Qian, *Chem. Soc. Rev.* **2018**, *47*, 5740-5785.

[40] D. Chen, M. Xu, P. Huang, *Sens. Actuators, B* **2016**, *231*, 576-583.

[41] A. Dhakshinamoorthy, H. Garcia, *Chem. Soc. Rev.* **2012**, *41*, 5262–5284.

[42] L. Chen, Q. Xu, *Matter* **2019**, *1*, 57-89.

[43] M. Mon, R. Bruno, J. Ferrando-Soria, D. Armentano, E. Pardo, *J. Mater. Chem. A* **2018**, *6*, 4912-4947.

[44] T. Kitao, Y. Zhang, S. Kitagawa, B. wang, T. Uemura, *Chem. Soc. Rev.* **2017**, *46*, 3108-3133.

[45] N. Ahmad, H. A. Younus, A. H. Chughtai, F. Verpoort, *Chem. Soc. Rev.* **2015**, *44*, 9-25.

[46] K. Liu, X. Zhang, X. Meng, W. Shi, P. Cheng, A. K. Powell, *Chem. Soc. Rev.* **2016**, *45*, 2423-2439.

Part-I

Stabilization and Functional Studies of Metal-Organic Polyhedra (MOP) / Cage

MOPs constructed through self-assembly of metal ions and organic linkers. Because of their intriguing structures, relevance to naturally occurring biological self-assembled systems, multifarious potential applications (molecule inclusion, catalysis, sensing, adsorption, ion channel, drug delivery etc), MOPs have great centre of research interest to scientific community in recent years. MOPs can be broadly divided into two classes based on their composition, that is, the types of ligand they are built upon: a) N-donor ligands *e.g.* pyridine/pyrimidine, b) O-donor ligands *e.g.* carboxylate. The N-donor ligand derived MOPs tend to be hydrolytically stable and are more relevant for their excellent solution chemistry. However, presence of extra framework anions, the solid-state applications have largely eluded with such N-donor ligand based MOPs due to lack of porous properties. Numerous phenolate-linker based MOPs which are consists of O-donor linkers, have reported but they have mostly been studied in solution phase, and the solid-state porous properties of these cages have not been explored. While, most of the reported carboxylate MOPs exhibited porous properties, but they mostly unable to stand against heat, water and/or chemical treatment. MOPs with solid-state porous properties are mostly constructed with carboxylate linkers and herein I will focus mainly on the solid-state applications of these MOPs.

Despite a few decades of research focused on exterior functionalization-friendly MOPs, there are two main obstacles to overcome in the quest of tailoring carboxylate MOPs with the desired extent of stability, more precisely: a) poor hydrolytic stability and b) aggregation of MOPs after solvent removal, either or both of which often restrict us to extract the full potentials from these materials. Carboxylate MOPs are generally constructed from weak and reversible M-O coordination bonds; such coordination bonds are promptly susceptible towards trace amounts of water or in some cases, are instantly decomposed even on exposure to atmospheric moisture content. Most of the carboxylate MOPs are sensitive towards water molecules which leads to the displacement of ligands, phase changes, structural decomposition before they may end up partially/entirely losing their porosity. That most of the MOPs are composed of transition metals to afford labile M-O bonds is in downright agreement with hydrolytic stability posing as the major bottleneck to block the progress of MOPs. Another challenge associated with MOPs is aggregation after guest removal. During their syntheses, some guest molecules get entrapped inside the host MOPs. So prior to their use for any purpose, activation *i.e.* the removal of guest molecules is an essential step to access their active sites. But, MOPs generally undergo random aggregation or reorganization or even structural collapse upon solvent removal due to the absence of any strong supramolecular interaction between the constituent neighbouring cages. Such rearrangement of cages results in blockage of pore windows among the neighbouring cages, thus restricts the diffusion of sorbate molecules through the aggregated MOP. Consequently, performances of MOPs being directly reliant on their featured porosity and/or exposed active sites decrease severely. In some cases, this corresponds to

MOPs barely adsorbing any molecules or their negligible catalytic activities, much against their anticipated execution, when correlated to their guest-removed porous void and/or active sites based on crystal structures of the solvated pristine host.

In this section, both the major shortcomings of MOP are resolved. The hydrolytic instability issue was resolved by using outer surface hydrophobic shielding strategy in chapter 2, while aggregation properties are restricted by covalent linking of cage into COF matrices in the subsequent chapter.

Chapter 2

Outer Surface Hydrophobic Shielding Strategy to Enhance the Chemical Stability of Metal-Organic Polyhedra

2.1 Introduction

Over the last few decades, there has been an astonishing evolution of crystalline porous solid materials and they have been the center of great attention to researchers across multiple disciplines.[1,2] Among the various crystalline porous solids, metal-organic frameworks (MOFs) and covalent-organic frameworks (COFs) have emerged as distinguished targets, and on account of their high surface area these materials have been explored for several applications, such as selective gas storage and separation ability, sensing, catalysis, energy storage and conversion capacity etc.[3-8] Carboxylate metal-organic polyhedra (MOP) form a subclass of crystalline porous materials which were proposed almost at the same time as MOFs.[9,10] Over the last few years realization of rational design strategies has yielded several hydrolytically stable MOFs and COFs[11-16] and actuated their development towards practical implementation, but a lack of systematic approaches to prepare stable MOPs has severely hindered the progress of carboxylate MOPs for application studies. Broadly, there are few strategies proposed for the synthesis of porous MOPs[17-20] but the majority of carboxylate MOPs reported in the literature have been found to be hydrolytically unstable. The solid-state applications of such MOPs are largely impeded owing to their instability and loss of crystallinity as an outcome of unavoidable aggregation-driven blockage of active sites upon guest removal.[21,22] Although some discrete reports have been proposed to improve the stability of MOPs by enhancing the metal–ligand bond strength[23-25] or appending long alkyl chains,[26] there is a lack of a broad design approach to attain chemically inert carboxylate MOPs. In principle, MOPs offer similar potential applications as MOFs, including additional advantages of solution processability[27] for MOPs in common organic solvents, a feature which is highly sought after for the easy fabrication of membranes, thin-film devices, preparation of electrolytic solutions, various active additives in polymers and ion channels, including various biochemical applications etc.[28, 29]

A generalized strategy for synthesizing chemically inert MOPs can contribute significantly to the development of crystal engineering based on structure-function relationships and boost the growth of MOPs in view of their miscellaneous applications. Herein, we develop a prototypal synthesis strategy which allows us to prepare a series of hydrolytically stable carboxylate MOPs by grafting of the hydrophobic exterior to basic building blocks, and in principle this versatile approach can be applied to stabilize any MOP structure, irrespective of metal ions and nature of coordinating ligands used in the synthesis. Amino acids are chosen as building blocks because their functional groups can be easily modulated,[30] and polar pore surfaces decorated with an electron-deficient anhydride often impart excellent guest-responsive characteristics of through the diimide linkers. Among the transition-metal ions, the binuclear copper paddle wheel is well recognized for easily affording carboxylate MOPs, owing to the four-connected secondary building units (for schematic see Figure 1).[31] With water stability being the

key targeted criterion, deliberately enhanced steric crowding surrounding the metal coordination sites results in an ultra-stable, and the first superhydrophobic MOP.[32] More importantly, as a consequence of increased hydrophobicity, a distinct enhancement of chemical stability was achieved by rationally tuning the alkyl functionality of the substituted diimide linkers, as was further supported by molecular simulation studies. We hereby present the quick (within seconds) multigram scale synthesis of a chemically ultra-stable (wide ranges of pH, oxidizing and reducing media) MOP by employing hydrophobicity increment principle.

.

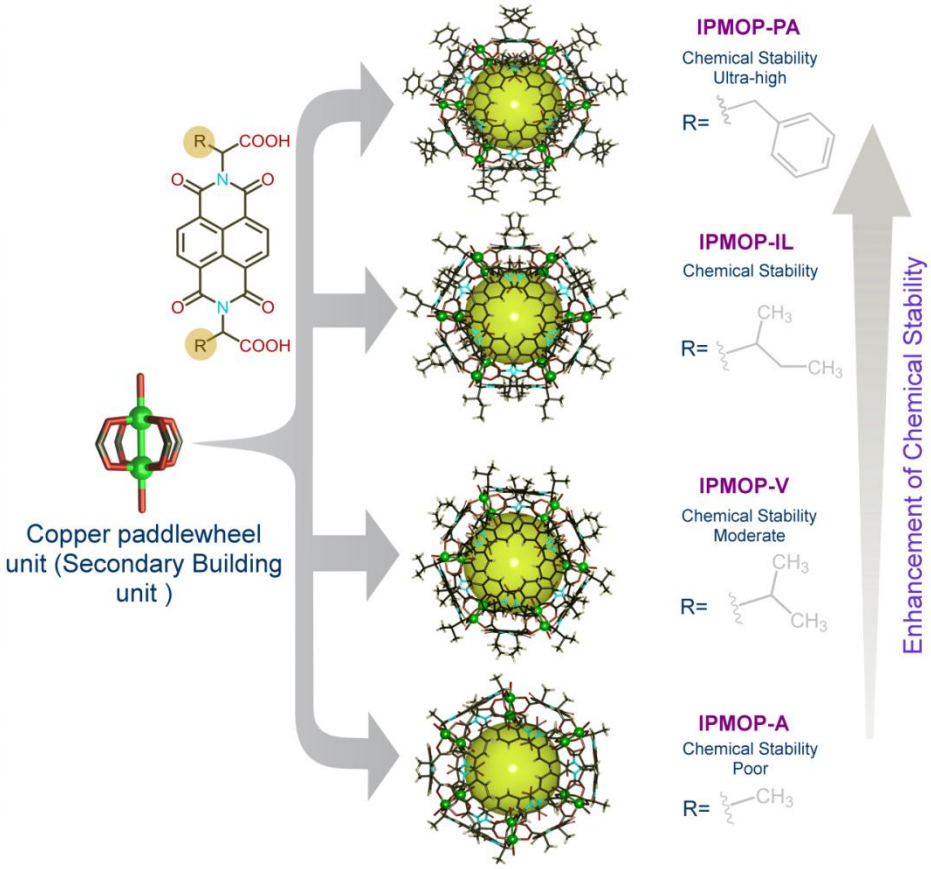

Figure 2.1. Schematic synthetic strategy for MOPs and their corresponding crystal structures following a systematic increment order of their chemical stabilities (as illustrated from bottom to top).

2.2 Experimental

2.2.1 Materials

1,4,5,8 naphthalenetetracarboxylic dianhydride and all four amino acids were purchased from Sigma-Aldrich. $Cu(NO_3)_2.3H_2O$ was purchased from Merck. All solvents including standard buffer solutions were purchased from Spectrochem and used without further purification. The reagents and solvents were commercially available and were not purified any further.

2.2.2 Synthesis

Synthesis of 2,2'-(1,3,6,8-tetraoxo-1,3,6,8-tetrahydrobenzo[lmn][3,8]phenanthroline-2,7-diyl)dipropionic acid (H_2L_A). A mixture of naphthalene dianhydride (3 g, 11.2 mmol) (Scheme 1) and L- Alanine (2.095 g, 23.5mmol) was refluxed in 80 mL Acetic acid for 36 h. The reaction mixture was allowed to cool to room temperature. The resulting solutions was concentrated to ~ 10 mL under reduced pressure and diluted with distilled water to give the final product. Yield 4.132 g, ~90%. Without further purification the ligands H_2L_A were used for crystallization.

Synthesis of 2,2'-(1,3,6,8-tetraoxo-1,3,6,8-tetrahydrobenzo[lmn][3,8]phenanthroline-2,7-diyl)bis(3-methylbutanoic acid) (H_2Lv). A mixture of naphthalene dianhydride (3 g, 11.2 mmol) (Figure S1) and L-Valine (2.753 g, 23.5mmol) was refluxed in 80 mL Acetic acid for 36 h. The reaction mixture was allowed to cool to room temperature. The resulting solutions was concentrated to ~ 10 mL under reduced pressure and diluted with distilled water to give the final product. Yield 4.749g, ~91%. Without further purification the ligands H_2L_V were used for crystallization.

Synthesis of 2,2'-(1,3,6,8-tetraoxo-1,3,6,8-tetrahydrobenzo[lmn][3,8]phenanthroline-2,7-diyl)bis(3-methylpentanoic acid) (H_2L_{IL}). A mixture of naphthalene dianhydride (3 g, 11.2 mmol) (Figure S1) and L-Isoleucine (4.797 g, 23.5mmol) was refluxed in 80 mL Acetic acid for 36 h. The reaction mixture was allowed to cool to room temperature. The resulting solutions was concentrated to ~ 10 mL under reduced pressure and diluted with distilled water to give the final product. Yield 5.6 g, ~89% .Without further purification the ligands H2LIL were used for crystallization.

Synthesis of 2,2'-(1,3,6,8-tetraoxo-1,3,6,8-tetrahydrobenzo[lmn][3,8]phenanthroline-2,7-diyl)bis(3-phenylpropanoic acid) (H_2L_{PA}). A mixture of naphthalene dianhydride (3 g, 11.2 mmol) (Figure S1) and L-Phenyl Alanine (4.797g, 23.5 mmol) was refluxed in 80 mL Acetic acid for 36 h. The reaction

mixture was allowed to cool to room temperature. The resulting solutions was concentrated to ~ 10 mL under reduced pressure and diluted with distilled water to give the final product. Without further purification the ligands H_2L_{PA} were used for crystallization.

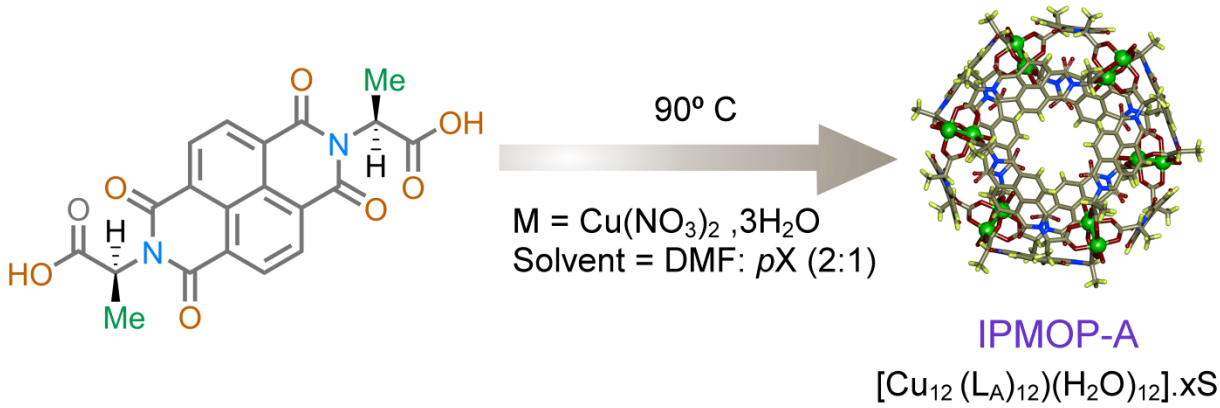

Scheme 2.1. Synthesis scheme of IPMOP-A.

Synthesis of $[Cu_{12}(L_A)_{12}(H_2O)_{12}].xS$ (IPMOP-A). A mixture of H_2L_A (20.5mg, 0.05 mmol), $Cu(NO_3)_2.3H_2O$ (12.1 mg, 0.05 mmol), DMF (2 mL) and p-xylene (1 mL) was placed in a Teflon capped glass vial. This was heated at 90 °C for 48 h and then slowly cooled to room temperature (RT) over the next 12h. Growth of green, cubic-shaped crystals was observed upon cooling to RT, the desired product $[Cu_{12}\ (L_A)_{12})(H_2O)_{12}].xS$ appeared in 4.6 mg yield.

Room Temperature Synthesis of IPMOP-A. A mixture of H_2L_A (2.050 gm, 5 mmol) in 100 mL DMF and $Cu(NO_3)_2.3H_2O$ (1.208 gm, 5 mmol) in 100 mL DMF were mixed properly. After that added 100 mL p-xylene and added 1 mL 2,6 Lutidine as a base. During addition of base solution cage precipitate is formed within seconds and after few hours green cubic shaped crystal is coming from precipitate.

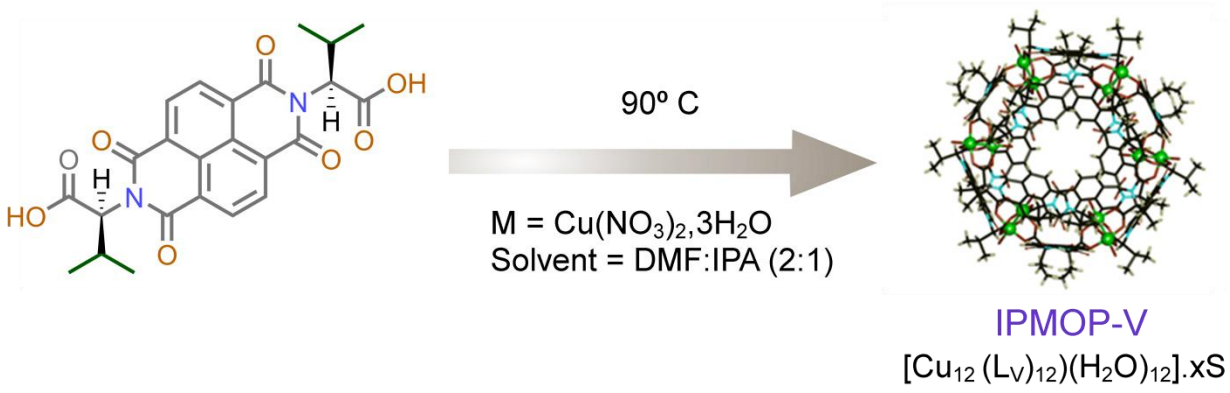

Scheme 2.2. Synthesis scheme of IPMOP-V.

Synthesis of $[Cu_{12}(L_V)_{12}(H_2O)_{12}].xS$ (IPMOP-V). A mixture of H_2L_V (24.7 mg, 5 mmol), $Cu(NO_3)_2.3H_2O$ (1.208 mg, 0.05 mmol), DMF (2 mL) and MeOH (1 mL) was placed in a Teflon capped glass vial. This was heated at 90 °C for 48h and then slowly cooled to room temperature over the next 12h. Growth of green, cubic-shaped crystals was observed upon cooling to RT, the desired product $[Cu_{12}(L_V)_{12}(H_2O)_{12}].xS$ appeared in 5.8 mg yield.

Room Temperature Synthesis of IPMOP-V. A mixture of H_2L_V (2.470 gm, 5 mmol) in 100 mL DMF and $Cu(NO_3)_2.3H_2O$ (12.08 mg, 0.05 mmol) in 100 mL DMF were mixed properly. After that added 100 mL MeOH and added 1 mL 2,6 Lutidine as a base. During addition of base solution cage precipitate is formed within seconds and after few hours green cubic shaped crystal is coming from precipitate.

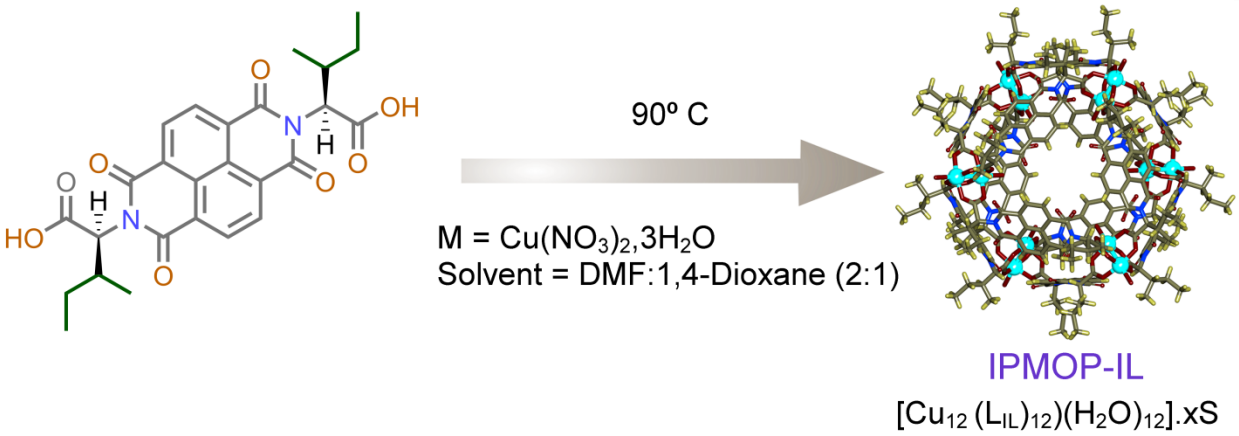

Scheme 2.3. Synthesis scheme of IPMOP-IL.

Synthesis of $[Cu_{12}(L_{IL})_{12}(H_2O)_{12}].xS$ (IPMOP-IL). A mixture of H_2L_{IL} (23.3 mg, 0.05 mmol), $Cu(NO_3)_2.3H_2O$ (12.1 mg, 0.05 mmol), DMF (2 mL) and 1,4 Dioxane (1 mL) was placed in a Teflon capped glass vial. This was heated at 90 °C for 48 h and then slowly cooled to room temperature over the next 12h. Growth of green, cubic-shaped crystals was observed upon cooling to RT, the desired product $[Cu_{12}(L_{IL})_{12})(H_2O)_{12}].xS$ appeared in 5.4 mg yield.

Room Temperature Synthesis of IPMOP-IL. A mixture of H_2L_{IL} (2.3 gm, 5 mmol) in 100 mL DMF and $Cu(NO_3)_2.3H_2O$ (1.208 gm, 5 mmol) in 100 mL DMF were mixed properly. After that added 100 mL 1,4Dioxane and added 1 mL 2,6 Lutidine as a base. During addition of base solution cage precipitate is formed within seconds and after few hours green cubic shaped crystal is coming from precipitate.

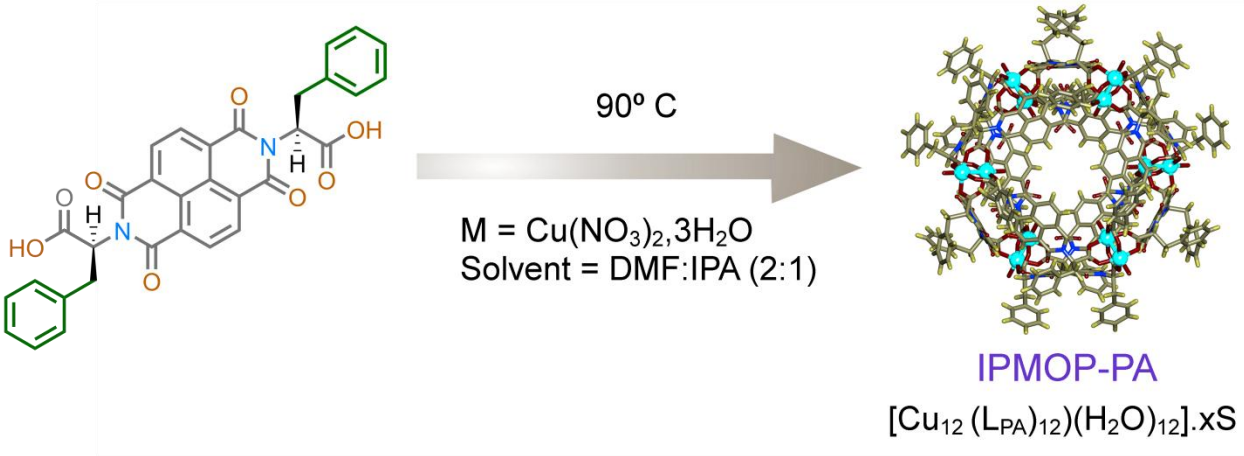

Scheme 2.4. Synthesis scheme of IPMOP-PA.

Synthesis of $[Cu_{12}(L_{PA})_{12}(H_2O)_{12}].xS$ (IPMOP-PA). A mixture of H_2L_{PA} (28.1 mg, 0.05 mmol), $Cu(NO_3)_2.3H_2O$ (12.1 mg, 0.05 mmol), DMF (2 mL) and IPA (1 mL) was placed in a Teflon capped glass vial. This was heated at 90 °C for 48 h and then slowly cooled to room temperature over the next 12 h. Growth of green, cubic-shaped crystals was observed upon cooling to RT, the desired product $[Cu_{12}(L_{PA})_{12})(H_2O)_{12}].xS$ appeared in 6.5 mg yield.

Room Temperature Synthesis of IPMOP-PA. A mixture of H_2L_{PA} (2.8 gm, 5 mmol) in 100 mL DMF and $Cu(NO_3)_2.3H_2O$ (1.208 gm, 5 mmol) in 100 mL DMF were mixed properly. After that added 100 mL isopropayl alcohol (IPA) and added 1 mL 2,6 Lutidine as a base. During addition of base solution cage precipitate is formed within seconds and after few hours green cubic shaped crystal is coming from precipitate.

2.2.3. Chemical Stability Test. For chemical stability test, the concentration of oxidizing and reducing media were taken as 0.2 mM in every cases and soaked the crystals directly to the respective solution for certain time. For pH stability test acid solutions are made from concentration HCl and the base solutions prepared from KOH. The unit cell parameters of IPMOP-PA crystals dipped in different conditions were recorded.

2.2.4. Physical Measurements

Single-crystal X-ray diffraction data of compound IPMOP-A was collected at 100 K on a Bruker D8 Venture Duo X-ray diffractometer (at 50 W: 50 kV/1mA) by graphite-monochromated Cu Kα radiation (λ = 1.5418Å), while IPMOP-V, IPMOP-IL and IPMOP-PA were measured at 296 K and 100 K with synchrotron radiation (λ = 0.65000 Å, 0.85000 Å and 0.65000 Å, respectively) on a ADSC Quantum-210 detector at 2D SMC with a silicon (111) double crystal monochromator (DCM) (See Supporting Information for more details). Powder X-ray diffraction were recorded on Bruker D8 Advanced X-Ray diffractometer using Cu Kα radiation (λ= 1.5406 Å) in 5° to 30° 2θ range. Gas adsorption measurements were recorded using BelSorp-max instrument from Bel Japan. Static contact angles were measured on pelletized MOP samples by a Contact Angle Meter (Model ID: HO-IAD-CAM-01; HolmarcOpto-Mechatronics Pvt. Ltd.), followed by LBADSA drop analysis (ImageJ software), which is composed on the fitting of the Young-Laplace equation to the image data. The Fourier transform infra-red (FT-IR) spectra were recorded on NICOLET 6700 FT-IR Spectrophotometer using KBr Pellets. Morphologies of the crystalline materials were recorded with Zeiss Ultra Plus field-emission scanning electron microscopy (FESEM) with integral charge compensator and embedded EsB and AsB detectors [Oxford X-max instruments 80 mm2. (Carl Zeiss NTS, Gmbh), Imaging conditions: 2 kV, WD = 2mm, 200 kX, Inlens detector.

2.2.5. Molecular Modelling Study

For each IPMOP, the energies of a unit cell (Euc) and a single cage (Ecage) were calculated using Forcite tool in Materials Studio; then the binding energy (ΔE) was estimated from $\Delta E = (E_{uc} - nE_{cage})/n$, where n denotes the number of cages in a unit cell. The interactions were described by the Lennard-Jones (LJ) and electrostatic potentials. The LJ potential parameters were adopted from the universal force field and the atomic charges were estimated using the Qeq method. The LJ interactions were determined using the atom-based method with a spherical cut off of 12 Å and a cubic spline width of 1.0 Å, while the electrostatic interactions were estimated by the Ewald summation method accuracy around10-3 kcal/mol.

2.3 Results and discussion

For practical Described herein is the construction of four Cu^{II}-based MOPs (coined as IPMOP-n; n denotes the carboxylate amino acid variant) from a naphthalene diimide (NDI) core and amino acids (Figure 2.1).[33-37] The syntheses and single crystal structures are reported. When the amino acids are alanine (A), valine (V), isoleucine (IL), and phenyl alanine (PA), the derived MOPs are denoted

IPMOP-A, IPMOP-V, IPMOP-IL, and IPMOP-PA respectively. In the current report, we describe the incremental attributes of chemical stability towards obtaining ultra-high stability under acidic/basic conditions, as well as under different oxidizing and reducing conditions. Solvothermal syntheses of the MOPs (A, V, IL and PA) led to green crystals (cube- and diamond-shaped, depending on specific MOPs systems). Optimization of the reaction conditions guided us to obtain IPMOP at room temperature (multigram scale) within seconds, in the presence of 2,6-lutidine as a base. Crystal structure of IPMOP-A was determined by single-crystal X-ray diffraction studies while those for IPMOP-V, IPMOP-IL, and IPMOP-PA were determined using synchrotron beamline radiation. Each MOP contains twelve ligand molecules and twelve water molecules to form neutral cages having the general formula: $[Cu_{12}(Lx)_{12}(H_2O)_{12}]$ [Lx: corresponding ligands system L_A, L_V, L_{IL} and L_{PA}]. Each cage molecule contains twenty-four alkyl groups which exohedrally decorate the entire outer surface of the spherical cages (see Figures 2.1). All the cages have eight triangular windows with an average aperture of about 2 Å, as well as an average internal cavity diameter of about 15 Å. Each bimetallic paddle-wheel Cu^{II} unit is coordinated to two terminal water molecules: one pointed into the internal cavity of the polyhedron and one pointed away from the polyhedron surface.

Thermogravimetric analysis (TGA) shows loss of guest molecules until about 250 °C (Appendix 2.1) for all four compounds. The slow loss of guest molecules can be ascribed to the presence of polar sites in the host cage having a limited aperture, which interacts strongly with guest solvent molecules. Most of the guest solvent molecules could be removed by a conventional activation protocol (heating under vacuum). CO_2 gas adsorption isotherms were recorded for the MOPs at 195 K,[38] (Appendix 2.2) and reflected similar saturation capacities for IPMOP-V (4.6 mmol), IPMOP-IL (4.3 mmol), and IPMOP-PA (4.5 mmol). This similarity is a result of their isoreticular nature.[39] The substantially lower saturation capacity for IPMOP-A (1.3 mmol) can be attributed to the aggregation of individual cages induced by solvent loss, as often observed for MOPs.[38] Although PXRD patterns of IPMOP-V indicates weak crystallinity (Appendix 2.3), similar saturation capacities for all three compounds (IPMOP-PA, IPMOP-IL, and IPMOP-V) suggests gas sorption occurs inside the intrinsic cavity of the cage molecules rather than within the extrinsic intercage pores. Because of the flexible nature of the pore window, gas sorption happens inside the cage cavity even though the aperture of the MOPs is smaller than the kinetic diameter of CO_2.

The chemical stability was examined by treating the crystals of IPMOP-PA in water and steam, as well as in solutions of widely varying pH, including harsh acidic solutions, buffer solutions, and diverse oxidizing and reducing media (Figure 2.2 and Appendix 2.4).[40] For assessment of water stability,

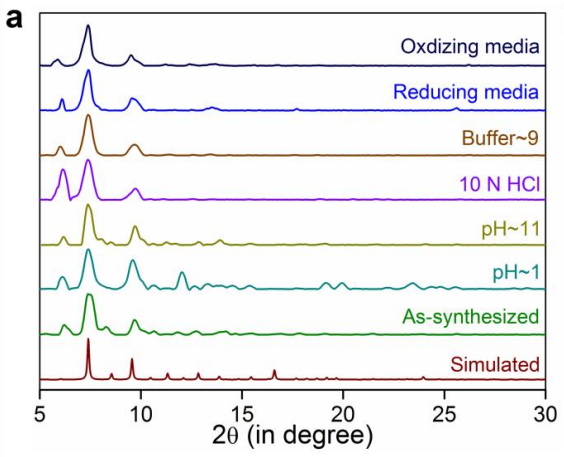

b

Condition	Time	Crystal System	a=b=c (Å)	V (Å^3)
Assynthesized	No	Cubic	29.2186	24944.74
pH~1	5 days	Cubic	29.2192	24944.88
pH~11	5 days	Cubic	29.2189	24944.83
Buffer solution (pH~9)	7 days	Cubic	29.2186	24944.78
Oxidizing agent (Fenton media)	30 days	Cubic	29.2197	24944.92
Reducing agent ($FeSO_4$ media)	30 days	Cubic	29.0218	24944.68

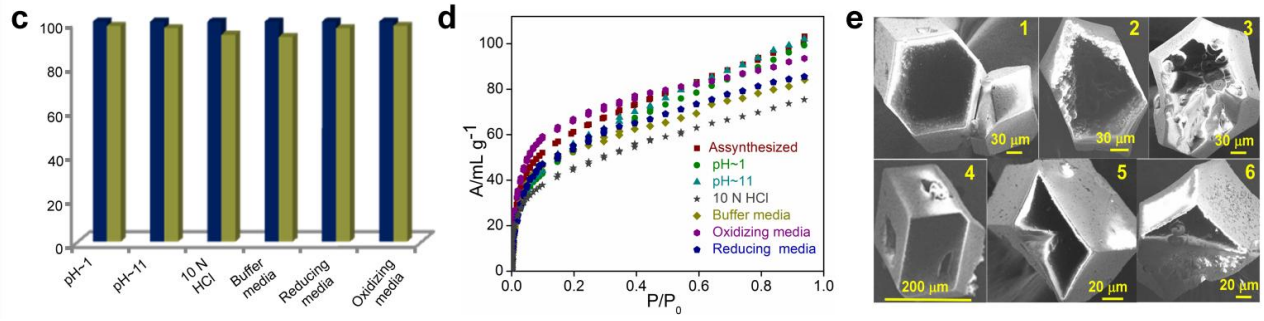

Figure 2.2. Characterization of stability confirmation for IPMOP-PA. (a) PXRD patterns under different conditions: pH~1 (5 days), pH~11(5 days), 10N HCl (6 h), buffer solution [pH~9] (7 days), reducing media ($FeSO_4$ solution; 30 days), oxidizing media (fenton solution; 30 days). (b) post-treatment SC-XRD data, under different conditions.(c) Bar diagram representing the reproducibility of IPMOP-PA miscellaneous harsh treatments, navy blue: before treatment of crystal, and dark yellow: after crystal treatment. (d) CO_2 gas sorption isotherms recorded after treating the adsorbent MOP under different harsh conditions: pH~1(5 days), pH~11(5 days), 10N HCl (6 h), buffer solution [pH~9] (7 days), reducing media ($FeSO_4$ solution; 30 days), oxidizing media (fenton solution; 30 days). (e) FE-SEM images after immersing IPMOP-PA crystals under different conditions: pH~1(5 days), pH~11(5 days),10NHCl (6 h), buffer solution [pH~9] (7 days), reducing media ($FeSO_4$ solution; 30 days), and oxidizing media (fenton solution; 30 days).

IPMOP-PA was soaked in water for several months, and unaltered PXRD patterns (Appendix 2.5) show the retention of both crystallinity and structural integrity in water. To further check the water stability under more harsh conditions, the sample was placed under steam for 5 days and the similarity of the PXRD patterns afterwards indicate structural robustness of the compound. Crystals of IPMOP-PA were

kept immersed in a wide range of solutions with varying pH (pH≈1-11) over 5 days, and the similarity of the resulting PXRD patterns (Figure 2.2a) confirmed its exceptional stability over a wide pH range. In addition to these studies, we looked at TGA, gas sorption, and FT-IR data for crystals immersed in solutions of different pH (pH≈1-11), this similarities in their profiles (Appendix 2.6 and 2.7) demonstrate retention of the framework. Crystals of IPMOP-PA were also examined under various harsh acidic conditions, and found to exhibit super-stability (Appendix 2.8). For further insight concerning the framework stability, we dipped the crystals of IPMOP-PA into oxidizing and reducing solutions over several weeks. Precise matching of all the main peaks in the experimental PXRD patterns (Appendix 2.9 and 2.10) implied that IPMOP-PA is exceptionally chemically stable. Inductively coupled plasma (ICP) analyses of supernatants from the different chemical environments (pH 1 and 11, 10 n HCl, and equivalent mixture of THF/water) were recorded. A negligible amount of copper leaching (Appendix Table 1) confirms the stability of IPMOP-PA in such chemical environments. For solution-phase stability of the cage molecules, we solubilized IPMOP-PA in THF and treated it under diverse conditions before performing UV/Vis measurements and ICP analyses. The UV/Vis spectra (Appendix 2.11) indicate that IPMOP-PA is also quite stable in such chemical environments in solution. IPMOP-IL and IPMOP-V are also chemically stable (Appendix 2.12-2.15) but not to the extent of IPMOP-PA. IPMOP-A is neither water-stable, nor chemically stable. In IPMOP-A, only twelve of the twenty-four outer methyl groups interact with the oxygen centers of the NDI moieties from their neighboring cages. These interactions are collectively insufficient to maintain the overall channel continuity in the architecture wherein the guest is removed. Besides, the methyl group is sp^3 hybridized, and anticipated to assume weak interactions with the NDI core. While in IPMOP-PA all benzyl groups interact with neighboring cages, sp^2-hybridized phenyl groups strongly interact with NDI moieties from the neighboring cages, thus maintaining their long-range order in the bulk phase. Therefore, such electrostatic interactions seem more prominent in IPMOP-PA, relative to IPMOP-A, and is further corroborated by molecular modelling results (Figure 2.3a). To present microscopic insights into the stability aspect of the IPMOPs, binding energies for the cages (most stable and least stable compounds) were estimated. For each IPMOP, energies for a single unit cell (Euc) and a single cage (Ecage) were separately calculated, followed by estimation of a binding energy (ΔE), that is, $\Delta E=(Euc-nEcage)/n$, where n is the number of cages in a unit cell. For IPMOP-A and IPMOP-PA, the binding energies are −94.06, and −150.74 kcal mol−1, respectively. This energy increases on the order of IPMOP-A<IPMOP-PA, and is attributed to the increasing size of alkyl functional group of the substituted diimide linkers. Figure 3a shows structures of the two IPMOPs, and the green circles highlight the contact areas between neighbouring cages. It is obvious that the contact area increases with increasing size of alkyl functional groups involved. In Figure 3 a, the CH_3 groups of

IPMOP-A offer only a small contact area while in IPMOP-PA, the aromatic groups interpenetrate between the neighbouring cages, leading to maximal contact area. With increasing contact area, the binding energy is increased and stronger interactions are formed, corresponding to the maintenance of long-range order in the solid state, and is thus consistent with our experimental observations.

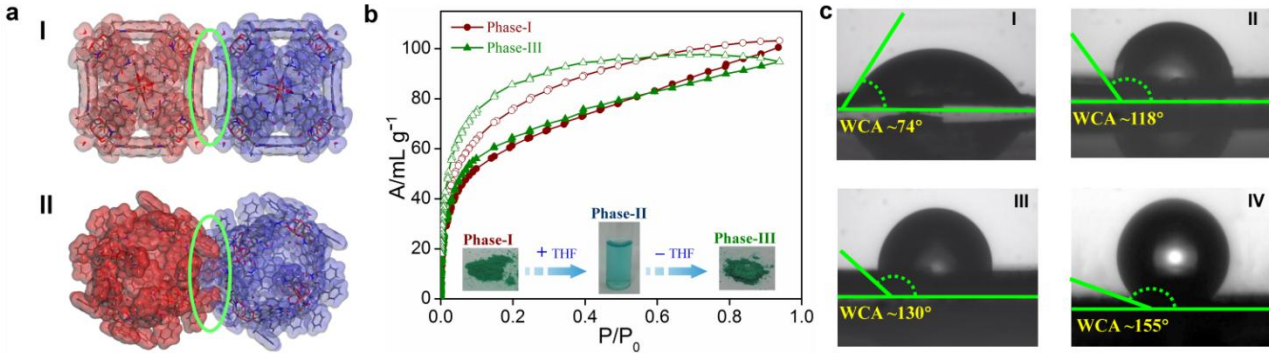

Figure 2.3. Structural insight and solution processability study of IPMOPs. (a) Contact areas between cages: (I) IPMOP-A; (II) IPMOP-PA. (b) 195 K CO_2 sorption isotherms for phase-I (as-synthesized), and phase-III (reprecipitation after dissolving in THF) of IPMOP-PA. Phase-II represents THF-dissolved solution phase for IPMOP-PA. (c) Water droplet cast on the surface of the pelletized IPMOPs: WCA values for (I) IPMOP-A: ~74°; (II) IPMOP-V: ~118°; (III) IPMOP-IL: ~130°; (IV) IPMOP-PA: ~155°.

Unlike extended frameworks, solution-processability of MOPs offer multifarious advantages over other porous materials.[41] Encouraged by our obtained results, solution-processability for IPMOP-PA was assessed and it was found to be solution-processable in tetrahydrofuran (THF), as confirmed by gas sorption measurements of Phase-I (as-synthesized) and Phase-III (reprecipitation after dissolving in THF; Figure 2.3b; Appendix 2.16-2.18). The hysteresis in the isotherm is due to strong supramolecular interaction between polar anhydride groups of the MOP molecules and CO_2 adsorbents. For this IPMOP series, we observed that the solubility increases with increasing size of the alkyl functional groups up to a certain point, beyond which the MOP solubility decreases with larger alkyl groups. Among the IPMOPs, IPMOP-A is insoluble in common solvents, while the rest are soluble in THF (Appendix Table 2), and thus solubility was found to increase from IPMOP-V to IPMOP-PA to IPMOP-IL. For hydrophobicity, the surface hydrophobicity was confirmed from water contact angle (WCA) measurements of all IPMOPs (Figure 2.3c), and the WCAs range from hydrophilic (WCA≈74°) to superhydrophobic (WCA≈155°; Appendix Table 3), observed for the first time for MOPs.

2.4 Conclusions

A potentially extensive class of ultra-stable materials is afforded by employing hydrophobic shielding as a cornerstone design principle. This basic principle can be used to attain chemical stability for MOP compounds, where the metal–ligand bond is weak in nature. The strategic decoration of the outer surface of the cages with diverse alkyl groups (stemming from the ligands) not only increases the hydrophobicity around the metal center, but also assists in retaining the robust nature of the overall framework, as affirmed from molecular simulations. We believe the present findings for the realization of chemically addressable MOPs will offer simple, straight-forward approaches for the development of diverse stable cage-based frameworks for future applications.

2.5 Appendix section

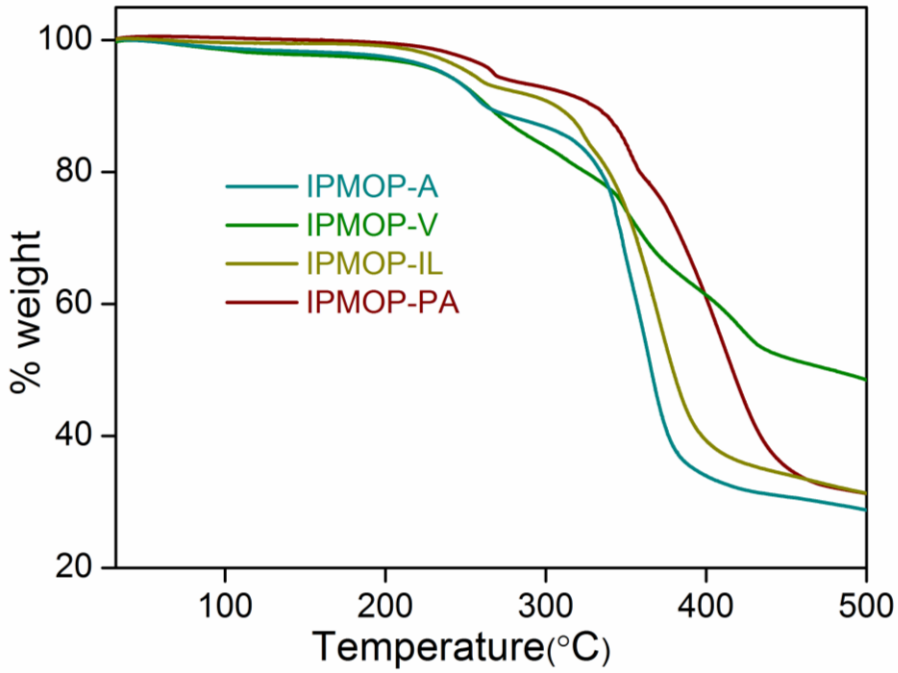

Appendix 2.1. CO_2 sorption study at 195 K for IPMOP-PA obtained at high temperature and immediate at room temperature (RT). Similar amount of gas uptake indicate the cage molecules are formed immediate at room temperature.

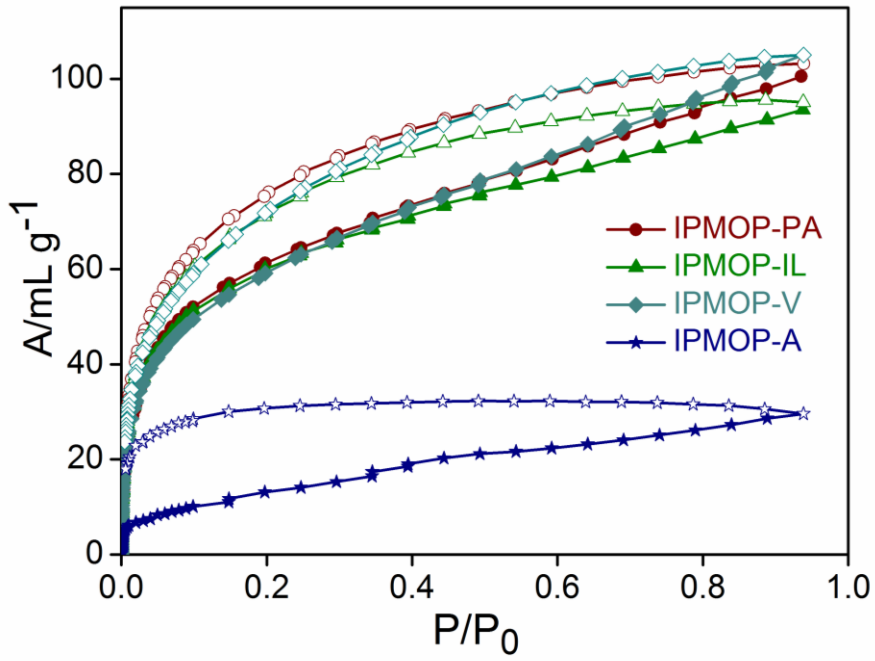

Appendix 2.2. CO_2 adsorption of all PMOPs at 195 K.

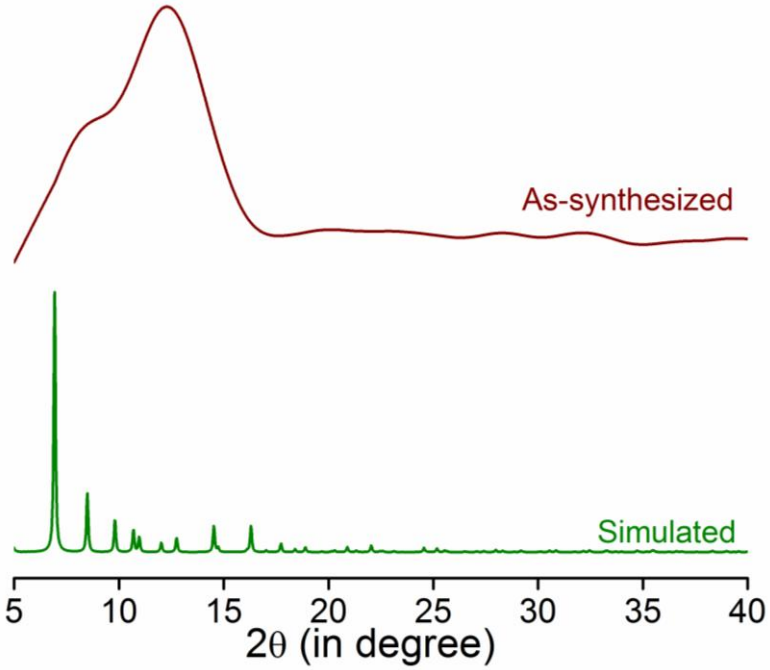

Appendix 2.3. PXRD patterns of IPMOP-V.

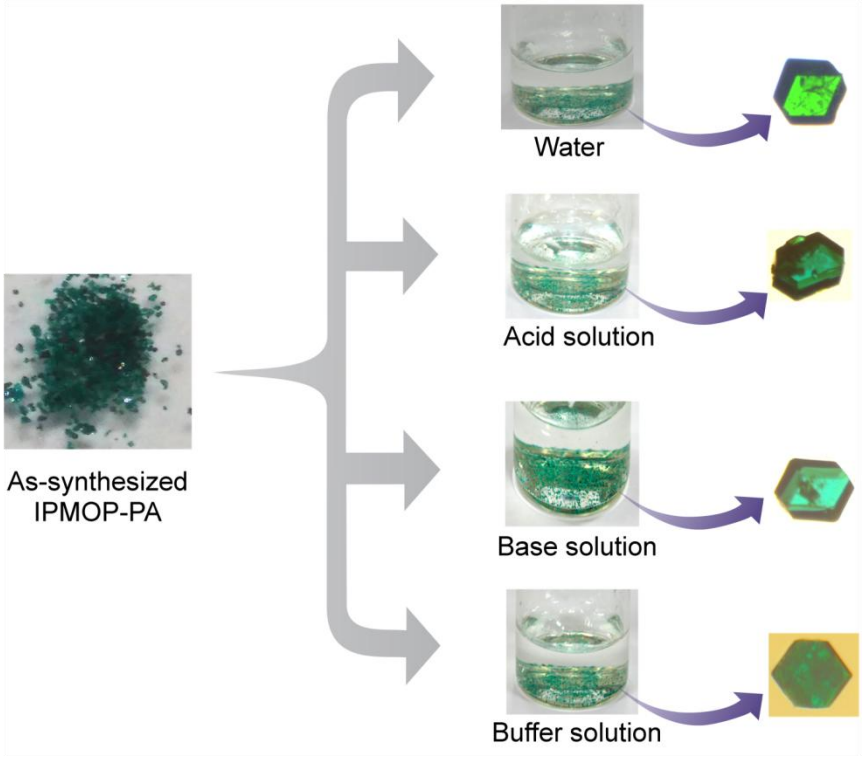

Appendix 2.4. Pictorial representation of IPMOP-PA at different conditions showing stability at respective media.

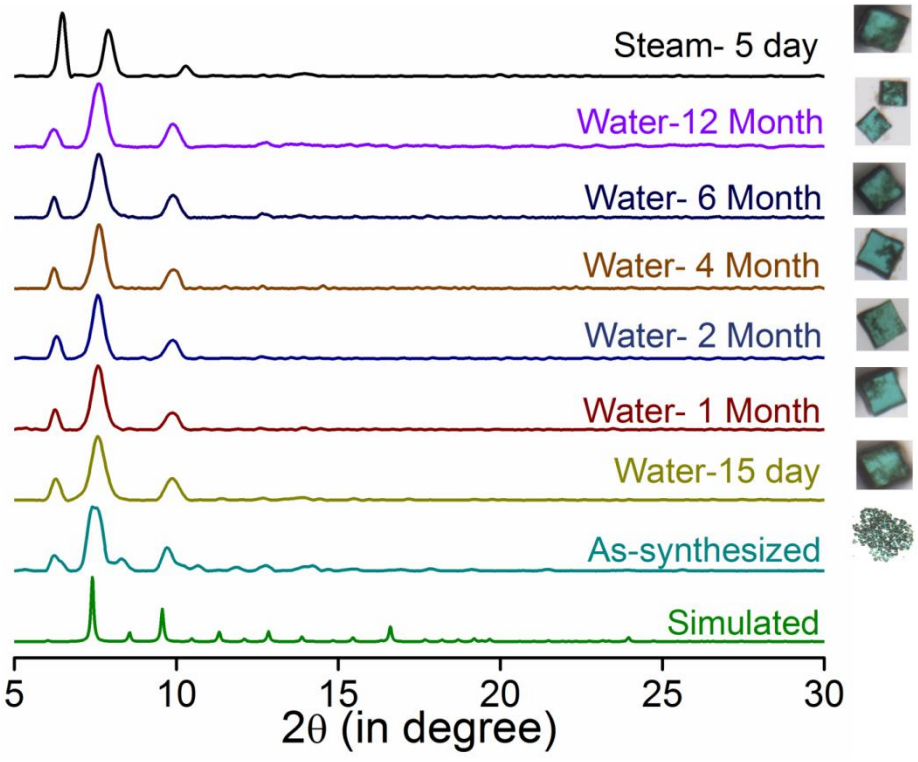

Appendix 2.5. PXRD patterns of IPMOP-PA in water and steam after different time of interval.

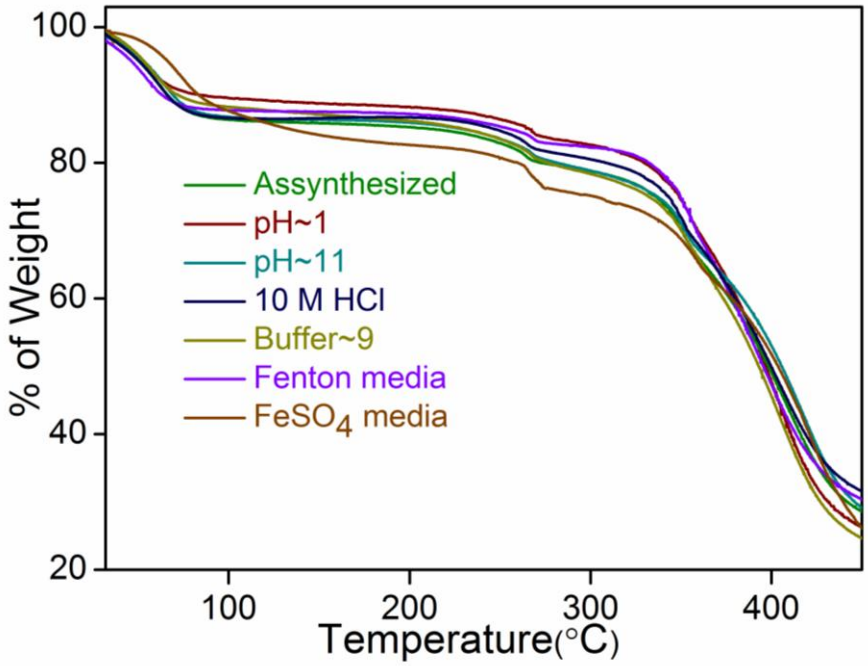

Appendix 2.6. TGA profiles of IPMOP-PAafter treatment of different condition.

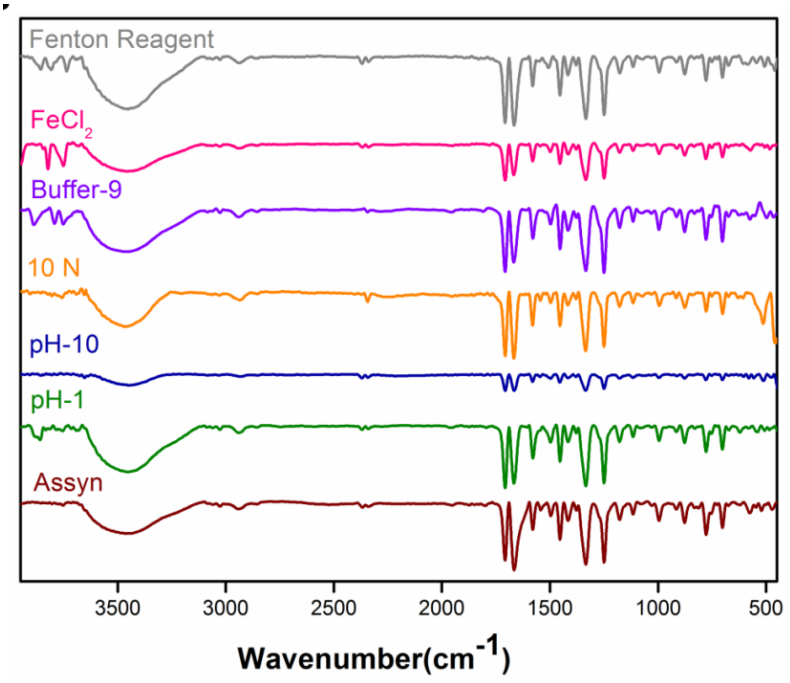

Appendix 2.7. FT-IR spectra of IPMOP-PA after treating in different conditions.

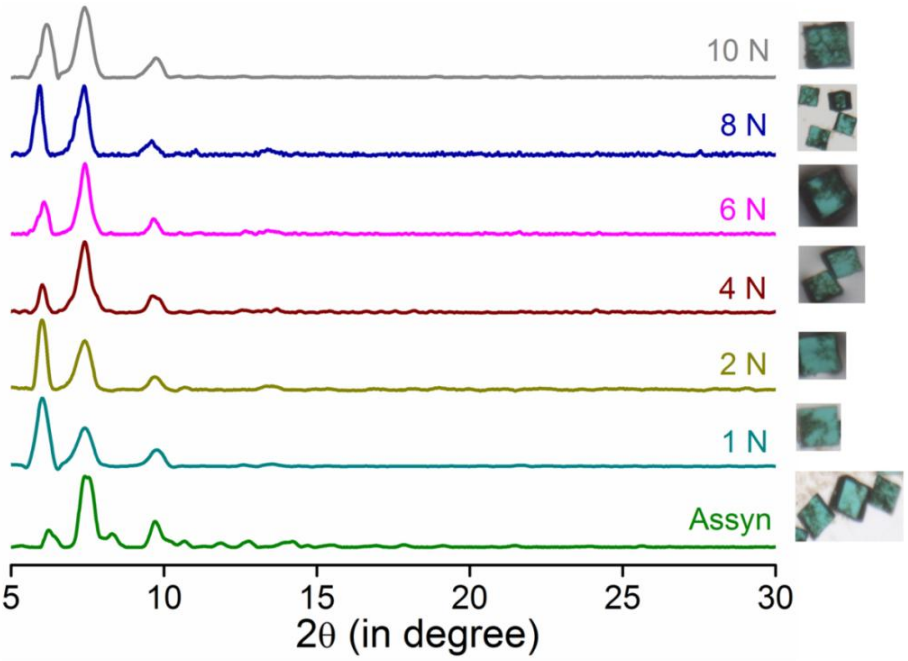

Appendix 2.8. PXRD patterns in different acidic solution of concentration HCl (after 6 h).

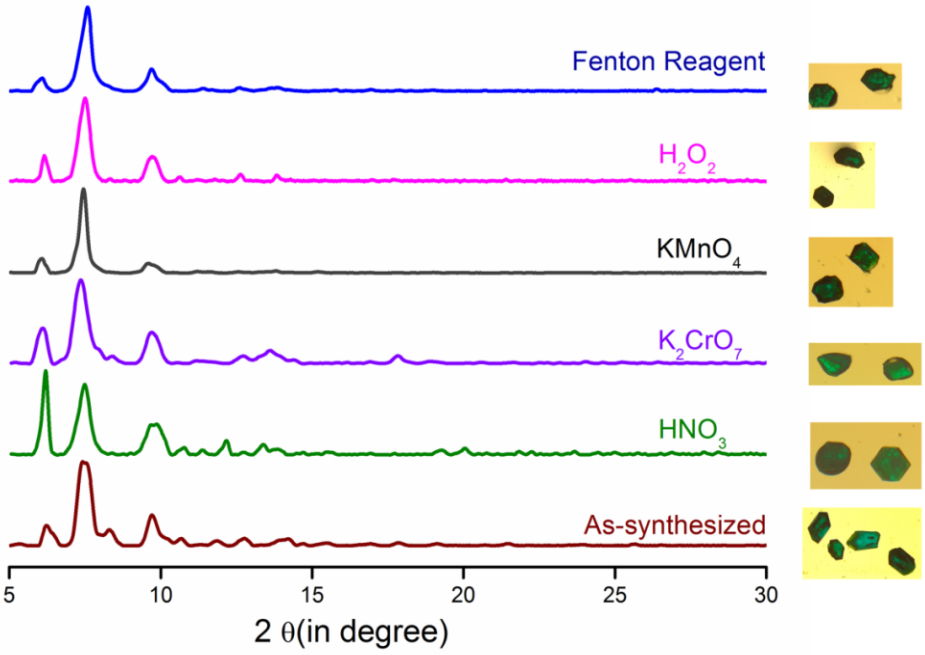

Appendix 2.9. PXRD patterns in different acidic Oxidizing agent after 30 days (Crystal of compounds obtained after immersed in Oxidizing agent solution). Crystal image obtained from randomly chosen crystal.

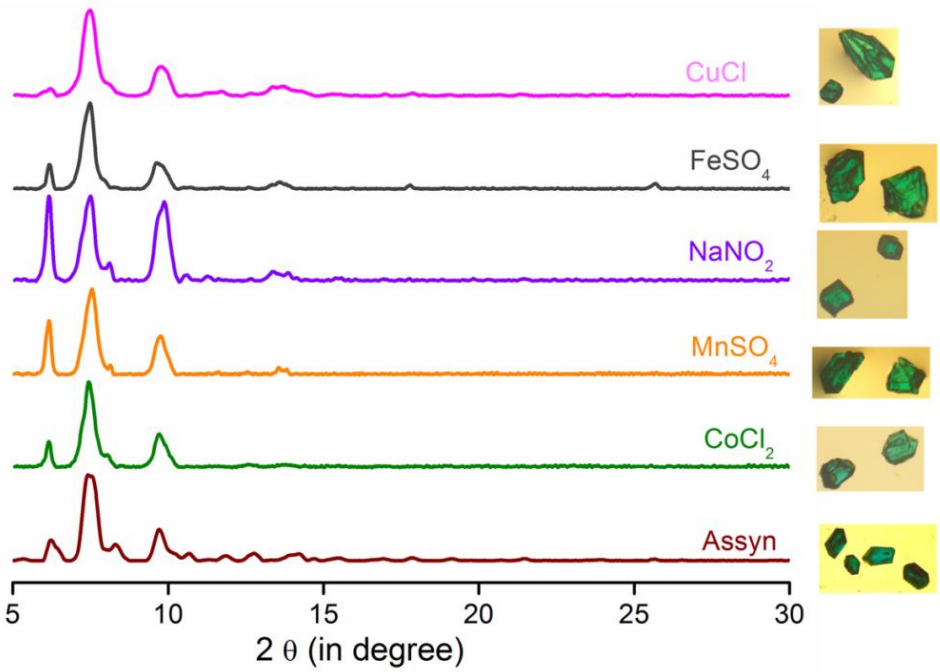

Appendix 2.10. PXRD patterns in different Reducing agent solution after 30 days(Crystal of compounds obtained after immersed in reducing solution). Crystal image obtained from randomly chosen crystal.

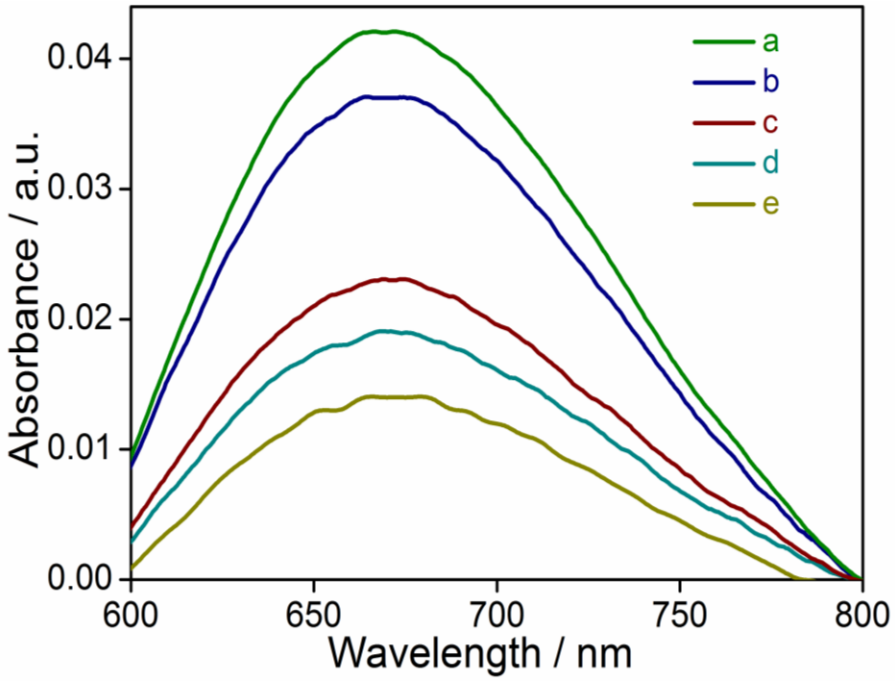

Appendix 2.11. Absorption spectra for IPMOP-PA.(a) Only cage molecule in tetrahydrofuran (THF) solution. (b) Cage molecules in equivalent amount of THF and water after 7 days. (c) pH=1 after 5 days in equivalent amount of THF and water mixture. (d) pH=11 after 5 days in equivalent amount of THF and water mixture. (e) 10 N HCl after 6 hours in equivalent amount of THF and water mixture.

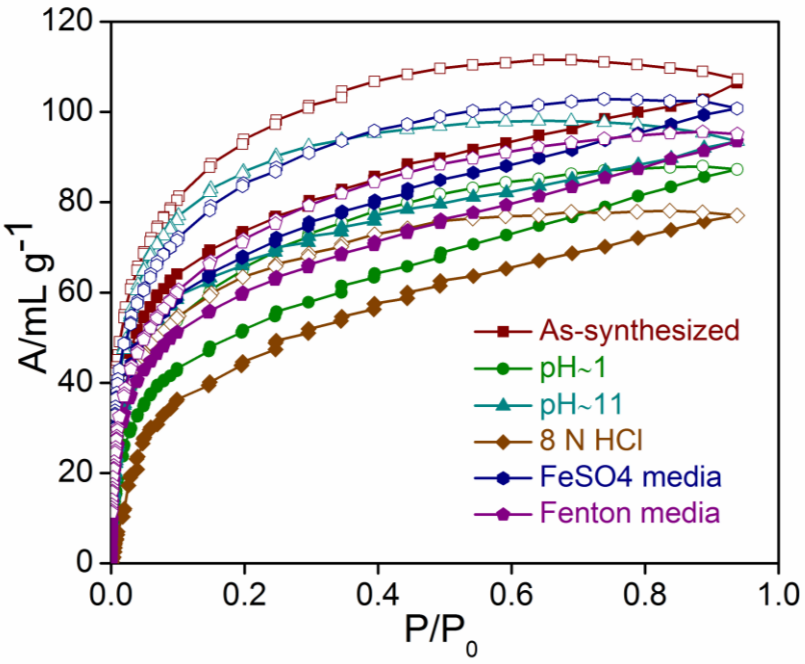

Appendix 2.12. Gas adsorption plots of IPMOP-IL after immersing the crystals in different solutions. Assynthesized, pH~1(after 3 days), pH~11 (after 3 days), 8 N HCl (after 3 h), $FeSO_4$ solution (after 20 days) , Buffer solution [pH~ 9] (after 5 days), Fenton solution (after 20 days).

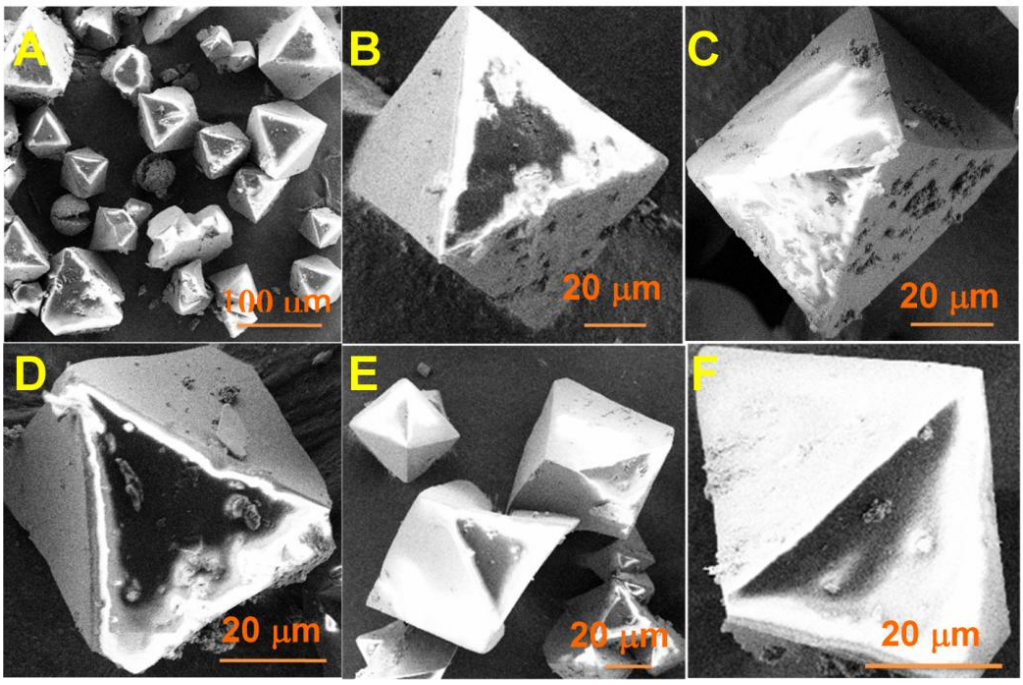

Appendix 2.13. FE-SEM images of IPMOP-IL after treatment of different conditions. (A) As-synthesized (B) pH~1(after 3 days) (C) pH~11 (after 3 days) (D) 8 N HCl (after 3 h) (E) $FeSO_4$ solution (after 20 days) (F) Fenton solution(after 20 days).

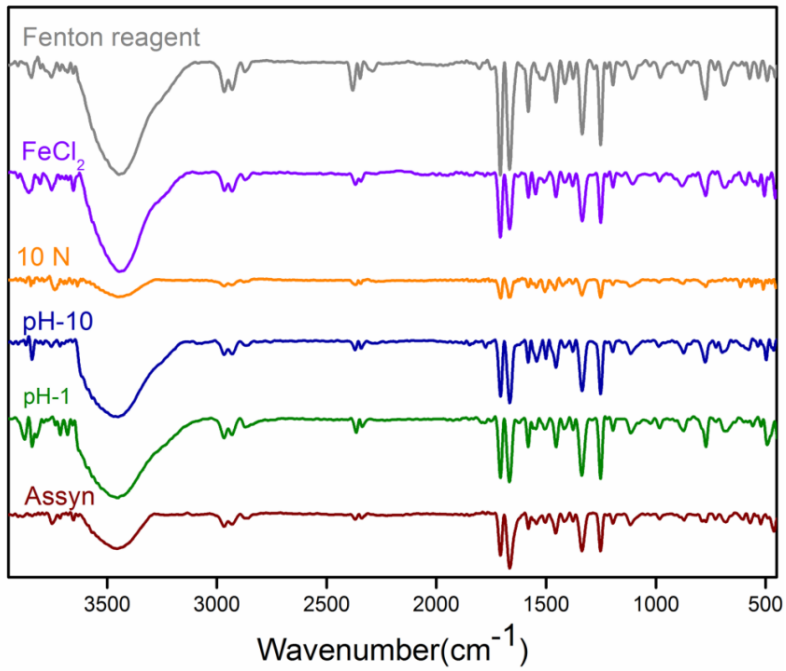

Appendix 2.14. FT-IR spectra of IPMOP-IL in different condition after different time of interval.

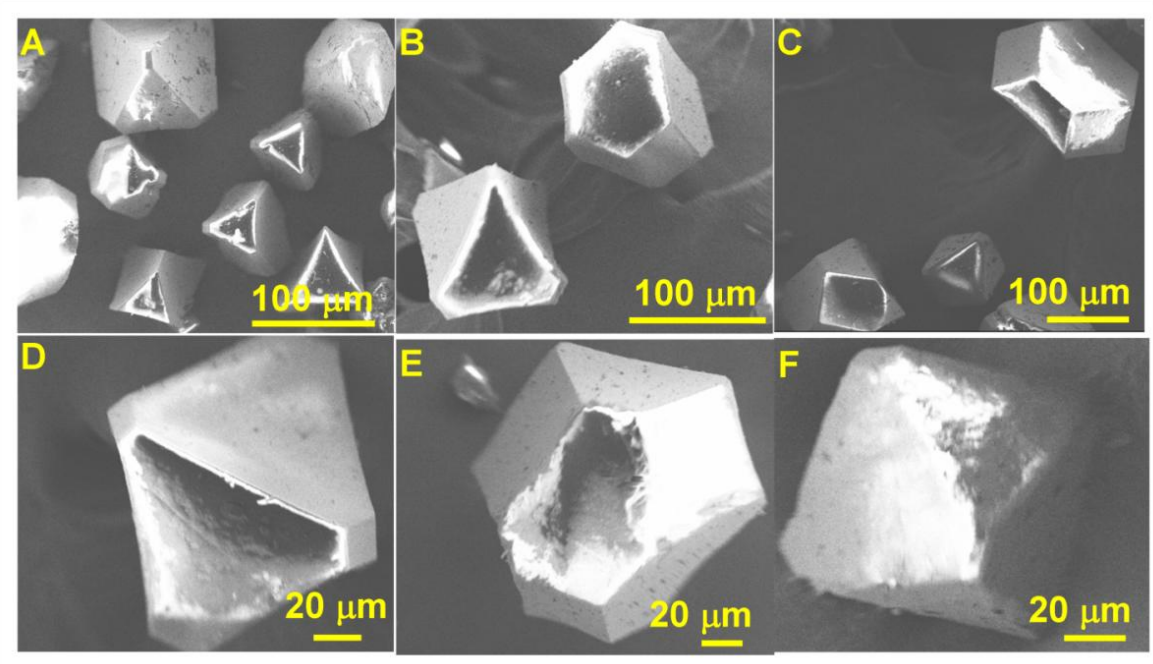

Appendix 2.15. FE-SEM images of IPMOP-V after treatment of different conditions. (A) As-synthesized (B) pH~1(after 2 days) (C) pH~11 (after 2 days) (D) 6 N HCl (after 2 h) (E) $FeSO_4$ solution (after 10 days) (F) Fenton solution (after 10 days).

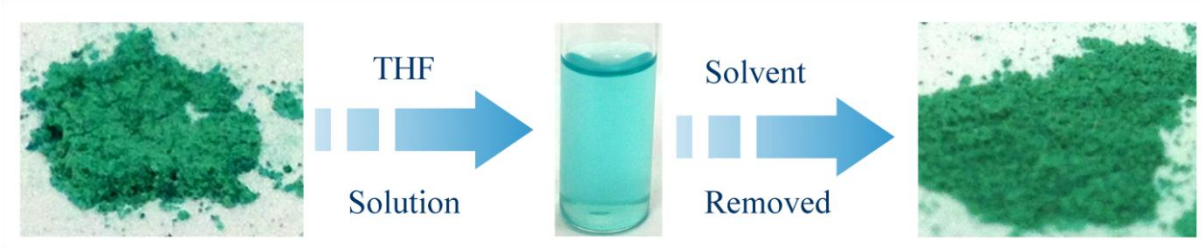

Appendix 2.16. Solution processability of IPMOP-PA.

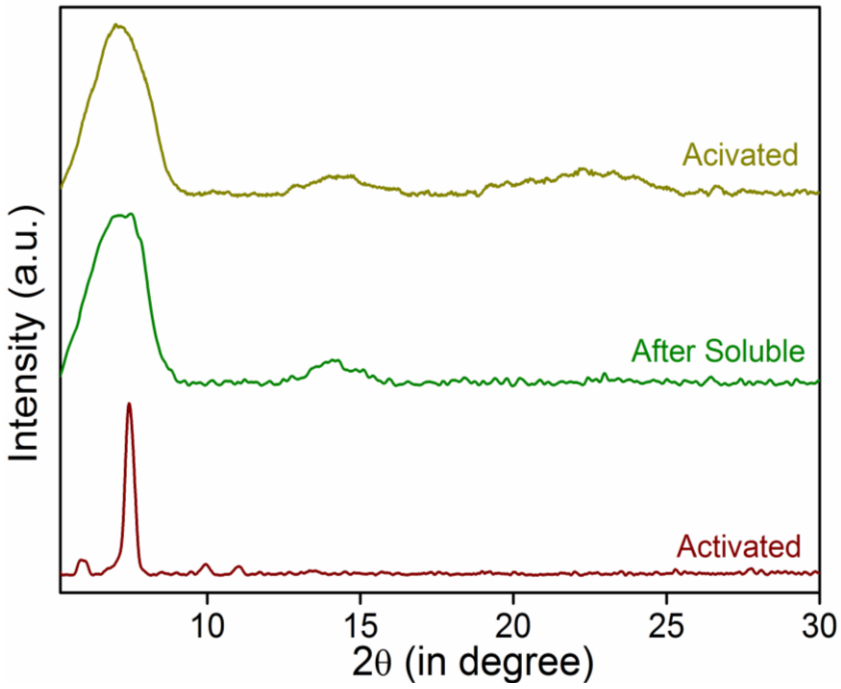

Appendix 2.17. PXRD patterns of IPMOP-PA before and after solution processabilty.

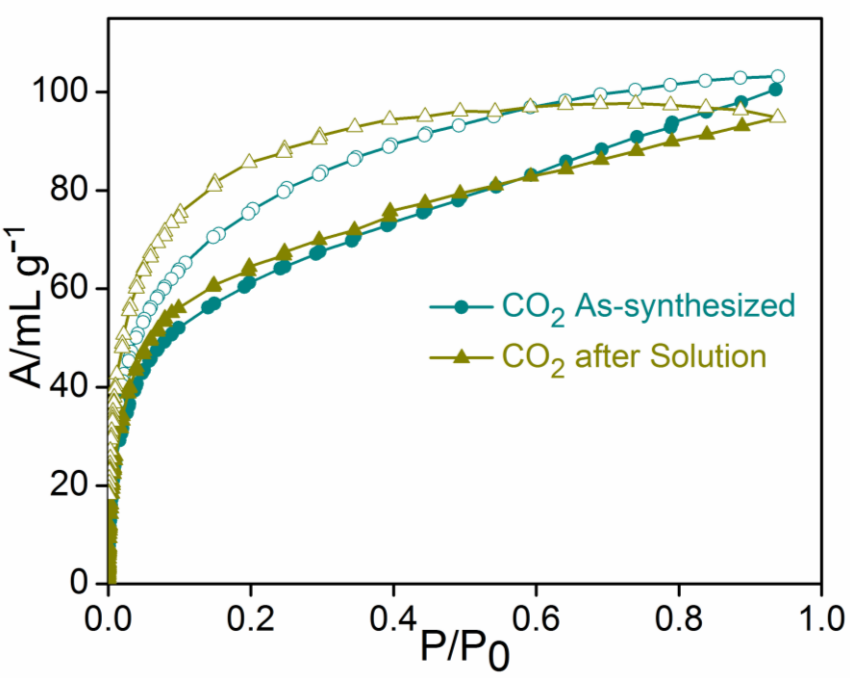

Appendix 2.18. PXRD patterns of IPMOP-PA before and after solution processabilty.

Appendix Table 2. Solubility of all IPMOPs in different solvents. THF-Tetrahydrofuran, DMA-N,N-Dimethylacetamide.

Compounds	**Hydrophobicity**	**Solubility**
IPMOP-A R: Me	Hydrophilic WCA: 74°	Insoluble
IPMOP-V R: $CH(Me)_2$	Hydrophobicity WCA: 118°	THF
IPMOP-IL R: CH(Me)(Et)	Highly Hydrophobic WCA: 130°	THF, DMA
IPMOP-PA R: CH_2Ph	Super-Hydrophobic WCA:154°	THF, DMA

Appendix Table 3. Contact Angle table of all IPMOPs.

IPMOP	**$[Cu_{12}(L_A)_{12}(H_2O)_{12}].xS$ IPMOP-A**	**$[Cu_{12}(L_V)_{12}(H_2O)_{12}].xS$ IPMOP-V**	**$[Cu_{12}(L_{IL})_{12}(H_2O)_{12}].xS$ IPMOP-IL**	**$[Cu_{12}(L_{PA})_{12}(H_2O)_{12}].xS$ IPMOP-PA**
WCA	~74 (Hydrophilic)	~118 (Hydrophobic)	~130 (Highly hydrophobic)	~155 (Superhydrophobic)

2.6 References

[1] I. V. Kolesnichenko, E. V. Anslyn, *Chem. Soc. Rev.* **2017**, *46*, 2385-2390.

[2] B. Moulton, M. J. Zaworotko, *Chem. Rev.* **2001**, *101*,1629-1658.

[3] O. K. Farha, I. Eryazici, N. C. Jeong, B. G. Hauser, C. E. Wilmer, A. A. Sarjeant, R. Q. Snurr, S. B. T. Nguyen, A. O. Yazaydin, J. T. Hupp, *J. Am. Chem. Soc.* **2012**, *134*,15016-15021.

[4] R. Matsuda, R. Kitaura, S. Kitagawa, Y. Kubota, R. V. Beloslu dov, T. C. Kobayashi, H. Sakamoto,

T. Chiba, M. Takata, Y. Kawazoe, Y. Mita, *Nature* **2005**, *436*, 238-241.

[5] Y. Cui, Y. Yue, G. Qian, B. Chen, *Chem. Rev.* **2012**, *112*,1126-1162.

[6] H.-C. Zhou, J. R. Long, O. M. Yaghi, *Chem. Rev.* **2012**, *112*,673-674.

[7] H.-C. Zhou, S. Kitagawa, *Chem. Soc. Rev.* **2014**, *43*,5415-54118.

[8] M. C. So, G. P. Wiederrecht, J. E. Mondloch, J. T. Hupp, O. K. Farha, *Chem. Commun.* **2015**, *51*,3501-3510.

[9] M. Eddaoudi, J. Kim, J. B. Wachter, H. K. Chae, M. O Q Keeffe, O. M. Yaghi, J. *Am. Chem. Soc.* **2001**, *123*,4368-4369.

[10] H. Abourahma, A. W. Coleman, B. Moulton, B. Rather, P. Shahgaldian, M. J. Zaworotko, *Chem. Commun.* **2001**, 2380-2381.

[11] A. J. Howarth, Y. Liu, P. Li, Z. Li, T. C. Wang, J. T. Hupp, O. K. Farha, *Nat. Rev. Mater.* **2016**, *1*, 15018.

[12] H. Assi, G. Mouchaham, N.Steunou, T. Devic, C. Serre, *Chem. Soc. Rev.* **2017**, *46*, 3431-3452.

[13] G. Mouchaham, S. Wang, C. Serre, The Stability of Metal-Organic Frameworks, Wiley-VCH, Weinheim, **2018**.

[14] P. G. M. Mileo, T. Kundu, R. Semino, V. Benoit, N. Steunou,P.L. Llewellyn, C. Serre, G. Maurin, S. Devautour-Vinot, *Chem. Mater.* **2017**, *29*,7263-7271.

[15] S. Kandambeth, V. Venkatesh, D. B. Shinde,S.Kumari, A. Halder, S. Verma, R. Banerjee, *Nat. Commun.* **2015**, *6*,6786-6795.

[16] M. Dan-Hardi, C. Serre, T. Frot, L. Rozes, G. Maurin, C. Sanchez, G. Ferey, *J. Am. Chem. Soc.* **2009**, *131*, 10857-10859.

[17] D. J. Tranchemontagne, Z. Ni, M. O QKeeffe, O. M. Yaghi, *Angew. Chem. Int. Ed.* **2008**, *47*,5136-5147.

[18] J. R. Li, H. C. Zhou, *Nat. Chem.* **2010**, *2*, 893-898.

[19] H. Furukawa, J. Kim, N. W. Ockwig, M.O QKeeffe,O.M.Yaghi, *J. Am. Chem. Soc.* **2008**, *130*,11650-11661.

[20] S. Leininger, B. Olenyuk, P. J. Stang, *Chem. Rev.* **2000**, *100*, 853-908.

[21] L.-B. Sun, J.-R. Li, W. Lu, Z.-Y. Gu, Z. Luo, H.-C. Zhou, *J. Am. Chem. Soc.* **2012**, *134*,15923-15928.

[22] Y.-H. Kang, X.-D. Liu, N. Yan, Y. Jiang, X.-Q. Liu, L.-B. Sun, J.-R. Li, *J. Am. Chem. Soc.* **2016**, *138*,6099-6102.

[23] S. Furukawa, N. Horike, M. Kondo, Y. Hijikata, A. Carne-Sanchez, P. Larpent, N. Louvain, S. Diring, H. Sato, R. Matsuda, R. Kawano, S. Kitagawa, *Inorg. Chem.* **2016**, *55*,10843-10846.

[24] J. Park, Z. Perry, Y.-P. Chen, J. Bae, H.-C. Zhou, *ACS Appl. Mater. Interfaces* **2017**, *9*,28064-28068.

[25] G. Liu, Y. D. Yuan, J. Wang, Y. Cheng, S. B. Peh, Y. Wang, Y. Qian, J. Dong, D. Yuan, D. Zhao, *J. Am. Chem. Soc.* **2018**, *140*, 6231-6234.

[26] D. Zhao, S. Tan, D. Yuan, W. Lu, Y. H. Rezenom, H. Jiang, L.-Q. Wang, H.-C. Zhou, *Adv. Mater.* **2011**, *23*,90-93.

[27] R. W. Larsen, *J. Am. Chem. Soc.* **2008**, *130*, 11246-11247.

[28] R. Kawano, N. Horike, Y. Hijikata, M. Kondo, A. Carne-Sanchez, P. Larpent, S. Ikemura, T. Osaki, K. Kamiya, S. Kitagawa, S. Takeuchi, S. Furukawa, *Chem* **2017**, *2*,393-403.

[29] N. Ahmad, H. A. Younus,A.H.Chughtai, F. Verpoort, *Chem. Soc. Rev.* **2015**, *44*,9-25.

[30] P. Horcajada, R. Gref, T. Baati, P. K. Allan, G. Maurin, P. Couvreur, G. Ferey, R. E. Morris, C. Serre, *Chem. Rev.* **2012**, *112*, 1232-1268.

[31] N. Ahmad, A. H. Chughtai, H. A. Younus,F.Verpoort, *Coord. Chem. Rev.* **2014**, *280*,1-27.

[32] J. G. Nguyen, S. M. Cohen, *J. Am. Chem. Soc.* **2010**, *132*,4560-4561.

[33] L. J. McCormick, D. R. Turner, *CrystEngComm* **2013**, *15*, 8234-8236.

[34] S. A. Boer, C. S. Hawes, D. R. Turner, *Chem. Commun.* **2014,** *50*, 1125-1127.

[35] S. A. Boer, D. R. Turner, *Chem. Commun.* **2015**, *51*,17375-17378.

[36] S. A. Boer, D. R. Turner, *Cryst. Growth Des.* **2016**, *16*, 6294-6303.

[37] S. A. Boer, D. R. Turner, *CrystEngComm* **2017**, *19*, 2402-2412.

[38] J.-R. Li, J, Yu, W. Lu, L.-B. Sun, J. Sculley, P. B. Balbuena, H.-C. Zhou, *Nat. Commun.* 2013, 4,1538-1545.

[39] O. M. Yaghi, M. O QKeeffe, N. W. Ockwig, H. Chae, M. Eddaoudi, J. Kim, *Nature* **2003**, *423*,705-714.

[40] Z. Lu, C. B. Knobler, H. Furukawa, B. Wang, G. Liu, O. M. Yaghi, *J. Am. Chem. Soc.* **2009**, *131*,12532-12533.

[41] T. Hasell, H. Zhang, A. I. Cooper, *Adv. Mater.* **2012**, *24*, 5732-5737.

Chapter 3

Hybridization of Cage and COF: A New Type of Hybrid Materials for Sequestration of oxoanions from Water

3.1 Introduction

Availability of safe drinking water is one of the distant dream to many around the globe in 21st century, especially in the developing countries.[1,2] Release of contaminated waste water from the widespread growth of industries and urban activities is a major sources of water pollution.[3] Contaminated water predominantly consists of various inorganic pollutants, which remain mostly in the form of oxoanions, as documented in the pollutants priority list of the Environment Protection Agency (EPA).[4] Therefore, proliferation of various toxic oxoanions present in the water stream is a pressing global concern and the battle to ameliorate oxoanions contamination is far from over. Currently, adsorptive separation by porous materials is regarded as a promising alternative to energy-intensive distillation techniques.[3,4] Adsorption based removal technique has been an escalating interest and is considered advantageous over other techniques due to its cost effectiveness, fast sorption kinetics and ease of operation.[5] But limited selectivity in the presence of large excess of interfering salts and poor capturing efficiency towards trace amounts of pollutants actuates the researchers to the development of new adsorbent materials for efficient decontamination of oxoanions from natural contaminated water.[6]

Advanced functions of various porous materials have been flourishing in recent years by controlled engineering at the molecular level.[7] Combined merits and maximized performance of different functional materials were achieved through synthesis of composite materials.[8-10] Of them, hybrid composite materials has moved to the forefront and spurred a great deal of attention due to creation of unique and multifunctional platforms to achieve desired applications.[11,12] Albeit there has been significant advancement in the composite material in recent time,[13] it remains a huge challenge to fabricate hybrid composite material.[12] Cage and COF are two widely known crystalline porous materials, assembled from organic linkers and metal ions (metal clusters) or with pure organic molecules, have been employed in a variety of areas such as gas storage, catalysis, sensing, photo-electric conversion, energy storage and biological activity.[14-17] But, molecular cages often unable to reach their full potential towards aforementioned applications due to unavoidable aggregation induced active sites blockage upon guest removal in the solid state.[18] Only a few efforts have been made to overcome such a cardinal issue by encasing cages inside porous materials (silica and MOF),[19,20] but hybridization of cage with such porous materials has yet remained an unmet challenge.

Herein, we have synthesized a rare class of hybrid cationic nanocomposite through covalent hybridization between cage and COF (Scheme 3.1). A water stable, amino-functionalized Zr(IV) SBU-based nano-sized cationic cage (diameter ~ 2.0 nm) was chosen as guest while a porous crystalline two

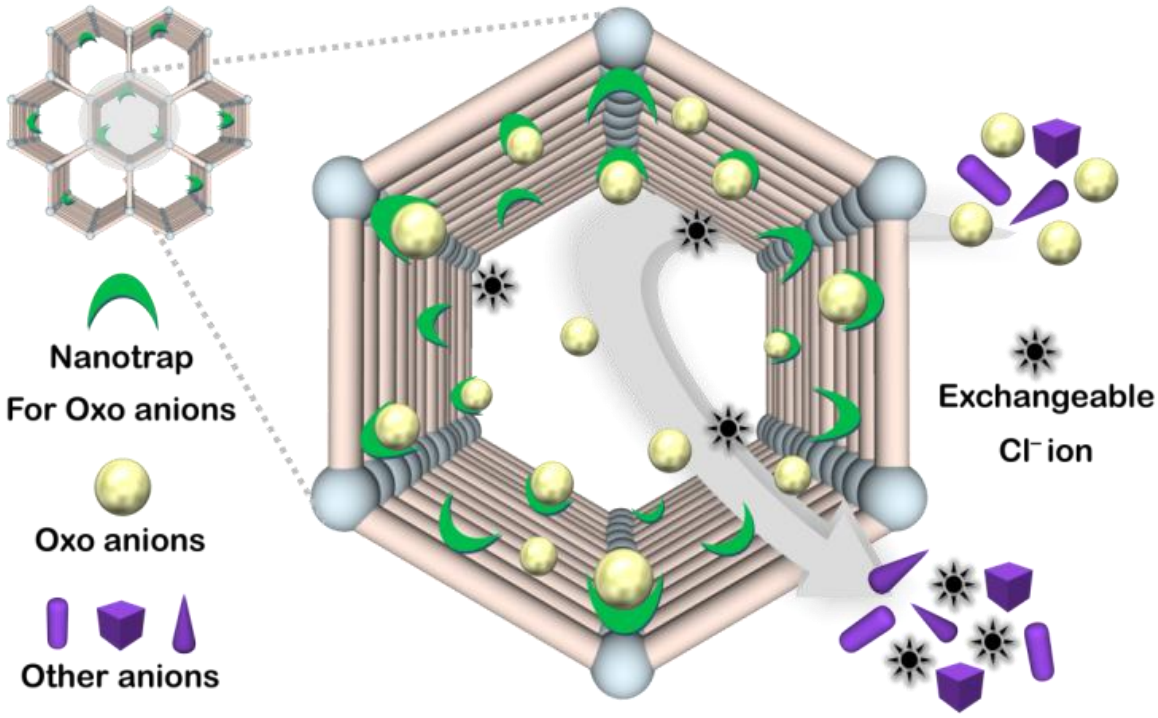

Scheme 3.1. Schematic representation of selective capture of specific oxoanions by a nanotrap grafted hybrid porous material.

dimensional TpPa-1-COF was selected as host matrix.[21,22] The hybrid material was utilized for capture study by virtue of its exchangeable Cl^- ions and availability of interacting sites of Zr (IV) SBU. The hybrid nano material can selectively remediate various metal-based toxic oxoanions (CrO_4^{2-}, $Cr_2O_7^{2-}$, $HAsO_4^{2-}$, SeO_4^{2-}, ReO_4^- and MnO_4^-) in a wide range of pH, different temperatures as well as from a mixture of salts commonly found in natural contaminated water body. The material was even able to efficiently sequestrate very trace amounts of oxoanions in the presence of large excess (~1000 folds) of other interfering salts. Finally, as a proof of principle, on the account of high selectivity, the nanoscavenger was utilized for treatment of natural Arsenic (model oxoanion pollutants) contaminated ground water.

3.2 Experimental

3.2.1 Materials

The starting materials 1,3,5- triformylpholoroglucinol (Tp) was synthesized by previously reported literature method.[1] All the reagents and solvents were commercially available and used as received. All the commercially available materials were bought from Sigma-Aldrich, TCI Chemicals, Avra Chemicals, Alfa aesar depending on their availability.

3.2.2 Synthesis

Synthesis of Metal-organic cage. The cage was synthesized accordance with literature report with slight modification. 2-aminoterephthalic acid (50 mg, 0.3 mmol) and zirconocene dichloride (150 mg, 0.5 mmol) were dissolved in N, N-dimethylacetamide (DMA, 10 mL) with a trace amount of water (40 drops) and kept it at room temperature and left undisturbed state for 72 hours. The yellow cubic block crystals were collected by filtration and dried under vacuum.

3.2.2.1. Synthesis of COF. The COF was synthesized accordance with literature report with slight modification.[2] In a typical synthesis protocol, first, Tp (42 mg, 0.2 mmol) was mixed with 1 mL dioxane and sonicated ~ 15 min to get homogeneous dispersion in a 15 mL drum vial. Next, p-phenylenediamine (PDA) (32 mg, 0.3 mmol) along with 1 mL dioxane solution was added to the reaction mixture and the resultant mixture was again sonicated for 3 min. Subsequently, acetic acid (3 M, 0.30 mL) was added and the vial was sealed and left undisturbed for 3 days at room temperature. The red precipitate was collected by centrifugation and washed with copious amount of anhydrous tetrahydrofuran, DMF, DMSO, dichloromethane, acetone and methanol separately. After washing, the red product was dipped in methanol for 4 days and dried at 120 C under vacuum for 12 h to give red powder.

3.2.2.2. Synthesis of hybrid Cage/COF composite. In a typical synthesis protocol, firstly, 100 mg of NH_2 functionalized cage was charged with Tp (42 mg, 0.2 mmol) and 200 μL 3M acetic acid in ethanolic solution for 12 hours at 65 °C under stirring condition. Next, the yellow colored precipitate was collected by centrifugation at 8,000 rpm for 5 min and dried under vacuum. In the second step, Tp functionalized cage was subjected to Tp (42 mg, 0.2 mmol) in 2.5 mL dioxane and stirring it for 10 min. Then, p-phenylenediamine (32 mg, 0.3 mmol) was added to the reaction mixture solution and again start to stirring for another 5 min. Subsequently, acetic acid (3M, 350 μL) was added to the whole reaction mixture and stirring for 2 min before left it undisturbed state for 7 days. The red product was collected by centrifugation and washed with copious amount of anhydrous tetrahydrofuran, dioxane, N, N-dimethyl

formamide, N, N-dimethylacetamide, methanol, acetone, dichloromethane. After washing, the product was dried under vacuum and soaked in anhydrous methanol for 7 days for solvent exchange. The collected powder Cage/COF was then desolvated at 120 °C for 12 h prior to characterization and capture studies. A series of Cage/COF hybrid composites were prepared following the aforementioned method where, the amount of cage gradually increased from 40 to 60 to 80 to 100 to 200 to 300 mg and keeping the fixed amount of COF components. The resultant hybrid composite materials are denoted as Cage/COF(40), Cage/COF(60), Cage/COF(80), Cage/COF(100), Cage/COF(200) and Cage/COF(300) respectively.

Additionally, we also synthesized non hybridized cage/COF(200) composite materials following the aforementioned reaction protocols (second step). In this case, cage with no functional group was selected i.e. cage contained terephthalic acid as building block. The amount of cage was used here 200 mg while keeping the aldehyde (Tp: 0.2 mmol) and amine (p-phenylenediamine: 0.3 mmol) remains constant.

3.2.3 Physical measurements

Powder X-ray diff reaction (PXRD) patterns were performed on a Bruker D8 Advanced X-ray diffractometer at room temperature using Cu Kα radiation (λ = 1.5406 Å) at a scan speed of 0.5 ° min^{-1} and a step size of 0.01° in 2θ. The morphology of the crystalline materials was recorded with a Zeiss Ultra Plus field-emission scanning electron microscope (FESEM) with an integral charge compensator and embedded EsB and AsB detectors (Oxford X-max instruments 80 mm^2 (Carl Zeiss NTS, GmbH). The samples were sputter-coated with a 5-10 nm Au film to reduce charging. The elemental analysis was carried out using voltage of 15 KV equipped with an EDX detector. Data acquisition was performed with an accumulation time of 600 s. For high-resolution TEM analysis, all the samples were dispersed in isopropanol (0.5 mg/mL) and sonicated for 30 min. Then, the samples were left for 2 min, and the upper part of the solution was taken for preparing TEM samples on a lacey carbon-coated copper grid (Electron Microscopy Science). TEM imaging and STEM-EDS were performed on the HRTEM (JEM-2200FS, JEOL) operating at acceleration voltage of 200 kV. Solid state NMR spectra were recorded on Bruker 400 MHz NMR spectrometer. Carbon chemical shifts are expressed in parts per million (δ scale). The IR Spectra were acquired by using NICOLET 6700 FT-IR spectrophotometer using KBr pellet in 500-4000 cm^{-1} range. Gas adsorption measurements were performed using BelSorp-Max instrument (Bel Japan). Prior to adsorption measurements, the activated samples were heated at 120 °C under vacuum for 6 hours using BelPrepvacII. UV-vis absorption studies were performed on a Shimadzu UV 3600 UV /vis /NIR spectrophotometer (with stirring attachment) in an optical quartz cuvette (10 mm path length) over

the entire range of 200-800 nm. The steady state photoluminescence studies were recorded on a Fluorolog-3 spectrofluorometer (HORIBA Scientific). The fluorescence imaging was recorded on HORIBA Scientific instrument. ICP-MS was performed on Quadrupole inductively coupled plasma mass spectrometry (Q-ICP MS) Thermo Scientific iCAP Q) instrument. ICP-AES analysis was performed on ARCOS, Simultaneous ICP Spectrometer. Multi-element standards were purchased from inorganic ventures.

3.2.4. Capture Study

3.2.4.1. Adsorption study. The standard procedure that we adopted for the adsorption experiments was as follows. The capture study of oxoanions CrO_4^{2-}, $Cr_2O_7^{2-}$, MnO_4^- and ReO_4^- were performed in a 50 mL beakers equipped with magnetic stir bars with constant stirring rate of 550 r.p.m. Firstly, 30 mg of Cage/COF(200) composite was taken in 10 mL of water and sonicated around 5 min to make well dispersed in aqueous media. Next, 25 mL stock solution of oxoanions was added to make the final concentration of 0.25 mmol for CrO_4^{2-} and $Cr_2O_7^{2-}$ and 0.2 mmol for ReO_4^-, 0.16 mmol for $HAsO_4^{2-}$, 0.26 mmol for SeO_4^{2-} and 0.5 mmol for MnO_4^-stirred for certain time. The kinetic adsorption study was monitored through ICP-AES/MS analysis ($HAsO_4^{2-}$ and SeO_4^{2-}) and UV-vis spectroscopy (for ReO_4^-, CrO_4^{2-}, $Cr_2O_7^{2-}$ and MnO_4^-). From this time dependent study we calculated the removal % and decreasing concentration of the oxoanions with time using the following equations: $D_t = (C_0-C_t)*100/C_0 = (A_0-A_t)*100/A_0$; Where, D_t = exchange capacity, C_0= initial concentration, A_0=initial absorbance, C_t= final concentration, A_t= final absorbance at specific time.

3.2.4.2. Capture study of oxoanions presence of other competing ions. For testing the influence of competing ions, equimolar as well as large excess (1,000 folds) of competing salts (NaCl, $NaNO_3$, KBr, Na_2SO_4, $NaClO_4$ were added to the oxoanions solution and carried out the capture studies by following the aforementioned method. The capture studies were monitored through UV-vis spectroscopy when competing ions are present equal amount compared to the oxoanions, while ICP-MS was used when competing ions are in large excess with oxoanions.

3.2.4.3. Preparation of the column. ~ 30 mg of Cage/COF(200) hybrid cationic composite and 4g of sand were mixed in mortar pestle and filled in a pencil glass column. To minimize the leaching possibility of the material, little amount of cotton was kept at the bottom of the composite and sand mixture. Prior to

the ion exchange studies, the column was washed with excess water and ~ 30 mL HCl (~ 1 M HCl) solution.

3.2.4.4. Column ion exchange studies. The CrO_4^{2-} and MnO_4^- contaminated colored solution (~ 0.1 mmol) were passed through the column containing composite materials and collected at the bottom in a glass beaker. Before and after exchange studies, the contaminated solutions were analyzed through UV-vis experiments.

3.2.4.5. pH-dependent capture study. The effect of pH on various oxoanions were recorded in a wide range of pH and compared with the data at pH-7 for relative performance. The variation of pH values were realized by addition of either acid (HCl) or base (KOH). Cage/COF(200) hybrid composite was immersed in 5 mL solution of 2.5 mM oxoanions and stirred continuously for 2 min. UV-vis (CrO_4^{2-}, $Cr_2O_7^{2-}$, ReO_4^-) as well as ICP-MS ($HAsO_4^{2-}$ and SeO_4^{2-}) studies were carried out for testing the removal efficiency of the composite materials.

3.2.4.6. Recyclability test. Oxoanions loaded composite was regenerated presence of saturated NaCl solution, where loaded materials were stirred for 5 hours.

3.2.4.7. Trace amount uptake studies. Trace amount (1,000 ppb) of oxoanions capture studies were performed in a 50 mL beakers equipped with magnetic stir bars at ambient temperature with constant stirring rate of 550 r.p.m. Firstly, 10 mg of Cage/COF(200) composite was taken in a10 mL of water and sonicated ~ 5 min to make it well dispersed in aqueous media. Next, 25 mL of oxoanions stock was added to make the final concentration of 1000 ppb for all oxoanions (CrO_4^{2-}, $Cr_2O_7^{2-}$, $HAsO_4^{2-}$, SeO_4^{2-}, ReO_4^- and MnO_4^-) and stirring it for certain time. During continuous stirring for 2 min, the solution was filtered with a syringe having 0.22 μm nylon membrane filter. The kinetic adsorption studies were monitored at different time interval through ICP-MS analysis technique.

3.2.4.8. Capacity Study. The amount of oxoanions adsorbed per gram was determined by exposing 5 mg of Cage/COF(200) hybrid material to 5 mL of 2.5 mM concentrated solution of oxoanions for 24 hours under stirring conditions. After 1 day, composite material was filtered off and filtrate was characterized through UV-vis (CrO_4^{2-}, $Cr_2O_7^{2-}$, ReO_4^-, MnO_4^-) as well as ICP-MS ($HAsO_4^{2-}$, SeO_4^{2-}) by diluting the solution. The capacity per gm was calculated using following equation: $Q_t = (C_0-C_t)*V/m$; where, Q_t, C_0, C_t, V and m are the capacity of adsorbent, initial concentration of the oxoanions solution, final concentration of oxoanions at specific time, volumes of the solution and mass of the Cage/COF used for the adsorption study respectively.

3.3 Results and discussion

The hydrolytically stable The hydrolytically stable cationic Zr(IV) based cage ({[$(C_5H_5)_3Zr_3\mu_3$-$O(\mu_2$-$OH)_3]_4(NH_2$-$C_6H_5)_6\}\cdot Cl_4$) was synthesized and characterized according to literature reports (Appendix 3.1).[21] Each cage molecules contained four Zr(IV) SBU, six organic linkers and four exchangeable Cl^- ions. In a typical cage/COF synthesis process, first, cationic cages were surface functionalized through 1,3,5-triformylphloroglucinol and in the second step, the functionalized cage reacts with 1,3,5-triformylphloroglucinol and p-phenylenediamine for the construction of desired cationic hybrid composite (Scheme 3.1, see Experimental Section for more details). Primary characterization of the composite was thoroughly performed prior to the subsequent capture studies. The structural analysis of the composite was confirmed by powder X-ray diffraction (PXRD), field emission scanning microscopic (FESEM), transmission electron microscopy (TEM), fourier transform infrared spectroscopy (FT-IR) and sorption studies. The formation of crystalline nature of the composite was first validated through PXRD studies (Appendix 3.1b and 3.1c).

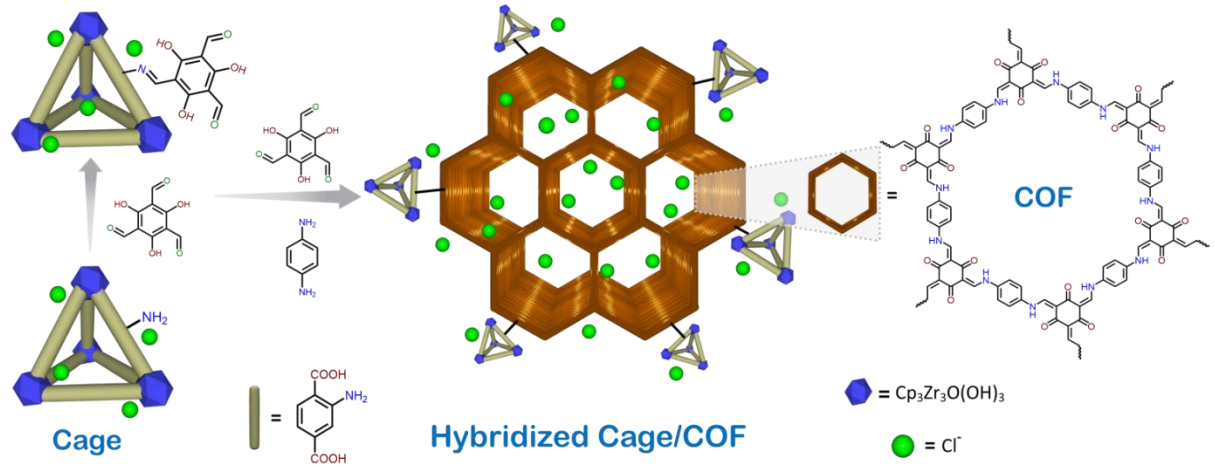

Figure 3.1. Schematic illustration of the synthesis of cationic cage/COF hybrid material.

The cage showed an amorphous character when treated with a similar condition to COF synthesis, which is common for cage molecules (Appendix 3.1d). The morphology of the cage/COF composite was investigated by the FESEM and TEM analysis. The FESEM images of the cage/COF composite showed distinctly different morphology (flower like) compare to the pristine cage as well as COFs material (Appendix 3.2). Similar Zr/Cl ratio (~3.0 in the composite material found in the EDS (energy-dispersive spectroscopy) analysis (Appendix Tables 3.1-3.7), confirm the presence of cage molecules in the composite material. The EDS elemental mapping of selected areas of the composite material evidenced

for distribution of cages throughout the composite materials (Appendix 3.3). Maximum loading of cages was achieved in the composite materials using 200 mg of cage in the reaction media (Appendix 3.4). TEM images revealed the presence of nano-sized cage molecules throughout the composite materials (Figure 1a, Appendix 3.5). Further, the integration of cage into the COF matrix was better realized by three dimensional tomography experiment. The nano-sized cage molecules were wrapped within the COF matrix in the composite material was clearly visualized from the three dimensional tomography experiment (Appendix 3.6). The peaks corresponding to the metal-carboxylate bonds found in the FT-IR spectrum of composite material, portraying the cages were successfully grafted into the COF matrix. The peak corresponds to free amine group can also be observed in the IR spectrum (Figure 3.1b) of composite material, indicating presence of free -NH_2 functional groups in the material. Nitrogen sorption isotherm at low temperature (77 K) showed comparatively less uptake by the cage/COF composite material compared to the pristine COF (Appendix 3.7), demonstrating that the cage molecules were successfully embedded to the COF frameworks. The cage/COF composite was further analysed through solid state NMR

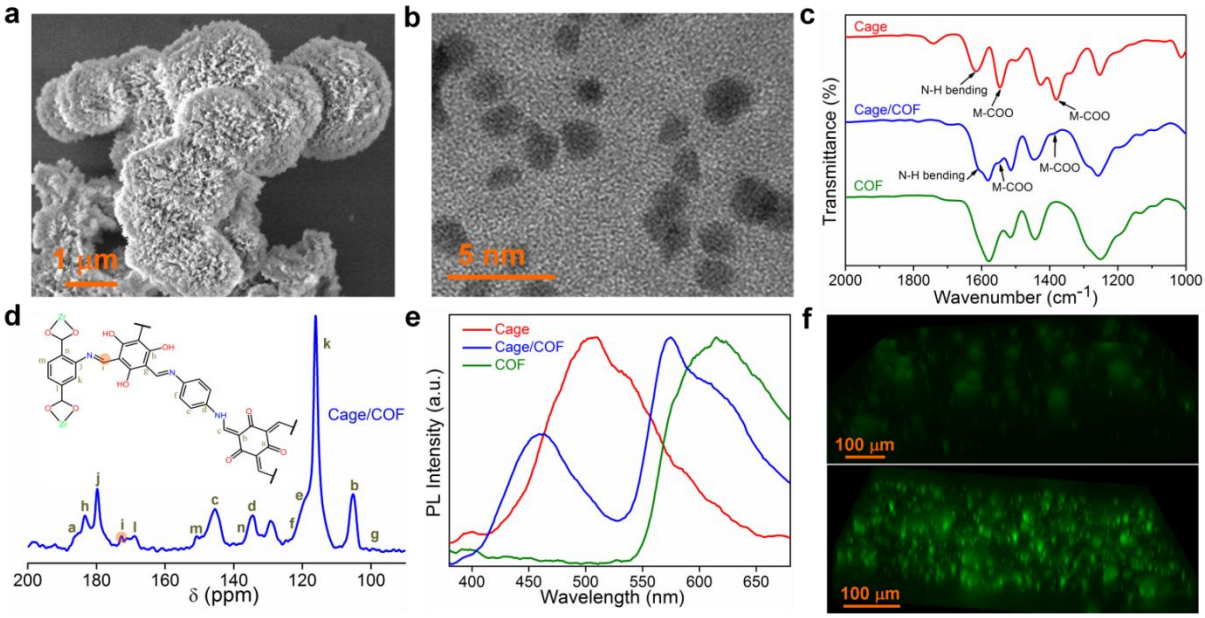

Figure 3.2. Characterizations of materials. (a) FESEM image of Cage/COF(200) hybrid material. (b) HR-TEM image of cage/COF(200) material. (c) FTIR spectra of cage, COF and cage/COF(200) composite material. (d) Solid-state ^{13}C NMR spectra of cage/COF(200) hybrid material. (e) Emission spectra of cage, COF and cage/COF(200) material with the excitation wavelength of 350 nm. (f) Fluorescence imaging of COF (top) and cage/COF(200) (bottom).

experiment to substantiate the type of interactions between cage and COF framework in the composite materials. Existence of characteristic signals of both cage and COF in the ^{13}C NMR spectrum of composite material (Figure 1c, Appendix 3.8), demonstrating that the composite materials consisted of both cage and COF. The appearance of a new peak at 172.66 ppm in the solidstate ^{13}C NMR spectrum in the composite material, formed due to formation of a new imine bond between building block of cage (amine) and COF framework (aldehyde), confirmed that the cage molecules covalently bonded with COF framework.[12] optical properties of the hybrid composite materials were also investigated along with structural characterizations for more details analysis of the hybrid composite. The UV-vis diffuse reflectance spectroscopy (DRS) spectrum of the hybrid composite materials display characteristic absorption peaks for both cage and COF (Appendix 3.9), providing evidence for the existence of both materials in the hybrid nanomaterial. The emission spectra of composite showed slightly blue-shifted of distinct characteristics peaks for both cage and COF in composite material (Figure 3.1d), suggesting interaction between cage molecules and COF matrix.[24] Furthermore, the fluorescence microscopic

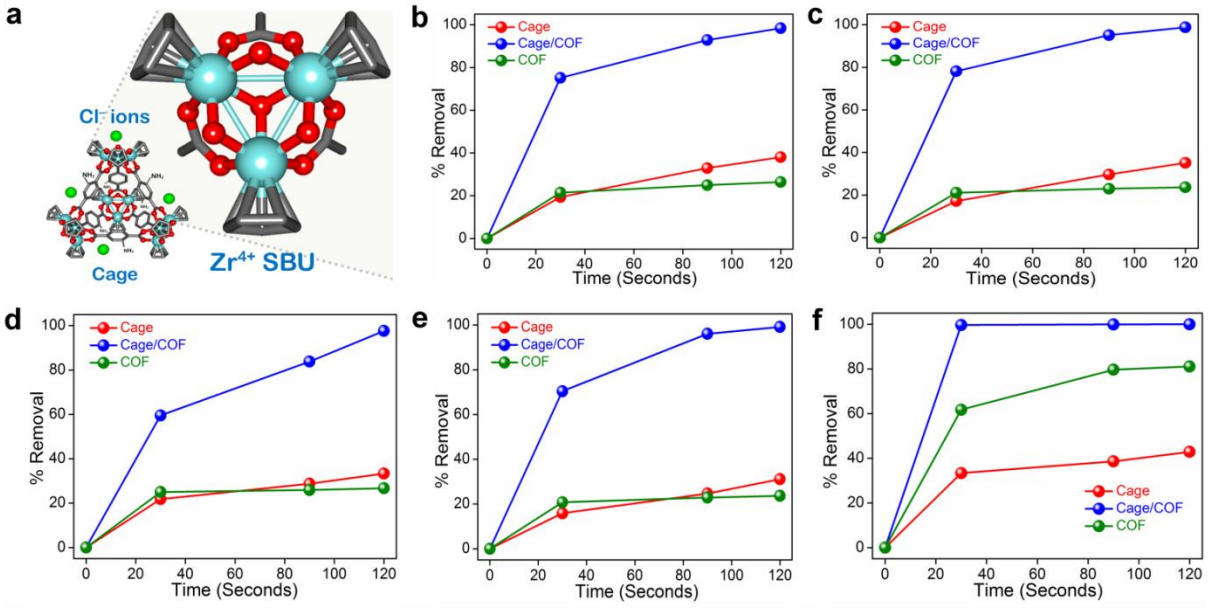

Figure 3.3. Removal % of large concentration (50 ppm) of oxoanions capture from the presence of mixture of ~1000 folds (each) other interfering anions viz. Cl^-, NO_3^-, Br^-, SO_4^{2-}, ClO_4^-. (a) Schematic diagram of composite material. (b) $HAsO_4^{2-}$; (c) SeO_4^{2-} ;(d) ReO_4^-; (e) CrO_4^{2-} and **f,** MnO_4^-.

imaging also highlights the transformation of the low emissive COF into a highly emissive material after successful grafting of the cage molecules (Figure 3.1f).

Presence of exchangeable Cl- ions and interaction sites (Zr(IV) SBU and additional amine functional groups) in the hybrid nanomaterial, actuated us to test its capture ability towards various toxic oxoanions in water.[25,26] Metal-derived oxoanions viz. CrO_4^{2-}, $Cr_2O_7^{2-}$, $HAsO_4^{2-}$, SeO_4^{2-}, ReO_4^- (surrogate anion for radioactive isotope TcO_4^-) and MnO_4^- were selected for capture experiments. For the initial screening test, cage/COF (200 mg) hybrid nanocomposite was dipped in coloured aqueous solutions of CrO_4^{2-} and MnO_4^- . the supernatant underwent decolouration within seconds (Appendix 3.10). Enthused by this observation, we sought to investigate the capture study of aforementioned oxoanions with cage/COF(200) hybrid nanoadsorbent (Figure 3.3, Appendix 3.11) and monitored through UV-vis spectroscopy (for CrO_4^{2-}, $Cr_2O_7^{2-}$, MnO_4^-, ReO_4^-) and ICP-AES analysis ($HAsO_4^{2-}$ and SeO_4^{2-}). The intensity of UV-vis spectra of the supernatant of CrO_4^{2-}, $Cr_2O_7^{2-}$, ReO_4^- and MnO_4^- continuously decreased with passage of treatment time (Appendix 3.12-3.16) which is supported our naked eye observation. The ICP-AES analysis also revealed significant lowering in the concentration of $HAsO_4^{2-}$ and SeO_4^{2-} with time in the supernatant (Appendix 3.12). The hybrid material has been showed better capture performance towards various oxoanions compared to its parent materials. Rapid entrapment of oxoanions was occurred across a wide

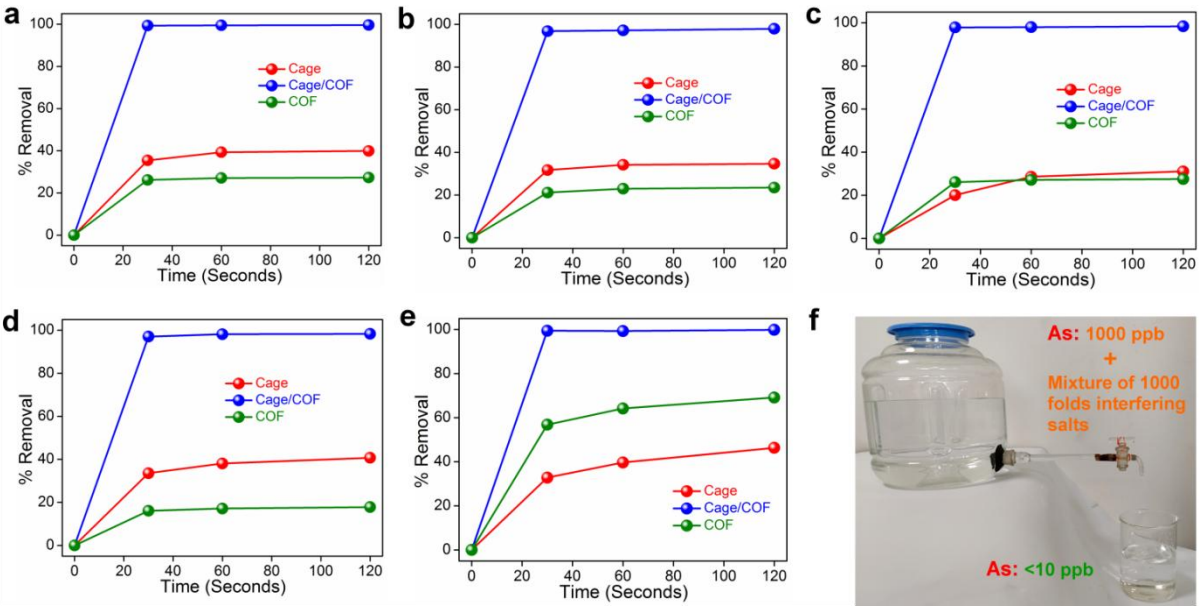

Figure 3.4. Removal % of trace amount (1 ppm) of oxoanions capture from the presence of mixture of ~1000 folds (each) other interfering anions viz. Cl^-, NO_3^-, Br^-, SO_4^{2-}, ClO_4^-. (a) $HAsO_4^{2-}$; (b) SeO_4^{2-}; (c) ReO_4^-; (d) CrO_4^{2-} and (e) MnO_4^-. (f) Mimic the real time applications where water of container contained As(1 ppm) along with mixture of ~1000 folds (each) other competitive ions.

range of pH as well as in various temperatures (Appendix 3.17-3.24) which is crucial for real practice in the industrial waste treatment. Industrial waste water bearing oxoanions commonly contains a high concentration of competitive anions viz. Cl^-, NO_3^-, Br^-, SO_4^{2-}, ClO_4^- etc, which affects severely to the adsorption process. To have a clear insight into the influence of interfering ions on the capture performance of the hybrid nanoadsorbent, exchange experiments were executed with time. The material retained its original capturing efficacy even in the presence of large excess of other interfering salts (Figure 3.3, Appendix 3.25-3.27), confirming no significant influence of other ions on the adsorption processes. The ultrafast sequestration efficiency and unprecedented selectivity towards variety of oxoanions render the cage/COF(200) hybrid material as a superior material in comparison to other adsorbents (Appendix Table 3.8).

The sequestration of all oxoanions by cage/COF(200) hybrid nanoscavenger follows the pseudo second order kinetics (Appendix 3.28 and 3.29). The hybrid material loaded with oxoanions readily regenerated using saturated Na_2SO_4 solutions by stirring it for ~ 12 hours. The hybrid nanoscavenger could be easily recycled without compromising its sorption efficiency even after several consecutive cycles (Appendix 3.30 and 3.31), validated its commendable regeneration ability for capture study. The hybrid material preserved its structural integrity even after the recycling process, reflected by its identical PXRD patterns (Appendix 3.32). There was a drastic reduction in the removal efficiency of the nonhybrid material BDC cage@COF (200) only after fourth cycle compared to the hybrid material (Appendix 3.33 and) due to leaching of cage molecules from the composite material during capture study. Therefore, hybrid composite is a better candidate compare to nonhybridized composite for effective sequestration of oxoanions from contaminated water.

The capture study has been focused mostly on storage capacity so far in the literature, but very little attention has been paid to the selectivity presence of competitive anions, which is equally important for realistic applications.[27] By virtue of rapid and efficient oxoanions adsorbing behaviour of the material, treatment of Cr(VI) contaminated waste water was performed, by mimicking the real time scenario. We conducted a chromatographic column exchange experiment where hybrid material was loaded in the column bed and aqueous solution of highly concentrated Cr(VI) along with other interfering ions were passed through the column (Appendix 3.34 and 3.35). It is noteworthy to mention that, tested water contain equal as well as 1000 fold excess of other interfering salts compared to the chromate anions. A distinct color change was observed by naked eye for the eluent as a consequence of adsorption by the hybrid nanoscavenger.

The concentration of Cr in the column eluted water was further analysed through UV-vis and ICP-AES analysis. Total Cr concentration of the column eluted water was well below (<50 ppb) in the plant discharge water suggested by USA-EPA and the EU (Appendix 3.36 and 3.37). Above and beyond our studies on synthetic contaminated water, we also tested if the current EPA standards for oxoanions in drinking water could be satisfied using this hybrid nanoadsorbent. In order to provide confirmation of the capturing ability of the material from drinking water, very low concentration capturing study in the presence of a large excess of other ions was also performed and monitored through ICP-AES analysis (Figure 3.4). The concentration of the oxoanions again decreased rapidly in the contaminated water. The outstanding adsorption performance features spurred their exploration into natural polluted water treatment. Arsenic contaminated ground water was selected as a model oxoanion for the real-world capture study. Therefore, arsenic adsorption of cage/COF(200) hybrid material was carried out on natural water samples collected from Kaliachak (District: Malda, State: West Bengal) of India, widely known as arsenic contaminated affected areas. The hybrid nanoadsorbent rapidly reduced the Arsenic levels in the drinking water (<10 ppb) to the EPA recommended levels (Figure 3.5a and 3.5b). The successful tests were confirming that, the hybrid nanocomposite is a promising candidate for remediation of toxic oxoanions from both effluents of industrial plants as well as from natural water samples. To the best of our

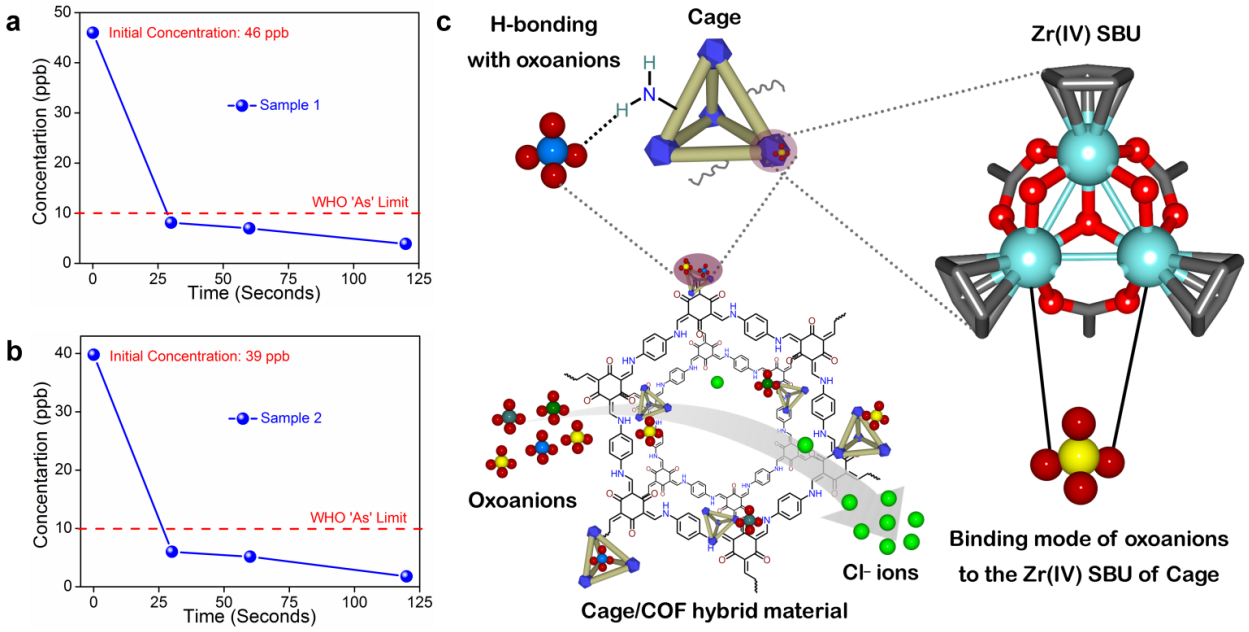

Figure 3.5. As removal studies on underground water and probable mechanism of capture studies by cage/COF(200) hybrid material. (a) and (b) Removal % of As form the natural drinking water samples. (c) Potential binding modes towards oxoanions with the hybrid material.

knowledge, rapid sequestration of a wide variety of metal-based oxoanion pollutants was successfully achieved for the first time. The ultrafast selectivity of this hybrid material towards oxoanions is attributed to the following reasons: (I) presence of exchangeable Cl- ions, [28] (II) Zr(IV) based SBU, which has been well documented for its strong interaction with oxoanions [29,30] and (III) existence of additional -NH_2 functional groups, coming from covalently-linked cage molecules in the hybrid material.[29,31,32] The proposed mechanism of the oxoanion capturing process is depicted in Figure 3.5c.

3.4 Conclusions

In summary, we have successfully designed and synthesized a cationic hybrid composite through covalent-linking between two individual materials viz. COF and cage molecules for the first time. To gain a detailed insight of the material, structural and optical characterizations have been systematically studied. The hybrid material has been utilized as a selective nanoscavenger for high as well as trace amount of metal-containing toxic oxoanions (CrO_4^{2-}, $Cr_2O_7^{2-}$, SeO_4^{2-}, $HAsO_4^{2-}$, ReO_4^- and MnO_4^-) from synthetic solutions as well as natural water samples. We believe the cooperation of multiple functionalities is the key factor for remarkable selectivity of the material towards oxoanions even from the mixture of high concentration (~1000 folds) of concurrent competing ions. The ultrafast uptake property, superior selectivity and good recyclability render the newly developed hybrid nanocomposite as promising candidate for potential applications in real practice and deserves further exploration. We anticipate that the present findings will be a stepping stone to the development of efficient and inexpensive hybrid nanoadsorbents for an alternative source of water purifier.

3.5 Appendix section

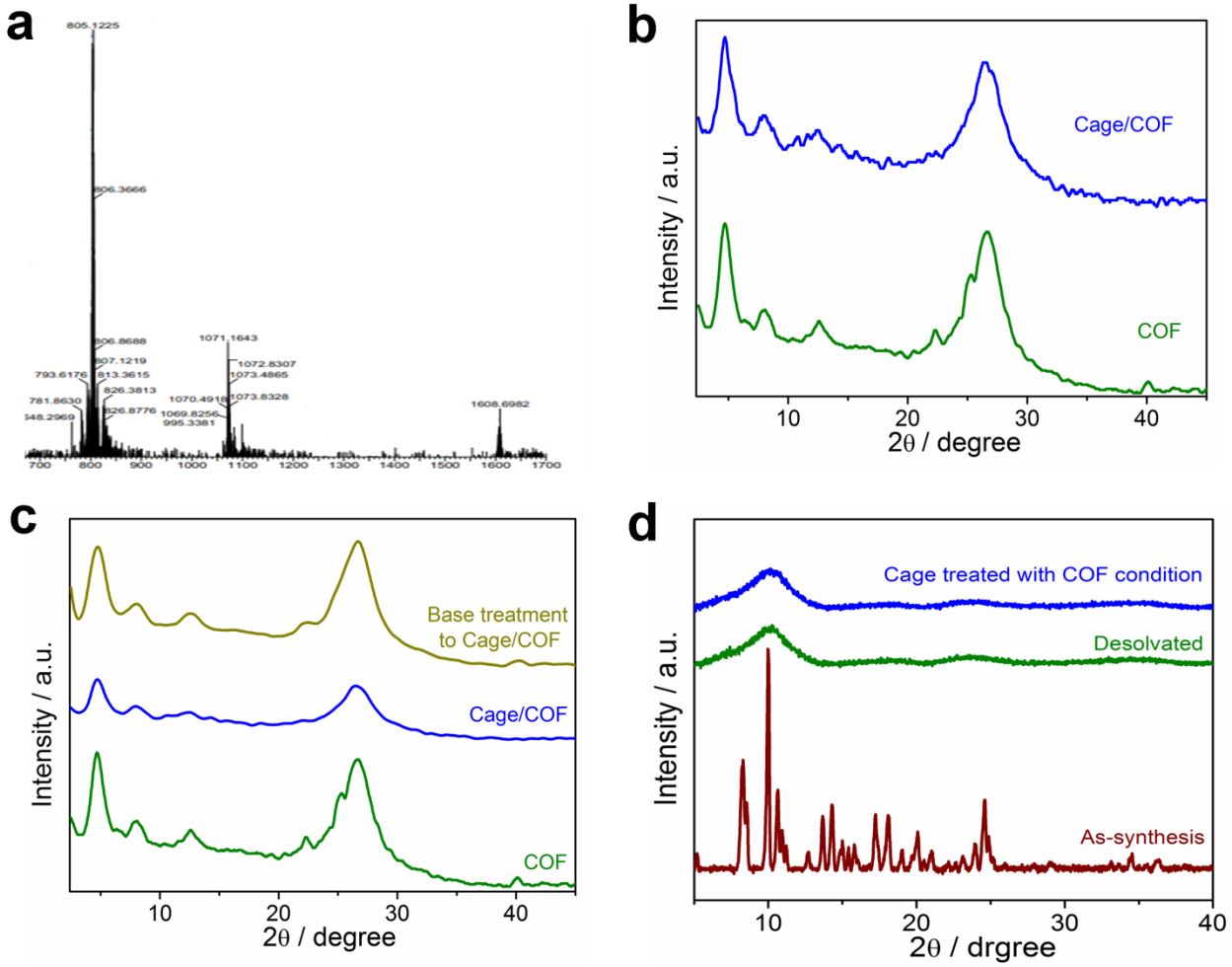

Appendix 3.1. Characterization of cage, COF and cage/COF(200) composite. **a,** ESI-TOF-MS analysis of as-synthesized BDC-NH_2 cage. **b,** PXRD patterns of pristine COF and cage/COF(200) composite. **c,** PXRD patterns of COF, cage/COF(200) before and after base treatment. **d,** PXRD patterns of cage in different conditions. The cage transformed into crystalline to amorphous phase when treated with a similar condition to COF synthesis, which is common for cage molecules.

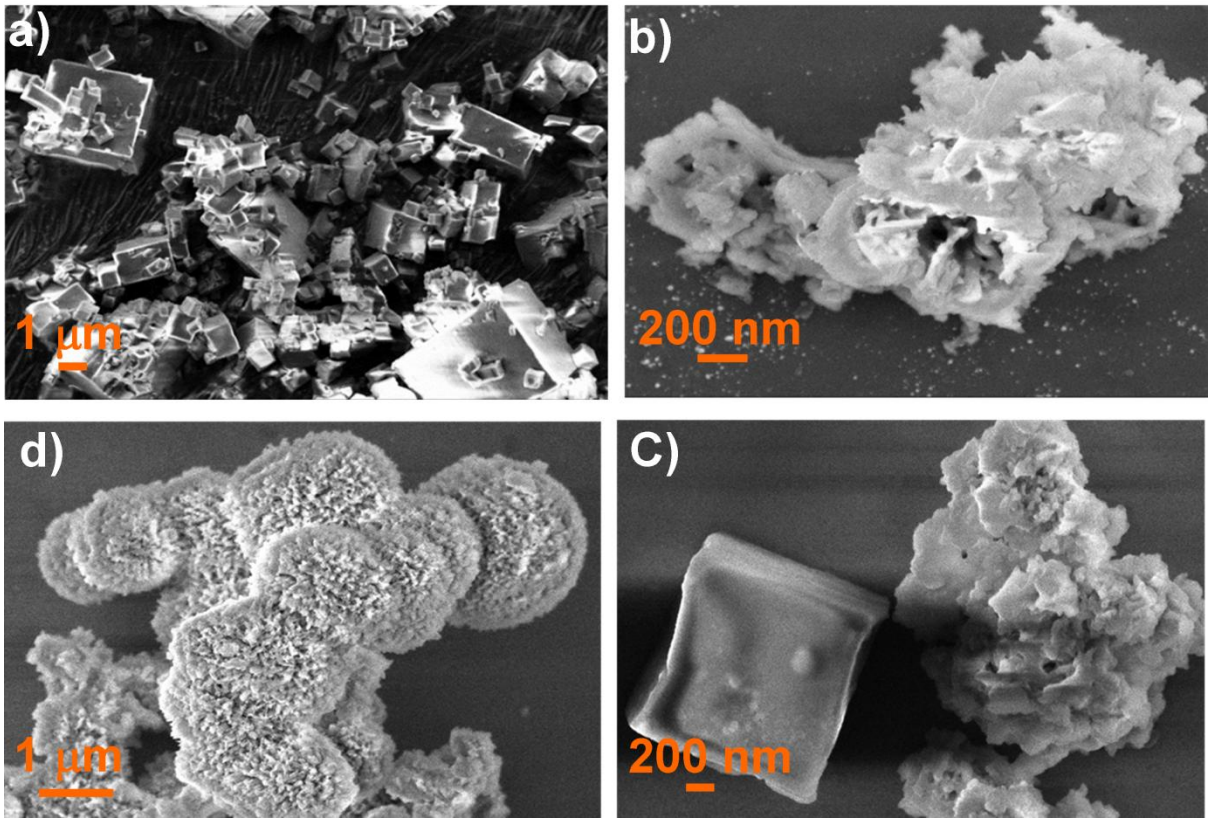

Appendix 3.2. FESEM images. **a,** Cage; **b,** COF; **c,** physical mixing of cage and COF; **d,** cage/COF(200) composite.

Appendix Table 3.1. EDX analysis from FESEM experiment of BDC-NH_2 cage molecule.

Element	Weight %	Atomic %
C K	49.02	67.86
N K	4.13	4.90
O K	20.78	21.59
Cl K	3.14	1.47
Zr L	22.94	4.18
Total	100.00	100.00

Appendix Table 3.2. EDX analysis of IPcomp-3(40) composite material containing 40 mg of MOP while COF amount remained same.

Element	Weight %	Atomic %
C K	57.84	64.46
N K	18.02	17.19
O K	21.51	17.96
Cl K	0.56	0.09
Zr L	2.07	0.30
Total	100.00	100.00

Appendix Table 3.3. EDX analysis of IPcomp-3(60) composite material containing 60 mg of MOP while COF amount remained same.

Element	Weight %	Atomic %
C K	57.93	64.70
N K	19.40	18.47
O K	19.85	16.55
Cl K	0.60	0.17
Zr L	2.21	0.45
Total	100.00	100.00

Appendix Table 3.4. EDX analysis of IPcomp-3(80) composite material containing 80 mg of MOP while COF amount remained same.

Element	Weight %	Atomic %
C K	66.05	74.35
N K	11.22	10.57

O K	16.08	13.84
Cl K	1.37	0.26
Zr L	5.28	0.72
Total	100.00	100.00

Appendix Table 3.5. EDX analysis of IPcomp-3(100) composite material containing 100 mg of MOP while COF amount remained same.

Element	Weight %	Atomic %
C K	63.38	72.61
N K	8.69	8.56
O K	20.10	17.34
Cl K	0.52	0.38
Zr L	7.31	1.11
Total	100.00	100.00

Appendix Table 3.6. EDX analysis of IPcomp-3(200) composite material containing 200 mg of MOP while COF amount remained same.

Element	Weight %	Atomic %
C K	44.54	61.08
N K	9.06	10.60
O K	23.94	24.51
Cl K	3.84	0.93
Zr L	18.61	2.88
Total	100.00	100.00

Appendix Table 3.7. EDX analysis of IPcomp-3(300) composite material containing 300 mg of MOP while COF amount remained same.

Element	Weight %	Atomic %
C K	42.54	60.86
N K	7.29	8.94
O K	22.80	24.49
Cl K	3.93	1.30
Zr L	23.44	4.41
Total	100.00	100.00

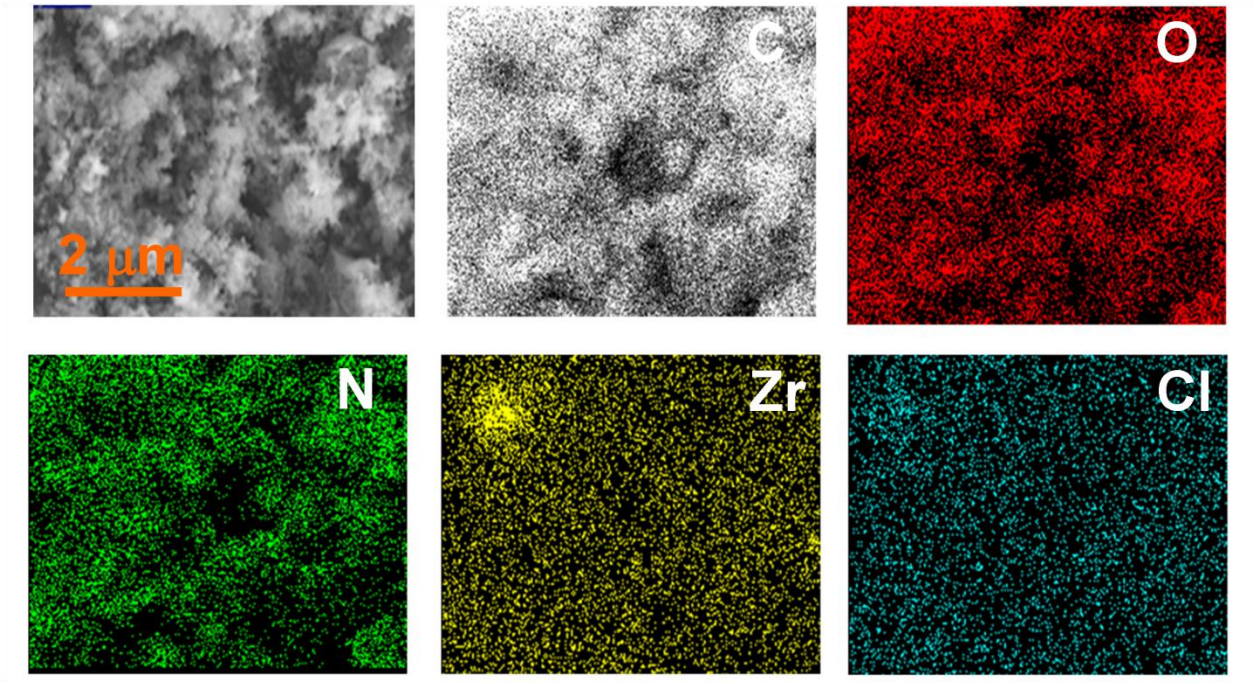

Appendix 3.3. Elemental mapping of cage/COF(200) composite material from FESEM experiment. Mapping analysis shows the Zr and Cl are present throughout the composite material.

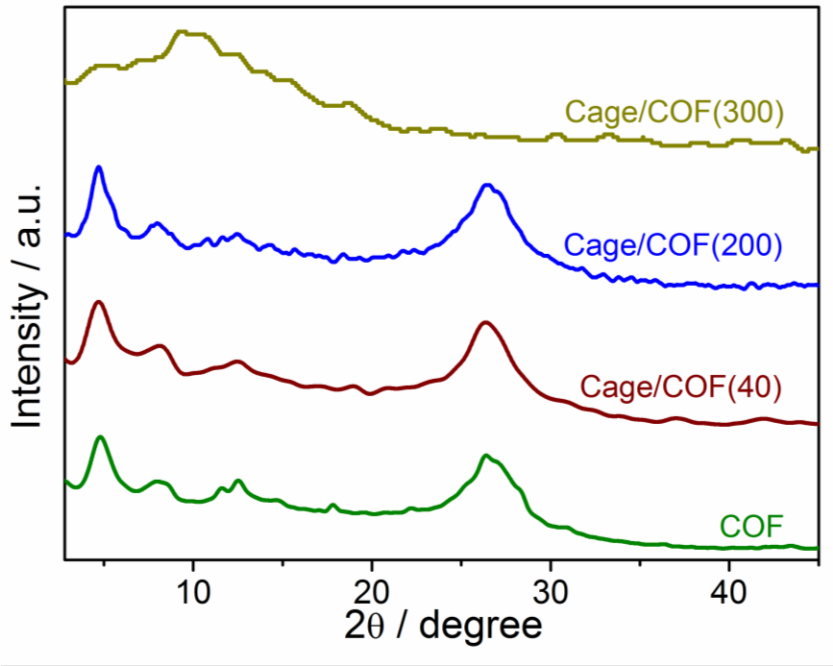

Appendix 3.4. PXRD patterns of COF, cage/COF(40), cage/COF(200) and cage/COF(300).

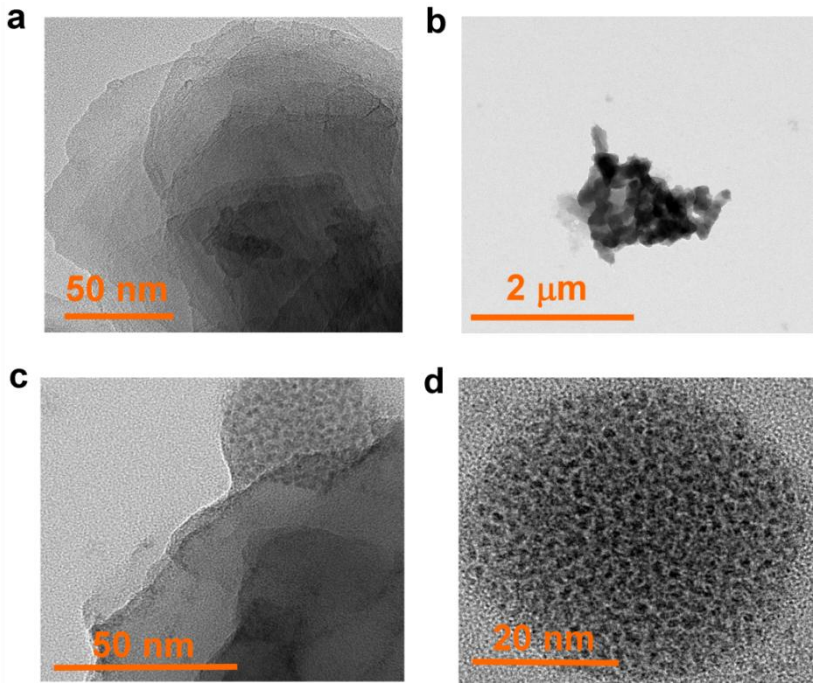

Appendix 3.5. TEM images. **a,** TEM images of COF. **b,** Cage molecules are embedded into the COF matrix. There are no cage nanoparticles outside the black zone which indicates the cage molecules have strong interaction with COF matrix. **c,** TEM images of cage/COF(200). **d,** Magnified TEM images of cage/COF(200).

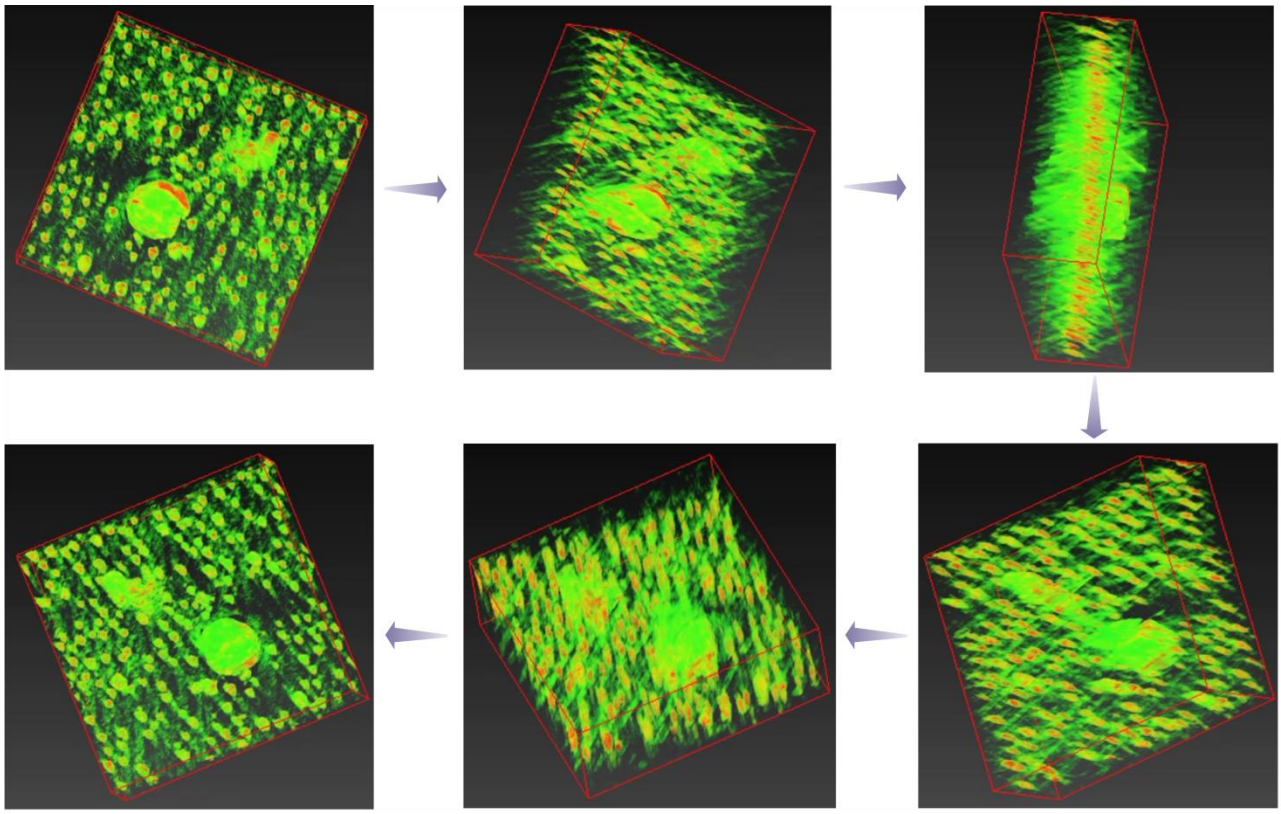

Appendix 3.6. Tomography images of cage/COF(200) in different angles (clock wise flipping). Two different color indicates there are two different electron cloud present in the composite material and red color cloud is embedded inside green cloud. Here green color indicate the COF matrix while red color indicate the loaded cage molecules.

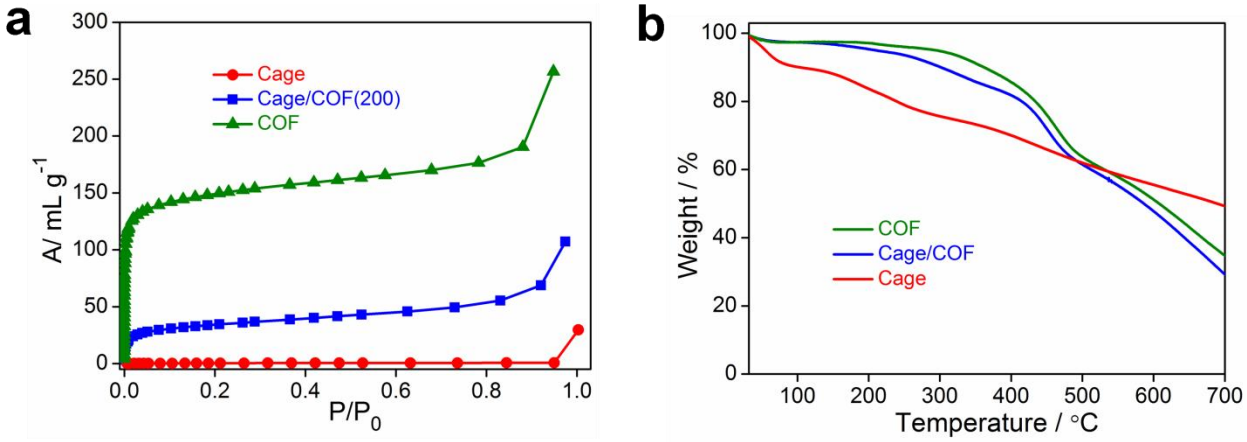

Appendix 3.7. a, N_2 sorption isotherm at 77 K. **b,** TGA curves of activated phases.

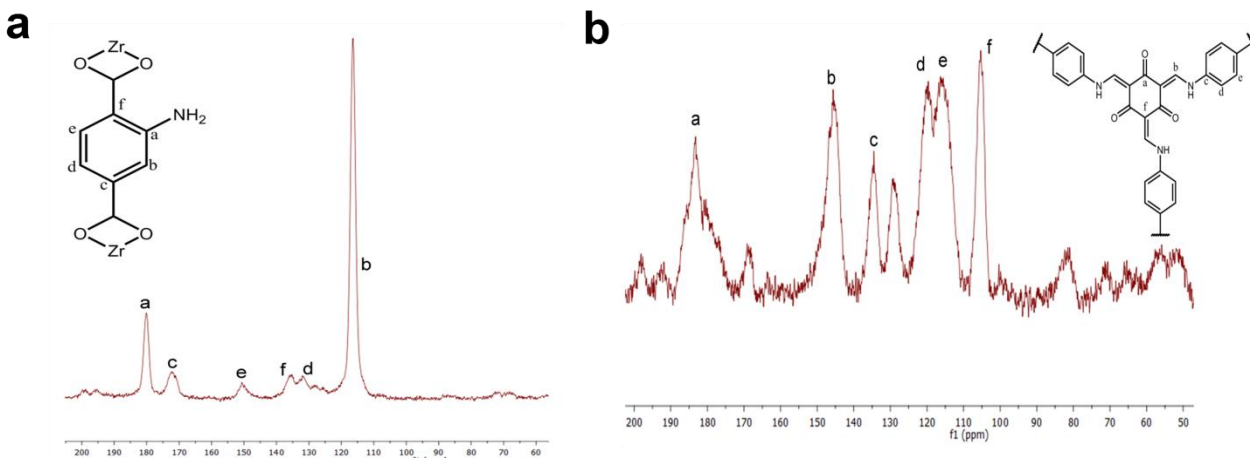

Appendix 3.8. NMR spectra. **a,** Solid state ^{13}C NMR spectra of Cage molecule. **b,** Solid state ^{13}C NMR spectra of COF.

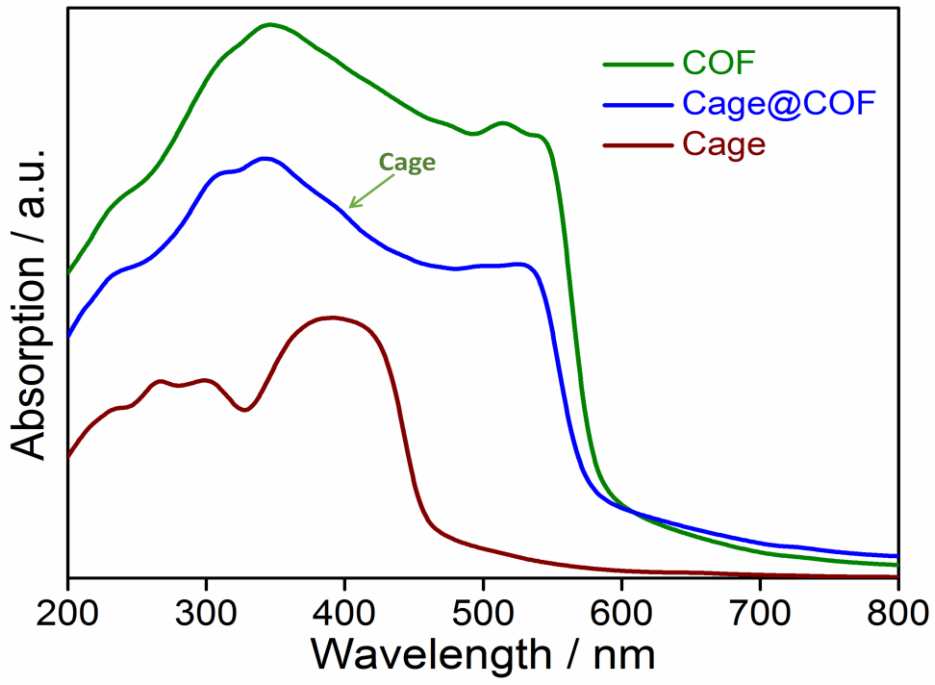

Appendix 3.9. Solid state UV plot of COF, cage and cage/COF composite material. Characteristics peaks of both cage and COF are present in the composite material, indicating both materials are present in the composite material.

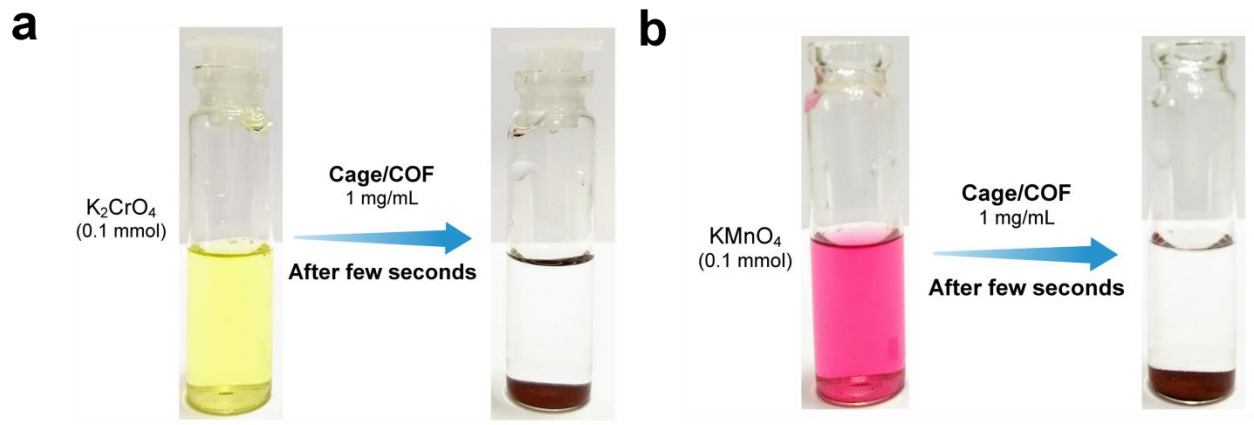

Appendix 3.10. a, Photographs of before and after CrO_4^{2-} capture study by hybrid cage/COF(200). **b,** Photographs of before and after MnO_4^- capture study by cage/COF(200).

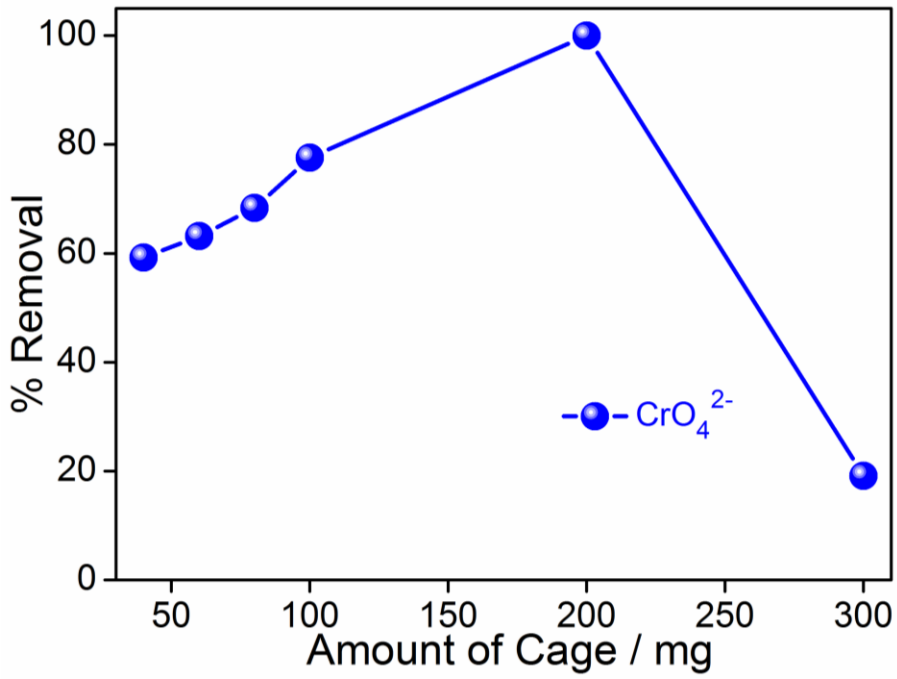

Appendix 3.11. CrO_4^{2-} capture study carried out using different hybrid composite materials: cage/COF(40), cage/COF(60), cage/COF(80), cage/COF(100), cage/COF(200) and cage/COF(300). The cage/COF(200) showing highest capture efficiency compare to other hybrid composite materials. The duration of capture study was 2 minutes.

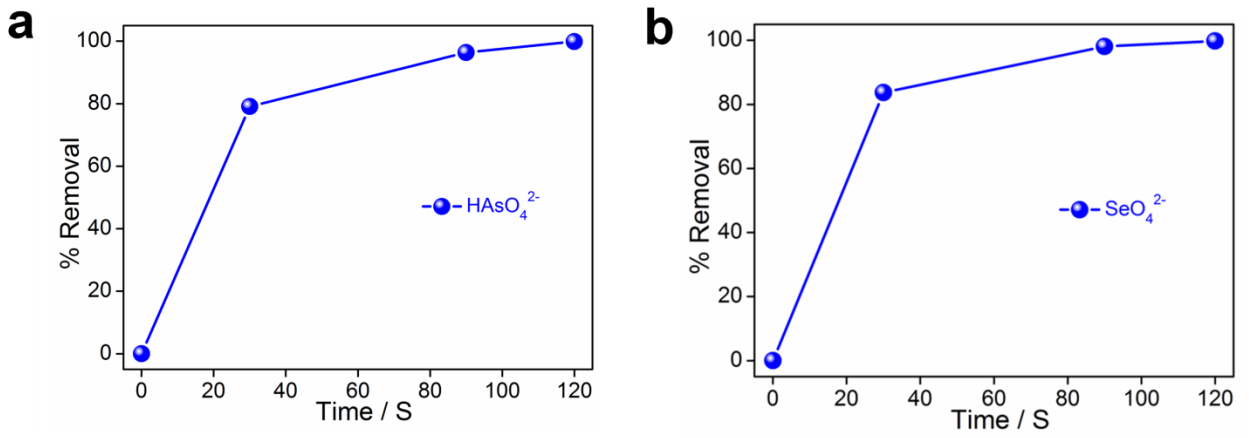

Appendix 3.12. a, % removal of $HAsO_4^{2-}$ at different time intervals by cage/COF(200) hybrid material. **b,** % removal of SeO_4^{2-} at different time intervals by cage/COF(200) hybrid material.

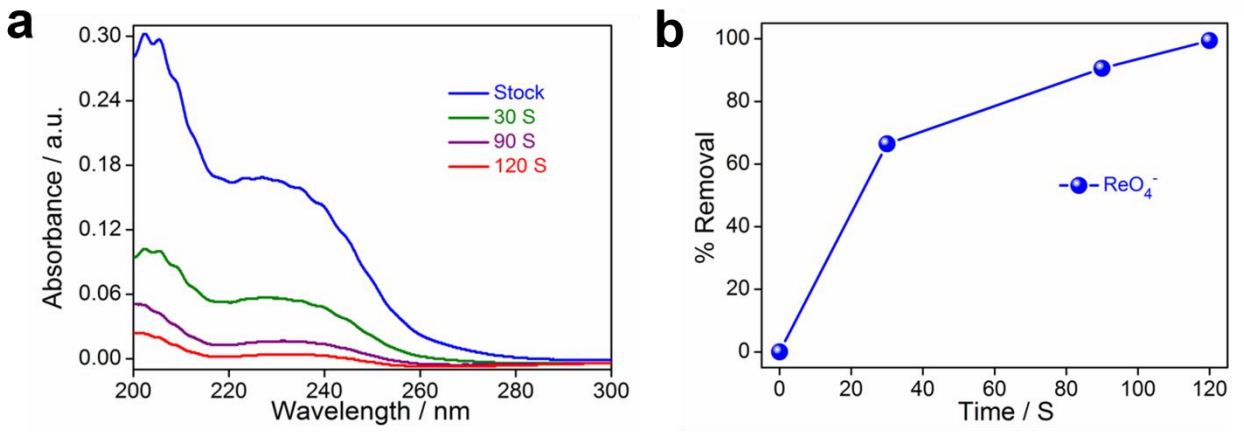

Appendix 3.13. a, UV-vis spectra of ReO_4^- in aqueous solution at different time intervals presence of Cage/COF(200) hybrid composite material. **b,** Removal % of ReO_4^- at different time intervals presence of Cage/COF(200) material.

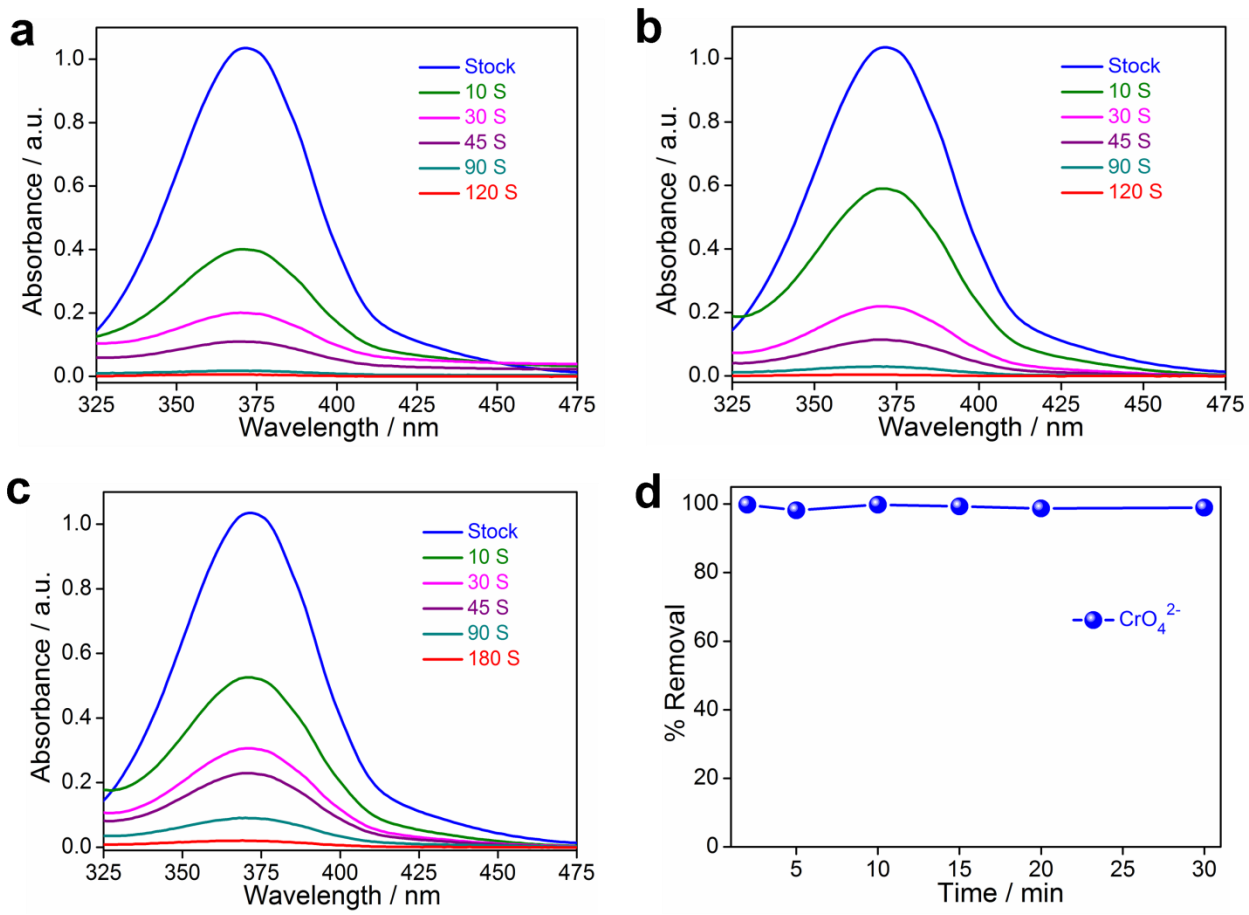

Appendix 3.14. UV-vis spectra of CrO_4^{2-} in aqueous solution at different time intervals. **a,** COF; **b,** cage; **c,** cage/COF(200) hybrid composite. **d,** Leaching test CrO_4^{2-} from cage/COF(200) hybrid composite with time.

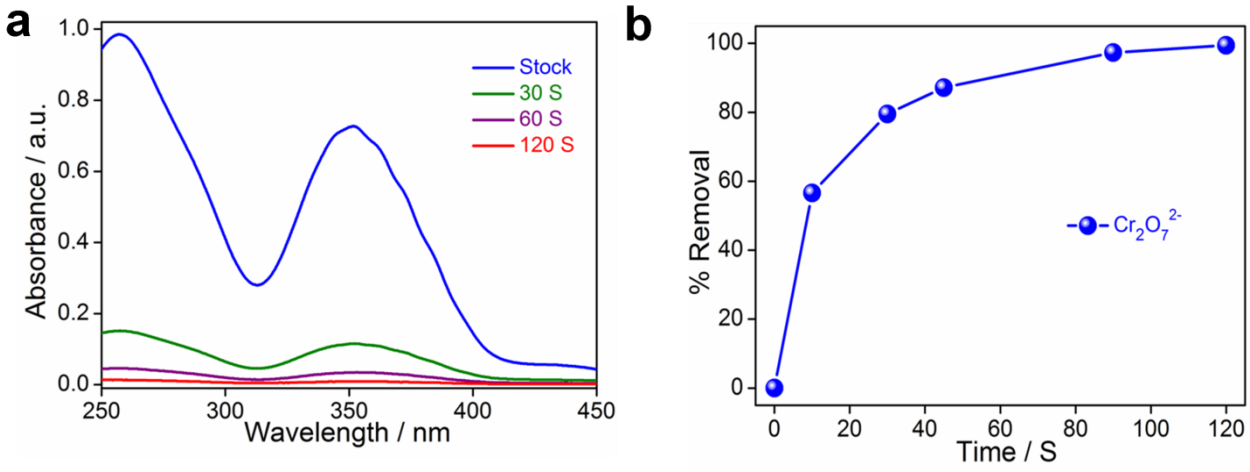

Appendix 3.15. a, UV-vis spectra of $Cr_2O_7^{2-}$ in aqueous solution at different time intervals presence of cage/COF(200) hybrid composite material. **b,** Removal % of $Cr_2O_7^{2-}$ at different time intervals presence of cage/COF(200) hybrid composite material.

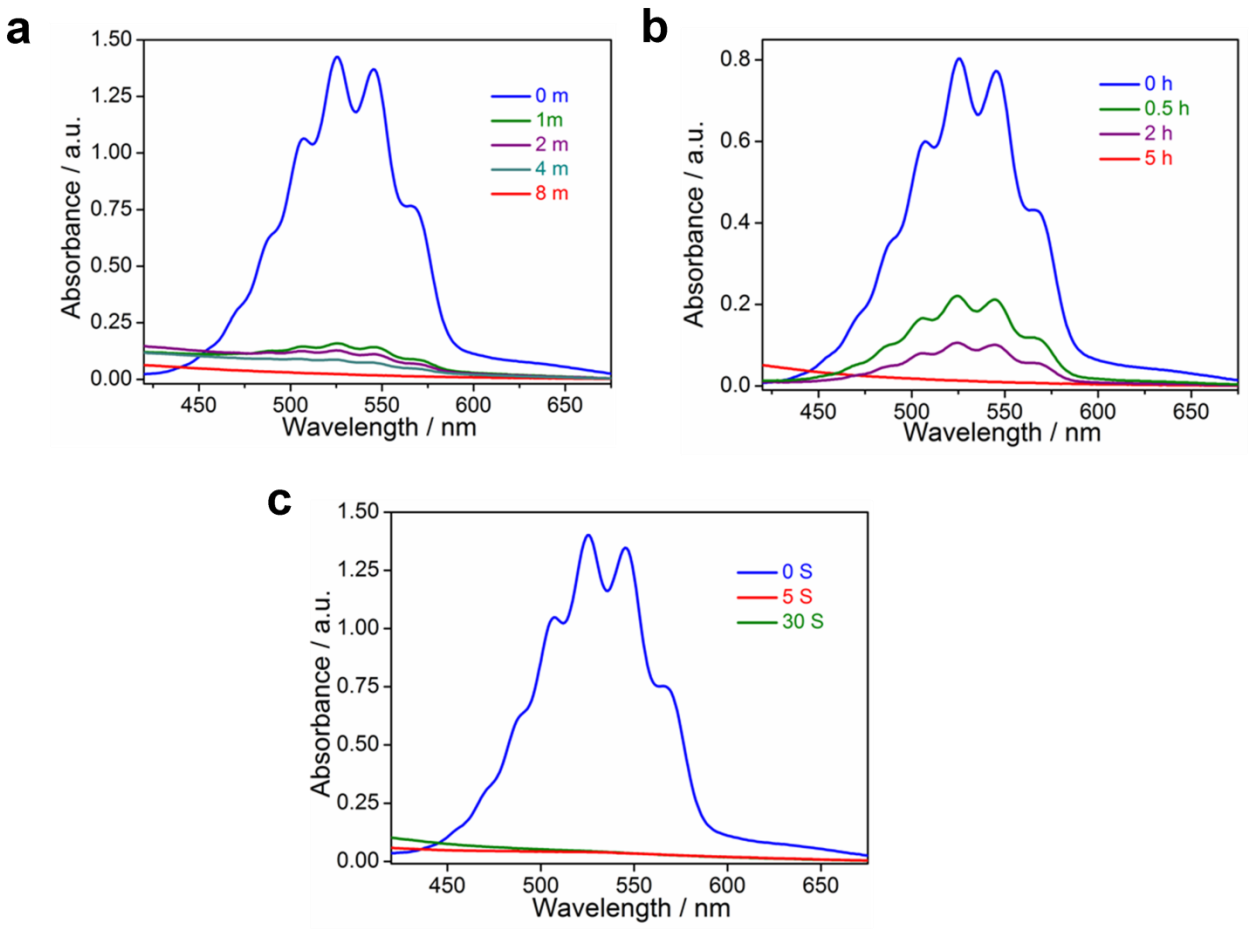

Appendix 3.16. UV-vis spectra of $KMnO_4$ in aqueous solution at different time intervals. **a,** COF; **b,** cage; **c,** cage/COF(200) hybrid composite.

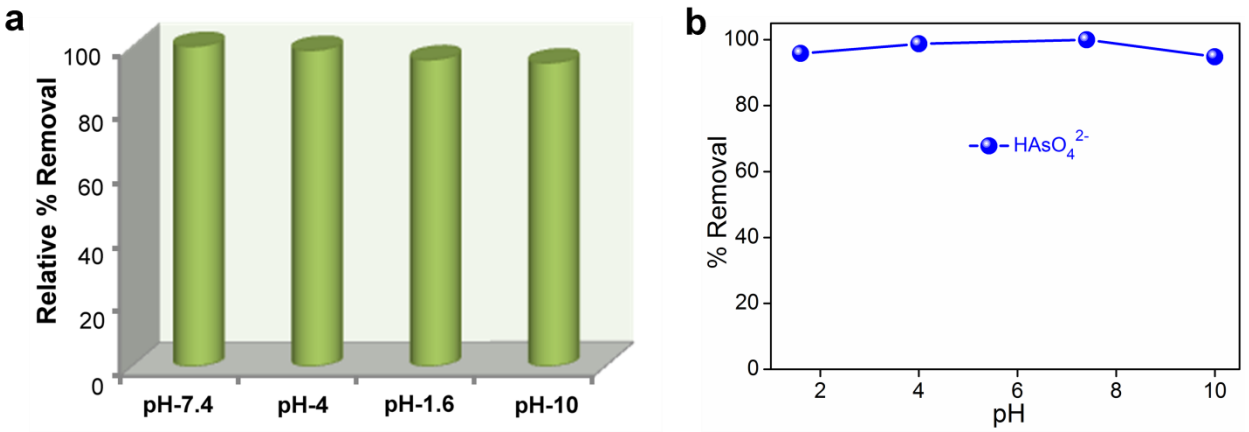

Appendix 3.17. a, Bar diagram representing relative % removal of $HAsO_4^{2-}$ from aqueous solution by Cage/COF(200) at different pH within 2 min. **b,** removal % of $HAsO_4^{2-}$ from different pH solution by Cage/COF(200) composite material.

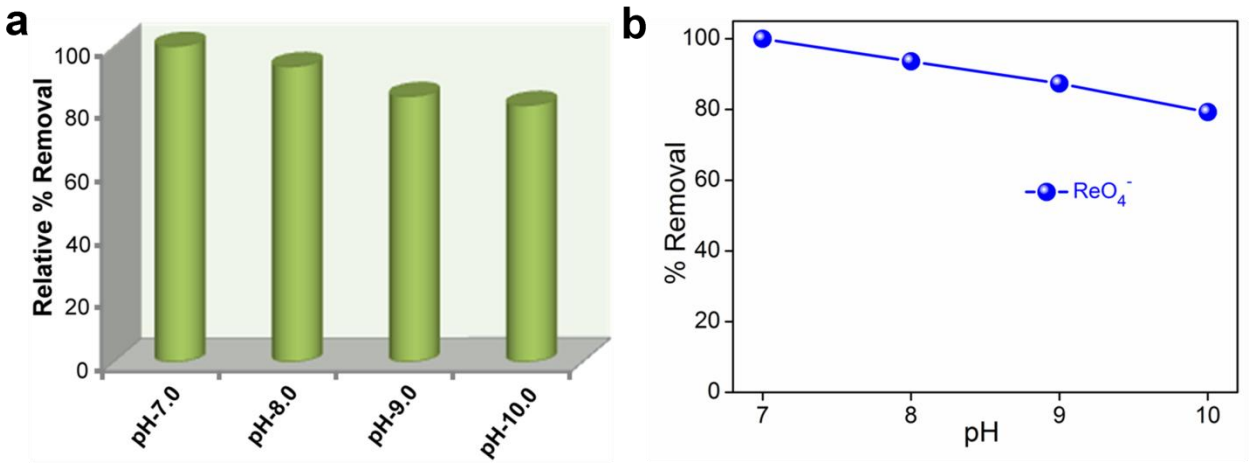

Appendix 3.18. a, Bar diagram representing relative % removal of ReO_4^- from aqueous solution by cage/COF(200) at different pH within 2 min. **b,** removal % of $ReO_4^-$from different pH solution by cage/COF(200).

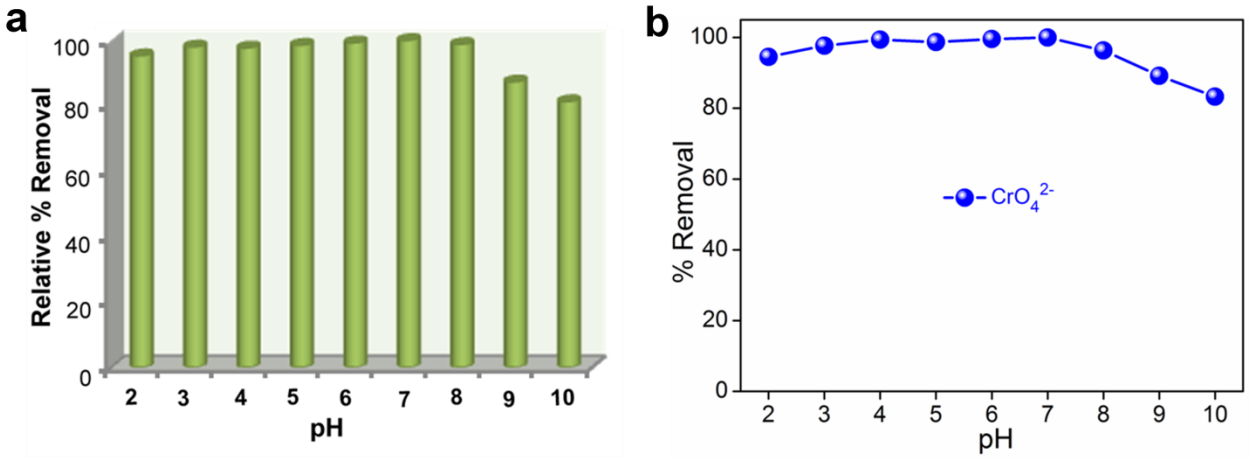

Appendix 3.19. a, Bar diagram representing relative % removal of CrO_4^{2-} from aqueous solution by cage/COF(200) at different pH within 2 min. **b,** removal % of CrO_4^{2-} from different pH solution by cage/COF(200) hybrid composite material.

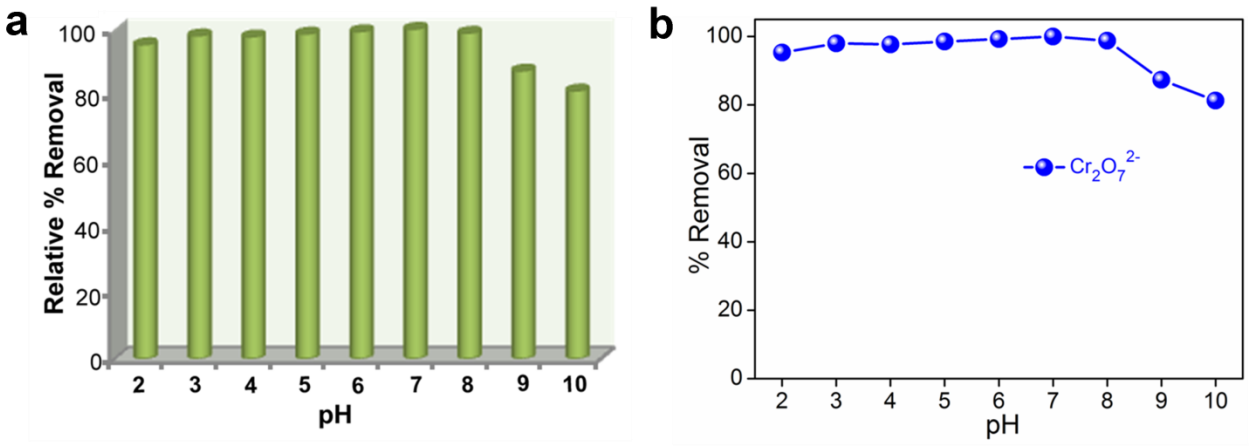

Appendix 3.20. a, Bar diagram representing relative % removal of $Cr_2O_7^{2-}$ from aqueous solution by cage/COF(200) at different pH within 2 min. **b,** removal % of $Cr_2O_7^{2-}$from different pH solution by cage/COF(200) hybrid composite material.

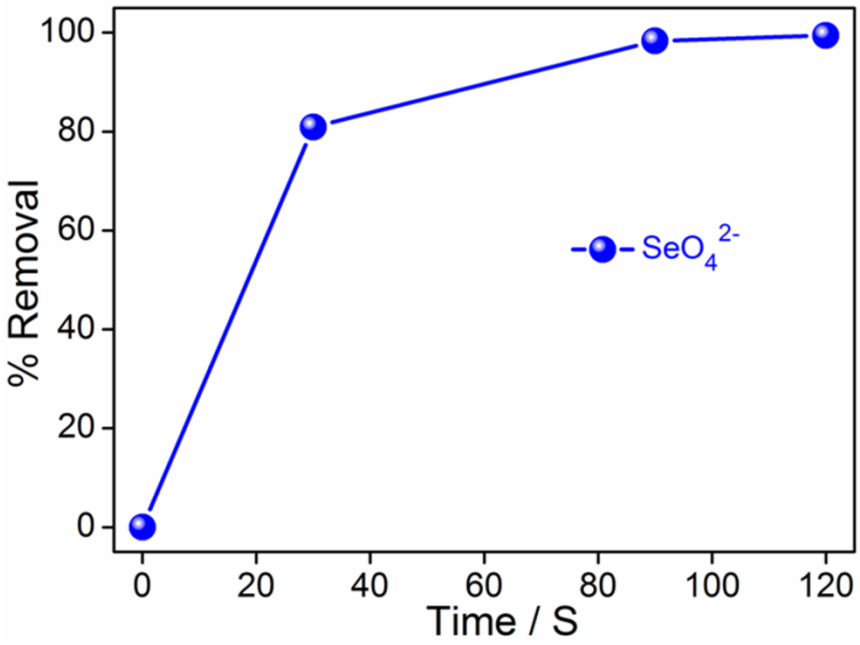

Appendix 3.21. Removal % of SeO_4^{2-} at different time intervals presence of Cage/COF(200) hybrid material at 40 °C.

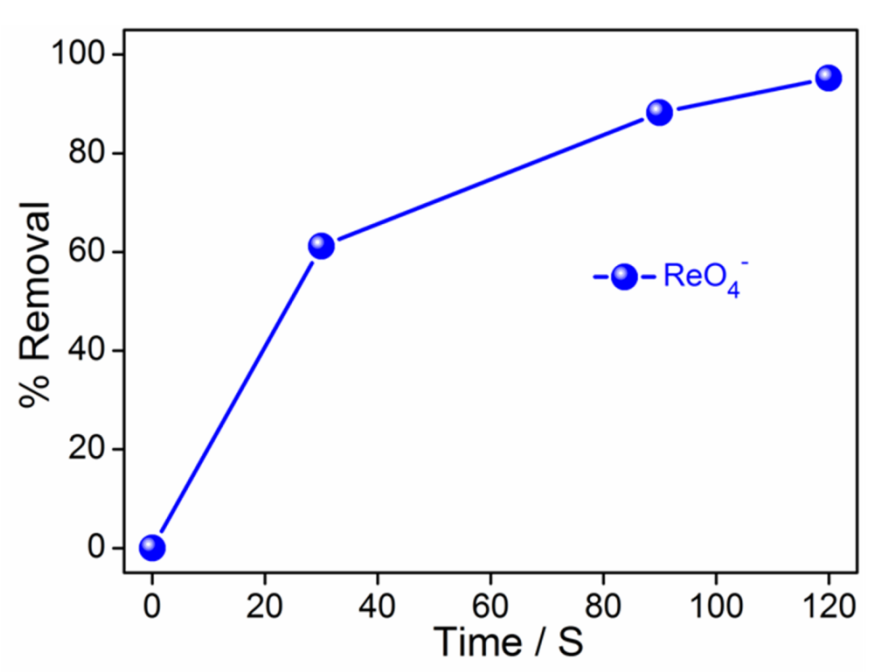

Appendix 3.22. Removal % of ReO_4^- at 40 °C, presence of cage/COF(200) hybrid material.

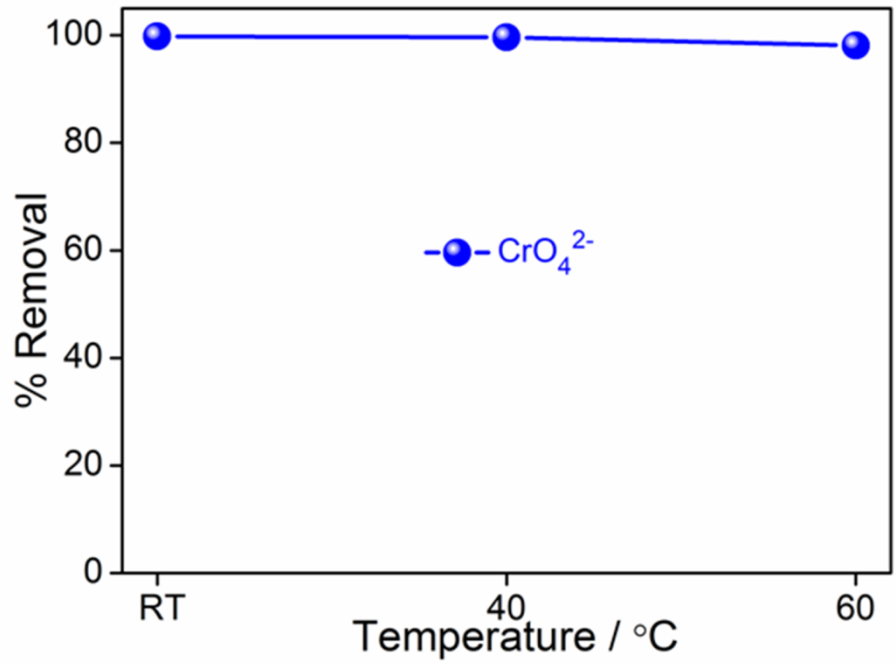

Appendix 3.23. Removal % of CrO_4^{2-} at different time intervals presence of cage/COF(200) hybrid material. **a,** Room Temperature; **b,** 40 °C; **c,** 60 °C; **d,** all temperature.

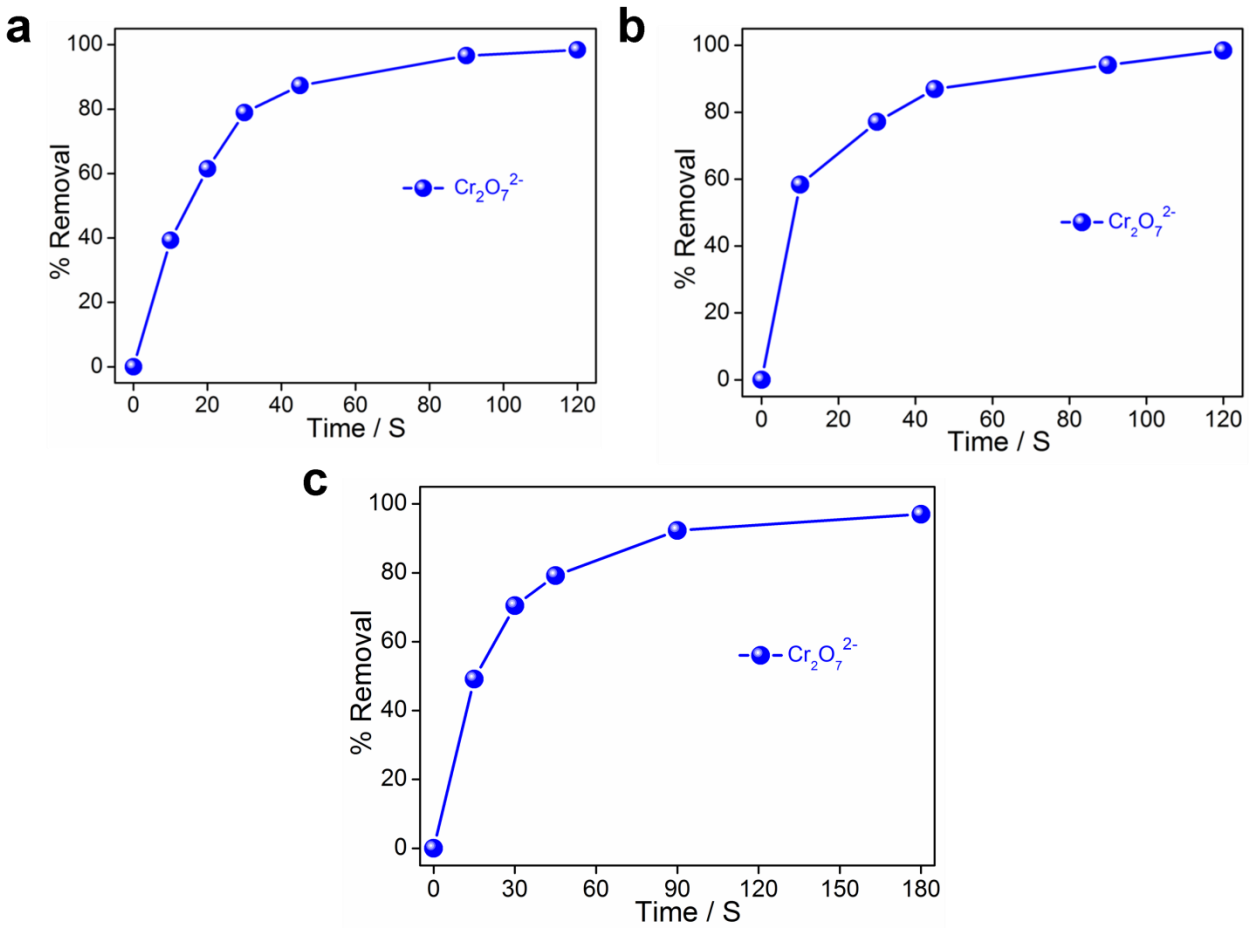

Appendix 3.24. Removal % of $Cr_2O_7^{2-}$ at different time intervals presence of cage/COF(200) hybrid material. **a,** Room temperature; **b,** 40 °C; **c,** 60 °C.

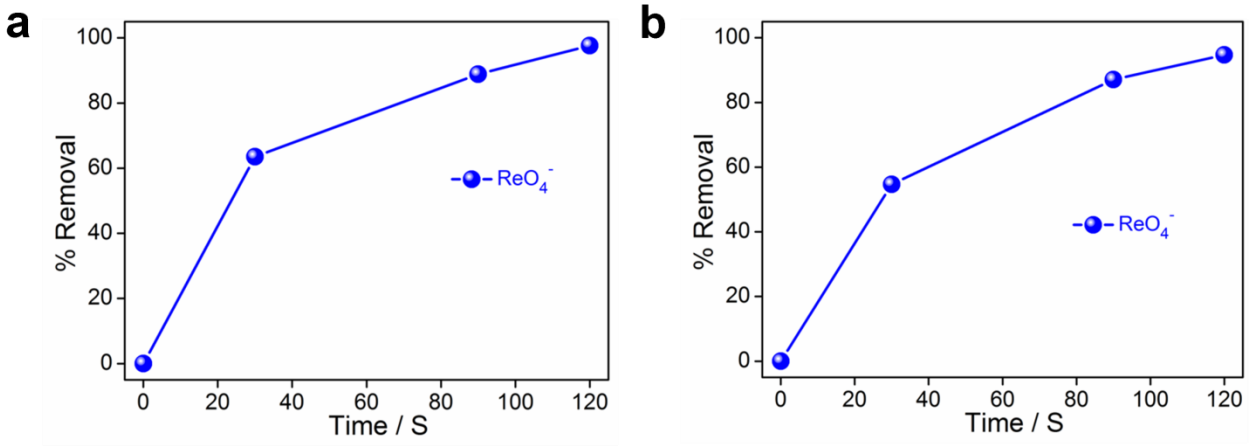

Appendix 3.25. Removal % ReO_4^- at different time intervals presence of Cage/COF(200) hybrid material. **a,** presence of only ReO_4^-; **b,** Presence of equal amount of ReO_4^- and other interfering ions at 40°C.

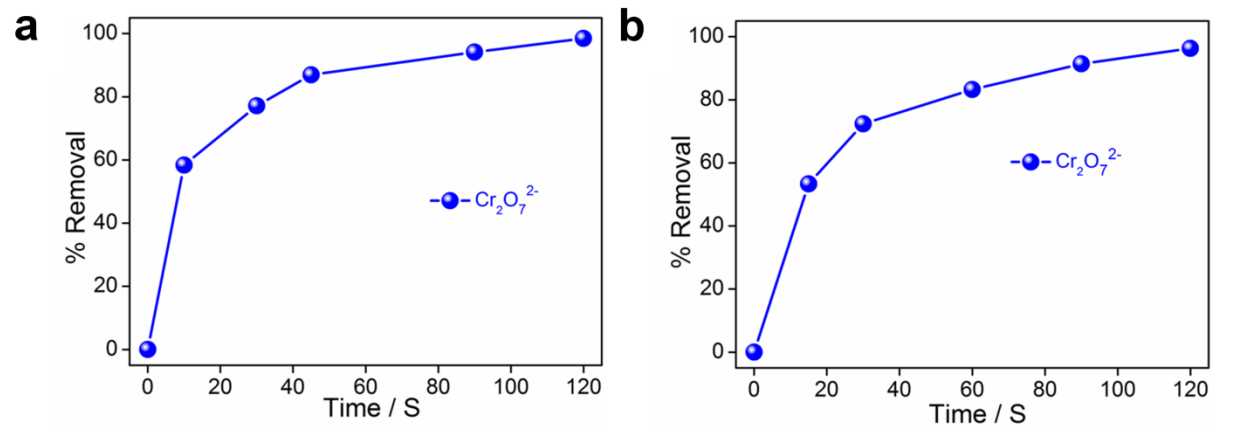

Appendix 3.26. Removal % of $Cr_2O_7^{2-}$ at different time intervals presence of Cage/COF(200) hybrid material. **a,** Presence of only $Cr_2O_7^{2-}$; **b,** presence of equal amount of $Cr_2O_7^{2-}$ and other interfering ions at 40°C.

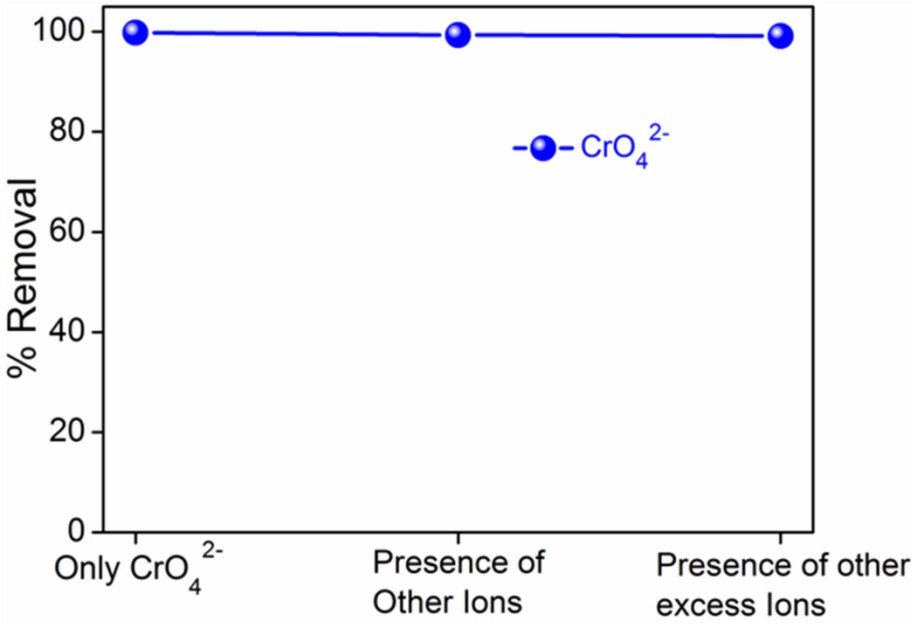

Appendix 3.27. Removal % of CrO_4^{2-} at different time intervals presence of Cage/COF(200) hybrid material. **a,** Presence of only CrO_4^{2-}; **b,** presence of equal amount of CrO_4^{2-} and other interfering ions; **c,** presence of CrO_4^{2-} and large excess (1000 times) of other interfering ions compare to CrO_4^{2-}; **d,** removal % of only CrO_4^{2-}, presence of equal amount of interfering ions and presence of large excess of other interfering ions.

Appendix Table 3.8. Comparison of this work with other related investigations of As(V) capture for various adsorbents. (N.D.: Not Done)

Compounds	Contact Time	Selectivity		Ref.
		Presence of Other Interfering ions		
		Binary mixture of ions	Mixture of ions (~ 1000 fold)	
Cage/COF(200)	<2 min	Cl^-, NO_3^-, Br^-, SO_4^{2-}, ClO_4^-	Cl^-, NO_3^-, Br^-, SO_4^{2-}, ClO_4^-	This Work
Fe-BTC	10 min	N.D.	N.D.	[33]
NH_2-MIL-88(Fe)	60 min	Mg^{2+}, Al^{3+}, Bi^{3+}, Ag^+, Cu^{2+}, Co^{2+}, Zn^{2+}, Ni^{2+}, Mn^{2+}, Pb^{2+}, Cr^{3+}, Ac^-, SO_4^{2-}, PO_4^{3-}, HCO_3, CO_3^{2-}, NO_3^-, Cl^-, Br^-	N.D.	[34]
Fe_3O_4@UiO-66	100 min	N.D.	N.D.	[35]
Zn-MOF-74	150 min	Cl^-, NO_3^-, PO_4^{3-}	N.D.	[36]
AUBM-1	3 h	CO_3^{2-}, NO_3^-	N.D.	[37]
MOF-808	4 h	N.D.	N.D.	[38]
ZIF-8	7 h	Cl^-, F^-, NO_3^-, SO_4^{2-}, PO_4^{3-}	N.D.	[39]
MIL-53(Al)	11 h	Cl^- ,F^-, NO_3^-, SO_4^{2-} , PO_4^{3-}	N.D.	[40]
UiO-66	24 h	Cl^-, NO_3^-, CO_3^{2-}, SO_4^{2-}	N.D.	[41]
Fe_3O_4@MIL-101(Cr)	24 h	Ca^{2+}, Mg^{2+}, PO_4^{3-}	N.D.	[42]
UiO-66-$(SH)_2$	24 h	N.D.	N.D.	[30]
Fe-Mn chitosan bead	36 h	SO_4^{2-}, HCO_3^-, SiO_3^{2-}, HPO_4^{2-}, Ca^{2+}, Mg^{2+}	N.D.	[43]

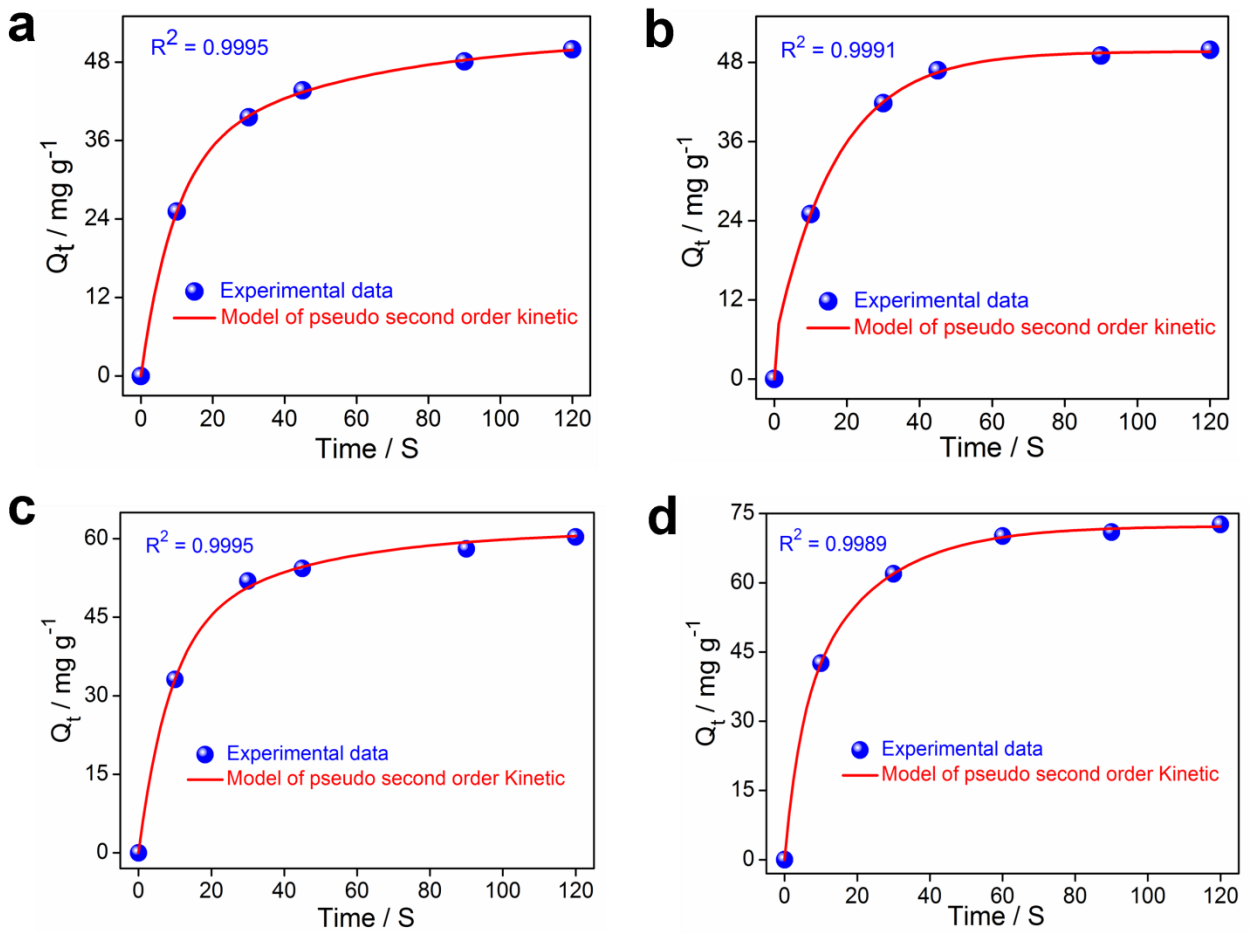

Appendix Figure 3.28. Kinetics study by cage/COF(200). **a,** $HAsO_4^{2-}$;**b,** SeO_4^{2-}; **c,** $CrO4^{2-}$; **d,** $Cr_2O_7^{2-}$.

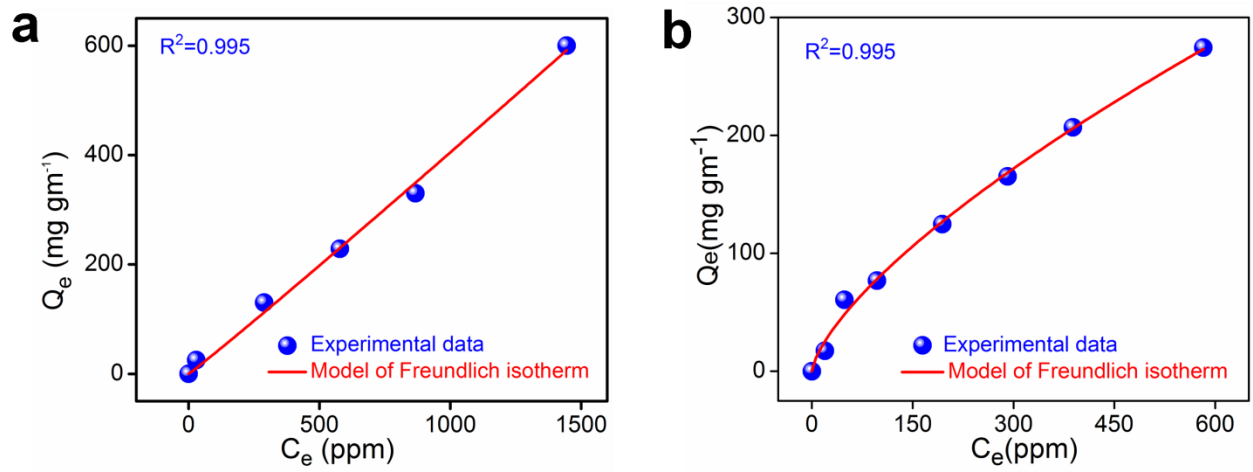

Appendix Figure 3.29. Freundlich model cage/COF(200) hybrid materials for **a,** ReO_4^{2-};**b,**$CrO4^{2-}$.

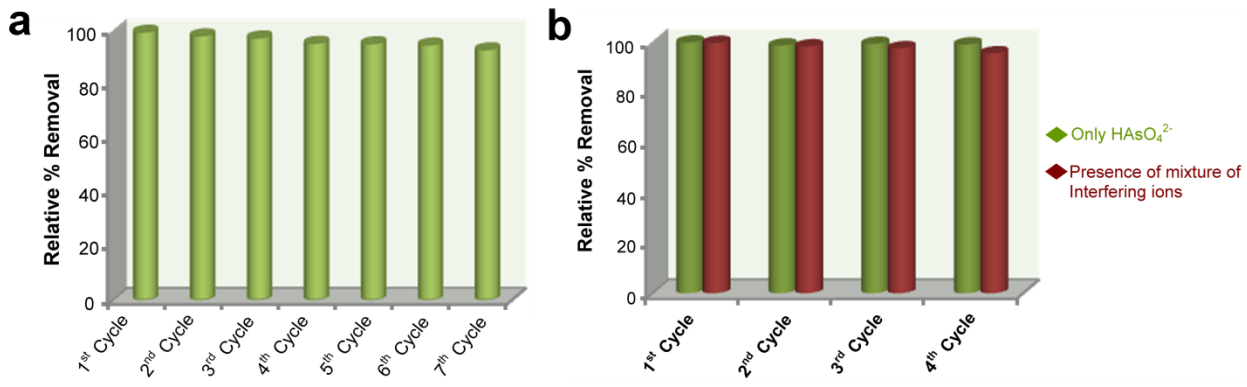

Appendix 3.30. a, Recyclability test of cage/COF(200) hybrid material for $HAsO_4^{2-}$ **b,** Recyclability test of cage/COF(200) hybrid material only for $HAsO_4^{2-}$ and presence of mixture of other interfering ions.

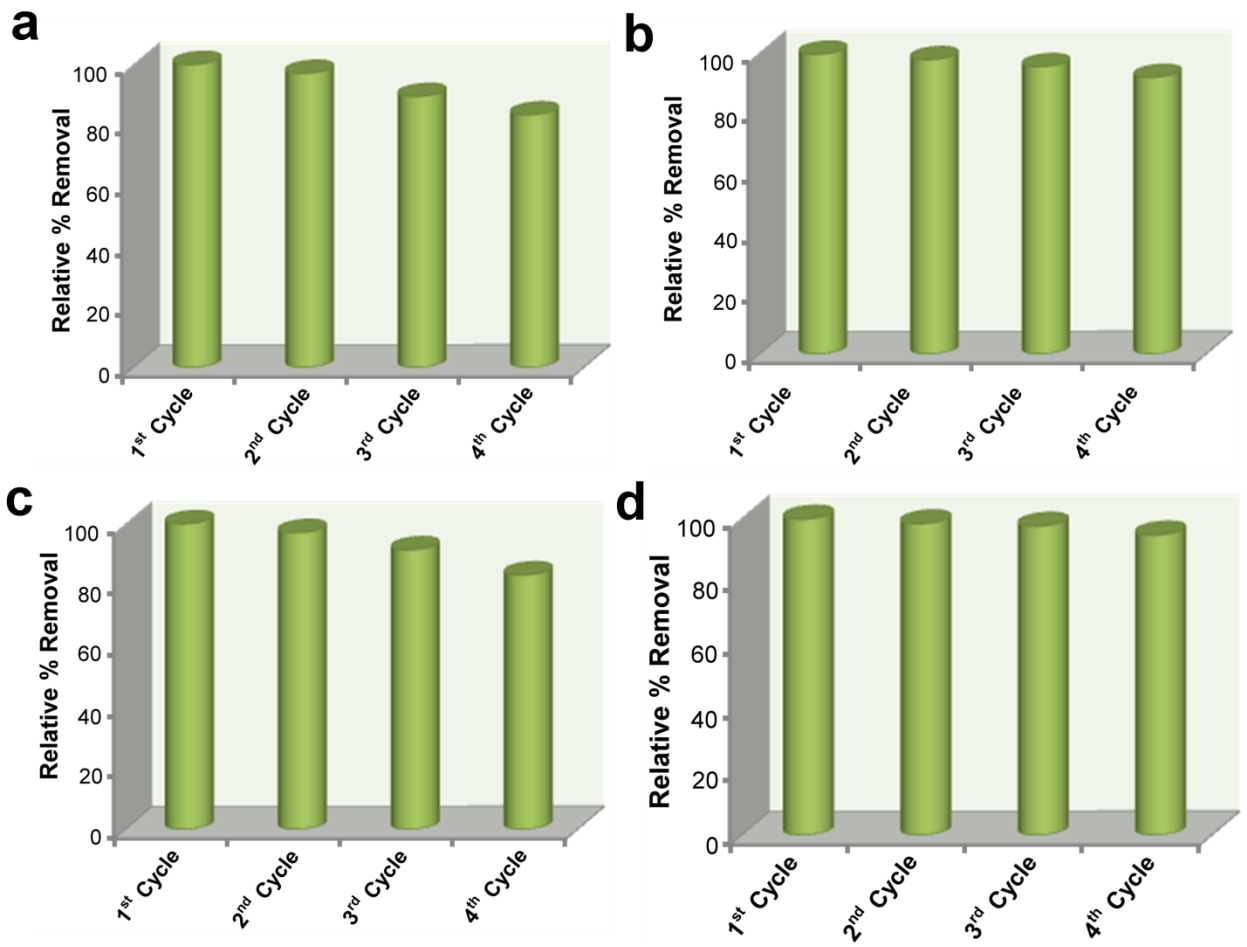

Appendix 3.31. Recyclability tests of cage/COF(200) hybrid material. **a,** SeO_4^{2-}; **b,** ReO_4^-; **c,** CrO_4^{2-}; **d,** $Cr_2O_7^{2-}$.

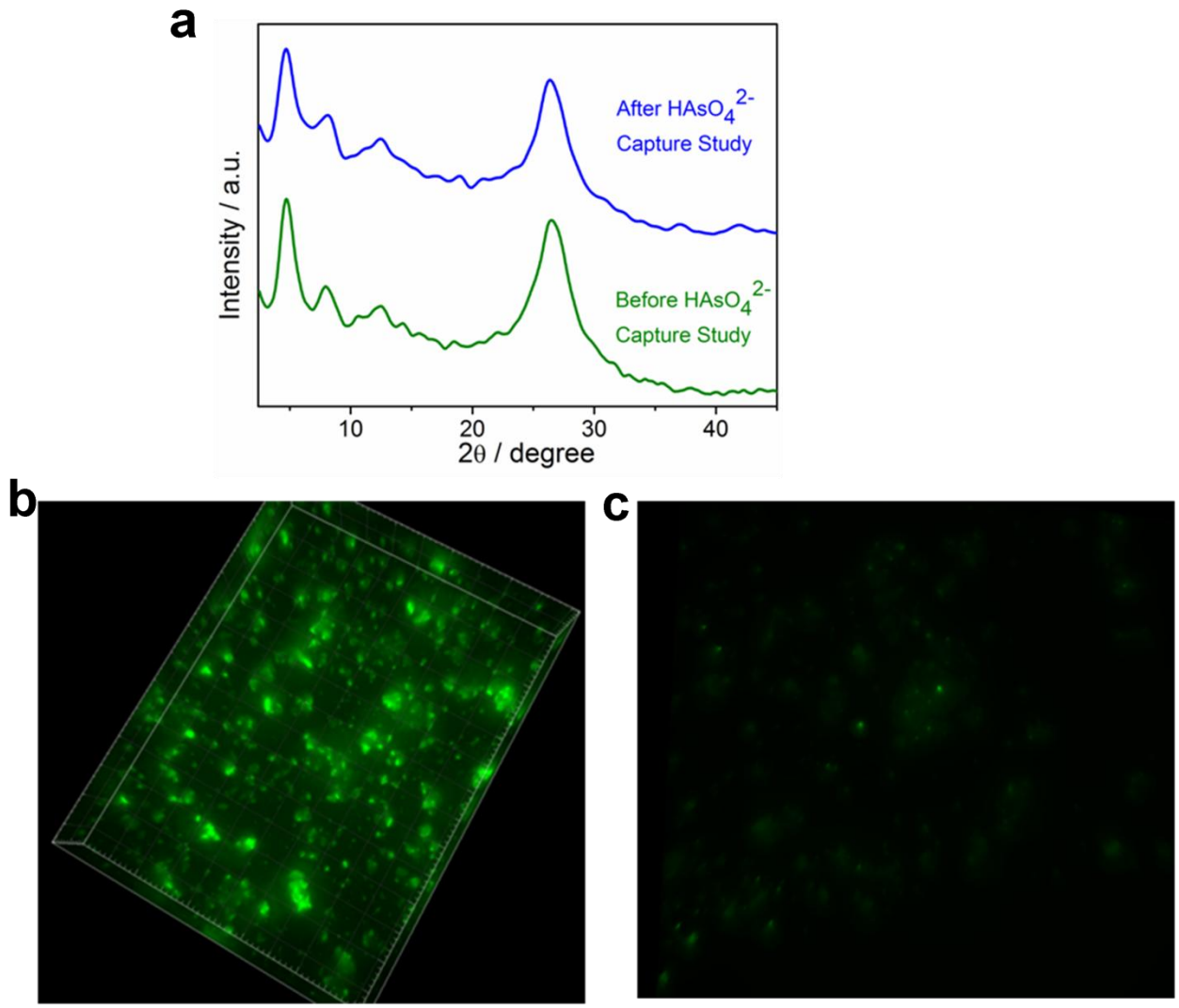

Appendix 3.32. a, PXRD patterns of cage/COF(200) hybrid material before and after capture study. **b,** and **c,** Fluorescence image of hybrid composite material before and after CrO_4^{2-} capture study.

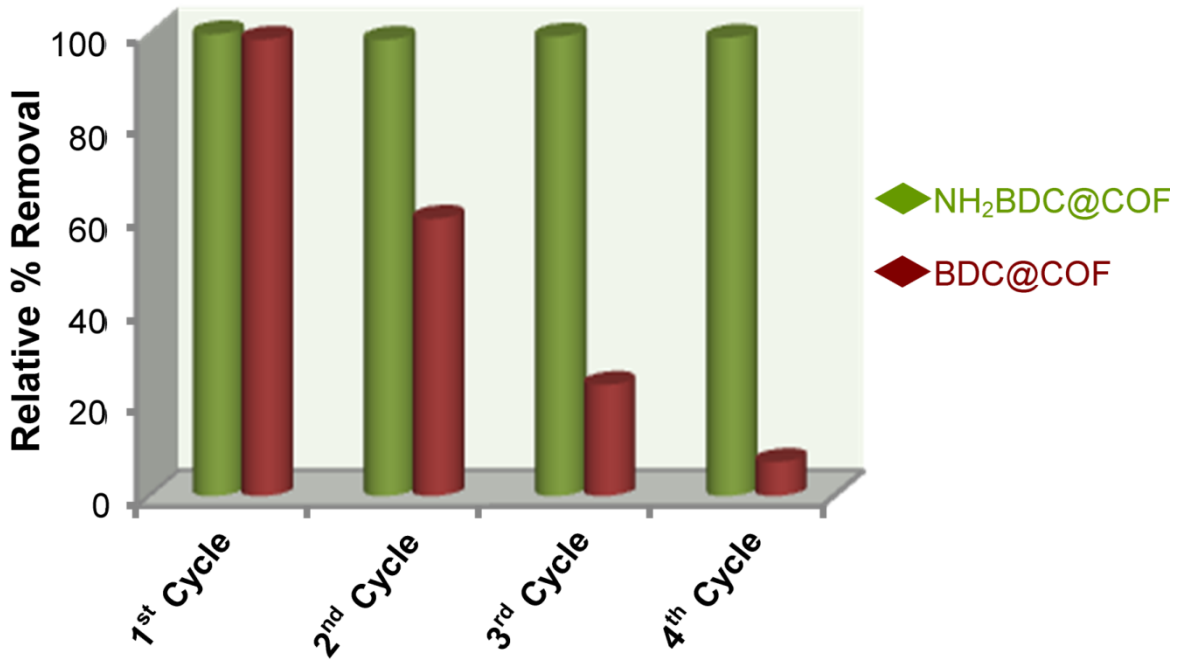

Appendix 3.33. Recyclability test of CrO_4^{2-} study by hybridized Cage/COF (NH_2BDC/COF)(200) composite and nonhybridized cage/COF (BDC/COF)(200) composite. The duration of experiment time was 2 min.

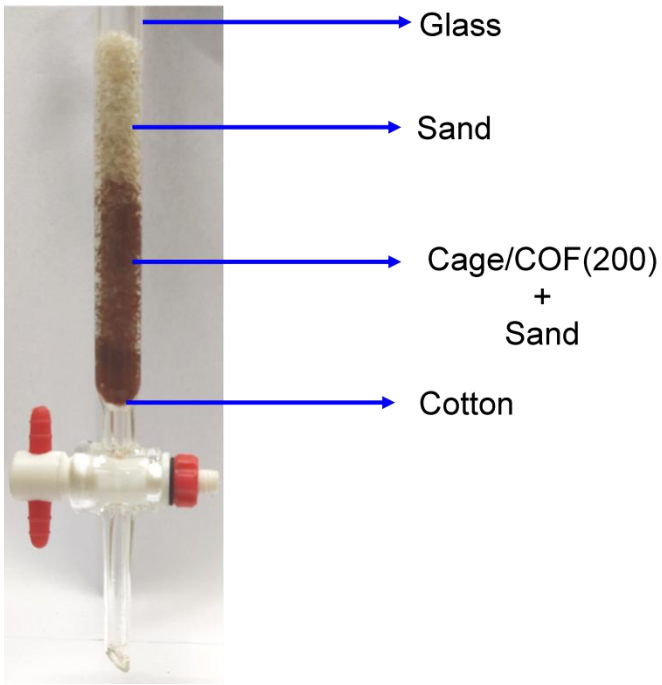

Appendix 3.34. Representation of the cage/COF(200) loaded column used for column chromatographic separation of oxoanion from water

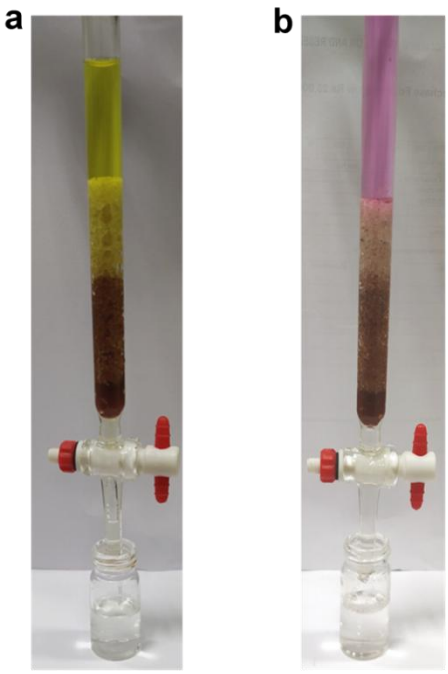

Appendix 3.35. Representation of the column exchange experiment presence of ~1000 folds mixture of other interfering salts by cage/COF(200) hybrid composite material. **a,** CrO_4^{2-}; **b,** MnO_4^-.

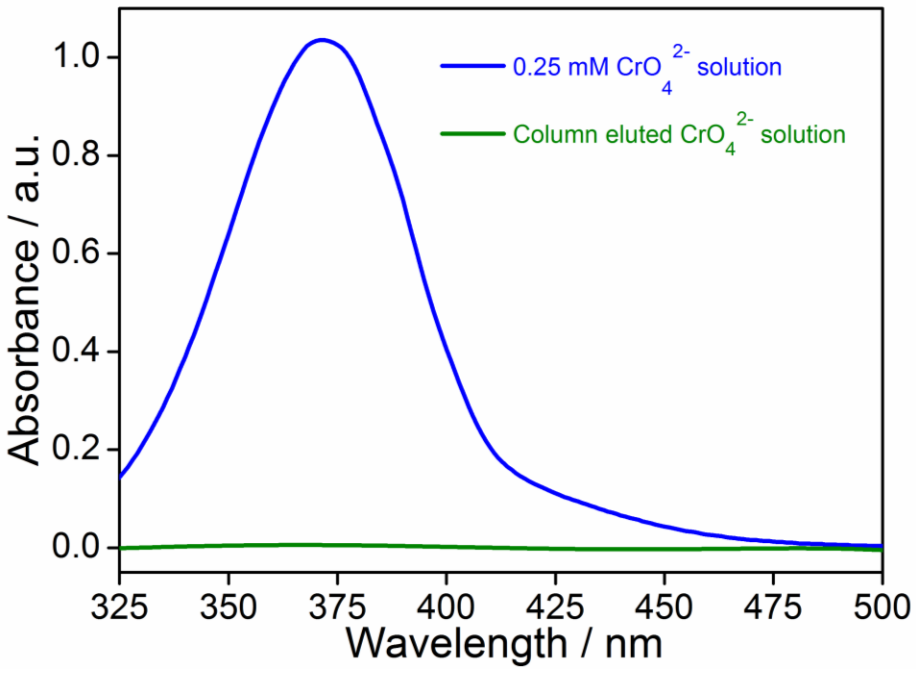

Appendix 3.36. UV-vis spectra of 0.25 mM CrO_4^{2-} solution before and after passage through the Cage/COF(200) loaded column. The final concentration of column eluted sample was reduce to well below < 50 ppb.

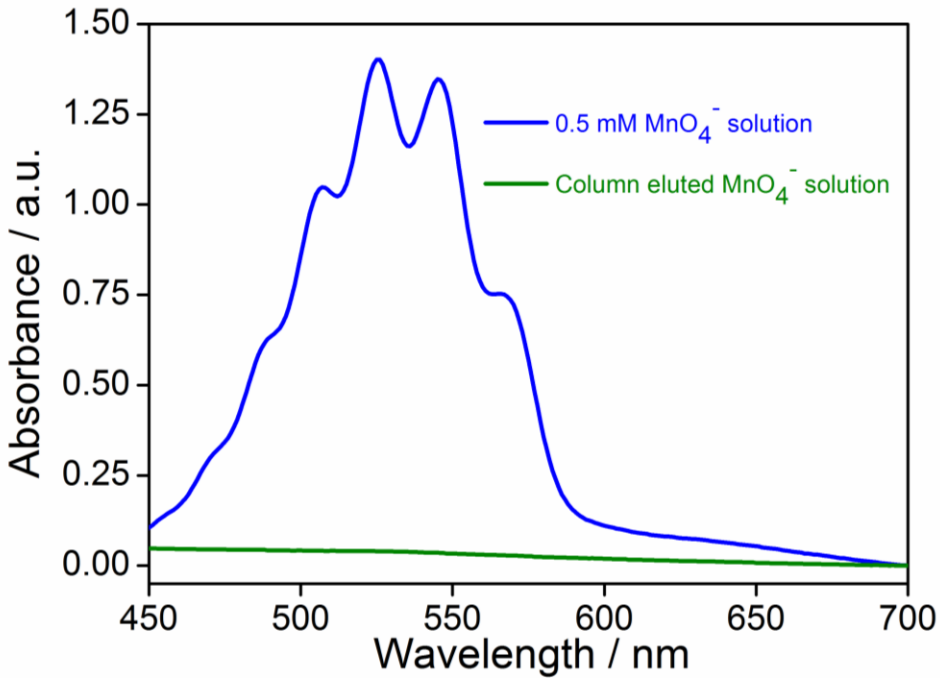

Appendix 3.37. UV-vis spectra of 0.25 mM MnO_4^- solution before and after passage through the Cage/COF(200) loaded column. The final concentration of column eluted sample was reduce to well below < 50 ppb.

3.6 References

[1] N. Middleton, The Global Casino: An Introduction to Environmental Issues, Routledge New York, 2013.
[2] F. Fu, Q. Wang, *J. Environ. Manage.* **2011**, *92*, 407-418.

[3] A .B. Pandit, J.K. Kumar, *Annu. Rev. Chem. Biomol. Eng.* **2015**, *6*, 217-246.

[4] L. H. Keith, W. A. Teillard, Environ. Sci. Technol. **1979**, *13*, 416-423.

[5] A. J. Howrath, Y. Liu, J. T. Hupp, O. K. Farha, *CrystEngComn*, **2015**, *17*, 7245-7253.

[6] P. Kumar, A. Pournara, K. Kim, V. Bansal, S. Rapti, M. J. Manos, *Prog. Mater. Sci.* **2017**, *86*, 25-74.

[7] B. Moulton, M. J. Zaworotko, *Chem. Rev.* **2001**, *101*, 1629-1658.

[8] Q.-L. Zhu, Q. Xu, *Chem. Soc. Rev.* **2014**, *43*, 5468-5512.

[9] C. R. Kim, T. Uemura, S. Kitagawa, *Chem. Soc. Rev.* **2016**, *45*, 3828-3845.

[10] S. Mollick, T. K. Mandal, A. Jana, S. Fajal, S. K. Ghosh, *Chem. Sci.* **2019**, *10*, 10524-10530.

[11] Y. Peng, M. Zhao, B. Chen, Z. Zhang, Y. Huang, F. Dai, Z. Lai, X. Cui, C. Tan, H. Zhang, *Adv. Mater.* **2018**, *30*, 1705454.

[12] F.-M. Zhang, J.-L. Sheng, Z.-D. Yang, X.-J. Sun, H.-L. Tang, M. Lu, H. Dong, F.-C. Shen, J. Liu, Y.-Q. Lan, *Angew. Chem. Int. Ed.* **2018**, *130*, 12282-12286.

[13] M. Muschi, C. Serre, *Cord. Chem. Rev.* **2019**, *387*, 262-272.

[14] C. S. Diercks, O. M. Yaghi, *Science* **2017**, *355*, eaal1585.

[15] M. S. Lohse, T. Bein, *Adv. Funct. Mater.* **2018**, *28*, 1705553.

[16] N. Ahmed, A. H. Chughtai, H. A. Younus, F. Verpoort, *Coord. Chem. Rev.* **2014**, *280*, 1-27.

[17] F. J. Rizzuto, L. K. S. Krbek, J. R. Nitschke, *Nat. Rev Chem.* **2019**, *3*, 204-222.

[18] S. Mollick, S. Fajal, S. Mukherjee, S. K. Ghosh, *Chem. Asian J.* **2019**, *14*, 3096-3108.

[19] X. Qiu, W. Zhong, C. Bai, Y. Li, *J. Am. Chem. Soc.* **2016**, *138*, 1138-1141.

[20] Y.-H. Kang, X.-D. Liu, N. Yan, Y. Jiang, X.-Q. Liu, L.-B. Sun, J.-R. Li, *J. Am. Chem. Soc.* **2016**, *138*, 6099-6102.

[21] G. Liu, Y. D. Yuan, J. Wang, Y. Cheng, S. B. Peh, Y. Wang, Y. Qian,J.Dong, D. Yuan, D. Zhao, *J. Am. Chem. Soc.* **2018**, *140*, 6231-6234.

[22] Y. Peng, W. K. Wong, Z. Hu, Y. Cheng, D. Yuan, S. A. Khan, D. Zhao, *Chem. Mater.* **2016**, *28*, 5095-5101.

[23] D. Aulakh, J. B. Pyser, X. Zhang, A. A. Yakovenko, K. R. Dunbar, M. Wriedt, *J. Am. Chem. Soc.* **2015**, *137*, 9254-9257.

[24] S. Mollick, T. N. Mandal, A. Jana, S. Fajal, A. V. Desai, S. K. Ghosh, *ACS Appl. Nano Mater.* **2019**, *2*, 1333-1340.

[25] A. V. Desai, B. Manna, A. Karmakar, A. Sahu, S. K. Ghosh, *Angew. Chem. Int. Ed.* **2016**, 55, 7811-7815.

[26] S. Rapti, A. Pournara, D. Sarma, I. T. Papadas, G. S. Armatas, A. C. Tsipis, T. Lazarides, M. G. Kanatzidis, M. J. Manos, *Chem. Sci.* **2016**, *7*, 2427-2436.

[27] T. He, Y.-Z. Zhang, X.-J. Kong, J. Yu, X.-L. Lv, Y. Wu, Z.-j. Guo, J.-R. Li, *ACS Appl. Mater. interfaces* **2018**, *10*, 16650-16659.

[28] L. Ma, S. M. Islam, H. Liu, J. Zhao, G. Sun, H. Li, S. Ma, M. G. Kanatzidis, *Chem. Mater.* **2017**, *29*, 3274-3228.

[29] A. J. Howarth, M. J. Katz, T. C. Wang, A. E. Platero-Prats, K. W. Chapman, J. T. Hupp, O. K. Farha, *J. Am. Chem. Soc.* **2015**, *137*, 7488-7494.

[30] C. O. Audu, H. G. T. Nguyen, C. Chang, M. J. Katz, L. Mao, O. K. Farha, J. T. Hupp, S. T. Nguyen, *Chem. Sci.* **2016**, *7*, 6492-6498.

[31] R. Lv, J. Wang, Y. Zhang, H. Li, L. Yang, S. Liao, W. Gu, X. Liu, *J. Mater. Chem. A* **2016**, *4*, 15494-15500.

[32] L. He, S. Liu, L. Chen, X. Dai, J. Li, M. Zhang, F. Ma, C. Zhang, Z. Yang, R. Zhou, Z. Chai, S. Wang, *Chem. Sci.* **2019**, *10*, 4293-4305.

[33] B.-J. Zhu, X-Y. Yu, Y. Jia, F.-M. Peng, B. Sun, M.-Y. Zhang, T. Luo, J.-H. Liu, X.-J. Huang, *J. Phys. Chem. C* **2012**, *116*, 8601-8607.

[34] D. Xie, Y. Ma, Y. Gu, H. Zhou, H. Zhang, G. Wang, Y. Zhang, H. Zhao, *J. Mater. Chem. A* **2017**, *5*, 23794-23804.

[35] J.-B. Huo, L. Xu, X. Chen, Y. Zhang, J.-C. E. Yang, B. Yuan, M.-L. Fu, *Microporous and Mesoporous Mater.* **2018**, *276*, 68-75.

[36] W. Yu, M. Luo, Y. Yang, H. Wu, W. Huang, K. Zeng, F. Luo, *Journal of Solid State Chemistry* **2019**, *269*, 264-270.

[37] H. Atallah , E. M. Mahmoud, A. Jelle, A. Lough, M. Hmadeh, *Dalton Trans.* **2018**, *47*, 799-806.

[38] Q.-Z. Li, C.-J. Yang, W.-K. Sui, N. Yin, *Materials Letters* **2015,** *160*, 412-414.

[39] J. Li, Y. Wu, Z. Li, B. Zhang, M. Zhu, X. Hu, Y. Zhang, F. Li, *J. Phys. Chem. C.* **2014**, *118*, 27382-27387.

[40] J. Li, N.-Y. Wu, Z. Li, M. Zhu, F. Li, *Water Sci. Technol*. **2014**, *70*, 1391-139.

[41] C. Wang, X. Liu, P. Chen, K. Li, *Sci Rep.* **2015**, *5*, 16613.

[42] K. Folens, K. Leus, N. R. Nicomel, M. Meledina, S. Turner, G. V. Tendeloo, G. D. Liang, P. V. D. Voort, *Eur. J. Inorg. Chem.* **2016**, 4395-4401.

[43] J. Qi, G. Zhang, H. Li, *Bioresource Technology* **2015**, *193*, 243-249.

Part-II

Stabilization and Functional Studies of Hybrid Halide Perovskite@APM Composite

The name perovskite is associated with the minerals calcium titanium oxide ($CaTiO_3$), which was discovered in the Ural Mountains by the German scientist Gustav rose in 19th century and named after the honour of the Russian Minister of Internal Affairs count Lev Perovski. The term perovskite now refers to any materials having the same type of structure as calcium titanium oxide ($CaTiO_3$). AMX_3 is the general formula of a pure perovskite, where A and M are the cations of different sizes (A being larger than B) and X is an anion. The monovalent A cation is located in the cavity of the four MX_6^{4-} octahedra and is surrounded by 12 nearest neighbors. Therefore, in the overall perovskite structure, they consist of anionic M-X semiconducting frameworks that are charge compensating by monovalent A cations. When the X is halogen (Cl, Br, I or combination of them), called as halide perovskite. The entire family of halide perovskite further divided into two categories based on their nature of monovalent cations. When A is organic ammonium cations termed as hybrid halide perovskite and is inorganic cations called as all-inorganic halide perovskite. The hybrid perovskite may exist in different dimensionality and it can vary from 0 to 3 dimension (D) depending on the size of organic ammonium cations. Small-sized ammonium cations perfectly fit into the PbX_6 octahedra and formed 3D framework. If the size of the ammonium cations increases, the dimensionality of overall frameworks changes to 2D, 1D to 0D.

The structural versatility and numerous compositional modifications of the halide perovskite enables the realization of exceptional range of functional properties. The lead halide perovskites hold great potentials towards photovoltaics and optoelectronic devices due to their appealing properties, which include high absorption coefficients, narrow line-width, high photoluminescence quantum yield (PLQY), tunable optical band gap, long charge carrier mobility, high defects tolerance, solution processability and cost-effectiveness. These materials as the light absorber in the solar cell have reached >23% efficiency in a very short period and became a frontline candidate for renewable energy sources. Other than photovoltaics such materials have potential applications in the field of lasing, light-emitting devices, photodetectors, field-effect transistors, X-ray imaging and many more. Despite being all potentials, the extremely poor stability perovskite restrict their outdoor applications. Without resolving this issue, it is almost impossible to transfer this material from laboratory to commercial sectors.

The entire hybrid perovskite family susceptible towards heat, moisture, polar solvents and light exposure or their combine affects which remains one of the biggest challenges for practical applications with these materials. The reasons for the very poor stability of these materials are mainly due to low formation energy (0.1-0.3eV) which results prompt formation as well as degradation upon exposure to environmental conditions. However, in recent times, plenty of efforts have been devoted to overcome the instability of HBP nanocrystals (NCs) among them, usage of purely inorganic mesoporous matrices (e.g. TiO_2 or Al_2O_3), silica, small molecules including inorganic salts, surfactants and organic polymer are

widely used. But, these processes have several limitations i.e. partially exposure of perovskite NCs, broad photoluminescence (PL) spectra, lower photoluminescence quantum yield (PLQY) and phase variation between NCs and protecting media. This demands urgent call for a type of host matrix that can efficiently stabilized the HBP NCs without compromising its original properties. In this context, APMs will be a potential alternative host matrix to stabilize HBP NCs owing to its well-ordered cavities by which it can accommodate a variety of guest molecules to nanosize region, minimizing the particle aggregation and increases the stability of NCs due to confinement effect.

This section is also consist of two chapters i.e. chapter 4 and chapter 5. In chapter 4, the HBP NCs were stabilized in MOF as an APM matrix and utilized for photocatalysis reactions in water media. While in the subsequent chapter, the blue-emitting HBP NCs was stabilized in another APM matrix i.e. porous MOG matrix and utilized for white light-emitting diode application. In both these chapters, APM matrices not only efficiently stabilized the extremely unstable HBP NCs from water as well as other chemical environments, but also manage to preserve their inherent properties which are reflected from their applications.

Part 4

Ultrastable Luminescent Hybrid Bromide Perovskite@MOF Nanocomposites for the Degradation of Organic Pollutants in Water

4.1 Introduction

Photoactive semiconducting materials are important for several photocatalytic reactions, solar cells, light-emitting devices, and many more optoelectronic devices.[1-3] Organic–inorganic hybrid bromide perovskites (HBPs), a subset of hybrid halide perovskites with general formula $APbBr_3$ (where A is monovalent organic cation), are well-known for band gap tunable photoactive materials which exhibit a high absorption coefficient and a small exciton binding energy.[4,5] However, the practical applications of entire hybrid halide perovskite family are facing critical challenges due to their weak resistance against heat, moisture, polar solvents, light exposure, and their combined effects.[6,7] Porous materials such as metal–organic frameworks (MOFs) can be well-suited as protecting matrices to stabilize the susceptible HBP-NCs (nanocrystals) from the influence of foreign species. MOFs are a unique class of porous materials that show potential applications in diverse areas like gas storage and separation, catalysis, sensing, drug delivery, biomedicine, ion-exchange, photonics, and so forth.[8-11] The scope of MOF-based composites is growing extensively in the past few years due to their well-ordered cavities that can accommodate a range of guest molecules to the nanosize region, minimizing the particle aggregation and enhancing the stability of the entrapped species. In addition, the pore surface character including window size and secondary functional sites can be regulated as per the demands of the targeted applications. To achieve chemically stable composite materials, the choice of the MOF with respect to stability is crucial, and hence we narrowed our attention of the well-studied MOF viz. ZIF-8 (zeolitic imidazolate framework).[12-17] ZIF-8, a relatively inert cage-based MOF with sodalitic topology, is an appropriate scaffold for growth of different nanoparticles (NPs) and also prevents them from escaping or agglomerating from cavities due to the limited size of pore aperture.[18,19] These properties of ZIF-8 motivated us to preserve the HBP-NCs inside the framework, preventing from any type of degradation.

Deterioration of organic pollutants is highly desirable because their contamination in aquatic ecosystem has become one of the serious concerns worldwide.[20] Although there are several MOF based, other composites were utilized as photocatalysts for toxic organic pollutants degradation[21-23] such as iron(III) based MOF/graphene oxide,[24] Ag_3PO_4/Bi_2S_3–HKUST-1,[25] BiOBr/UiO-66,[26] and so forth, but the HBP@MOF composite has never been employed as photocatalyst in aqueous media. In this work, we report a pore-encapsulated solvent-directed (PSD) technique to stabilize HBP-NCs inside ZIF-8 cavities at ambient conditions in scalable amounts. These materials showed outstanding chemical stability in a wide range of polar solvents including water (also in boiling conditions) and durability under UV light irradiation and at high temperature for a long time retaining their structural integrity as well as luminescence properties. Enthused by these results, we have demonstrated the function of

the HBP@MOF composite for the first time as a heterogeneous photocatalyst to decompose toxic organic pollutants directly in water.

4.2 Experimental

4.2.1 Materials

Lead(II) bromide ($PbBr_2$, 99.999%), hydrobromic acid (HBr, 48%), zinc nitrate hexahydrate $Zn(NO_3)_2.6H_2O$, 99.999%) were purchased fromSigma-Alrich. Methylamine (40%), ethylamine (70%), n-octylamine ($CH_3(CH_2)_7NH_2$, 99%), 2-methylimidazole (2-MIM) were purchased from Spectrochem. All solvents were purchased from Spetrochem and used without further purification. Methylammonium bromide (CH_3NH_3Br, MABr), n-octylammonium bromide ($CH_3(CH_2)_7NH_3Br$, OABr), and ethylammonium bromide ($CH_3CH_2NH_3Br$, EABr) were synthesized by previously reported literature method.

4.2.2 Synthesis

Room temperature synthesis of $MAPbBr_3$@ZIF-8. $Zn(NO_3)_2.6H_2O$ (297 mg, 1 mmol), 2-methylimidazole (656 mg, 8 mmol), $PbBr_2$ (367 mg, 1 mmol), MABr (112 mg, 1 mmol) and OABr (210 mg, 0.6 mmol) were added into methanol (9 mL) and DMF (1 mL) mixture and stirred vigorously for 1 h at room temperature (RT). After that solvents were decant from the reaction mixture and 10 mL of toluene was added into it and stirring was continued for additional 3 h. Next, the composite was collected by filtration and washed with excess amount of DMF and water. After washing, it was dried under vacuum and then the materials kept inside programmable oven at 120 °C for 1 h. $EAPbBr_3$@ZIF-8 composite was also synthesized following aforementioned method. Here, EABr was used instead of MABr, keeping all other materials and their amounts intact. $MAPbBr_3$ and $EAPbBr_3$ NPs and were prepared following the literature methods.[29,30]

Mixed cation hybrid perovskites were synthesized with slight modification of literature report,[31] where all perovskite and MOF precursors were taken in similar (1:1) molar ratios.

Large scale synthesis of $MAPbBr_3$@ZIF-8. Above mentioned procedure was adopted for large scale synthesis of composite by increasing the amount of starting compounds. The amounts of starting materials are given below: $Zn(NO_3)_2$ (17.82 g, 30 mmol), 2-methylimidazole (19.68 g, 240 mmol), $PbBr_2$

(11 g, 30 mmol), MABr (3.36 g, 30 mmol) and OABr (2.268 g, 18 mmol), methanol 150 mL and DMF 15 mL.

4.2.3 Physical measurements

Unless otherwise noted, all the reagents and solvents were commercially available and used without further purification. Powder X-ray diffraction (PXRD) patterns were measured on Bruker D8 Advanced X-Ray diffractometer at room temperature using Cu-Kα radiation (λ= 1.5406 Å) with a scan speed of 0.5° min^{-1} and a step size of 0.01° in 2 theta. Inductively coupled plasma atomic emission spectroscopy (ICP-AES) measurements were performed on a Perkin Elmer Optima 7000dv instrument. Thermo gravimetric analyses (TGA) were recorded on Perkin-Elmer STA6000, TGA analyser under N_2 atmosphere with heating rate of 10 °C/min. The morphology of the crystalline materials was recorded with Zeiss Ultra Plus field-emission scanning electron microscopy (FESEM)-Ultra Plus Field Emission Scanning Electron Microscope with integral charge compensator and embedded EsB and AsB detectors [Oxford X-max instruments 80mm^2 (Carl Zeiss NTS, Gmbh). The steady state photoluminescence studies were performed on a Fluorolog-3 spectrofluorometer (HORIBA Scientific) and PL spectra at varying temperature were recorded by increasing the temperature by a step width of 10 °C of cuvette holder enabled with a digital temperature controller. The PL decay dynamics (time correlated single photon counting (TCSPC) were measured using FLS 980 (Edinburgh Instruments) using a 405 nm pulse laser irradiation with a pulse repetition rate of 500 kHz. UV-Vis absorption studies were carried out on Shimadzu UV3600 UV/Vis/NIR spectrophotometer in an optical quartz cuvette (10 mm path length) over the entire range of 200-800 nm. Photo stability test was carried out using 365 nm UV light (Spectroline ENF-240C/FE) while for photocatalysis degradation, UV-visible light of 60 W green LED (ibrae+, locally made, λ_{max} ~ 530 nm) was used. For high-resolution TEM analysis, all the samples were dispersed in toluene (10 mg/ml) and sonicated for 30 minutes. Then, the samples were left for 2 minutes and upper part of the solution was taken for preparing TEM samples on lacey carbon-coated copper grid (Electron Microscopy Science). TEM imaging and STEM-EDS were carried out on the HRTEM (JEM-2100F, JEOL) operating at acceleration voltage of 200 kV. XPS measurements were performed on the photoelectron spectrometer (Thermo, K-alpha). Decay profiles were fitted to multiple-exponential decay curves and the calculations of average lifetimes were measured using the equation $\boldsymbol{\tau_{avg}} = \frac{\sum A_i \tau_i^2}{\sum A_i \tau_i}$ where Ai and τ_i are the amplitude and lifetime of the *i*-th component respectively.

4.2.3.1 Low Pressure gas Sorption Measurements. Low pressure gas sorption measurements were performed using BELSORP-max and BELSORP-aqua3 adsorption analyzers (BEL Japan, Inc.) respectively, both equipped with constant temperature bath. All the gases used were of 99.999% purity,

and solvents adhering to HPLC grade. Compounds were heated at 120 °C under vacuum for 10 h, and desolvation was confirmed by thermogravimetric analysis (TGA). Prior to adsorption measurement, the guest free samples were again pre-treated at 100 °C under vacuum for 6h, using BelPrepvacII, and purged with N_2 on cooling.

4.2.3.2 PL quantum yield (PLQY). The PLQY of $MAPbBr_3$ composite were measured by comparison with standard dye (fluorescein), using the following equation

$$QY = QY_R \times \frac{I}{I_R}\frac{A_R}{A} \times \frac{\eta^2}{\eta_R^2}$$

Where, I and I_R are the integrated fluorescence intensity of the composite and fluorescein respectively. A and A_R are the absorbance values at the excitation wavelength of composite and fluorescein respectively. QY and QY_R are the quantum yields of composite and reference dye respectively. η and η_R are the refractive indices of the solvents in which the composite and dye are prepared. We performed the relative PLQY according to previous literature method.[27] Briefly, prepared five different samples of each $MAPbBr_3$ composite (dispersed phase) and fluorescein dye as a reference having absorbances between 0.01 to 0.1 at the excitation wavelength 377 nm. Then fluoroscence spectra were measured from 480 nm to 580 nm with the prepared samples using same excitation wavelength. After that we calculated the integrated fluorescence intensity from the spectrum and evaluate the fluorescence quantum yield using aforementioned equation. We also executed absolute PLQY measurements using Quanta-Phi integrating sphere according literature method[28] and found that both relative and absolute PLQY are almost similar.

4.2.4 Stability Experiments

4.2.4.1 Solvent stability test. The solvent stability tests were performed in 5 ml glass vials. Each glass vials contained 5 mg of composite materials, dipped into 3 ml of respective solvents having dielectric constants from 2.38-80.1. All the vials were kept in open atmosphere for 90 days and during this period of time photoluminescence behaviour of the materials were regularly examined in dispersed phase. Both qualitative and quantitative (ICP-MS) analysis of the supernatant liquid were also regularly examined to check leaching of Pb(II) content from the materials.

4.2.4.2 Qualitative test for Pb(II). During stability test in various polar solvents including water, leaching of Pb atoms from composite materials were regularly examined by qualitative method. For this assessment, supernatant solution of composite was taken time to time and added to aqueous solution of

potassium iodide solution. There was no yellow precipitation (PbI_2)[32] were found indicating no leaching of Pb atoms form the composite materials.

4.2.4.3 Quantitative test for Pb(II). Leaching of Pb atoms was also confirmed by quantitative method. For this, we analyzed ICP-AES of supernatant solution of diversely treated polar solvents of composites after 90 days and found negligible amount of Pb content in supernatant solution.

4.2.4.4 Photo-stability test. For photo stability tests in a dark place have been performed in 5 ml glass vials. Each glass vials contained 5 mg of the solid compounds and kept under UV light (365 nm) for 20 days in ambient condition. During this period PL emission (disperse phase in toluene) and PXRD of the materials were regularly examined.

4.2.4.5 Thermal stability test. Thermal stability tests were carried out in 5 ml glass vials inside programmable ovens. Each glass vials contained 5 mg of solid composites and placed at different temperatures (100 °C and 140 °C) inside different programmable ovens for 20 days. The PL (disperse phase in toluene) and PXRD experiments were carried out time to time.

4.2.5 Photocatalytic experiments. Photocatalytic experiments were carried accordance with literature report.[20-23] Briefly, visible light of 60W LED lamp (λ_{max} ~ 530 nm) in a closed box (40 X 40 cm^2) was used for photocatalysis reaction. The distance between the lamp and reaction mixture was kept 20 cm. For photocatalytic degradation reaction each glass vial contain exact 2 mg of composite and 2.2 mL of solution (2 mL water and 200 μL of 1mM respective organic pollutants) and exposed to LED lamp. Then after certain time intervals supernatant was collected from the solution and UV-visible spectra measured to monitor degradation process. Recyclability test for photocatalytic degradation was performed by collecting the composite material after first degradation cycle through filtration and dried in open air. Then the material was again used for photocatalytic degradation of organic pollutants adopting the above mentioned procedure. The composite exhibited almost same efficacy for photocatalytic degradation even 3rd cycle.

4.2.6 $MAPbBr_3$@ZIF-8 composite coating on UV Light Emitting Diodes (LEDs). 300 mg of composite was mixed with 1.2 g of ethyl-cellulose in 4 mL of toluene and sonicated for 2 h to obtain a homogeneous gel. After that UV LEDs were immersed in resulting gel material for dip coating and dried for another 5 h before using.

4.2.7. Preparation of thin film. The prepared $MAPbBr_3$@ZIF-8 composite was carefully ground with a mortar and pestle to get fine particles. Then the material was dispersed in toluene by sonication for 30 min. After that the prepared solution was drop-casted on a clean glass slide followed by drying in open air to ensure complete evaporation of solvent. The purpose of thin films was only to use them for stability tests not for morphological studies.

4.3 Results and discussion

Herein, A series of HBP-NCs having methylammonium (MA^+) cations, ethylammonium (EA^+) cations, or both MA^+ and EA^+ were incorporated inside the ZIF-8 in a large scale at room temperature following the PSD method (Appendix Table 4.1). In this typical synthetic procedure, all building blocks of ZIF-8 and perovskite zinc(II) nitrate, 2-MIM, MA/EABr, $PbBr_2$, and OABr were dissolved in a mixture of polar solvents MeOH and DMF (9:1). After a few minutes of stirring, white precipitates started to form, indicating formation of ZIF-8 particles; consequently, the perovskite precursors were entrapped by the pores of ZIF-8. Then, an excess amount of less polar solvent toluene was added for nucleation of perovskite NCs (Scheme 4.1).

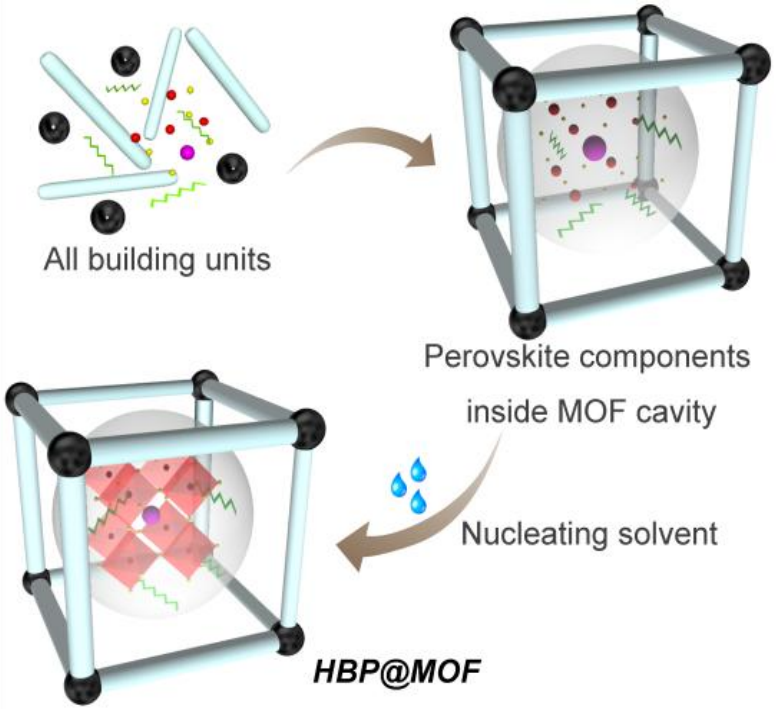

Scheme 4.1. Pore-encapsulated solvent directed (PSD) procedure for preparing HBP@MOF composites.

The composites were collected by filtration and washed several times with copious amounts of DMF and water for removal of perovskite NPs from the surface of MOF. Then, the composites were dried at 120 °C for 1 h to obtain a better quality of materials (Appendix 4.1). Adopting this protocol, we prepared a mass amount (>10 g) of perovskite composite materials at ambient condition (Appendix 4.2). Formation of perovskite NPs was confirmed by PL and UV-vis spectra. The PL spectra of $MAPbBr_3$ composite exhibit an emission peak at 527 nm compared to bare NCs (532 nm), manifesting a relatively smaller size of perovskite NCs in the composite material which is narrower than that of naked $MAPbBr_3$ NPs (28 nm, Figure 1a and Appendix 4.3 and 4.4). This indicates that perovskite NCs are formed inside the ZIF-8 matrix.[33] The green emissive $MAPbBr_3$@ZIF-8 used as a coating material emits intense green light by applying a voltage of 3.0 V and passing a current of 60 μA, shown in inset of Figure 4.1a. A relatively smaller Stokes shift (~40 meV) demonstrated the nanomaterial has fewer surface defects, and PL emission resulted from direct exciton recombination.[34] It is noteworthy that the relative PLQY of $MAPbBr_3$@ZIF-8 is as high as >80%, which is comparable to other reported $MAPbBr_3$ NCs encapsulated inside porous matrices,[35-38] and to the best of our knowledge this is the highest PLQY for MOF based perovskite composites.[14] The TRPL decays of the composite were fitted to triexponential decay functions and (Appendix 4.5 and Appendix Table 4.2) exhibited that three processes were involved in the decay channel, namely, a short-lifetime process (7 ns), an intermediate lifetime process (31 ns), and a long-lived component (146 ns). The average lifetime of the $MAPbBr_3$ composite (τ_{avg} = 102 ns) was higher than that of the bare $MAPbBr_3$ NCs (τ_{avg} = 41 ns) which could be due to a decrease in the nonradiative recombination pathway of $MAPbBr_3$ nanocrystals inside the ZIF-8 matrix. The formation of perovskite NCs inside the cavity or surface of MOF was assured by a follow-up experiment (Appendix 4.6) which confirmed encapsulation of perovskite NPs inside the MOF cavity and a better quality of perovskite composite produced only by our PSD approach. Maximum emission intensities were obtained using 1:1 MOF and perovskite precursors ratio (Appendix 4.7). Another advantage of our strategy is reproducibility, which was confirmed from luminescent behaviors (identical peak position, PL peak intensity, and fwhm for different batches) of this material (Appendix 4.8). The coexistence of both ZIF-8 and perovskite NCs' diffraction peaks was observed (Appendix 4.9) in powder X-ray diffraction (PXRD). Broadening of PXRD patterns also occurred in the $MAPbBr_3$ composite than that of only $MAPbBr_3$ NCs, signifying the formation of a nanosized particle inside the MOF cavity.[39] The FESEM image showed the $MAPbBr_3$@ZIF-8 composite material is microsized in nature (Appendix 4.10). SEM-EDX (energy-dispersive X-ray) analysis revealed that the Br/Pb molar ratio in the composite was 3.67 (Appendix Table 4.3) suggesting the existence of excess Br-rich surface of $CH_3NH_3PbBr_3$ NCs.[39] The nitrogen sorption

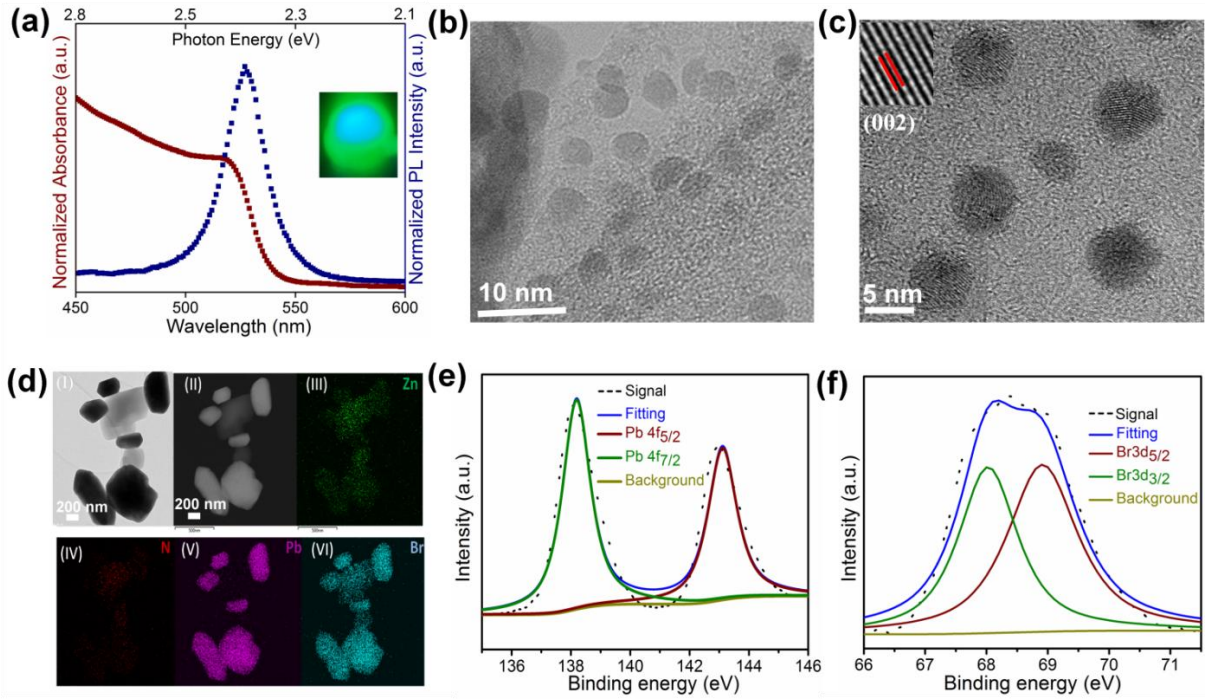

Figure 4.1. Characterization of $MAPbBr_3$@ZIF-8 material. (a) Absorption (wine) and PL (blue) spectra of composite. The inset photograph of green LED obtained after coating on a UV-LED with green emissive $MAPbBr_3$ composite. (b) TEM image of composite material. (c) HR-TEM image of composite material. The inset figure shows the lattice fringe of individual $MAPbBr_3$ nanocrystal. (d) (I) HR-TEM image of composite. Most of the area has brighter contrast as compared to other marked by green line. This indicates most of the nanoparticles were encapsulated by ZIF-8. (II) HAADF-STEM image. STEM-EDS elemental maps of Zn, N, Pb, Br (III-VI) respectively. (e) XPS spectra of Pb 4f. (f) XPS spectra of Br 3d.

measurement showed quite less amount of gas uptake for $MAPbBr_3$ composite (276 m^2/g) compared to pristine ZIF-8 (780 m^2/g), confirming the existence of perovskite NCs inside MOF cavities (Appendix 4.11).[38] The shape and size of the materials were confirmed from electron microscopy analyses. Bare ZIF-8 exhibited mono dispersed cubic morphology with edge length 230 nm (Appendix 4.12), whereas $MAPbBr_3$ NPs in the composite were spherical in shape with diameter 6-8 nm (Figure 4.1b). The interplanar distance for $MAPbBr_3$ NPs in the nanocomposite from lattice fringes is about 2.98 Å, corresponding to the characteristic (002) planes (Figure 4.1c) of cubic phase which matches well with the reported lattice parameter of about 5.93 Å.[39] In this nanocomposite, larger size HBP NCs are occupied inside the smaller cavity of ZIF-8 because of structural defects of the framework. The defect structure

might be formed due to missing linkers in the framework, which is a well-known observed phenomenon for MOF based composites.[40-43] From TEM analysis it is clear that both perovskite NPs ($MAPbBr_3$ and $EAPbBr_3$) were encapsulated by MOF and well dispersed inside it (Appendix 4.13 and 4.14). Though unencapsulated NPs were not observed in the TEM image, a few bare MOFs were observed in Figure 4.1d. Black spots were observed for $MAPbBr_3$ composite whereas bare ZIF-8 was transparent. Elemental mappings of two types of area in $MAPbBr_3$ composite revealed that transparent area contained only Zn and N, indicating the presence of only MOF, whereas the black spot contained Zn, N, Pb, and Br, supporting the encapsulation of $MAPbBr_3$ NCs inside the ZIF-8. Such a composite was particularly obvious in the high-angle annular electron microscopy (HAADF-STEM) images (Figure 4.1d), in which the encapsulated $MAPbBr_3$ composite appeared as brighter contrast due to the larger atomic mass of Pb as compared to Zn.

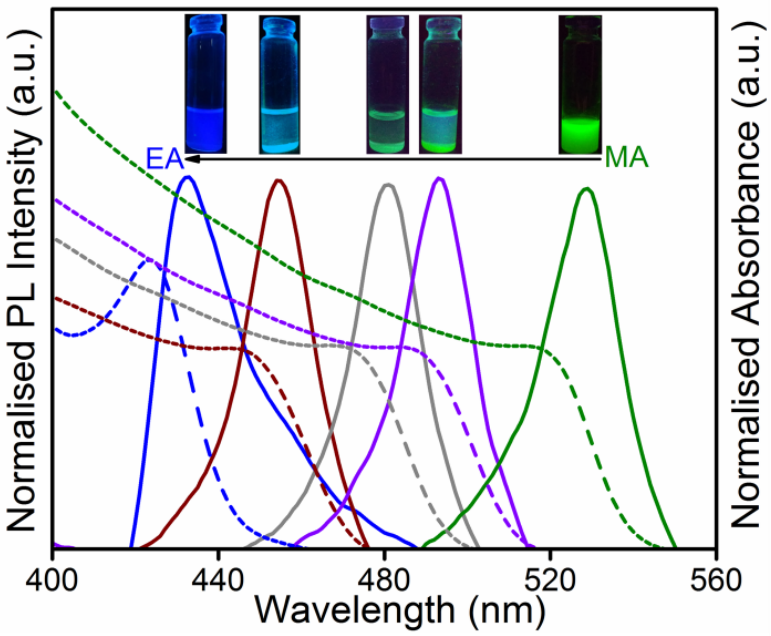

Figure 4.2. Series of HBP@MOF composites. Absorption (dotted line) and PL spectra (solid lines) of different ratio of hybrid bromide perovskite composites along with photograph (under UV light) in inset figure. The emission and absorption peak of the mixed cation hybrid perovskite composite were readily tuned from $MAPbBr_3$ to $EAPbBr_3$ composite. When the ratios of MA and EA cations were 3:1, 1:1 and 1:3 the respective PL emission peaks of composites were at 493 nm, 481 nm and 455 nm while absorption peaks appeared at 486 nm, 472 nm and 446 nm respectively indicating colour tuning from green to blue.

The surface properties of HBP NPs were investigated through X-ray photoelectron spectroscopy (XPS) analysis (Figure 4.1e,f). In the $MAPbBr_3$@ZIF-8 composite two sharp Pb 4f peaks without any shoulder at 138 and 143 eV corresponding to the Pb $4f_{7/2}$ and Pb $4f_{5/2}$ (Figure 4.1e) strongly support the formation of a nanosized structure in the MOF matrix.[44] The Br 3d spectrum (Figure 4.1f) was resolved into two peaks at 67.9 eV (Br $3d_{5/2}$) and 68.7 eV (Br $3d_{3/2}$), corresponding to the inner and surface ions, respectively.[44,45] Upon introduction of a larger size cation like EA^+ into the core geometry of the methylammonium perovskite framework, the main absorption band of $MAPbBr_3$ NCs in the composite has been blue-shifted from 518 to 423 nm and emission maxima blue-shifted from 529 to 433 nm, resulting in the color tuning from green to blue in the visible spectrum (Figure 4.2, and Appendix Table 4.4).[45]

4.3.1 Chemical stability test

The chemical stability tests of HBP@MOF composites were executed maintaining the same conditions where the perovskite NCs were prone to degrade, i.e., long-time storage in open air, dipping in different solvents including water, continuous heating at elevated temperature, and UV-light irradiation.[46,47] Figure 4.3a shows almost the same luminescent intensity (~85%) over a period of several months in open air for the $MAPbBr_3$@ZIF-8 composite, demonstrating its long-term environmental stability also in film form. For solvent stability test, a wide range of solvents was chosen having dielectric constants from 2.38 to 80.1. The nanocomposite was individually immersed into the diverse solvents for a period of 90 days, and its PL spectra as well as qualitative and quantitative experiments were regularly conducted (see the Experimental Section for more details). Figure 4.3b shows PL intensity (~80%) sustained over a long period (Appendix 4.15-4.20), indicating solvent resistance capacity of the $MAPbBr_3$ composite. The effect of temperature on $MAPbBr_3$ composite was performed by heating the material at elevated temperature for 20 days; however, the PL intensity before and after heat treatment (Figure 4.3c) remained almost similar (~70%), while naked perovskite NPs degraded severely and the PL intensity decreased more than 95% within 5 h (Appendix 4.21). This result connoted the super stability of composite material even at high temperature. Figure 4.3c confirms that even after continuous UV light irradiation for 20 days PL intensity (~90%) (Appendix 4.22), indicating outstanding photostability of this material. Figure 4.3d shows a comparison list, where PLQY of the material was measured before and after immersion in different polar solvents for 90 days. We have found a retention of PLQY of ~90% for all solvents, indicating remarkable stability of the material for such a long time due to confinement of perovskite NCs inside the MOF cavity. Temperature-dependent PL spectra (Appendix 4.23) imply temperature-

independent chromaticity of the material.[48] The $EAPbBr_3$@ZIF-8 composite also showed excellent stability in water as well as various polar solvents up to 90 days (Appendix 4.24). Such outstanding chemical, heat, and photostability of HBP@MOF composite were attributed to the hydrophobic MOF wall protecting the perovskite NPs from various chemical environments.

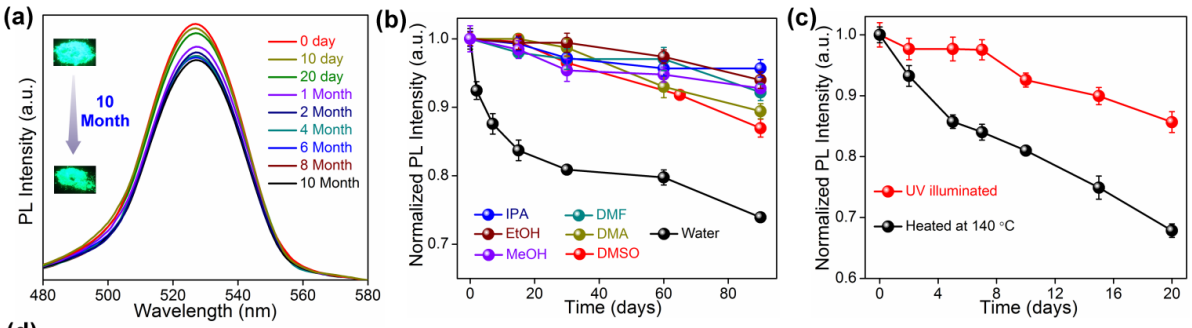

(d)

Polar Solvent	Water	DMSO	DMA	CH_3CN	DMF	CH_3OH	NMP	GBL	C_2H_5OH	Acetone	IPA	n-Butanol
Dielectric Constant (DC)	80	47	38	38	37	33	32	28	25	21	18	18
PLQY (%) before immersion	71	78	76	72	74	81	78	79	83	85	85	86
PLQY (%) after immersion	67	75	72	69	70	77	73	76	81	83	84	84
Retention of PLQY (%)	94	96	95	96	95	95	94	96	98	98	99	98

Figure 4.3. Stability studies of $MAPbBr_3$@ZIF-8 composite. (a) PL spectra of composite stored under ambient condition for several months. The inset shows color of the solid material under UV light (365 nm) before and after 300 days. (b) Normalized PL intensity as a function of time in different polar solvents over a period of 90 days. (c) Normalized PL intensity as a function of time under continuous heat treatment (140^{o}C) and prolonged UV light illumination (365 nm). (d) Table for PLQY in different solvents showing change in PLQY before and after immersion in various polar solvents over a period of 90 days.

4.3.2 Heterogeneous photocatalysis

These HBP@ZIF-8 composites have the narrow band gap (2.26-3.1 eV), which renders excellent light absorption character in the visible region. Moreover, the additional feature of extreme water resistance bestows an advantage for usage as heterogeneous photocatalyst in water to degrade toxic organic pollutants. $MAPbBr_3$@ZIF-8 was used as a prototype photocatalyst, and two dyes (methyl orange, MO, and methyl red, MR) and one antibiotic (nitrofurazone, NFZ) were selected as model pollutants

(Appendix 4.25-4.27) to demonstrate photocatalytic degradation. Although the degradation rate is not so high enough compared to other standard materials,[20] utilization of photoactive MOFs can further enhanced the rate of the reactions.[49-51] The photocatalytic degradation of MO by $MAPbBr_3$ composite was investigated under both visible (Figure 4.4a) and sunlight, and the results showed comparable

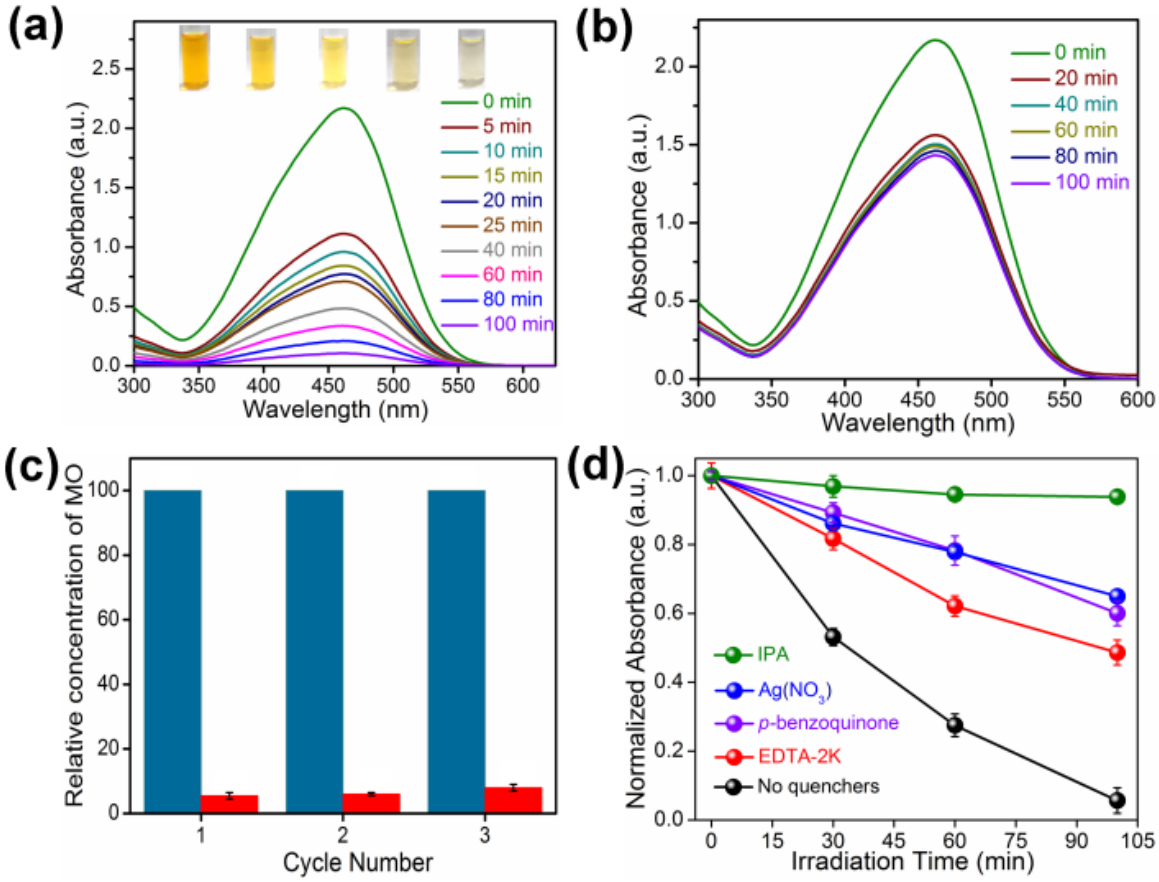

Figure 4.4. Photocatalytic activity of $MAPbBr_3$@ZIF-8 composite. (a) Absorption spectra changes of MO solution degraded by $MAPbBr_3$ composite under visible light irradiation for different time of intervals. The inset photograph shows degradation MO by composite for 0 min, 10 min, 25 min, 60 min and 100 min (from left to right). (b) Degradation of MO by ZIF-8 under visible light. (c) Recyclability test for $MAPbBr_3$ composite after photocatalytic degradation. The blue colour denotes the concentration of MO molecules before photocatalysis reaction and red colour denotes the concentration of MO molecules after photocatalysis reaction. (d) Effects of different quenchers for degradation of MO by the composite under visible light. The graph shows the degradation of MO is much prevented for IPA solution (green line) a widely used hydroxyl radical scavenger, confirming that hydroxyl radicals that are produced during the process are mainly responsible for photocatalytic dissociation of MO.

degradation behavior in both conditions (Appendix 4.28). MOF alone could not degrade MO molecules, and after a certain time the absorbance intensity remained the same (Figure 4.4b), indicating adsorption of pollutants on the MOF surface. A slight decomposition (<10%) occurred for MO in dark conditions (Appendix 4.29) in the presence of composite, and also a minute amount (<10%) of deterioration was observed for only MO under visible and sunlight (Appendix 4.30). For reusability test, the composite was used to degrade MO molecule for three consecutive cycles under visible light and found >90% (Figure 4.4c) degradation even after the last cycle (Appendix 4.31). No significant changes in PXRD peaks were observed even after the third cycle, implying the composite material maintaining its framework integrity (Appendix 4.32). We performed an indirect chemical probe experiment to know which active species were playing the key role to degrade MO molecules.[52] For this experiment we performed the photocatalytic degradation reaction individually using $Ag(NO_3)$ (radical scavenger), EDTA-2K (h^+ scavenger), isopropyl alcohol (·OH scavenger), and *p*-benzoquinone ($\cdot O_2^-$ scavenger). In the presence of isopropyl alcohol the photocatalytic degradation was predominantly inhibited (Figure 4.4d) This preliminary experiment states that degradation mechanism occurred through *in situ* hydroxyl radical generation (see Experimental Section for more details, Appendix 4.33).

4.4 Conclusions

In conclusion, we have synthesized a series of HBP@MOF composites that were realized by the controlled and uniform growth of perovskite NCs inside a well-oriented MOF cavity via the pore-encapsulated solvent-directed (PSD) strategy. It is anticipated that this approach can be extended for stabilization of unstable nanomaterials in various porous matrices. Here, MOF walls functioned as protecting layer for the HBP-NCs and prevented them from any type of degradation, giving rise to the extreme robustness of the materials. These composite materials have been employed as potential heterogeneous photocatalysts to degrade lethal organic pollutants directly in aqueous media. Although the toxic nature of lead used in these materials is of great concern, replacement of lead with other nontoxic elements[53-54] can provide a greener approach without compromising the ability to degrade fatal organic pollutants. We believe that the present findings will open up a new avenue in stable perovskite materials toward various water based energy storage and conversion reactions.

4.5 Appendix section

Appendix Table 4.1. Molar ratios of precursor materials for the preparation of methyl/ethyl/mixed methyl-ethyl perovskite NCs inside ZIF-8. Here M and E stand for MABr and EABr respectively.

Composition (M:E)	$Zn(NO_3)_2.6H_2O$ mmol	2-MIM mmol	$PbBr_2$ mmol	MABr mmol	EABr mmol	OABr mmol
1:0	1	8	1	1	-	0.6
3:1	1	8	1	0.7	0.3	0.6
1:1	1	8	1	0.5	0.5	0.6
1:3	1	8	1	0.3	0.7	0.6
0:1	1	8	1	-	1	0.6

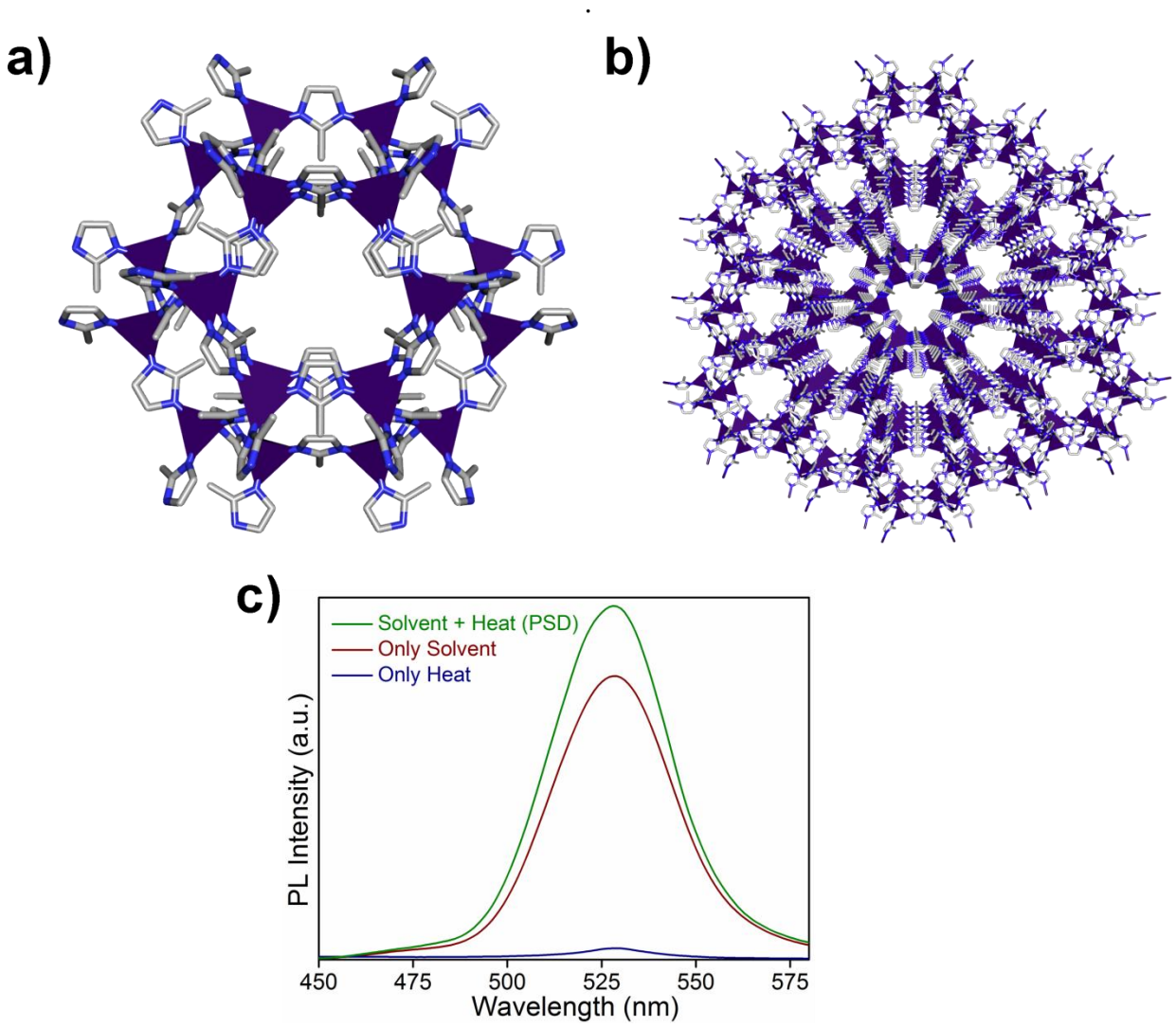

Appendix 4.1. (a) and (b) chemical structures of ZIF-8 (hydrogens are deleted for clarity) (Color code; Carbon: gray, Nitrogen: blue, Zinc: dark blue). (c) PL spectra of $MAPbBr_3$@ZIF-8 composites obtained by different procedures. The maximum emission intensity of composite was obtained by our pore encapsulated solvent directed (PSD) approach (combination of both solvent and heat) than other procedures.

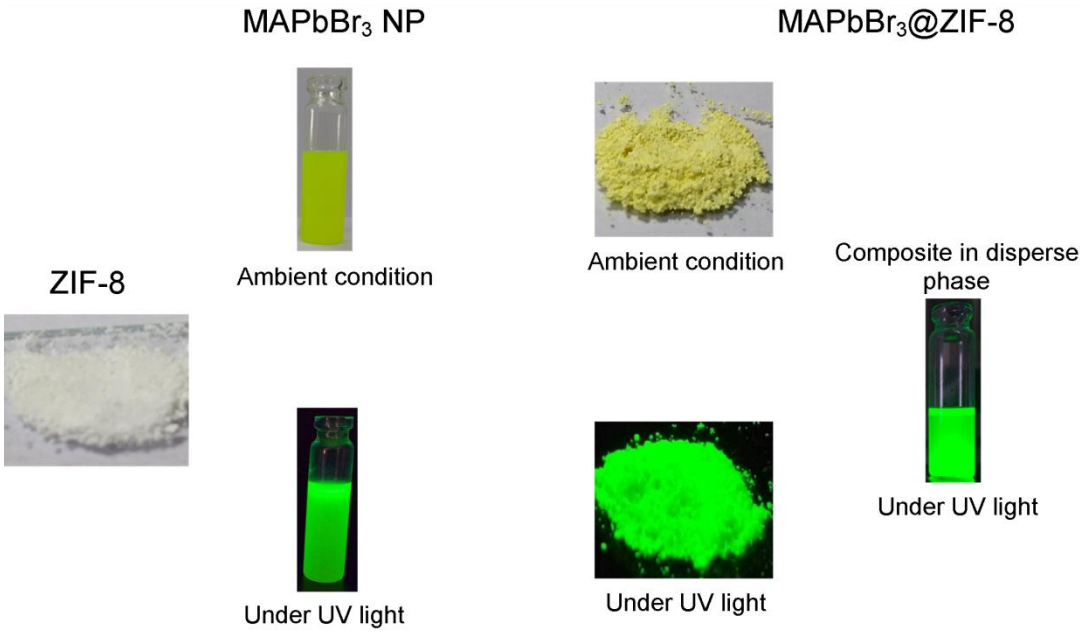

Appendix 4.2. Photographs of ZIF-8, $MAPbBr_3$ NPs and composite at ambient condition and under UV light (365 nm). ZIF-8 is colorless both in ambient condition and UV light. Dispersed $MAPbBr_3$ NPs in toluene is yellow in ambient condition while green color under UV light. In ambient condition $MAPbBr_3$@ZIF-8 composite is yellowish while under greenish under UV light both in solid and disperse phase.

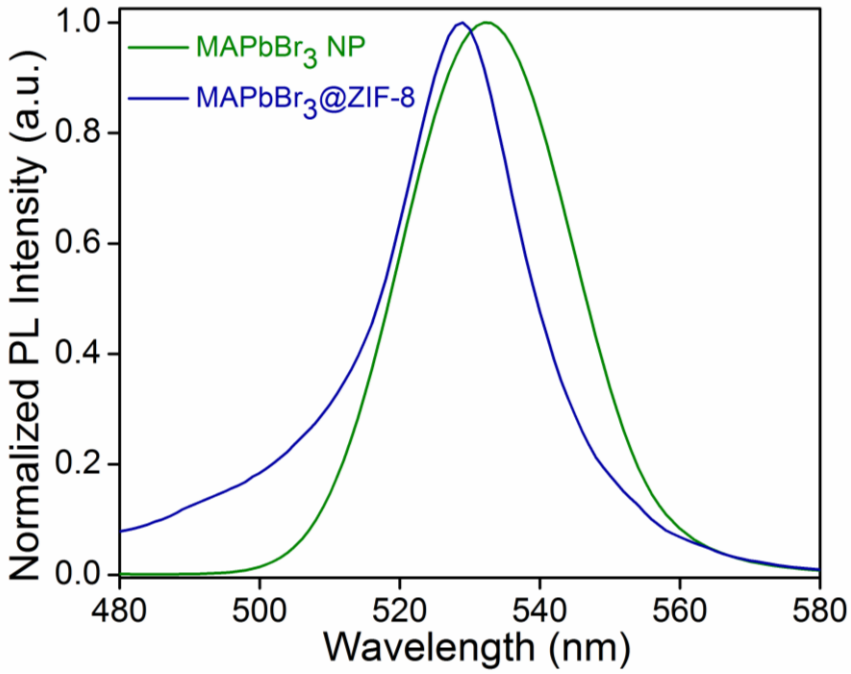

Figure 4.3. PL spectra of $MAPbBr_3$@ZIF-8 (FWHM; 24 nm) and $MAPbBr_3$ NPs (FWHM; 28 nm). Emission spectra of composite blue-shifted by 5 nm compared to bare $MAPbBr_3$ NPs due to smaller size.

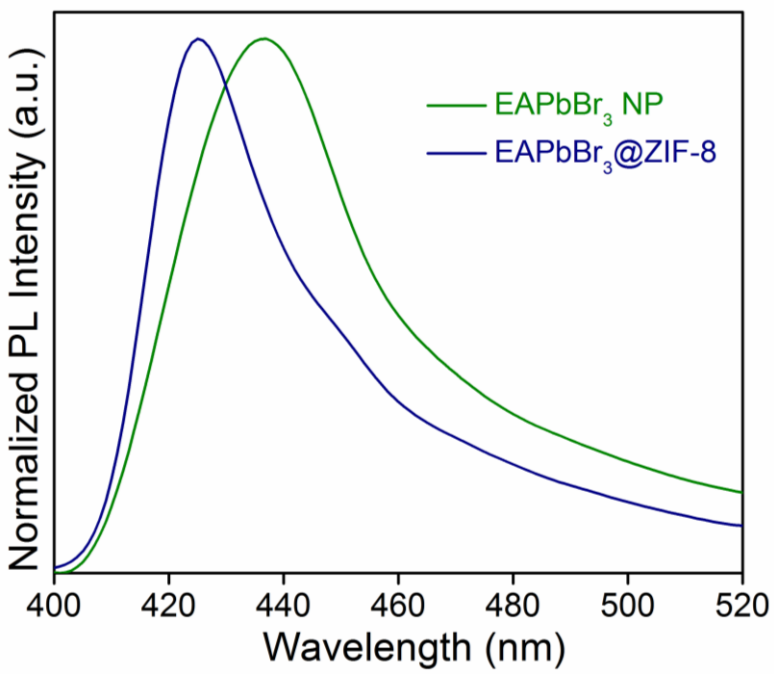

Figure 4.4. PL spectra of $EAPbBr_3$ NPs and $EAPbBr_3$@ZIF-8 composite. Emission peak of composite blue shifted by 12 nm compared to $EAPbBr_3$ NPs showing confinement of $EAPbBr_3$ NPs inside MOF cavity.

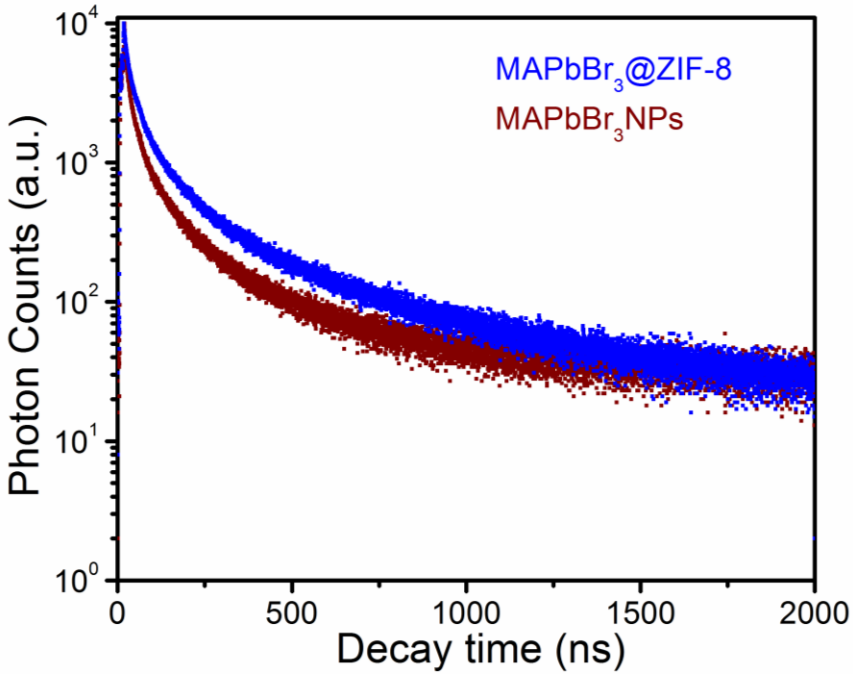

Appendix 4.5. Time resolved PL spectra of $MAPbBr_3$ NPs and composite. The average lifetime of composite larger than naked perovskite indicating confinement of PNC inside MOF cavity.

Appendix Table 4.2. PL Decay parameters of $MAPbBr_3$ NPs and of $MAPbBr_3$@ZIF-8 composite.

Compounds	τ_1(ns)	A_1	τ_2(ns)	A_2	τ_3(ns)	A_3	χ^2	τ_{avg}(ns)
$MAPbBr_3$@ZIF-8	6.62	0.35	30.26	0.44	146.08	0.18	1.09	101.6
$MAPbBr_3$ NP	3.84	0.39	13.27	0.35	54.81	0.24	1.07	40.8

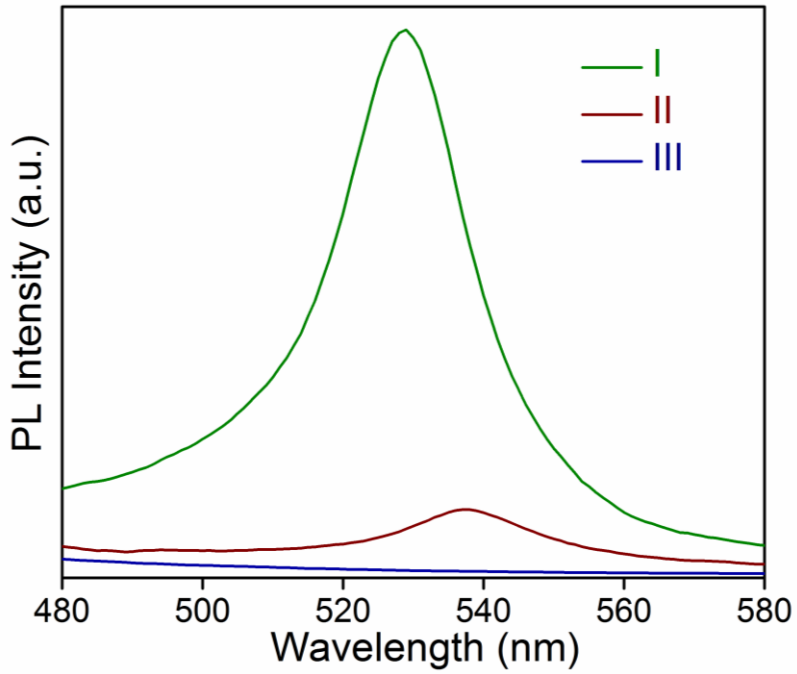

Appendix 4.6. (I) PL spectra of $MAPbBr_3$@ZIF-8 composite prepared by our methodology (PSD approach). (II) PL spectra of composite prepared via well known infiltration method. (III) PL spectra of composite after washing (prepared via infiltration method) indicating degradation of the material.

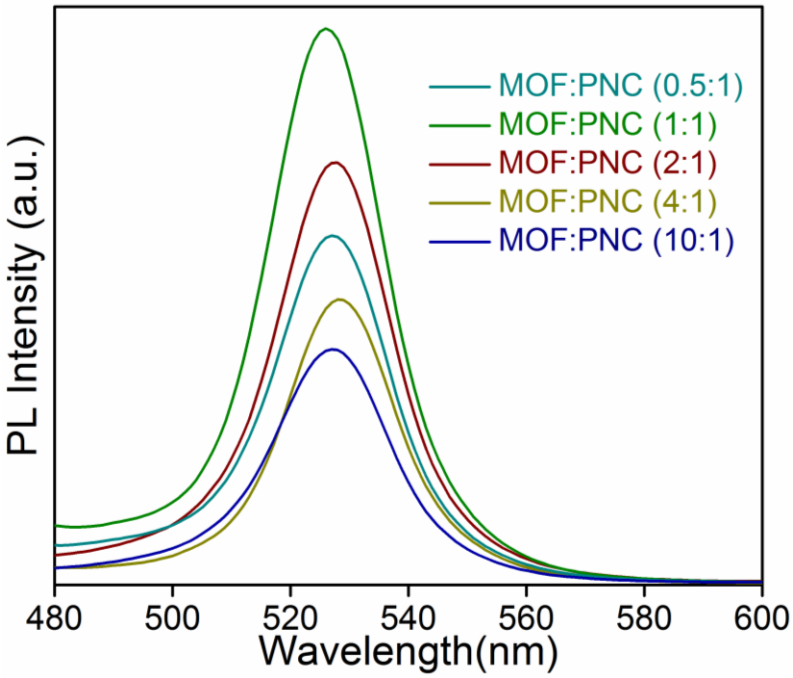

Appendix 4.7. PL spectra $MAPbBr_3$@ZIF-8 composite in presence of different ratio of MOF where PNC represents perovskite nanocrystals. PL spectra showing 1:1 molar ratio MOF and PNC gives better quality of composite material.

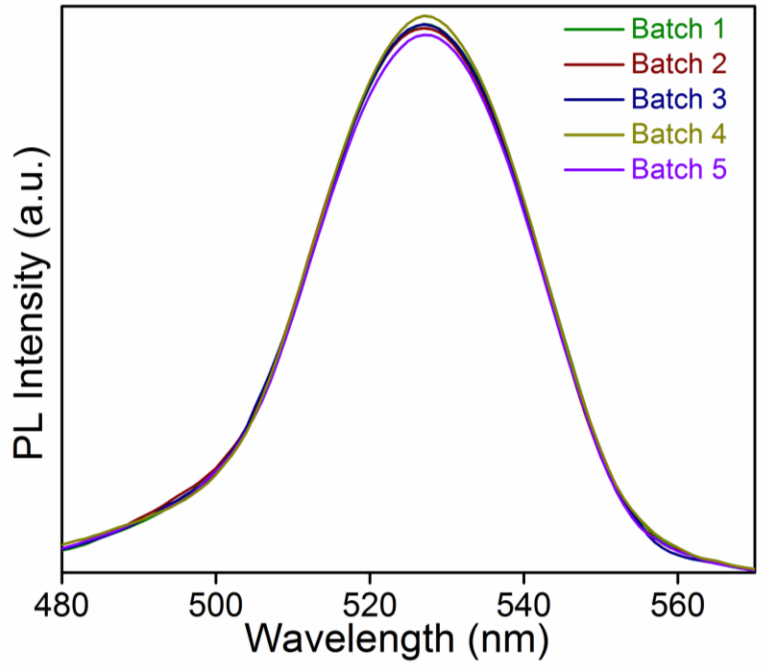

Appendix 4.8. Emission spectra for different batches of $MAPbBr_3$@ZIF-8 composite material. PL peak position, PL intensity and FWHM are same for all batches confirming its reproducibility.

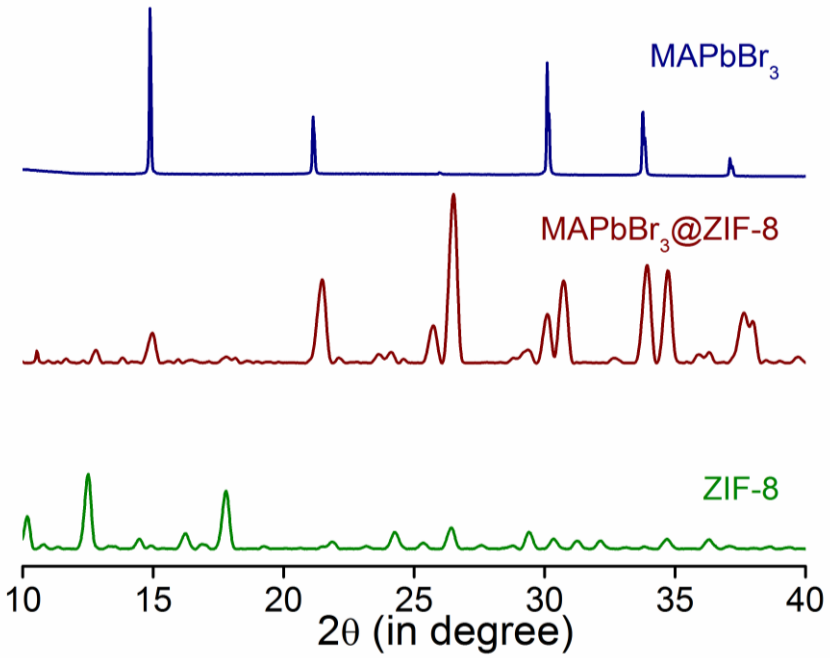

Appendix 4.9. Comparison of PXRD patterns of ZIF-8, $MAPbBr_3$@ZIF-8, $MAPbBr_3$.

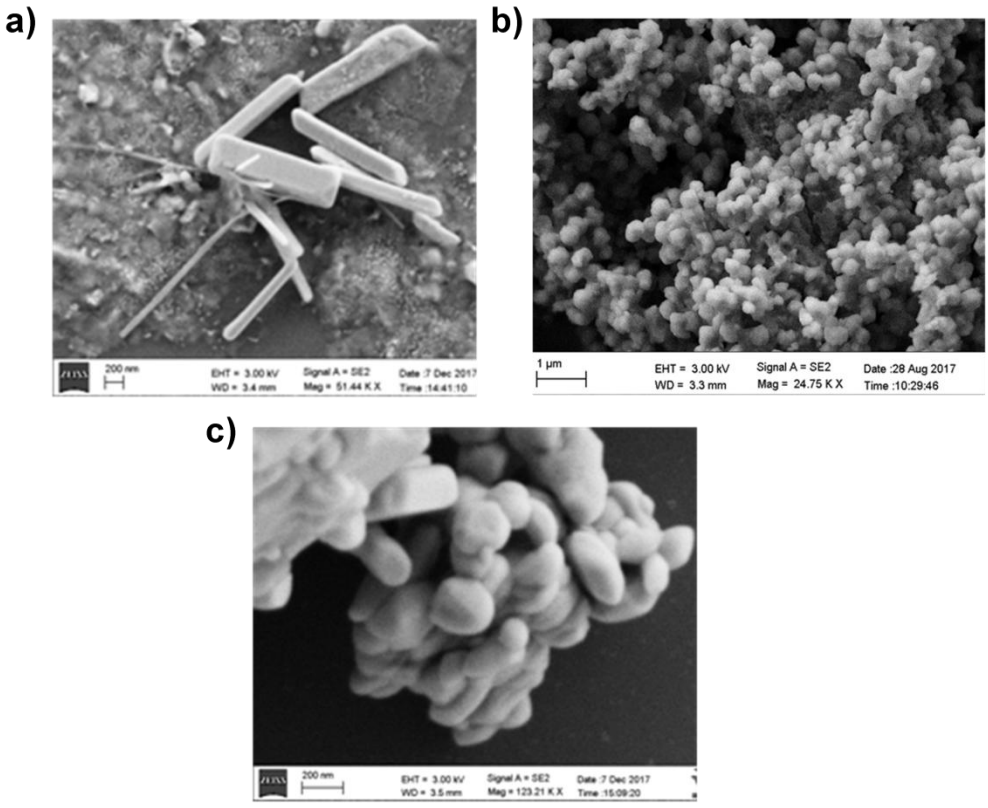

Appendix 4.10. FE-SEM image of (a) $MAPbBr_3$ nanoparticles, (b) ZIF-8 and (c) $MAPbBr_3$@ZIF-8 composite.

Appendix Table 4.3. Br/Pb ratio of $MAPbBr_3$@ZIF-8 composite is 3.67. Higher ratio of Br than Pb indicates the formation of $MAPbBr_3$ perovskite NPs in composite material.

Element	Molar Ratio
Pb	1.34
Br	4.92

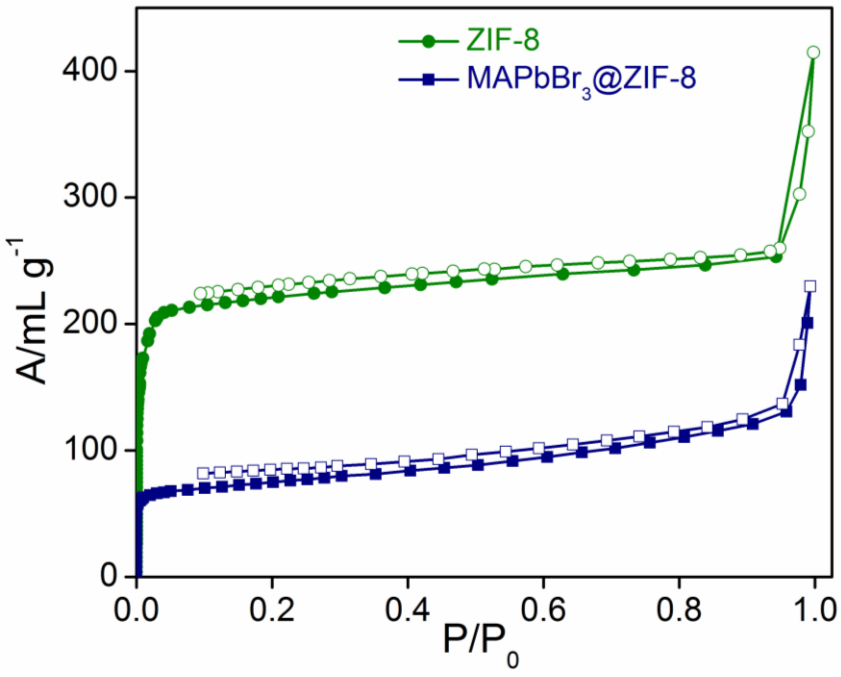

Appendix 4.11. N_2 gas adsorption at 77 K for ZIF-8 and $MAPbBr_3$@ZIF-8 composite. The gas uptake amount for composite is relatively low due to formation of $MAPbBr_3$ NCs inside ZIF-8 cavity.

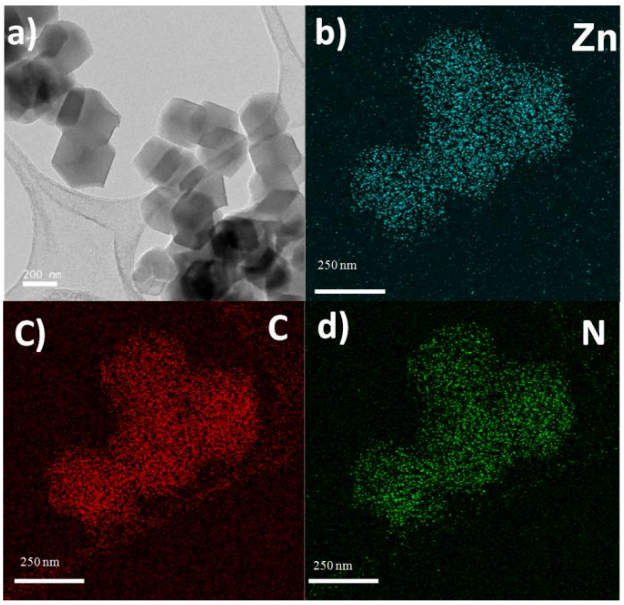

Appendix 4.12. a) HR-TEM image of ZIF-8. STEM-EDS elemental maps of ZIF-8: b) Zn elemental map c) C elemental map and d) N elemental map. TEM and STEM-EDS images have been shown in above figs. Bare ZIF-8 exhibits mono-dispersed cubic morphology with edge length 230 nm. STEM-EDS measurements supports that the ZIF-8 particles contain only the Zn, C, and N elements and that no detectable impurities are present Figs. 1b-d.

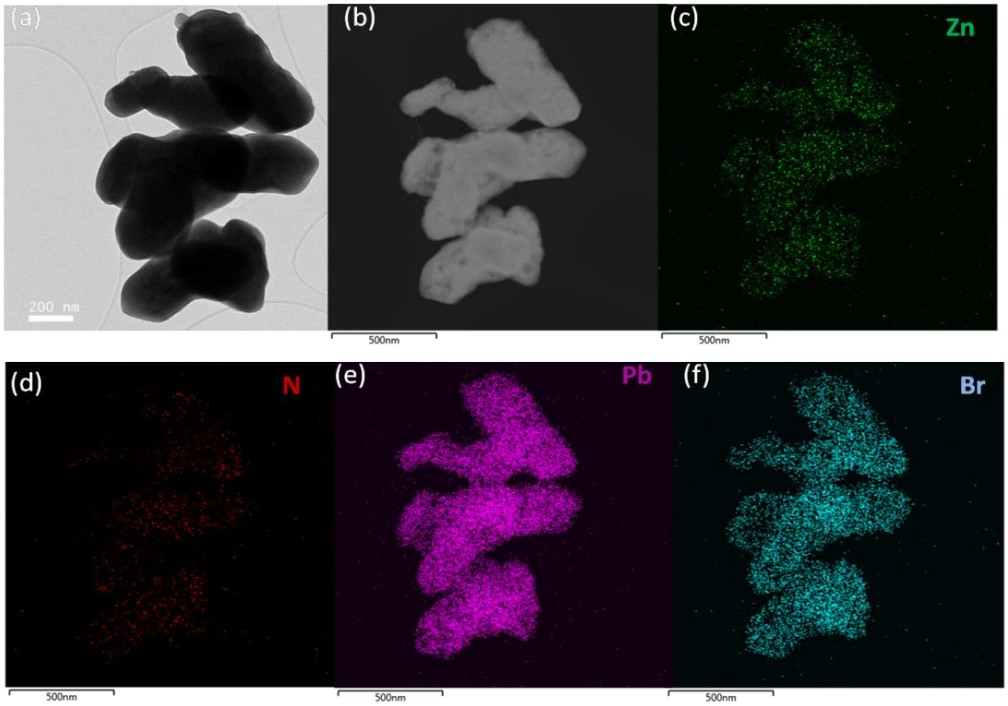

Appendix 4.13. HRTEM image of $MAPbBr_3$@ZIF-8. (a) STEM-EDS elemental maps of the $MAPbBr_3$@ZIF-8:(b) HAADF-STEM image (c) Zn elemental map, (d) N elemental map, (e) Pb elemental map, (f) Br elemental map.

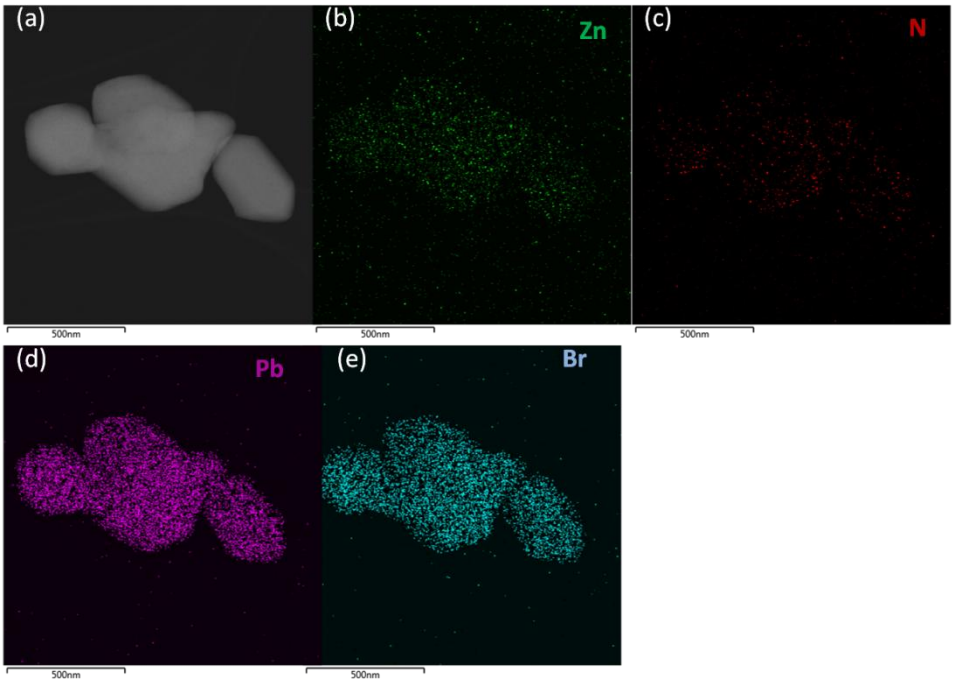

Appendix 4.14. STEM-EDS elemental maps of the $EAPbBr_3$@ZIF-8.(a) HAADF-STEM image (b) Zn elemental map, (c) N elemental map, (d) Pb elemental map, (e) Br elemental map.

Appendix Table 4.4. Band gap energies (eV) for different composites. M stands for MABr while E represent EABr. λ_{abs} indicates wavelength at absorbance maxima while λ_{em} is the wavelength at emission maxima. The excitation wavelength for every cases was same and 370 nm was the excitation wavelength

Composition (M:E)	λ_{abs} (nm)	λ_{em} (nm)	Band gap (eV)
1:0	518	529	2.26
3:1	486	493	2.43
1:1	472	481	2.73
1:3	446	455	2.88
0:1	423	433	3.1

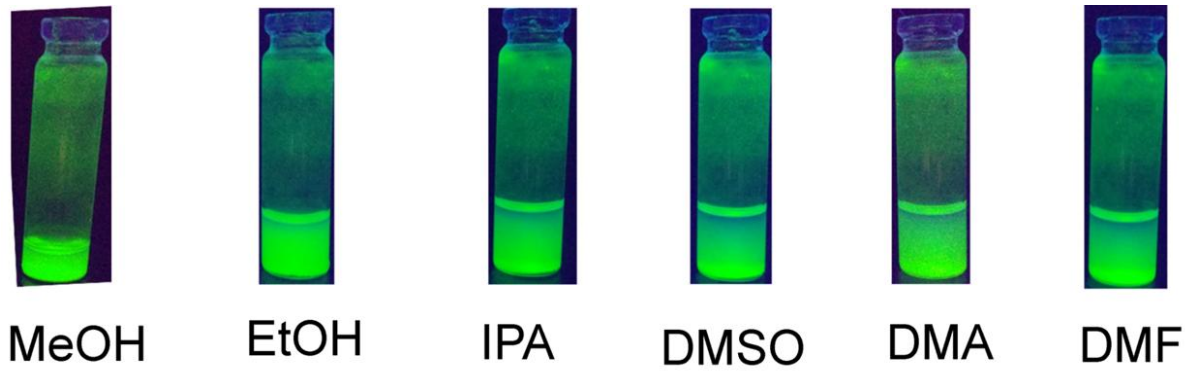

Appendix 4.15. Photograph of $MAPbBr_3$ composite in presence of different polar solvents under UV light. Retaining of color of the material confirming its stability in presence of polar solvents.

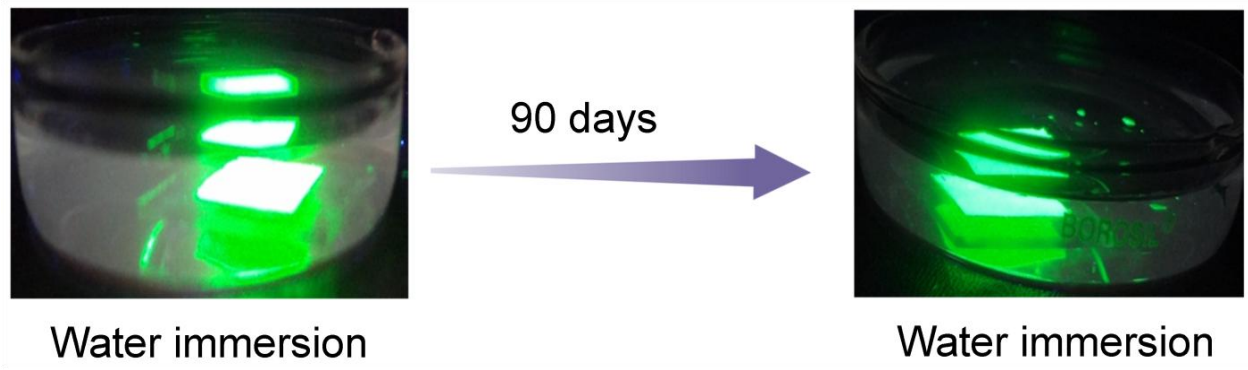

Appendix 4.16. Photograph of $MAPbBr_3$ composite in water immersion showing long term stability presence of water.

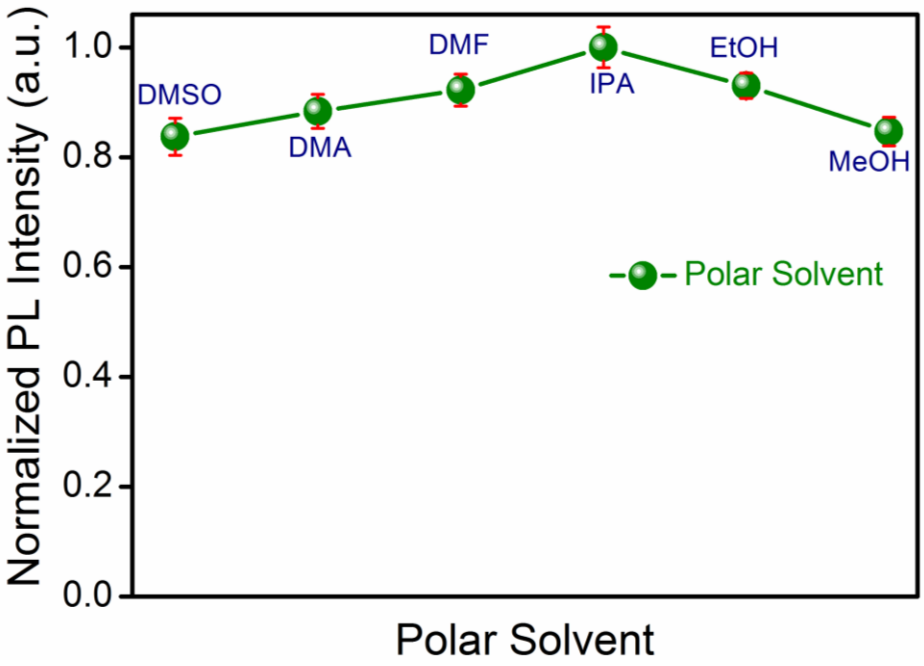

Appendix 4.17: PL intensity versus different of various polar solvents for $MAPbBr_3$ composite.

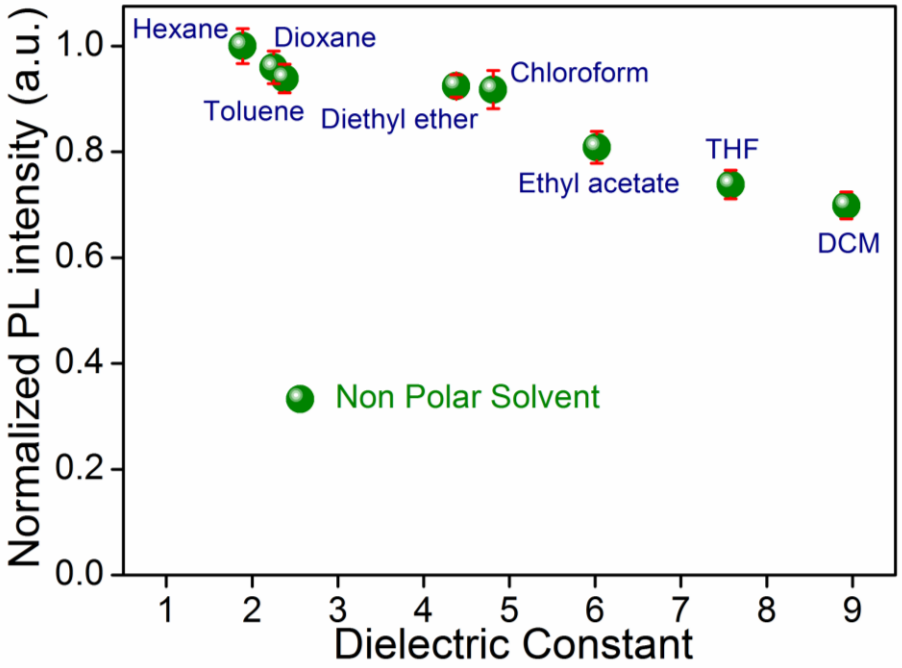

Figure 4.18. PL intensity versus dielectric constant of various non-polar solvents for $MAPbBr_3$ composite showing extra-stability of the material.

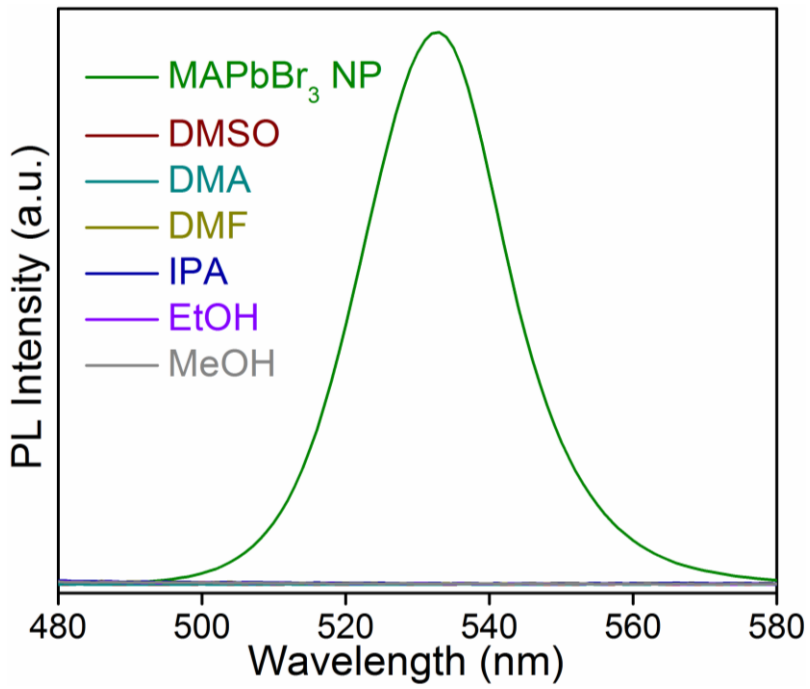

Appendix4.19. PL spectra of $MAPbBr_3$ NPs before and after immersion in different polar solvents showing immediate degradation after immersion in polar solvents.

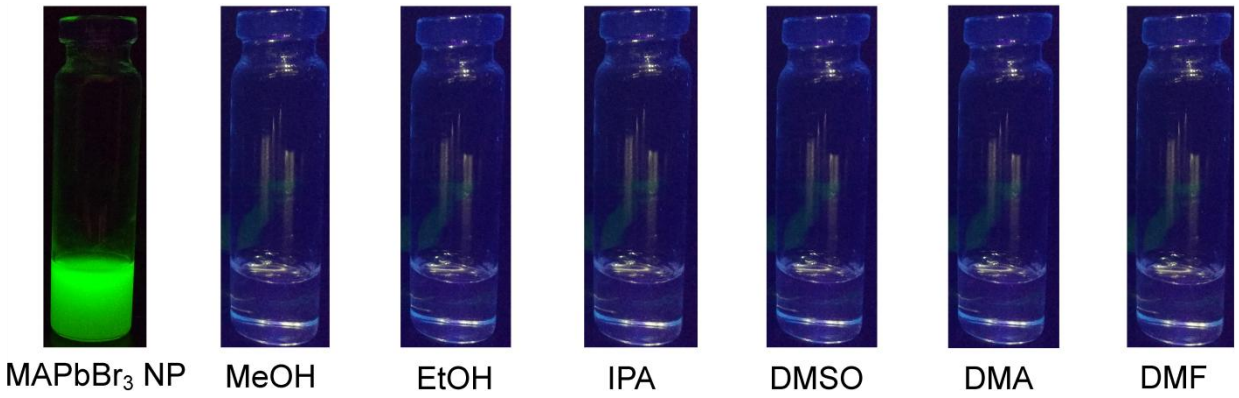

Appendix 4.20. Photographs of $MAPbBr_3$ NPs (under UV light) and after addition of different polar solvents, showing degradation of $MAPbBr_3$ NCs in presence of diverse polar solvents.

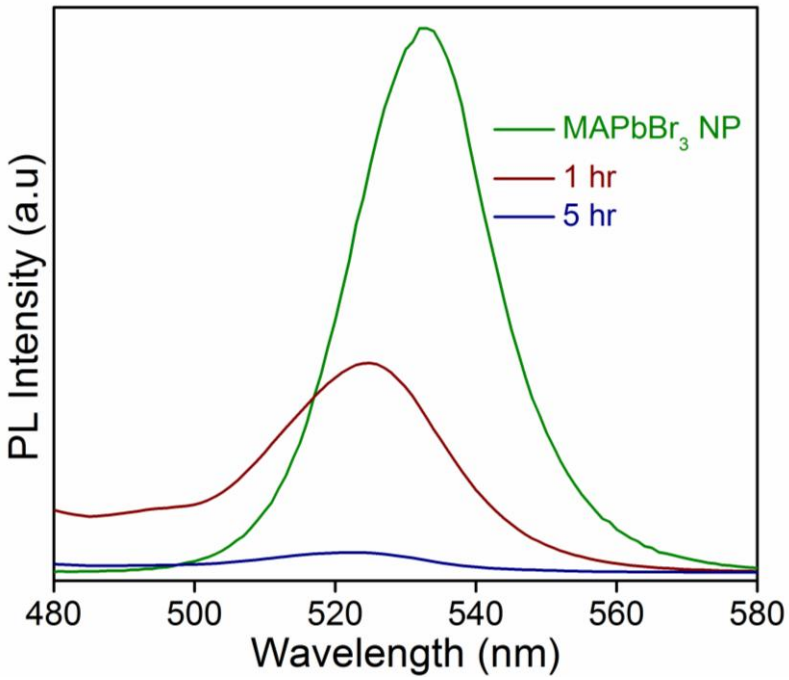

Appendix 4.21. Effect of luminescent property as a function of temperature of $MAPbBr_3$ NPs. This graph shows gradual degradation of PL intensity after storage of the material at high temperature (140 °C).

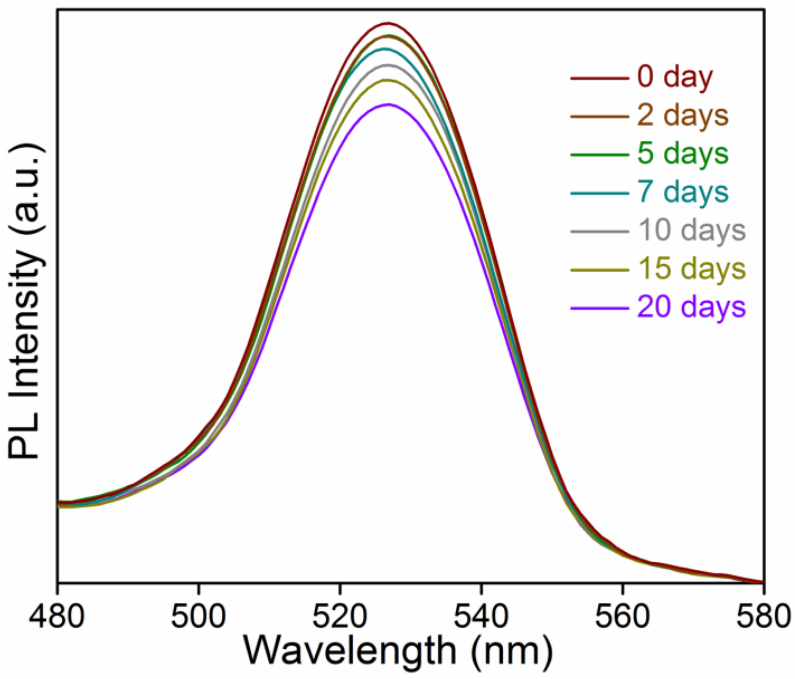

Appendix 4.22. Time dependent PL spectra of $MAPbBr_3$ composite after keeping under UV light (365 nm) irradiation for 20 days in dark condition.

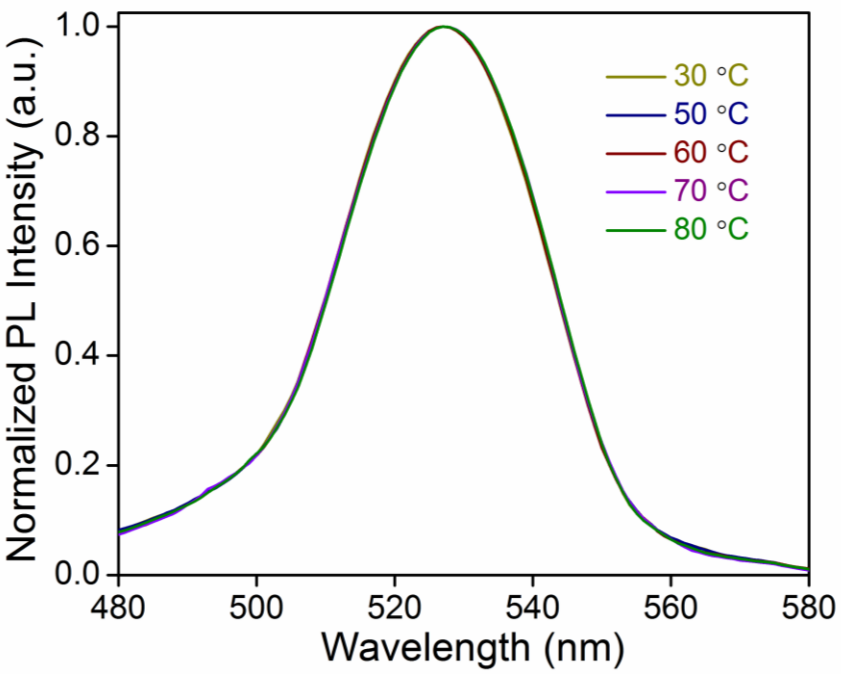

Appendix 4.23. Temperature dependent PL spectra of $MAPbBr_3$ composite showing temperature independent chromaticity.

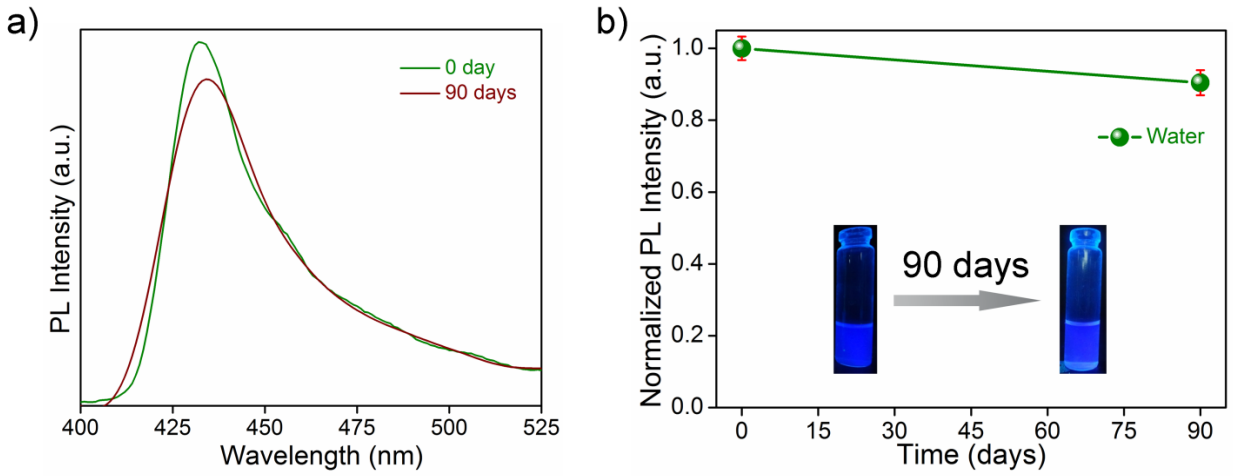

Appendix 4.24. a) Time dependent PL spectra of $EAPbBr_3$ composite after immersing in water for 90 days. b) PL intensity of composite remained almost same with time in water medium showing its exceptional water stability. Inset figure shows the color of composite remained also similar for 30 days.

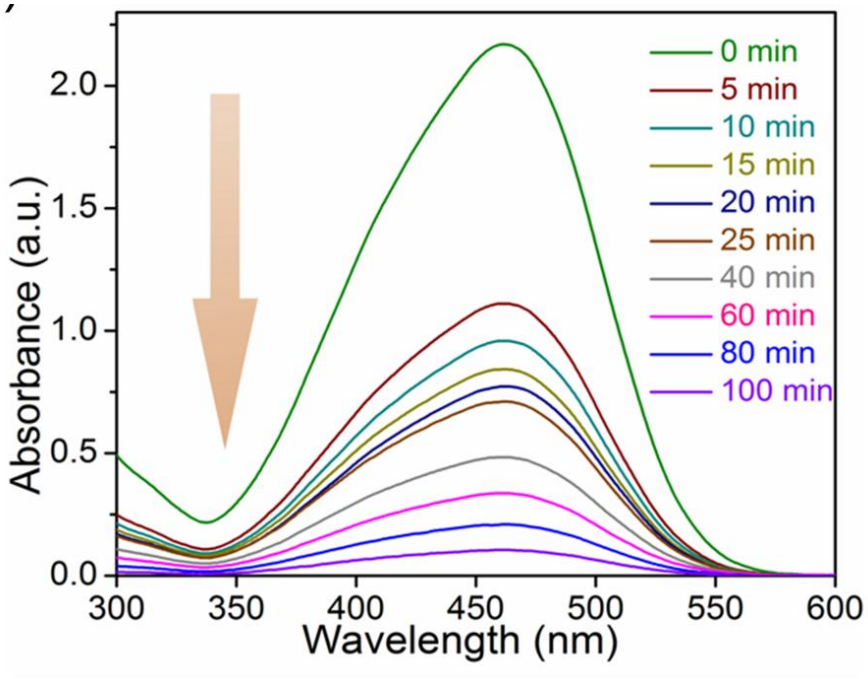

Appendix 4.25. Degradation of Methyl Orange (MO) in presence of visible light by $MAPbBr_3$ composite in water medium.

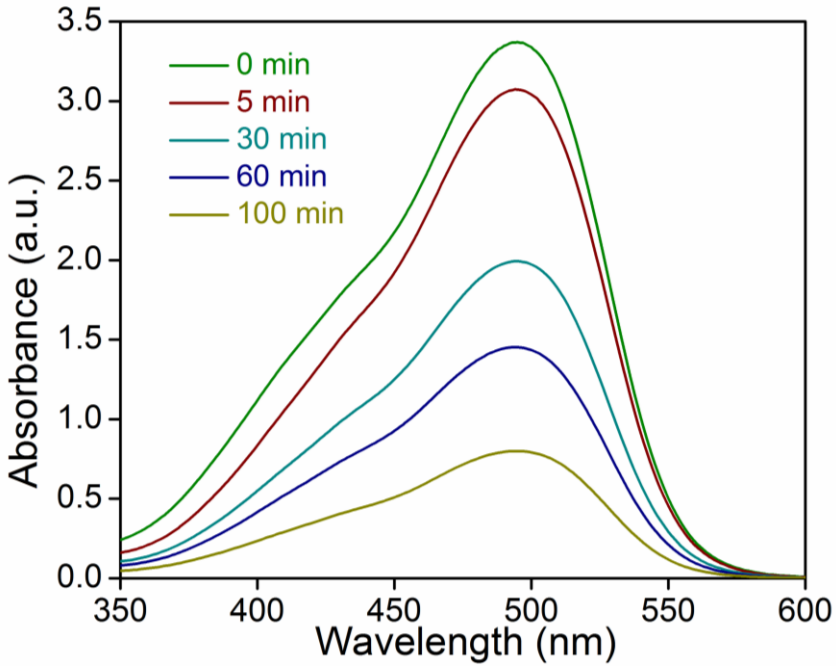

Appendix 4.26. Degradation of Methyl Red (MR) in presence UV light by $MAPbBr_3$ composite in aqueous solution.

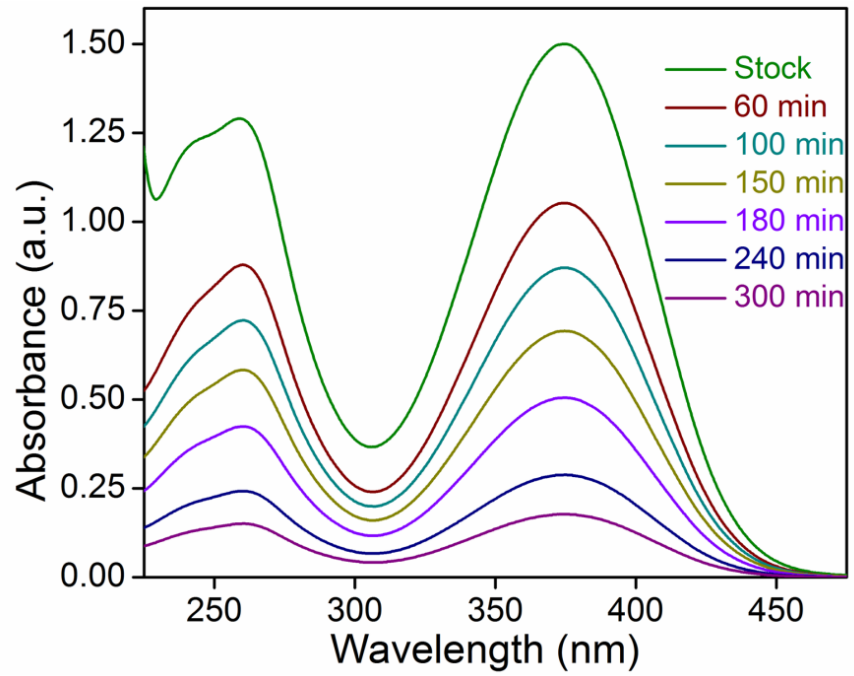

Appendix 4.27. Degradation of Nitrofurazone (NFZ) antibiotic in presence of visible light by $MAPbBr_3$ composite in aqueous media.

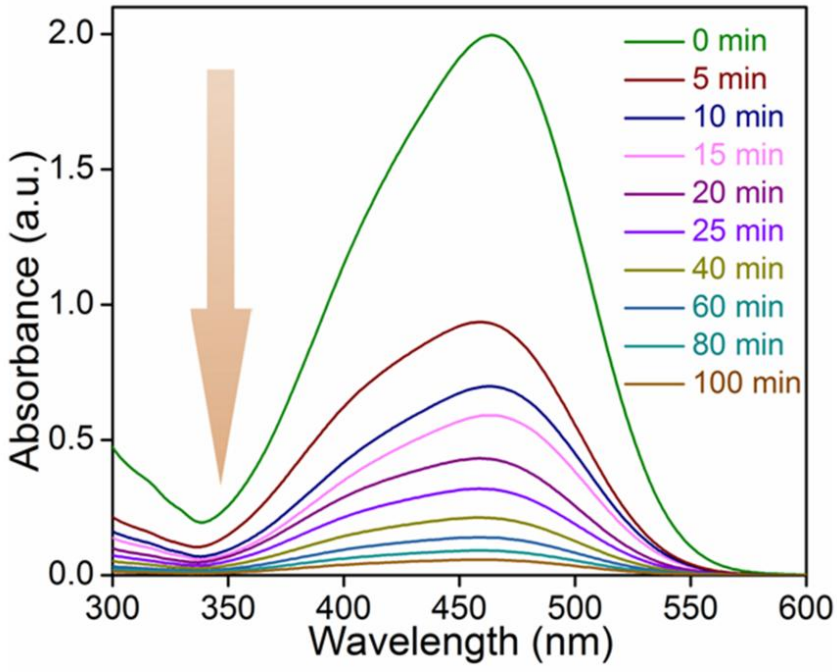

Appendix 4.28. Degradation of MO in presence of sun light by $MAPbBr_3$ composite.

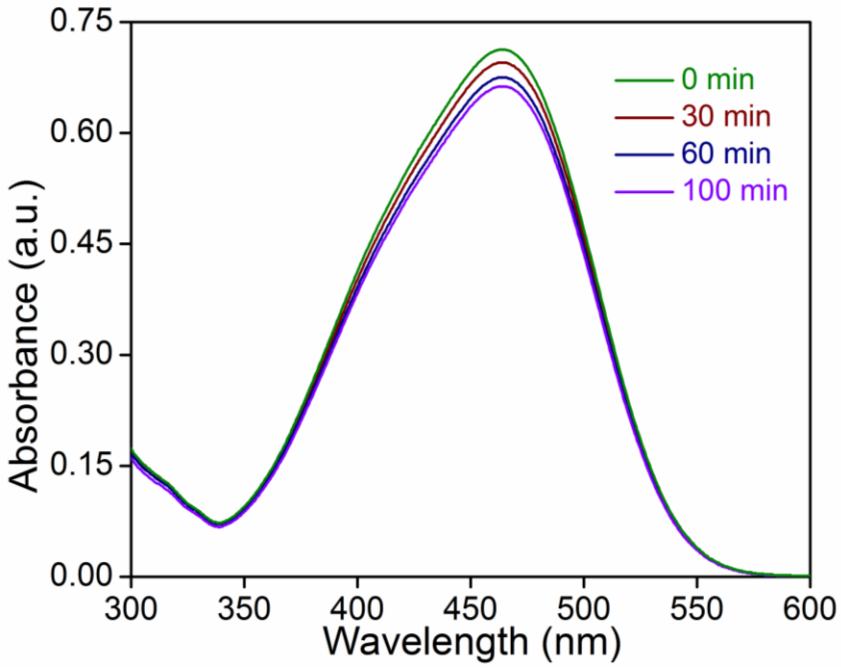

Appendix 4.29. Degradation of MO in dark condition by $MAPbBr_3$ composite, showing minute amount (< 10%) of degradation under dark condition.

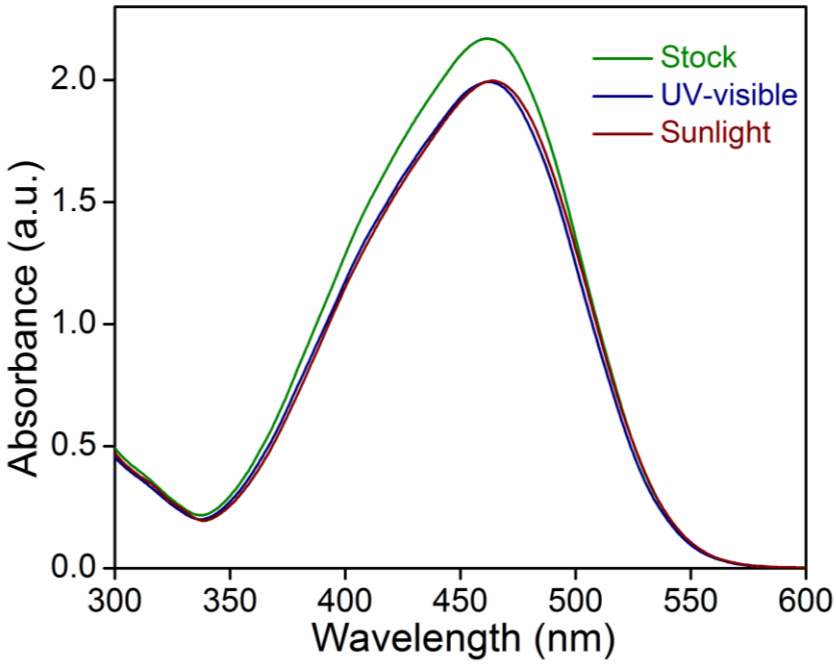

Appendix 4.30. Degradation profile of MO without the composite. Almost no degradation (<10%) observed for MO in absence of composite even after storage under such conditions for 24 h.

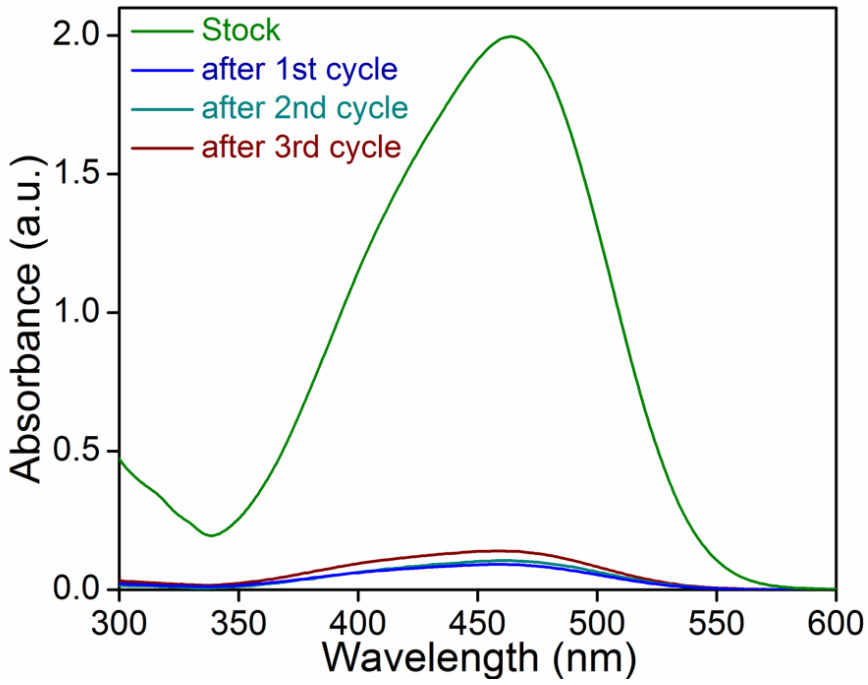

Appendix 4.31. Absorption spectra of MO after degradation, showing even after third cycle $MAPbBr_3$ composite able to degrade MO molecules with almost same efficiency.

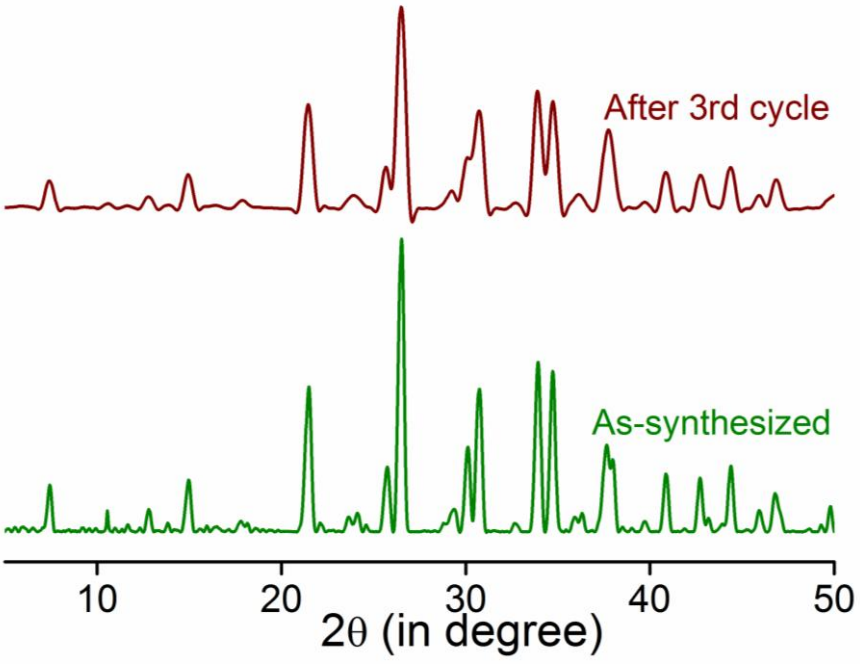

Appendix 4.32. PXRD patterns of $MAPbBr_3$@ZIF-8 composite before and after photocatalytic reaction. There is no phase change observed after third cycle implying maintaining its framework integrity.

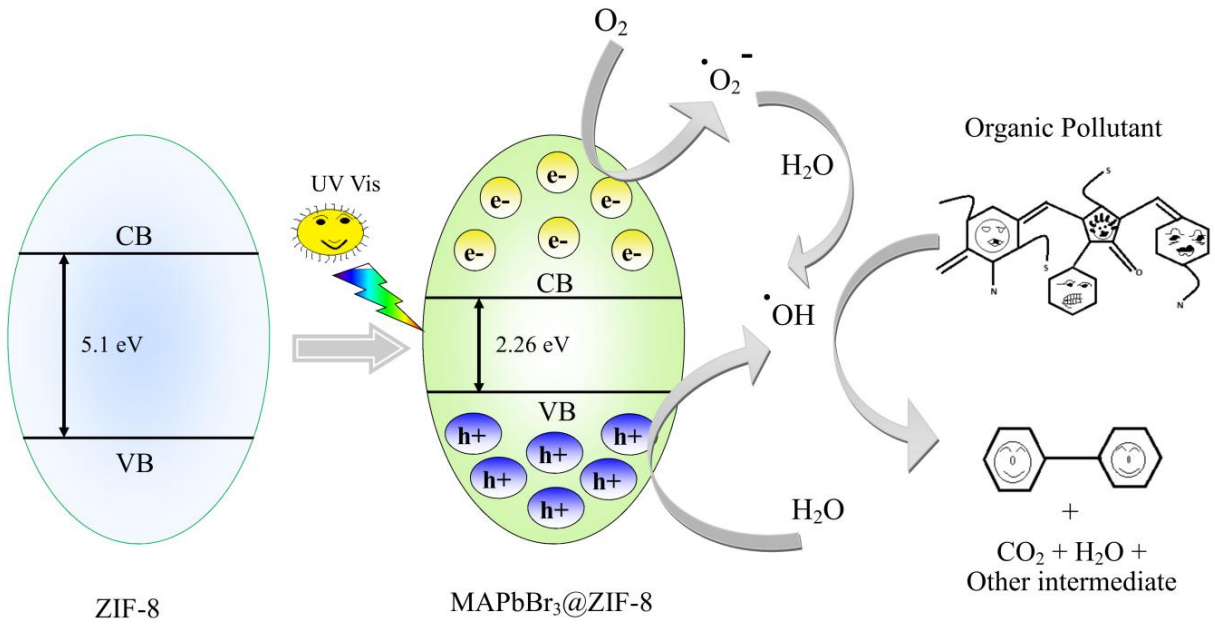

Appendix 4.33. Schematic of photocatalysis reaction mechanism.

The perovskite materials are superior visible light absorber in the solar spectrum. So it is expected that these materials have potential as photocatalyst in presence of light. The band gap of ZIF-8 is ~5.1 eV while for $MAPbBr_3$@ZIF-8 composite materials is ~2.26 eV. It is widely known that photocatalysis reaction rate increases with decreases in band gap.[1-5] Since the band gap of composite materials decreases from 5.1 eV to 2.26 eV, the overall composite showing photocatalysis reactions in visible light. We speculate that the photocatalytic degradation of organic pollutants occurred as follows: after irradiation of light to the composite materials, electron excited from valence band (VB) to conduction band (CB) and leaving the holes (h^+) in the VB. The photo generated electrons reduce the oxygen to oxygen radicals ($^{\cdot}O_2^-$) and ultimately converted to hydroxyl radicals ($^{\cdot}OH$) while holes oxidize water to hydroxyl radicals ($^{\cdot}OH$) respectively. The highly active species hydroxyl radicals finally decompose the organic pollutants in water.

4.6 References

[1] J. Heo, S. H. Im, J. H. Noh, T. N. Mandal, C.-S. Lim, J. A. Chang, Y. Lee, H. -J. Kim, A. Sarkar, M. K. Nazeeruddin, M. Grätzel, S. I. Seok, *Nat. Photon.* **2013**, *7*, 486-491.

[2] F. Deschler, M. Price, S. Pathak, L. E. Klintberg, D. D. Jarausch, R. Higler, S. Huttner, T. Leijtens, S. D. Stranks, H. J. Snaith, M. Atature, R. T. Phillips, R. H. Friend, *J. Phys. Chem. Lett.* **2014**, *5*, 1421-1426.

[3] Z.-K. Tan, R. S. Moghaddam, M. L. Lai, P. Docampo, R. Higler, F. Deschler, M. Price, A. Sadhanala, L. M. Pazos, D. Credgington, F. Hanusch, T. Bein, H. J. Snaith, R. H. Friend, *Nat. Nanotechnol.* **2014**, *9*, 687-692.

[4] F. P. Garcia de Arquer, A. Armin, P. Meredith, E. H. Sargent, *Nat. Rev. Mater.* **2017**, *2*, 16100-16116.

[5] J. Kurpiers, T. Ferron, M. Jakoby, T. Thiede, F. Jaiser, S. Albrecht, B. A. Collins, I. A. Howard, D. Neher, *Nat. Commun.* **2018**, *9*, 2038-2046.

[6] Q. A. Akkerman, G. Raino, M. V. Kovalenko, L. Manna, *Nat. Mater.* **2018**, *17*, 394-405.

[7] Z. Wang, Z. Shi, T. Li, Y. Chen, W. Huang, *Angew. Chem., Int. Ed.* **2017**, *56*, 1190-1212.

[8] H.-C. Zhou, S. Kitagawa, *Chem. Soc. Rev.* **2014**, *43*, 5415-5418.

[9] A. H. Chughtai, N. Ahmad, H. A. Younus, A. Laypkov, F. Verpoort, *Chem. Soc. Rev.* **2015**, *44*, 6804-6849.

[10] L. E. Kreno, K. Leong, O. K. Farha, M. Allendorf, R. P. Duyne, J. T. Hupp, *Chem. Rev.* **2012**, *112*, 1105-1125.

[11] C. Y. Lee, O. K. Farha, B. J. Hong, Sarjeant, A. A. Sarjeant, S. T. Nguyen, J. T. Hupp, *J. Am. Chem. Soc.* **2011**, *133*, 15858-15861.

[12] C. R. Kim, T. Uemura, S. Kitagawa, *Chem. Soc. Rev.* **2016**, *45*, 3828-3845.

[13] Z. Chen, Z. -G. Gu, W. -Q. Fu, F. Wang, J. A Zhang, *ACS Appl. Mater. Interfaces* **2016**, *8*, 28737-28742.

[14] C. Zhang, B. Wang, W. Li, S. Huang, L. Kong, Z. Li, L. Li, *Nat. Commun.* **2016**, *8*, 1138-1146.

[15] H. Yang, S. J. Bradley, X. Wu, A. Chan, G. I. N. Waterhouse, T. Nann, J. Zhang, P. E. Kruger, S. Ma, S. G. Telfer, *ACS Nano* **2018**, *12*, 4594-4604.
[16] D. Zhang, Y. Xu, Z. Xia, *Inorg. Chem.* **2018**, *57*, 4613-4619.

[17] J. Aguilera-Sigalat, D. Bradshaw, *Coord. Chem. Rev.* **2016**, *307*, 267-291.

[18] G. Lu, S. Li, Z. Guo, O. K. Farha, B. G. Hauser, X. Qi, Y. Wang, X. Wang, S. Han, X. Liu, J. S. Duchene, H. Zhang, Q. Zhang, X. Chen, J. Ma, S. C. J. Loo, W. D. Wei, Y. Yang, J. T. Hupp, F. Huo, *Nat. Chem.* **2012**, *4*, 310-316.

[19] K. S. Park, Z. Ni, A. P. Cote, J. Y. Choi, R. Huang, F. J. Uribe-Romo, H. K. Chae, M. O'Keeffe, O. M. Yaghi, *Proc. Natl. Acad. Sci., U.S.A.* **2006**, *103*, 10186-10191.

[20] C.-C. Wang, J. -R. Li, X. -L. Lv, Y. -Q. Zhang, G. Guo, *Energy Environ. Sci.* **2014**, *7*, 2831-2867.

[21] J. Qiu, X. Zhang, Y. Feng, X. Zhang, H. Wang, J. Yao, *Appl. Catal., B* **2018**, *231*, 317-342.

[22] D. Jiang, P. Xu, H. Wang, G. Zeng, D. Huang, M. Chen, C. Lai, C. Zhang, J. Wan, W. Xue. *Coord. Chem. Rev.* **2018**, *376*, 449-466.

[23] M. N. Chong, B. Jin, C. W. K. Chow, C. Saint, *Water Res.* **2010**, *44*, 2997-3027.

[24] Y. Wu, H. Luo, H. Wang, *RSC Adv.* **2014**, *4*, 40435-40438.

[25] S. Mosleh, M. R. Rahimi, M. Ghaedi, K. Dashtian, *Ultrason. Sonochem.* **2016**, *32*, 387-397.

[26] Z. Sha, J. Wu, *RSC. Adv.* **2015**, *5*, 39592-39600.

[27] A. T. Williams, S. A. Winfield, J. N. Miller, *Analyst* **1983**, *108*, 1067-1071.

[28] J. C. de Mello, H. F. Wittmann, R. H. Friend, *Adv. Mater.* **1997**, *9*, 230-232.

[29] Q. Wang, J. Ren, X.-F. Peng, X.-X. Ji, X.-H. Yang, *ACS Appl. Mater. Interfaces* **2017**, *9*, 29901-29906.

[30] L. C. Schmidt, A. Pertegas, S. González-Carrero, O. Malinkiewicz, S. Agouram, G. Mínguez Espallargas, H. J. Bolink, R. E. Galian, J. Pérez-Prieto, *J. Am. Chem. Soc.* **2014**, *136*, 850-853.

[31] M. Mittal, A. Jana,; S. Sarkar, P. Mahadevan, S. Sapra, *J. Phys. Chem. Lett.* **2016**, *7*, 3270-3277.

[32] A. I. Vogel, Textbook of Macro and Semimicro Qualitative Inorganic Analysis; Longmans Group Limited: London, 5th edn, Chapter I, pp 193-195, 1979.
[33] P. Tyagi, S. M. Arveson, W. A. Tisdale, *J. Phys. Chem. Lett.* **2015**, *6*, 1911-1916.

[34] A. Swarnkar, R. Chulliyil, V. K. Ravi, M. Irfanullah, A. Chowdhury, A. Nag, Angew. Chem., Int. Ed. **2015**, *54*, 15424-15428.

[35] Q. Zhong, M. Cao, H. Hu, D. Yang, M. Chen, P. Li, L. Wu, Q. Zhang, *ACS Nano* **2018**, *12*, 8579-8587.

[36] V. Malgras, J. Henzie, T. Takei, Y. Yamauchi, *Angew. Chem.* **2018**, *130*, 9019-9023.

[37] S. Huang, Z. Li, L. Kong, N. Zhu, A. Shan, L. Li, *J. Am. Chem. Soc.* **2016**, *138*, 5749-5752.

[38] S.-T. Ha, R. Su, J. Xiang, Q. Zhang, Q. Xiong, *Chem. Sci.* **2017**, *8*, 2522-2536.

[39] F. Zhang, H. Zhong, C. Chen, X.-G. Wu, X. Hu, H. Huang, J. Han, B. Zou, Y. Dong, *ACS Nano* **2015**, *9*, 4533-4542.

[40] S. Hermes, M. -K. Schroter, R. Schmid, L. Khodeir, M. Muhler, A. Tissler, R. W. Fischer, R. A. Fischer, *Angew. Chem. Int. Ed.* **2005**, *44*, 6237-6241.

[41] H.-L. Jiang, T. Akita, T. Ishida, M. Haruta, Q. Xu, *J. Am. Chem. Soc.* **2011**, *133*, 1304-1306.

[42] C. Wang, K. E. deKrafft, W. Lin, *J. Am. Chem. Soc.* **2012**, *134*, 7211-7214.

[43] A. Aijaz, Q. Xu, *J. Phys. Chem. Lett.* **2014**, *5*, 1400-1411.

[44] H. Huang, J. Raith, S. V. Kershaw, S. Kalytchuk, O. Tomanec, L. Jing, A. S. Susha, R. Zboril, A. L. Rogach, *Nat. Commun.* **2017**, *8*, 996.

[45] Z.-J. Li, E. Hofman, J. Li, A. H. Davis, C.-H. Tung, L.-Z. Wu, W. Zheng, *Adv. Funct. Mater.* **2018**, *28*, 1704288-1704295.

[46] A. Loiudice, S. Saris, E. Oveisi, D. T. Alexander, R. Bouonsanti, *Angew. Chem., Int. Ed.* **2017**, *56*, 10696-10701.

[47] H. Sun, Z. Yang, M. Wei, W. Sun, X. Li, S. Ye, Y. Zhao, H. E. Tan, L. Kynaston, T. B. Schon, H. Yan, Z. -H. Lu, G. A. Ozin, E. H. Sargent, S. Seferos, *Adv. Mater.* **2017**, *29*, 1701153-1701162.

[48] C. Yu, Z. Chen, J. J. Wang, W. Pfenninger, N. Vockic, J. T. Kenney, K. Shum, *J. Appl. Phys.* **2011**, *110*, 063526-063530.

[49] M. A. Nasalevich, M. G. Goesten, T. J. Savenije, F. Kaptejin, J. Gascon, *Chem. Commun.* **2013**, *49*, 10575-10577.

[50] X. Mu, J. Jiang, F. Chao, Y. Lou, J. Chen, *Dalton Trans*. **2018**, *47*, 1895-1902.

[51] A. Wang, Y. Zhou, Z. Wang, M. Chen, L. Sun, X. Liu, *RSC Adv.* **2016**, *6*, 3671-3679.

[52] X. Yuan, H. Wang, Y. Wu, G. Zeng, X. Chen, L. Leng, Z. Wu, H. Li, *Appl. Organometal. Chem.* **2016**, *30*, 289-296.

[53] N. K. Noel, S. D. Stranks, A. Abate, C. Wehrenfennig, S. Guarnera, A.-A. Haghighirad, A. Sadhanala, G. E. Eperon, S. K. Pathak, M. B. Johnston, *Energy Environ. Sci.* **2014**, *7*, 3061-3068.

[54] Z. Shi, J. Guo, Y. Chen, Q. Li, Y. Pan, H. Zhang, Y. Xia, W. Huang, *Adv. Mater.* **2017**, *29*, 1605005-1605033.

Chapter 5

Hybrid Blue Perovskite@Metal-Organic Gel (MOG) Nanocomposite: Simultaneous Improvement of Luminescence Property and Stability

5.1 Introduction

Organic-inorganic hybrid perovskite nanocrystals (NCs) have attracted significant interest both in fundamental and applied research owing to their spectacular optoelectronic properties.[1-3] In particular, tunable light emission across the visible region, with high color purity, has seen them be used widely as active materials for lighting and display technology.[4-6] Recently, a significant amount of research has been concentrated to achieve highly luminescent red and green light-emitting perovskites.[7,8] Nevertheless, blue light-emitting perovskites which are essential for full-color display applications, lags significantly behind its green and red counterparts.[9,10] The bottleneck of the growth is attributed to relatively low defects tolerance, short charge carrier mobility, low photoluminescence quantum yield (PLQY), existence of detrimental non-radiative trap states, high materials cost, and inferior stability.[11,12] Currently, most of the commercially available blue emitters also suffer from low luminous efficiency and high material cost.[13] Hence, recent attention has turned towards development of hybrid blue light-emitting materials due to their high synthetic feasibilities and cost-effectiveness.[14,15] But, most of them are fall in the sky-blue region i.e. 480-500 nm, which are not adequate enough to satisfy the required color standard as defined by the National Television System Committee (NTSC) and is incompetent for the wide-color-gamut display.[16,17] Therefore, the development of intense blue (λ_{max}<440 nm) hybrid perovskites is almost indispensable to meet NTSC color standard. However, the production of intense blue perovskite remains extremely challenging to date, especially in terms of luminescence property and materials stability. [18,19]

Encapsulation strategies have been considered as efficient approach to enhance optical property as well as chemical stability of perovskite NCs, and porous metal-organic frameworks (MOFs) are the latest addition in this context.[20-22] However, heterogeneous property of MOFs is one of the key issues that restrict further utilization of perovskite-MOF nanocomposite in the form of thin films or different workable structures.[23] In the light of growing interest for flexible electronics, perovskite NCs embedded with soft materials could offer high tolerance to structural deformation.[24] We envisioned that, soft porous metal-organic gel (MOG) could be a suitable choice as hosting matrix, having dual characteristics of both MOF and gel in terms of tunable porosity, high specific surface area along with high crack resistance capability and good foldability afford them to form desired shapes.[25] Plenty of efforts have been devoted towards integration of diverse nanoparticles into gel matrices,[25] however, to the best of our knowledge, embedding perovskite NCs inside a MOG matrix has not been reported yet.

Herein, we report a readily scalable Al(III) based hydrolytically stable MOG that was utilized as protecting host matrix to stabilize hybrid bromide perovskite NCs (HBP-NCs) from aerial or chemical

degradation. We have also demonstrated that weakly blue light-emitting $EAPbBr_3$ NCs (PLQY ~ 5%) through encapsulation within MOG matrix, results in an unprecedented 10-fold enhancement of PLQY (~ 53%) without altering the PL peak position. It is noteworthy that, for the first time, simultaneous improvement of both PLQY and water stability is achieved for intense blue emitting hybrid perovskites NCs. These materials maintained their basic structures as well as photoluminescence behaviors even after immersing in water or UV light irradiation for prolonged period of time. Furthermore, flexible HBP@MOG nanocomposites were easily molded into various artificial three dimensional sculptures by virtue of the soft nature of nanocomposites. To validate the proof of concept, the blue emissive $EAPbBr_3$@MOG was selected to fabricate white light emitting diode (WLED) by combining with green and red emitting materials on a UV LED chip. The as-fabricated device exhibited wide color gamut (144% of NTSC standard) and provide its potential application in display technology.

5.2 Experimental

5.2.1 Materials

Lead (II) bromide ($PbBr_2$, 99.999%), hydrobromic acid (HBr, 48 %), $Al(NO_3)_3.9H_2O$ (99.997 %), trimesic acid (98%) were purchased from Sigma-Aldrich. Methylamine (40 %), ethylamine (70 %), n-cotylamine (99 %) were purchased from Spectrochem. All solvents were purchased from Finer India and all were used without further purification. Ethylamonium bromide ($CH_3CH_2NH_3Br$, EABr, methylammonium bromide (CH_3NH_3Br, MABr), n-octylammonium bromide ($CH_3(CH_2)_7NH_3Br$, OABr) were synthesized by previously reported literature method. 1 W UV LED (wavelength ~ 380 nm) was used for fabrication of white light emitting LED.

5.2.2 Synthesis

Synthesis of $EAPbBr_3$@MOG. In a typical synthesis protocol, firstly 105 mg of trimesic acid (0.5 mmol) was dissolved in 14 ml of DMF in a drum vial and followed by addition of 281.4 mg of $Al(NO_3)_3.9H_2O$ (0.75 mmol) to this solution mixture. Next, 70 μL of triethylamine (0.5 mmol) was added to this reaction mixture and sonicate it to form clear solution. After that added 183 mg of $PbBr_2$ (0.5 mmol), 63 mg of EABr (0.5 mmol) and 63 mg of OABr (0.3 mmol) were added to whole reaction mixture and again sonicate to from clear solution. Finally, the whole reaction mixture kept at 110 °C for 24 hours and then cool to room temperature over 10 hours, leading to synthesis of colorless jelly type metal-organic gel (MOG) materials. During the heating process MOG was formed where the perovskite

components were entrapped inside MOG matrix. This MOG materials were dried at 120 °C for 2 hours leading to formation of yellowish color xerogel. This xerogel was subjected to stir for next 24 hours in presence of 30 mL toluene (nucleating solvent) to obtain $EAPbBr_3$@MOG composite material. At last, the resulting composite was collected by filtration and dried under vacuum overnight to get the final product. The $MAPbBr_3$@MOG composite was also prepared by following same aforementioned procedure where only MABr was used instead of EABr and all other components and their amounts intact.

Red emitting Mn(II) doped $EAPbBr_3$. The red emitting Mn (II) doped $EAPbBr_3$ was prepared by following the literature reported protocol.[26] In a typical synthesis, 36.7 mg of $PbBr_2$(0.1 mmol), 11.2 mg of EABr (0.1 mmol) and 12.6 mg of OABr (0.06 mmol), were grinded with a mortar pestle at RT for 30 min. Next 4.3 mg of $MnBr_2$ (0.02 mmol) was added to it and grinded another 30 min. After that, 3 mL acetone was added to it and immediately centrifuged at 5000 rpm for 2 min. Precipitate was collected and dried it in vacuum for further used as a red emitting materials.

5.2.3 Physical Measurements

Powder X-ray diff raction (PXRD) patterns were performed on a Bruker D8 Advanced X-ray diffractometer at room temperature using Cu Kα radiation (λ = 1.5406 Å) at a scan speed of 0.5 ° min^{-1} and a step size of 0.01° in 2θ. The morphology of the crystalline materials was recorded with a Zeiss Ultra Plus field-emission scanning electron microscope (FESEM) with an integral charge compensator and embedded EsB and AsB detectors (Oxford X-max instruments 80 mm^2 (Carl Zeiss NTS, GmbH). The elemental analysis was carried out using voltage of 15 KV equipped with an EDX detector. The steady state photoluminescence studies were recorded on a Fluorolog-3 spectrofluorometer (HORIBA Scientific). Absolute PLQY measurements for the composites (dispersed in toluene) materials were recorded using an integrating sphere. UV-vis absorption studies were performed on a Shimadzu UV 3600 UV /vis /NIR spectrophotometer in an optical quartz cuvette (10 mm path length) over the entire range of 200-800 nm. The IR Spectra were acquired by using NICOLET 6700 FT-IR spectrophotometer using KBr pellet in 400-4000 cm^{-1} range. Gas adsorption measurements were performed using BelSorp-Max instrument (Bel Japan). Prior to adsorption measurements, the activated samples were heated at 130 °C under vacuum for 6 hours using BelPrepvacII. For high-resolution TEM analysis, all the samples were dispersed in toluene (3 mg/mL) and sonicated for 30 min. Then, the samples were left for 2 min, and the upper part of the solution was taken for preparing TEM samples on a lacey carbon-coated copper grid (Electron Microscopy Science). TEM imaging and STEM-EDS were performed on the HRTEM (JEM-

2100F, JEOL) operating at acceleration voltage of 200 kV. XPS measurements were performed on the photoelectron spectrometer (Thermo, K-alpha). The PL decay dynamics (time-correlated single photon counting (TCSPC) were measured with a FLS 980 (Edinburgh Instruments) using 405 nm pulse laser irradiation with a pulse repetition rate of 500 kHz. Decay profiles were fitted to multi-exponential decay curves, and the calculations of average lifetimes were measured using the equation $\boldsymbol{\tau_{avg}} = \frac{\sum A_i \tau_i^2}{\sum A_i \tau_i}$ where A_i and τ_i are the amplitude and lifetime of the *i*-th component respectively.

4.2.4 Stability Test

4.2.4.1 Water Stability. The water stability tests were executed in a 5 ml glass vial. Each glass vial contained 6 mg of composite materials and immersed in 2.5 ml water in open air for 12 hours and during this period of time PL spectra regularly examined in dispersed phase.

4.2.4.2 Photo Stability. Photostability tests were performed in a dark place in 5 ml glass vial. Each glass vial contained 6 mg of composite materials and placed under 365 nm UV light for 300 hours in open air. After that, PL emission spectra (disperse phase in toluene) and PXRD were examine.

4.2.5 Fabrication of Thin Film. The pristine composite materials were dispersed in toluene and kept it for 3 days leading to formation of jelly type morphology. The obtained jelly type materials were kept on a glass slide and kept in open air for another 7 days for formation of thin film.

4.2.6 Preparation of various Sculptures. A variety of desired geometrical shaped and sized sculptures were prepared by using pristine composite materials. First pristine composite materials were dispersed in minimum amount of toluene and sonicated it for 2 hours. After sonication, the composite materials were stirred for one day and kept it for another 3 days without stirring at room temperature. The obtained jelly type materials were poured on different shaped moulds and kept it for another 3 days to obtain various shaped sculptures.

4.2.6 Fabrication of WLED. Proper ratio of blue, green and red emitting materials (Mn^{2+} doped $EAPbBr_3$) were grinded thoroughly for 1.5 hours and dispersed in toluene solution. The resulting mixture solution was sonicated for 5 min and then coated on a UV LED. Finally, the coated UV LED was kept at room temperature for next 2 days to obtain WLED.

5.3 Results and discussion

The hydrolytically stable Al(III) based porous MOG was synthesized and thoroughly characterized according to the literature report by Fischer and co-workers (Appendix 5.1 and 5.2).[27] EA/MAPbBr$_3$@MOG nanocomposites (MA denotes methylammonium) were prepared rapidly via two step synthetic protocol. In a typical synthesis process, in first step, all reacting components were mixed in DMF and heated at 110 °C for 24 hours. During this process, colorless MOG was formed where perovskite precursors were entrapped inside MOG matrix. In second step, nucleation of the perovskite NCs was initiated with addition of copious amount of nucleating solvent (toluene) (Scheme 1, Appendix 5.3).[22]

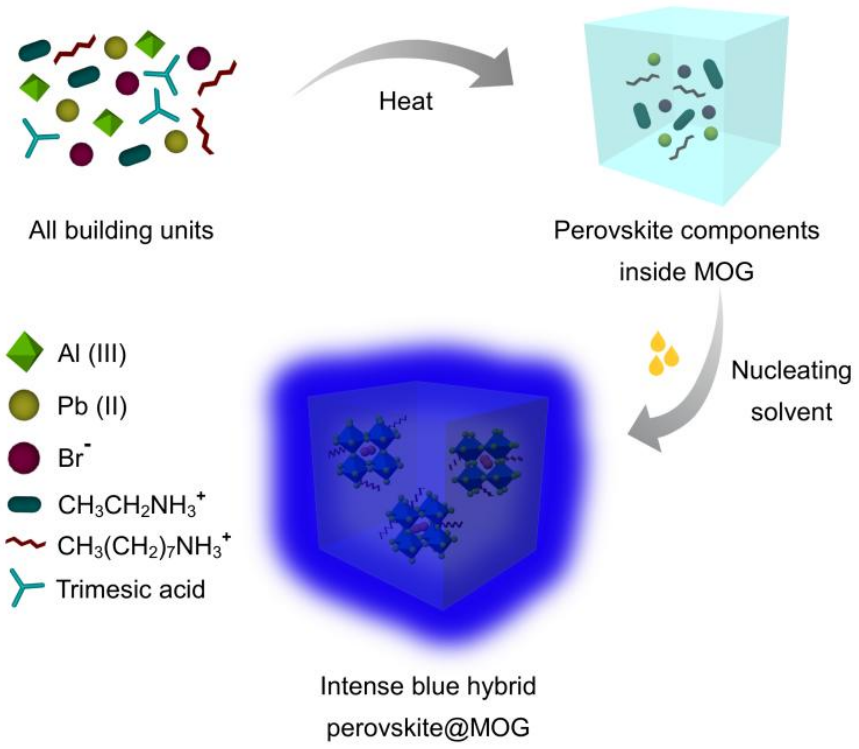

Scheme 5.1. Schematic synthetic procedure for synthesis of intense blue hybrid perovskite@MOG nanocomposite.

The structural analysis of nanocomposites were confirmed by field emission scanning electron microscopy (FESEM), and powder X-ray diffraction (PXRD) and transmission electron microscopy (TEM) studies. FESEM images of EAPbBr$_3$@MOG composite (Appendix 5.4) showed distinctly different morphology as compared to bare perovskite NCs as well as MOG materials and evidence for their micro-sized nature. The SEM-EDS (energy-dispersive spectroscopy) analysis revealed that existence of excess Br-rich (Appendix Table 5.1) in EAPbBr$_3$@MOG surface which also indicated the generation

of high emissive perovskite NCs.[28] Elemental mapping analysis (Appendix 5.5) evidenced for homogeneous distribution of $EAPbBr_3$ NCs throughout the composite material. The formation of crystalline HBP-NCs in the nanocomposites was analysed through PXRD (Appendix 5.6) and the appearance of Bragg's diffraction patterns confirmed the encapsulation of nano-sized HBP-NCs inside the MOG matrix (Figure 5.1a). The existence of diffraction peaks at 11.2°, 26.9° and 30.8° in $EAPbBr_3$@MOG composite is assigned for $EAPbBr_3$ NCs' PXRD pattern, which are in accord with literature report.[29] Structural evolutions of the material were studied by TEM analysis and TEM images (Figure 5.1b) confirmed the encapsulation of $EAPbBr_3$ NCs inside MOG matrix. From large area TEM images (Figure 5.1b) it is clear that $EAPbBr_3$ NCs are dispersed uniformly throughout MOG matrix. The particle size distribution curve of $EAPbBr_3$@MOG (Appendix 5.7) shows that $EAPbBr_3$ NCs are spherical in shape with an average diameter of 5.5 nm. The high-resolution TEM (HRTEM) images of $EAPbBr_3$@MOG composite reveals well-defined lattice spacing according to the crystallographic parameters for $EAPbBr_3$ NCs. Inset Figure 5.1b, the composite shows an interplanar distance of 0.296 nm attributed to (002) plane of $EAPbBr_3$ NCs.[29] Fourier transform infrared spectroscopy (FT-IR) measurements (Appendix 5.8) also confirms the presence of HBP-NCs inside MOG matrix. Nitrogen sorption isotherms (Appendix 5.9) show considerable less amount of gas uptake in case of both composites (514 m^2/g for $EAPbBr_3$@MOG while 522 m^2/g for $MAPbBr_3$@MOG) compared to the parent material i.e. MOG (778 m^2/g). It suggests the successful encapsulation of perovskite NCs in MOG matrix.[30] The full range XPS spectra of the compounds are shown in figure 5.1d and the binding energy positions of different atoms are similar to the literature report.[27,31] In case of the nanocomposites, appearance of new signals for bromine and lead atoms (Appendix 5.10) proves the formation of HBP-NCs in the MOG matrix. Detailed analysis of X-ray photon spectroscopy (XPS) data (Figure 5.1e) showed, the peak of Al 2p shifted to lower binding energies from 74.5 to 74.1 eV with slight peak broadening for $EAPbBr_3$@MOG compared to host MOG, suggested the change in coordination environment around Al(III) atoms.

It is notable that, negative shift of binding energy for $EAPbBr_3$@MOG occurred due to strong interaction between MOG framework with perovskite NCs. The absorption and emission peaks of $EAPbBr_3$@MOG appeared at 398 nm and 436 nm, respectively while $MAPbBr_3$@MOG showed absorption peak at 475 nm and emission band at 492 nm (Appendix 5.11-5.15). The full width at half-maxima (FWHM) of $EAPbBr_3$@MOG composite found to be 18.4 nm (Appendix 5.11).[32] Similar PL peak position, PL intensity and FWHM of different batches of composites were confirmed the reproducibility of these materials through this two-step synthetic methodology (Appendix 5.15). The absolute value of PLQY for $EAPbBr_3$@MOG nanocomposite was found to be 53 % (Figure 5.1d) and it is noteworthy that, until now

this is one of the highest reported PLQY among blue emitting hybrid perovskite materials.[13,29,32] Time resolved photoluminescence (TRPL) spectra of perovskite NCs and composites are shown in Appendix 5.16-5.18 and the fitting parameters are listed in Appendix Tables 5.2 and 5.3.

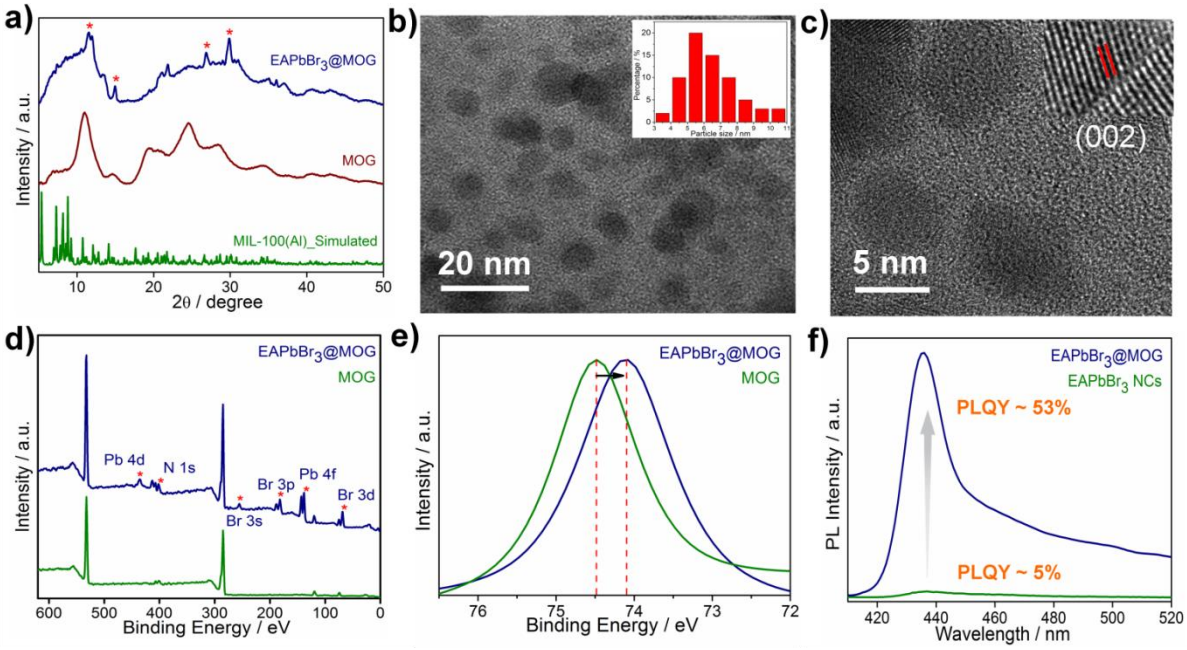

Figure 5.1. Characterization of $EAPbBr_3$@MOG nanocomposite. (a) PXRD patterns of simulated MIL-100(Al), MOG (pristine) and $EAPbBr_3$@MOG nanocomposite. (*) represent the characteristic diffraction peaks for $EAPbBr_3$ NCs. (b) TEM image of $EAPbBr_3$@MOG nanocomposite. The inset Fig. shows size distribution histogram of $EAPbBr_3$@MOG nanocomposite. Average size of $EAPbBr_3$ NPs is 5.5 nm in composite materials. (c) HR-TEM image of $MAPbBr_3$ composite material. The inset Fig. shows the lattice fringe of individual $EAPbBr_3$ NC. (d) Full range of XPS spectra of MOG and $EAPbBr_3$@MOG nanocomposite. Star indicates the characteristic peaks for $EAPbBr_3$ perovskite NCs. (e) XPS spectra of Al 2p for MOG and $EAPbBr_3$@MOG nanocomposite. (f) PL spectra of $EAPbBr_3$ NCs (PLQY ~ 5 %) and $EAPbBr_3$@MOG nanocomposite (PLQY ~ 53 %).

The decay profiles of both $EAPbBr_3$ NCs and $EAPbBr_3$@MOG composite are fitted to biexponential functions suggesting two different components are associated in the emission spectra. The average lifetime of $EAPbBr_3$@MOG nanocomposite (3.03 ns) is much longer compare to $EAPbBr_3$ NCs (0.70 ns) (Table S3) implying successful encapsulation of NCs inside MOG matrix.[33] The detrimental nonradiative decay rate constant drops (k_{nr}, 0.16 ns^{-1}) significantly compare to parent $EAPbBr_3$ NCs (k_{nr}, 1.39 ns^{-1}) (Table S3) results in improved emission behaviour of $EAPbBr_3$@MOG nanocomposite.[34] The strong

interactions between MOG matrix and perovskite NCs efficiently suppress the surface trap-state that trigger reduction of nonradiative channels thus increasing the PLQY of nanocomposites.

All the stability related experiments of the nanocomposites were executed maintaining the similar conditions where bare NCs were readily prone to decompose.[22,35] To ensure open-air stability, both composites were kept in open-air for few months (Figure 5.2a) and found retention of original PL intensity (> 80%), demonstrating their long-term air stability over such long period of time.

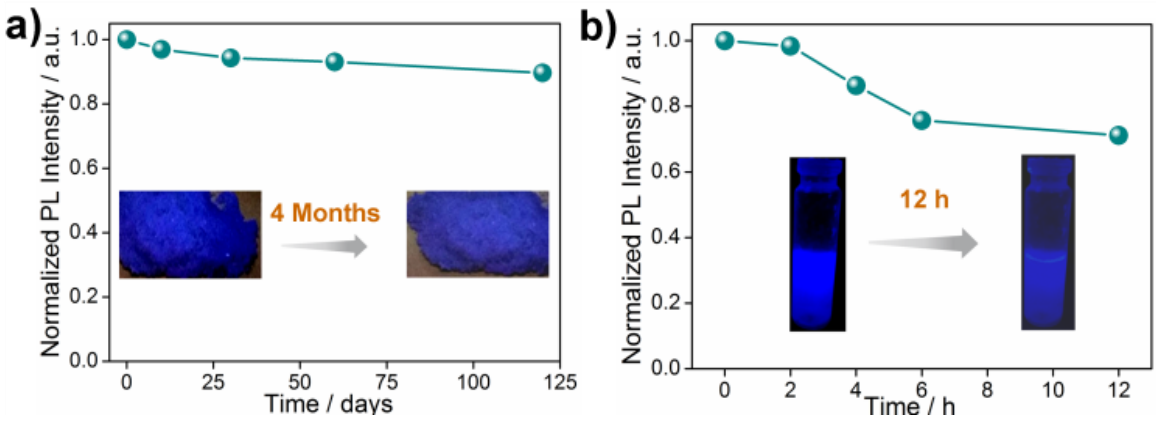

Figure 5.2. Stability studies of $EAPbBr_3$@MOG nanocomposite. (a) Normalized PL intensity as a function of time stored under open air over a period of 4 months. The inset photograph shows color of the solid material under UV light (365 nm) before and after 4 months. (b) Normalized PL intensity as a function of time in water for different time intervals. Inset photograph shows the color of the composites under UV light (365 nm) before and after 12 hours immersed into water.

The inset figures of 5.2a illustrates the color in solid state and PL intensity of $EAPbBr_3$@MOG remained almost similar even after keeping for four months in open air, proving its long term environmental stability. Water stability experiments were conducted by immersing the composite materials into water and found that even after 12 hours of immersion; PL spectra remained almost similar confirming their outstanding water stability (Figure 5.2b). Photo-stability tests were executed by measurements of PL intensity as a function of time under continuous UV light (365 nm) illumination at ambient condition for 300 hours and found that retention of PL intensity (>80%,) (Appendix 5.19) of $EAPbBr_3$@MOG remained intact demonstrating its excellent photo-stability. The $MAPbBr_3$@MOG composite also showed outstanding stability in open-air, UV and even in water media (Appendix 5.20-22).

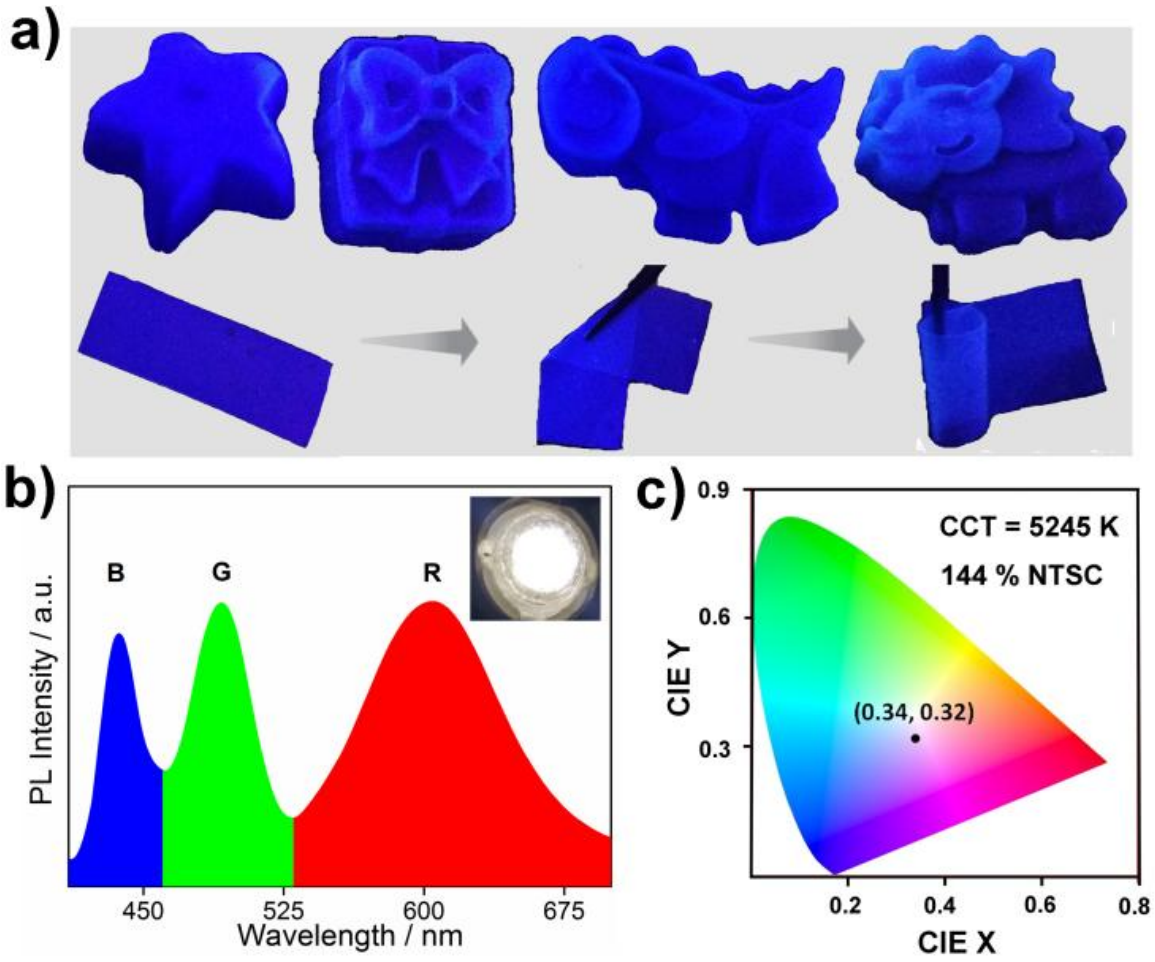

Figure 5.3. Different sculptures and characterization of as-fabricated WLEDs. (a) Various sculptures and flexible thin films were fabricated from blue emissive $EAPbBr_3$@MOG nanocomposite. The photographs of sculpture and thin film are under UV light (365 nm), showing bright intense blue fluorescence. (b) Emission spectrum of white LED fabricated by combination of blue emitting $EAPbBr_3$@MOG (B), green emitting $MAPbBr_3$@MOG (G) and red emitting Mn(II) doped $EAPbBr_3$ NCs (R) deposited on a UV chip. Inset Fig. shows the photographs of white LED with applied current of 20 mA. (c) CIE color coordinates of as-fabricated white LEDs (x: 0.34, y: 0.32).

The excellent air, water and photo stability of the composites were attributed to the hydrolytically stable MOG framework which efficiently screened the perovskite NCs from different kinds of environmental degradation.[22] Additionally, a variety of well-defined smooth and crack free artificial shapes and sculptures were successfully fabricated with these composites without addition of any external binder (Figure 5.3a, Appendix 5.23 and 5.24). Flexible thin films were successfully prepared using these

composites for diverse practical applications (Figure 5.3a). Appendix Table 5.4 shows a comparison of PL properties and stability of intense blue emitting (λ_{max}<440 nm) hybrid perovskites developed so far. This table highlighted PL properties of our system are comparable to those brightest blue emitters related with hybrid perovskite materials and superior stability over other systems. As a proof of concept for lighting applications, blue emissive $EAPbBr_3$@MOG, green emissive $MAPbBr_3$@MOG and red emissive Mn(II)-doped $EAPbBr_3$@MOG (prepared through mixing Mn(II) salt with $EAPbBr_3$ NCs) (Appendix 5.25) were mixed in proper ratios and then coupled with commercially available UV chip to fabricate WLED device (Appendix 5.26).[36,37] Figure 5.3b shows the positions of emission peak maximum were obtained for WLED, which is in good agreement with steady-state PL peaks. The photograph of operating WLED is shown as an inset in Figure 5.3b. The coordinate of Commission Internationale de l'Eclairage (CIE) chromaticity of as prepared WLED was (0.34, 0.32) and the color gamut coverage is as high as 144 % (Figure 5.3c) of the National Television System Committee (NTSC) standard, benefited from the narrow emission spectra of blue and green emissive perovskite composites. The correlated color temperature (CCT) was 5245 K, which corresponded to the so-called white daylight. The WLED maintained its colour purity of all components even after 24 hours at open air confirming its stability at ambient condition (Appendix 5.27).

5.4 Conclusions

In summary, we have developed a straightforward two-step approach for synthesis of bright intense blue light-emitting perovskite@MOG nanocomposite, where perovskite NCs were embedded inside a porous MOG matrix. Here, the MOG matrix offers dual benefits to perovskite NCs i.e. it serves as a protective barrier against degradation under working conditions and enhanced the luminescence property dramatically. Additionally, the flexible nanocomposites were easily fabricated into different desired three dimensional artificial structures for practical utility. Finally, the as-synthesized nanocomposites were demonstrated

5.5 Appendix section

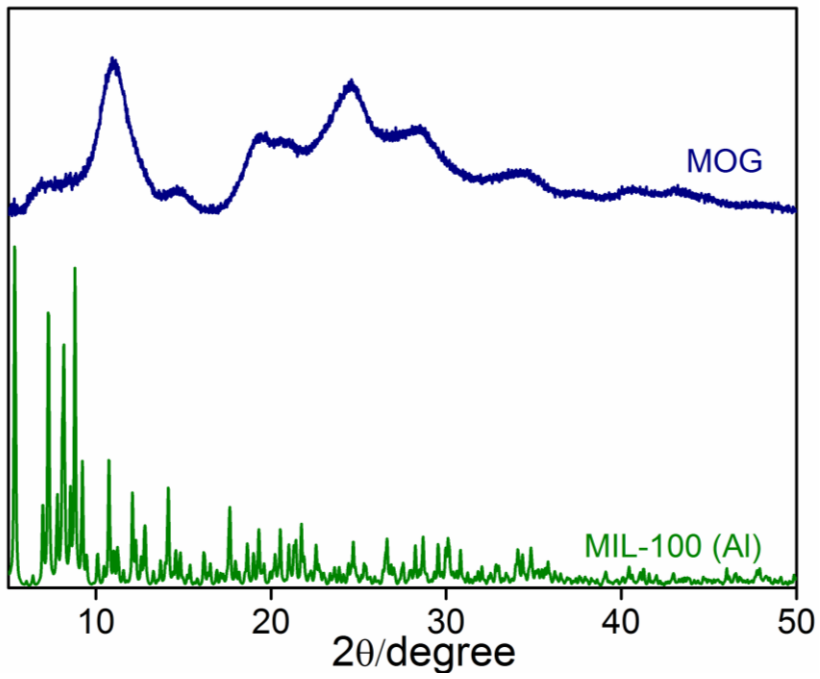

Appendix 5.1. Comparison of PXRD patterns of MIL-100 (Al) and metal-organic gal (MOG).

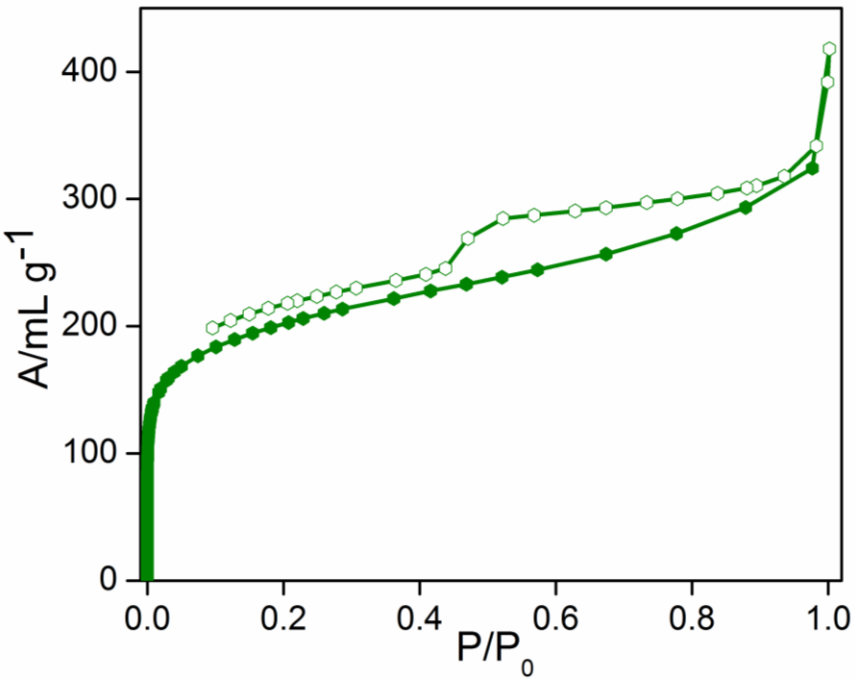

Appendix 5.2. N_2 sorption study at 77 K for pristine MOG.

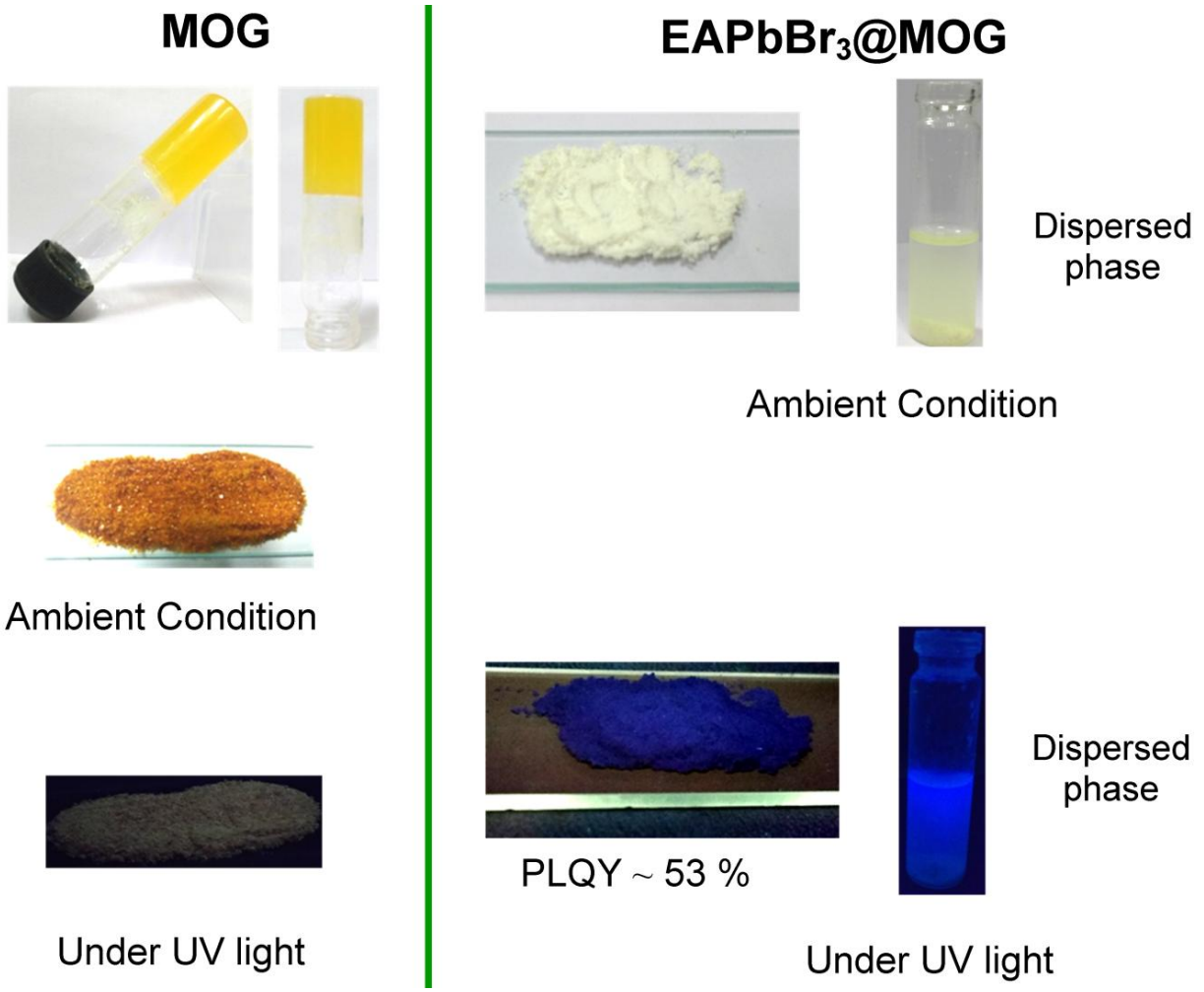

Appendix 5.3. Photographs of Pristine MOG and $EAPbBr_3$@MOG at ambient conditions and under UV light (365 nm). Toluene solvent was used for dispersion of $EAPbBr_3$@MOG composite.

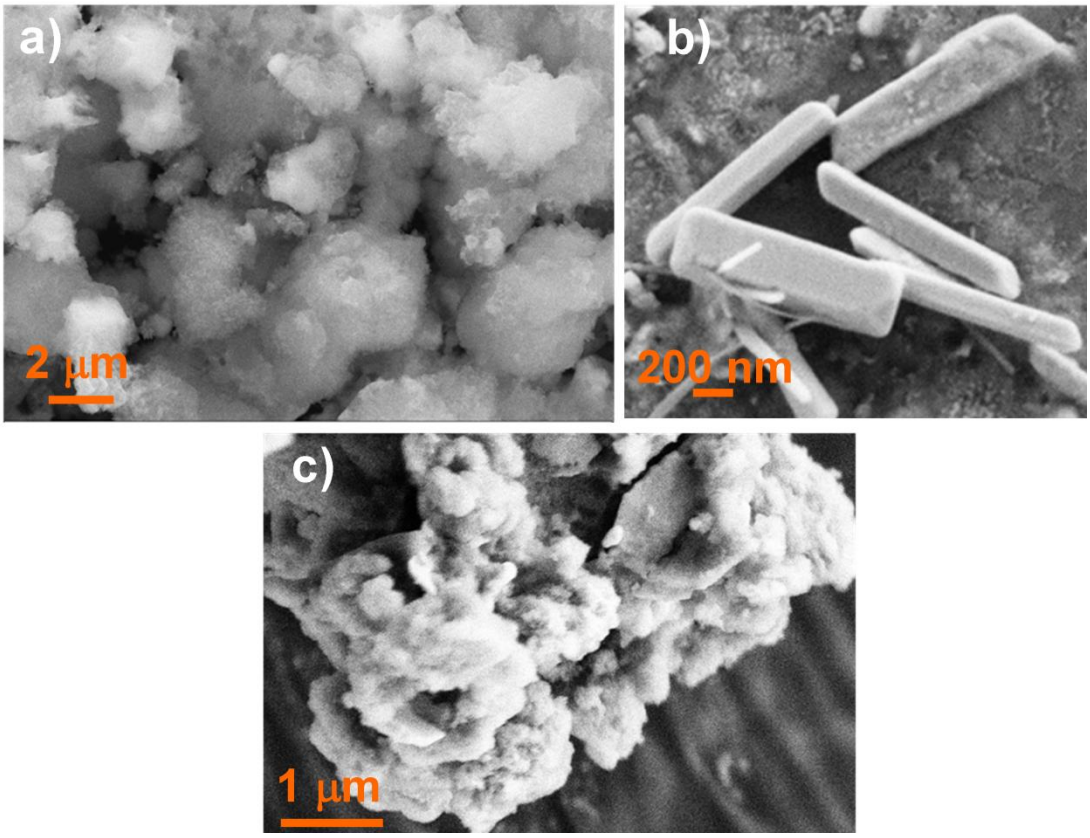

Appendix 5.4. FESEM image. a) MOG, b) $EAPbBr_3$ QD and c) $EAPbBr_3$@MOG composite.

Appendix Table 5.1. Br/Pb ratio of $MAPbBr_3$@ZIF-8 composite is 3.62. Higher ratio of Br than Pb indicates the formation of $EAPbBr_3$ perovskite NPs in composite material.

Element	Molar Ratio
Pb	1.54
Br	5.57

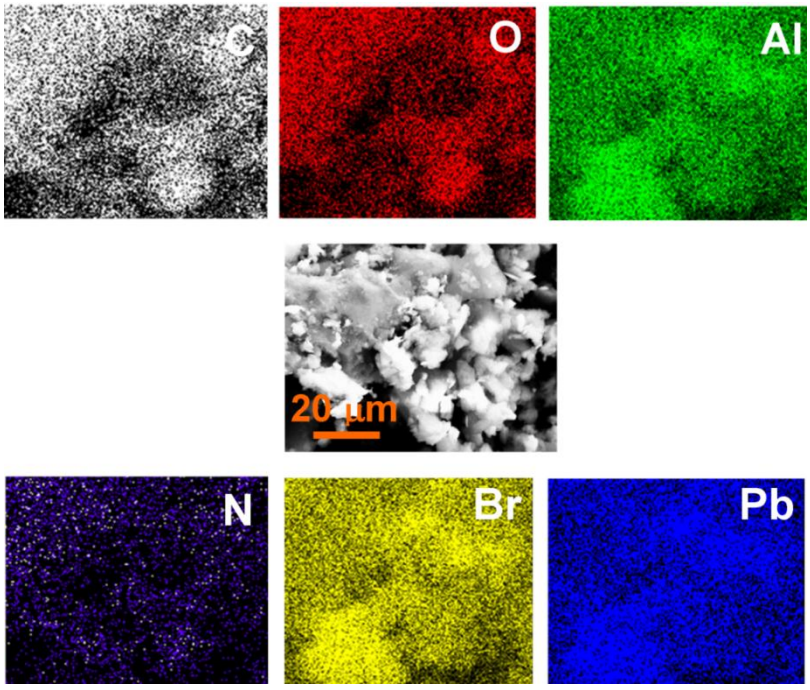

Appendix 5.5. Elemental mapping of EAPbBr$_3$@MOG composite. Elemental mapping analysis shows that Pb and Br are present throughout the composite which indicates the homogeneous formation of perovskite NCs in composite.

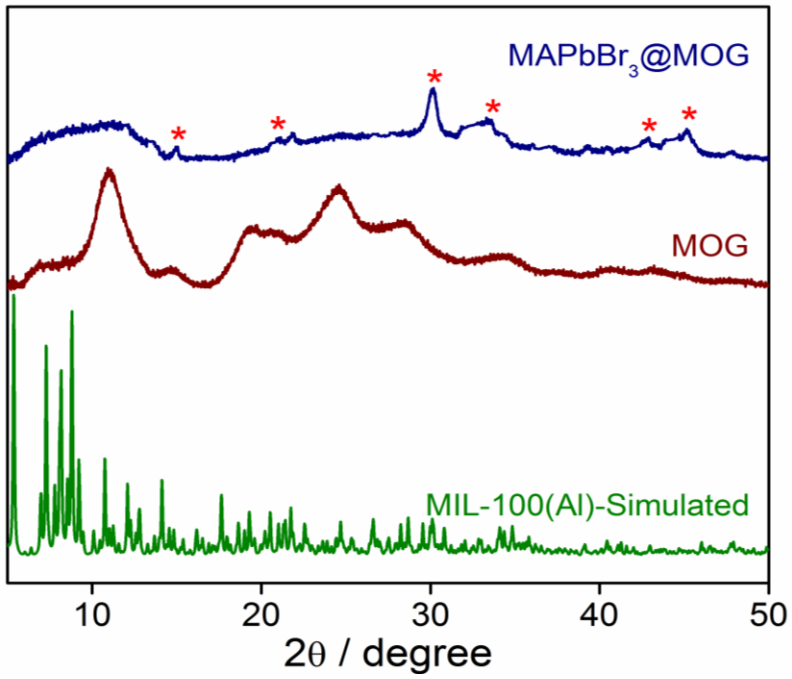

Appendix 5.6. Comparison of PXRD patterns of MIL-101 (Al), MOG and MAPbBr$_3$@MOG composites. Star represent the peak position of MAPbBr$_3$ NPs, indicating formation of MAPbBr$_3$ NCs in composite material.

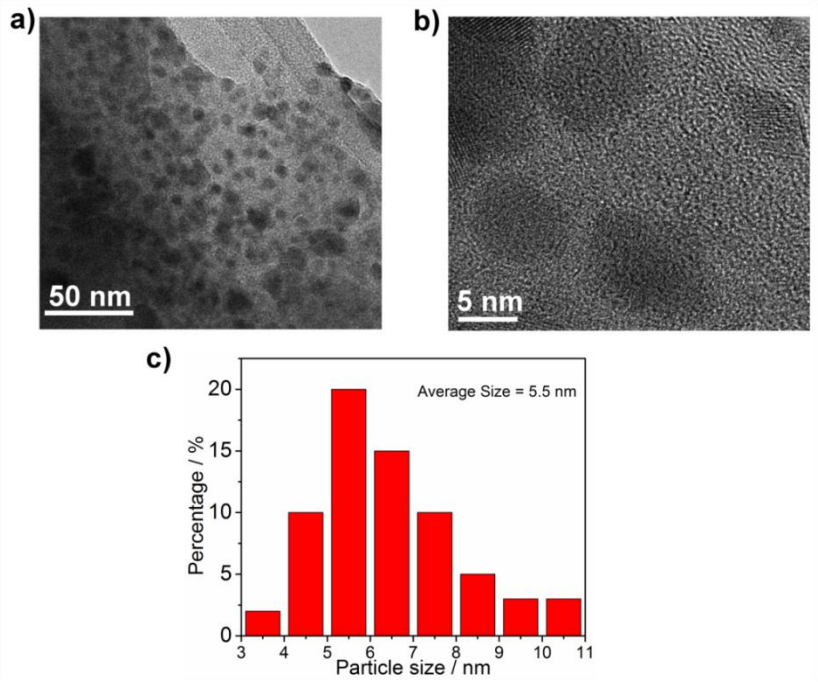

Appendix 5.7. TEM image of $EAPbBr_3$@ MOG nanocomposites. a) Large area TEM image. b) HRTEM image. c) Size distribution of $EAPbBr_3$@MOG nanocomposite. Average size of $EAPbBr_3$ NPs is 5.5 nm in composite materials.

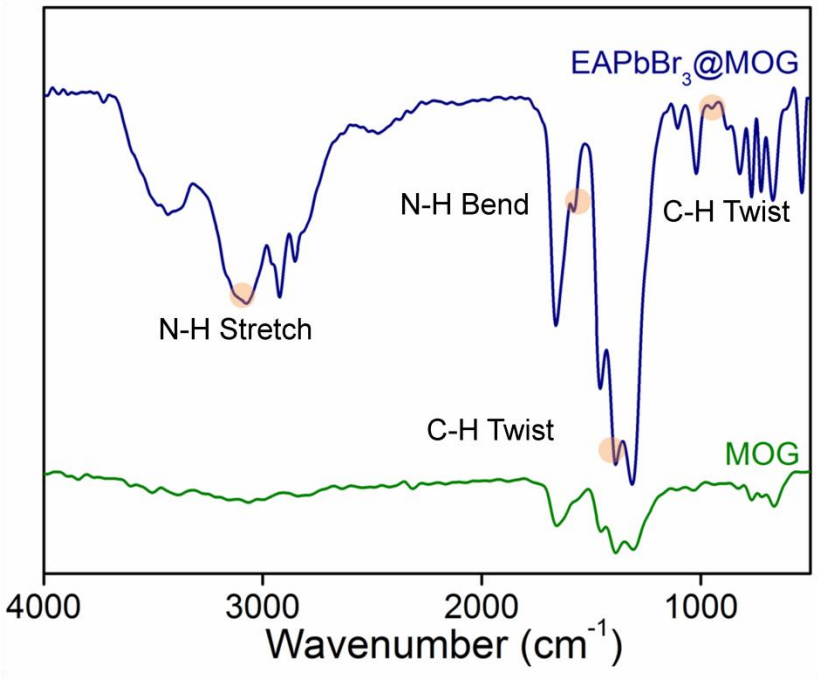

Appendix 5.8. FT-IR spectra of MOG and $EAPbBr_3$@MOG. Highlighted peaks indicate the characteristic peaks for $EAPbBr_3$ perovskite material, representing formation of $EAPbBr_3$ NCs in composite materials.

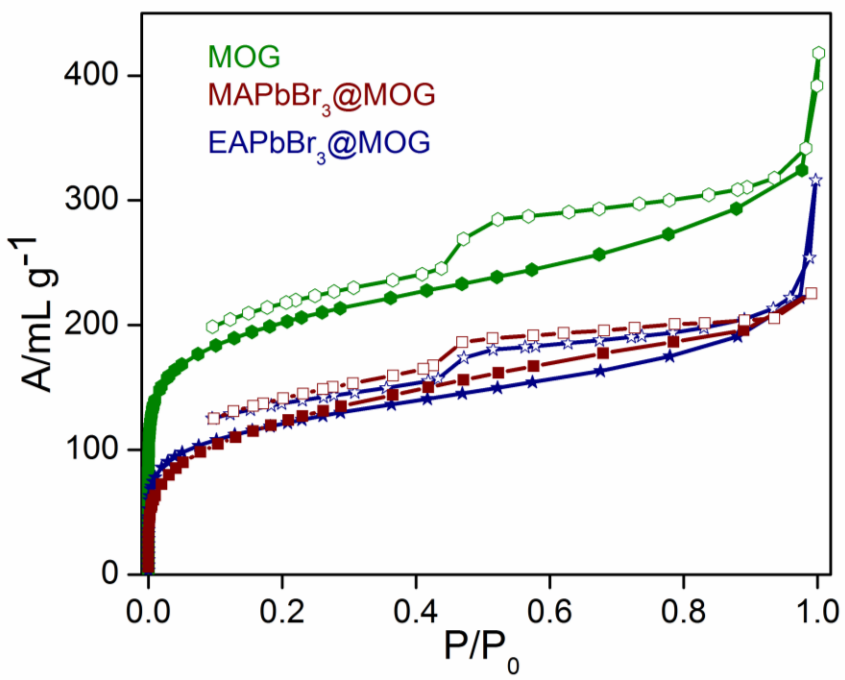

Appendix 5.9. N_2 Sorption study of MOG, $MAPbBr_3$@MOG and $EAPbBr_3$@MOG composites at 77 K.

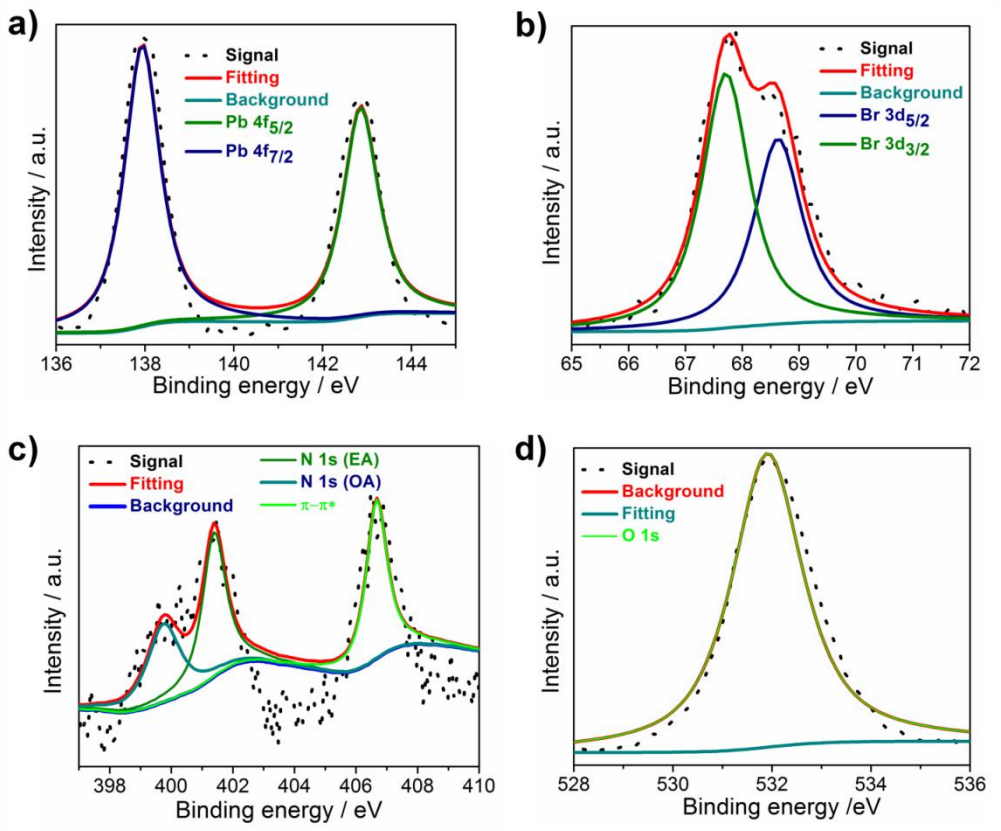

Appendix 5.10. XPS spectra of $EAPbBr_3$@MOG. a) Pb $4f_{5/2}$ and Pb $4f_{7/2}$; b) Br $3d_{5/2}$ and Br $3d_{3/2}$; c) N 1s (EA), N 1s (OA) and π-π*; d) O 1s.

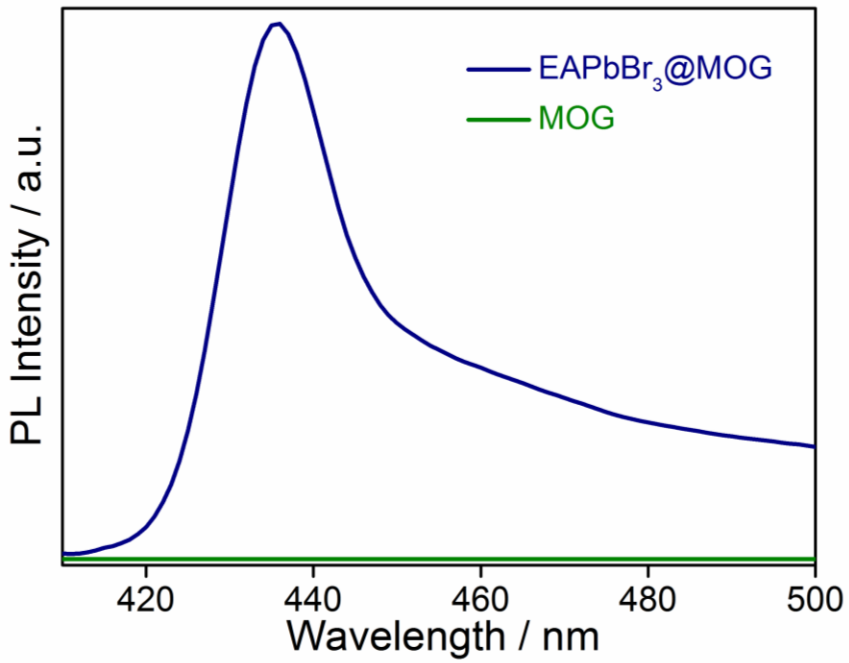

Appendix 5.11. PL spectra of MOG and $EAPbBr_3$@MOG.

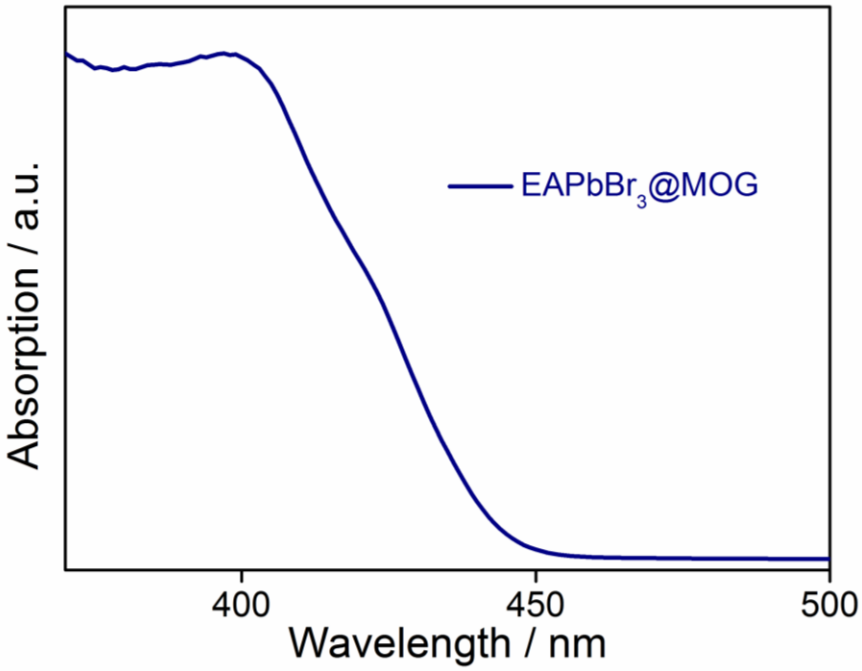

Appendix 5.12. Solid state UV plot of $EAPbBr_3$@MOG composite material.

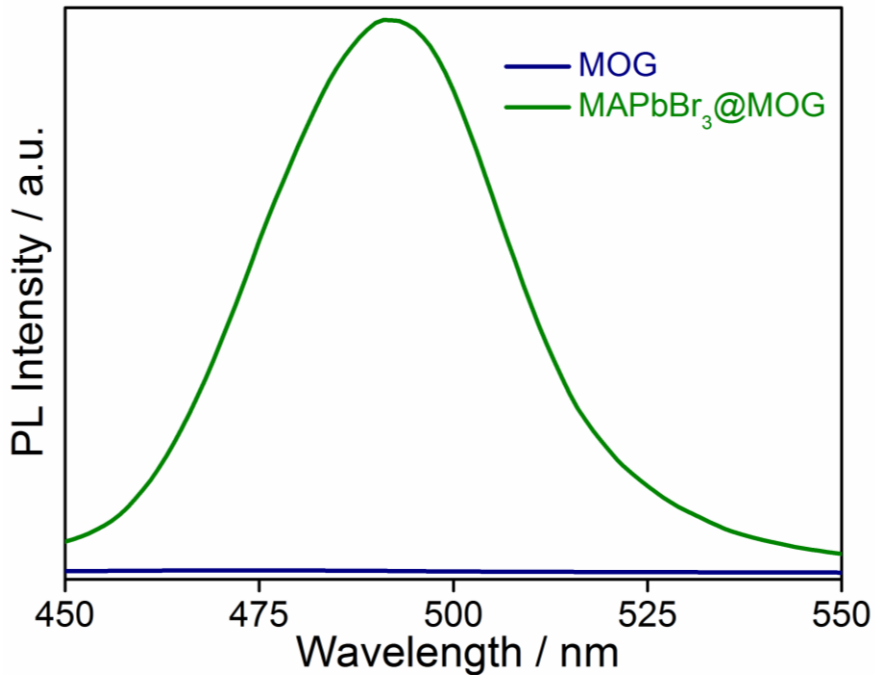

Appendix 5.13. PL spectra of MOG and $MAPbBr_3$@MOG.

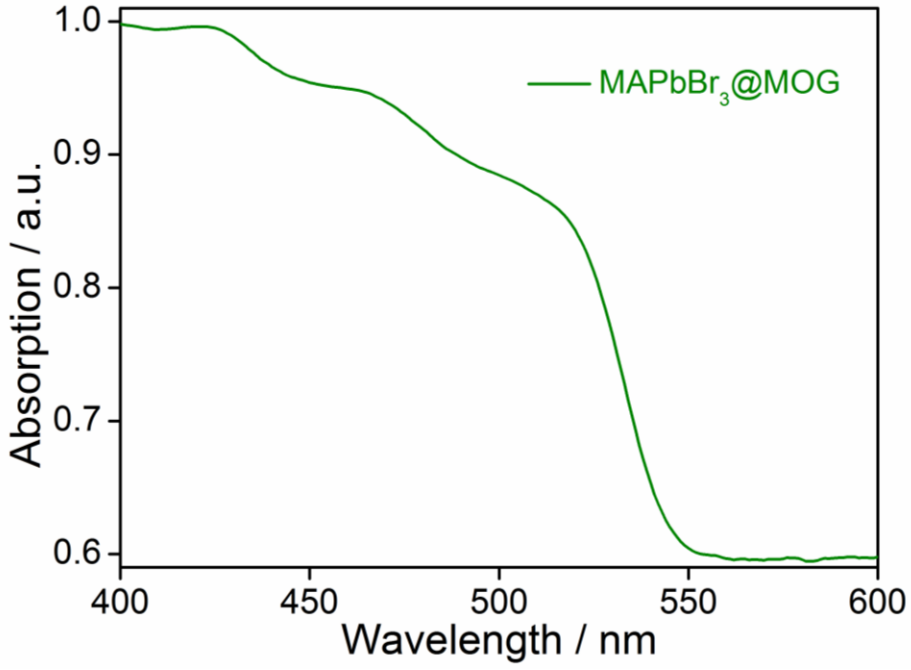

Appendix 5.14. Solid state UV plot of $MAPbBr_3$@MOG composite material.

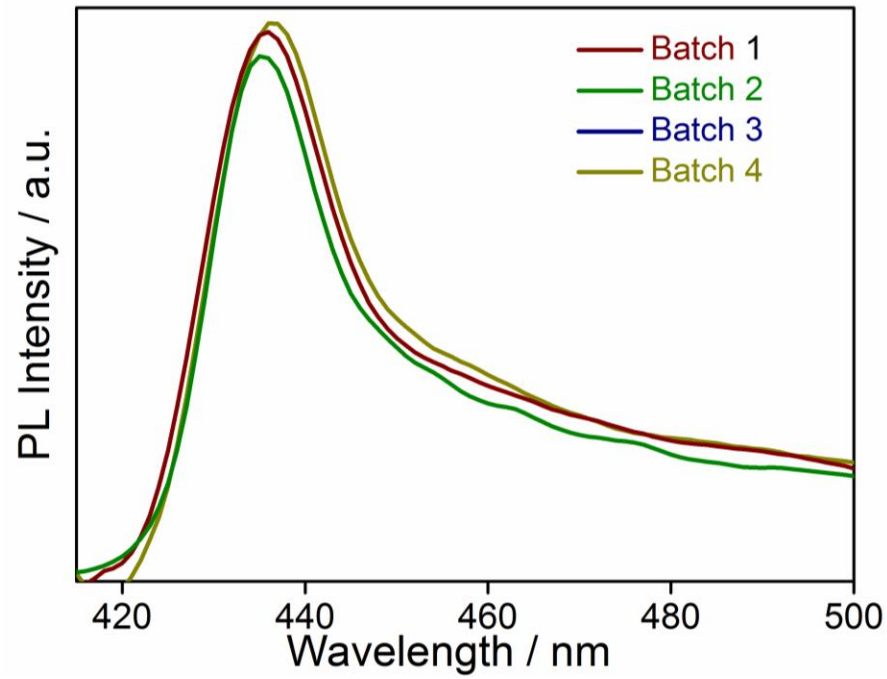

Appendix 5.15. PL spectra of different batches of $EAPbBr_3$@MOG composites.

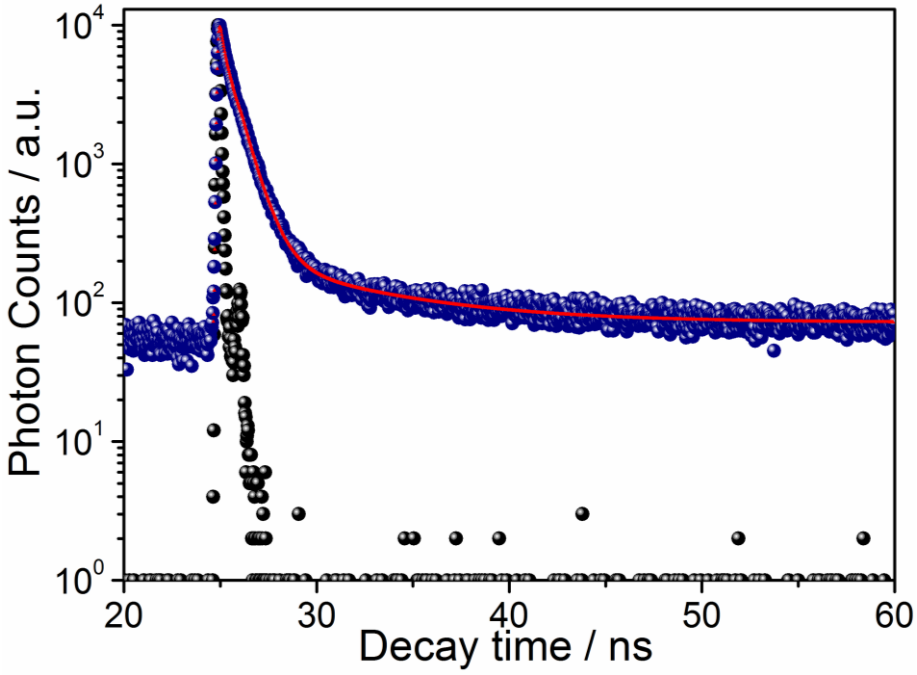

Appendix 5.16. Time resolved PL spectra of $EAPbBr_3$ NPs.

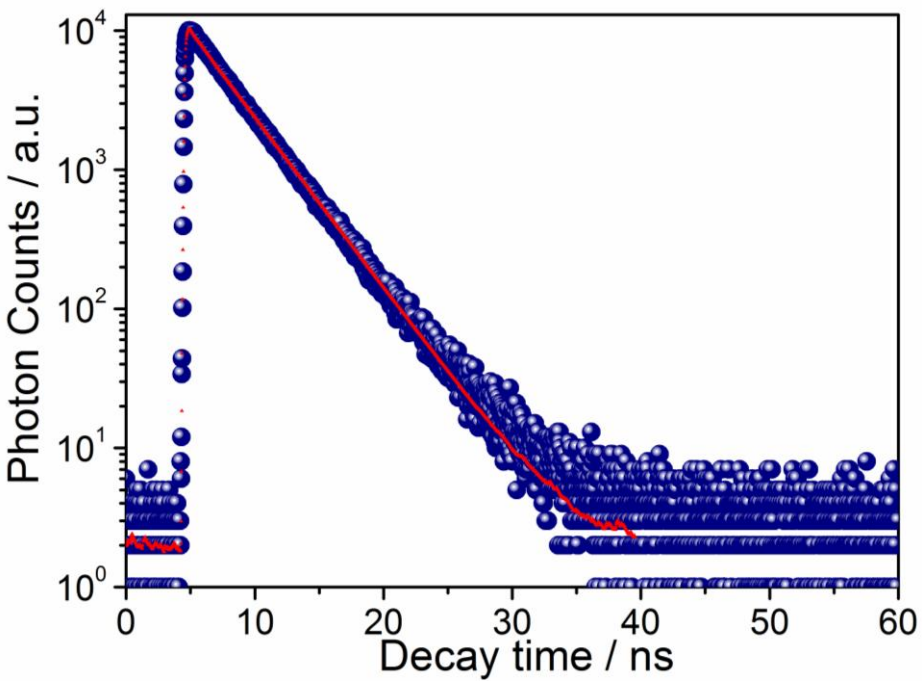

Appendix 5.17. Time resolved PL spectra of $EAPbBr_3$@MOG nanocomposite. The average lifetime of composite larger than naked perovskite indicating confinement of PNC inside MOG.

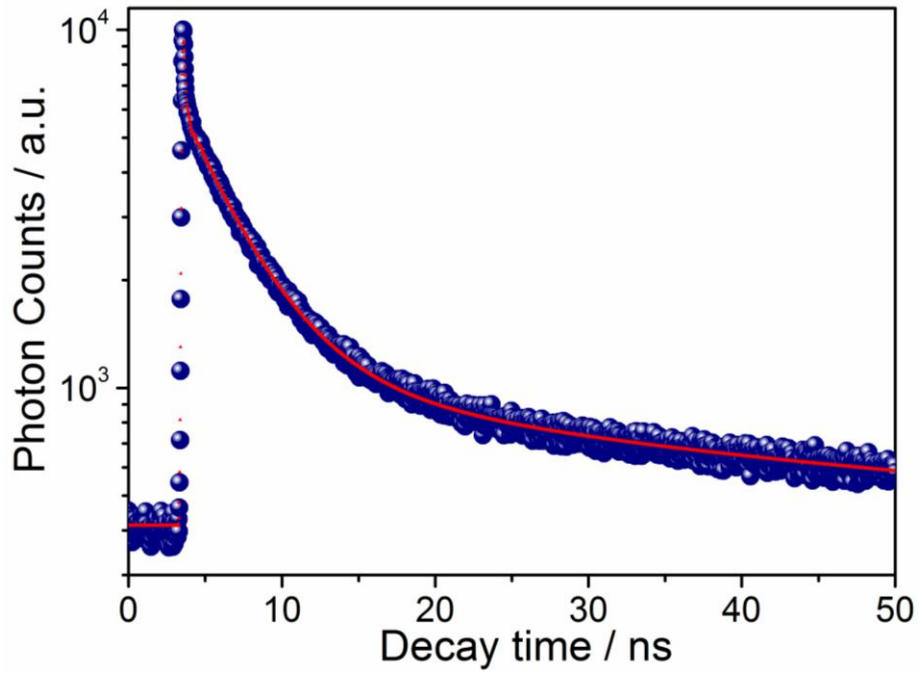

Appendix 5.18. Time resolved PL spectra of $MAPbBr_3$@MOG nanocomposite.

Appendix Table 5.2. PL Decay parameters of $EAPbBr_3$ NC and $EAPbBr_3$@MOG composite.

Compounds	τ_1(ns)	A_1	τ_2(ns)	A_2	χ^2	τ_{avg}(ns)	K_r(ns)	K_{nr}(ns)	K_r:K_{nr}
$EAPbBr_3$ NC	0.10	0.56	0.80	0.44	1.16	0.71	0.03	1.39	0.02
$EAPbBr_3$@MOG	0.32	0.67	3.53	0.33	1.12	3.03	0.18	0.16	1.13

Appendix Table 5.3. PL Decay parameters of $EAPbBr_3$@MOG and $MAPbBr_3$@MOG composites.

Compounds	τ_1(ns)	A_1	τ_2(ns)	A_2	τ_3(ns)	A_3	χ^2	τ_{avg}(ns)
$EAPbBr_3$@MOG	0.32	0.67	3.53	0.33	-	-	1.12	3.40
$MAPbBr_3$@MOG	3.25	0.44	10.30	0.35	40.55	0.21	1.07	22.41

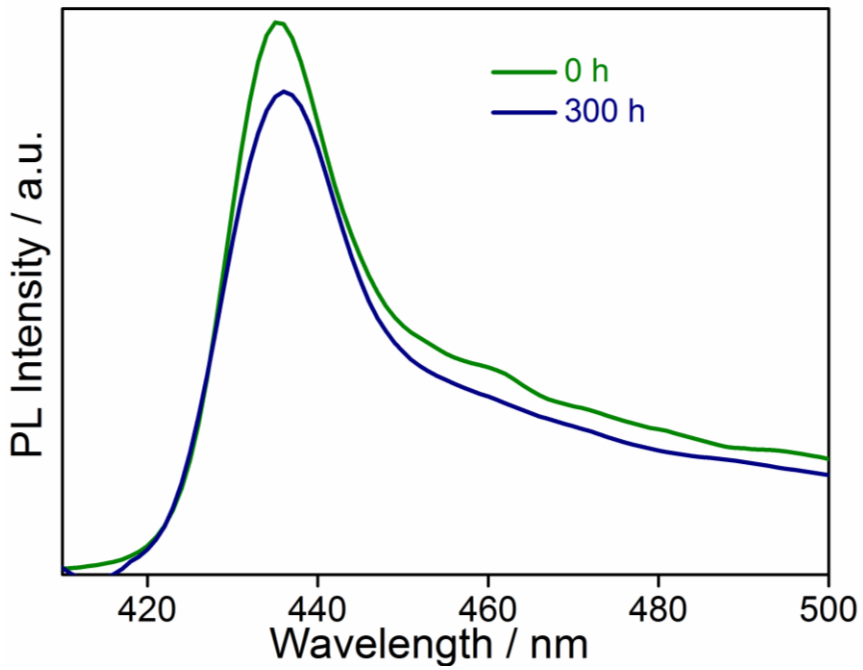

Appendix 5.19. Time dependent PL spectra of $EAPbBr_3$@MOG, before and after keeping under UV light (365 nm) irradiation in dark condition upto 300 hours.

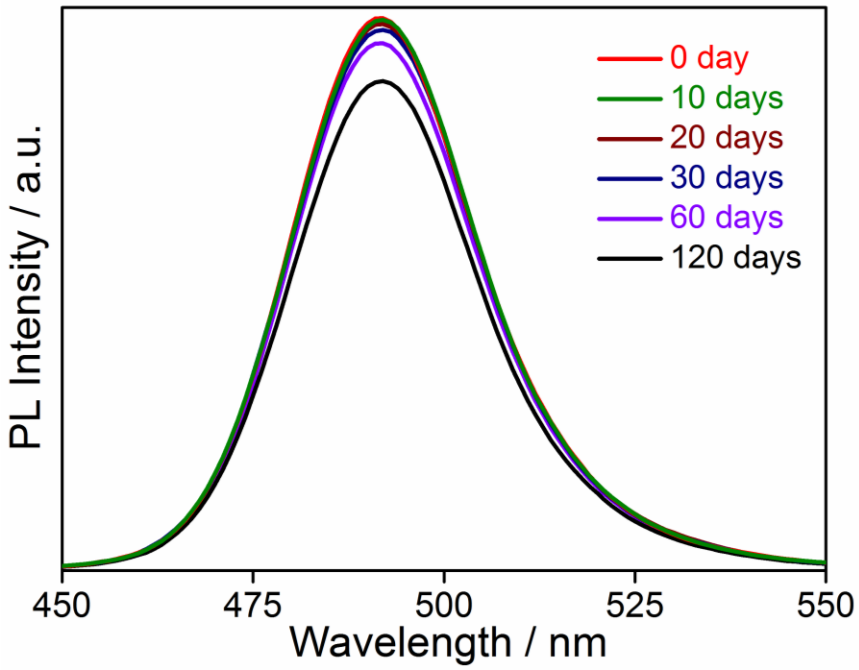

Appendix 5.20. Time dependent PL spectra of $MAPbBr_3$@MOG composite materials stored under several months in open air**.**

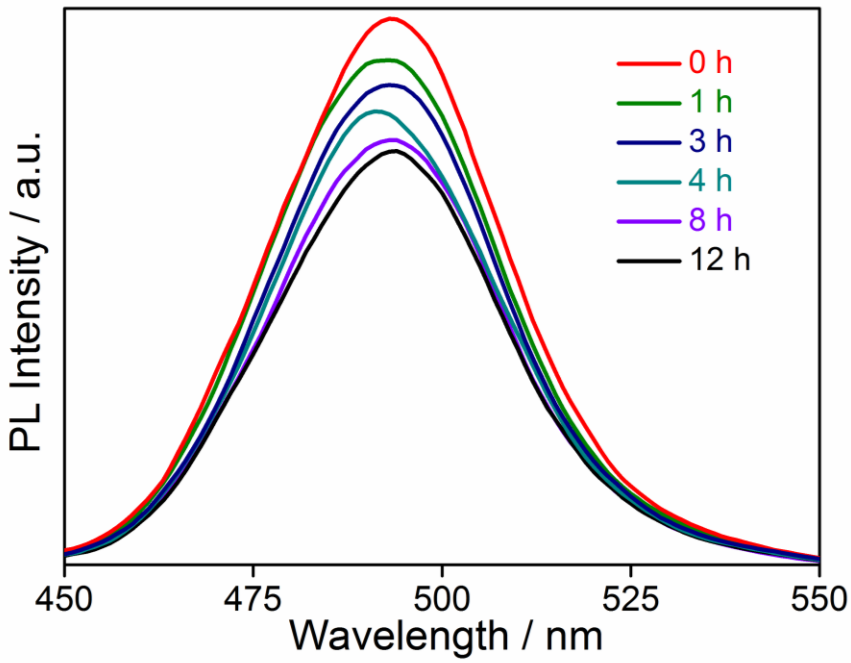

Appendix 5.21. Time dependent PL spectra of $MAPbBr_3$@MOG in presence of water.

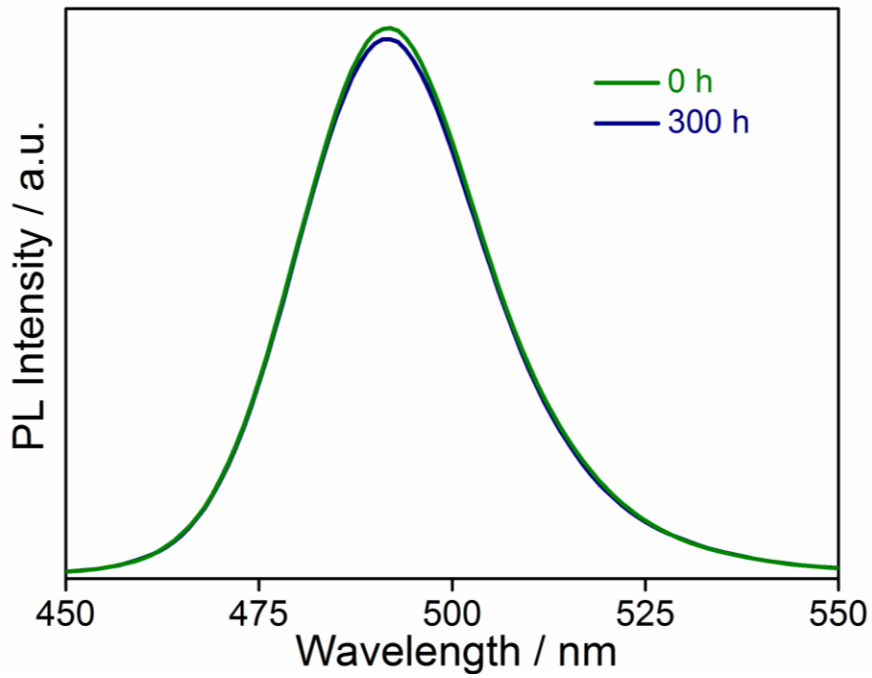

Appendix 5.22. Time dependent PL spectra of $MAPbBr_3$@ZIF-8 composite under UV light (365 nm) irradiation for 300 h at dark condition.

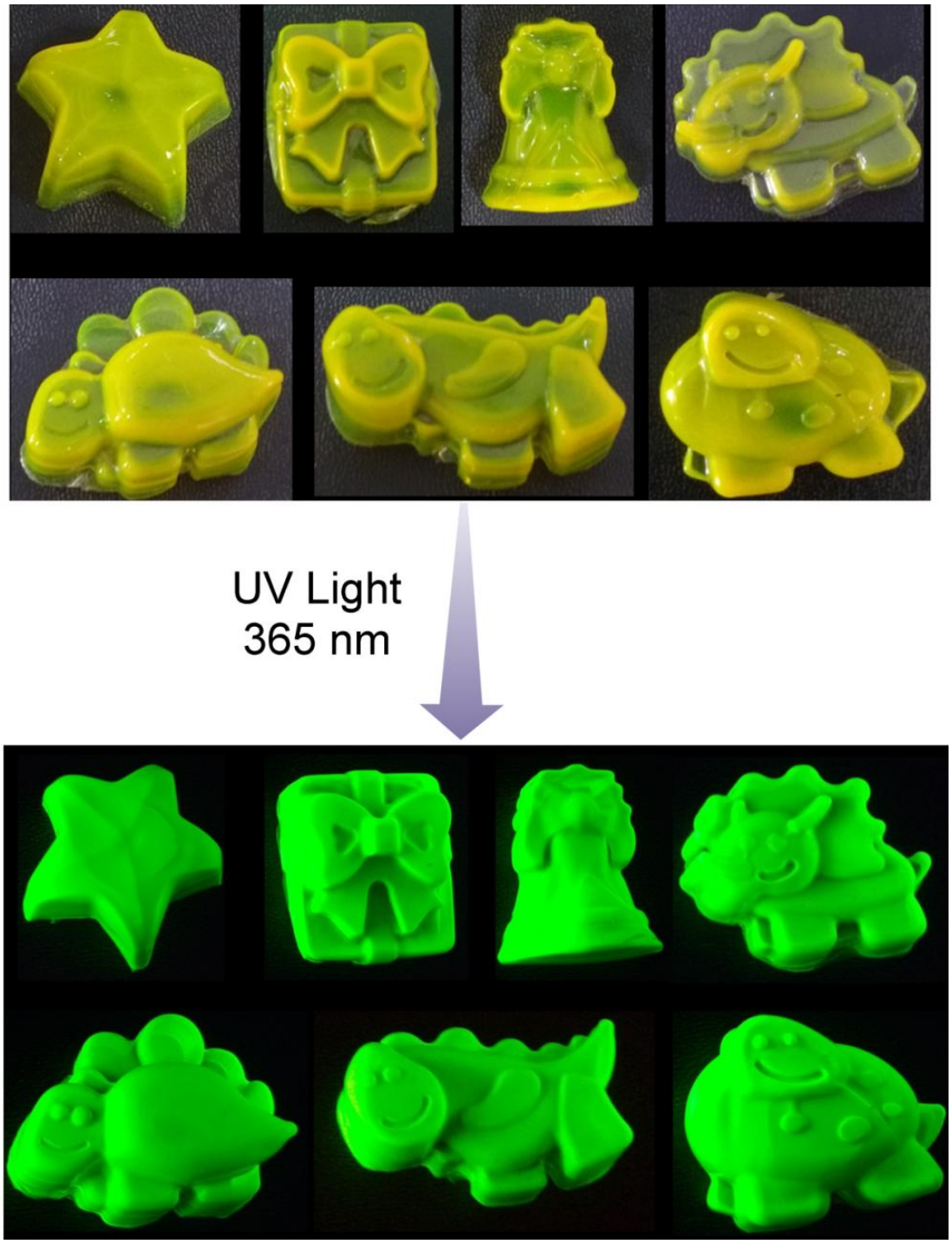

Appendix 5.23. Photographs of various shaped sculptures synthesis from $MAPbBr_3$@MOG composites materials. The photographs shows the color at ambient condition and under UV light (365 nm).

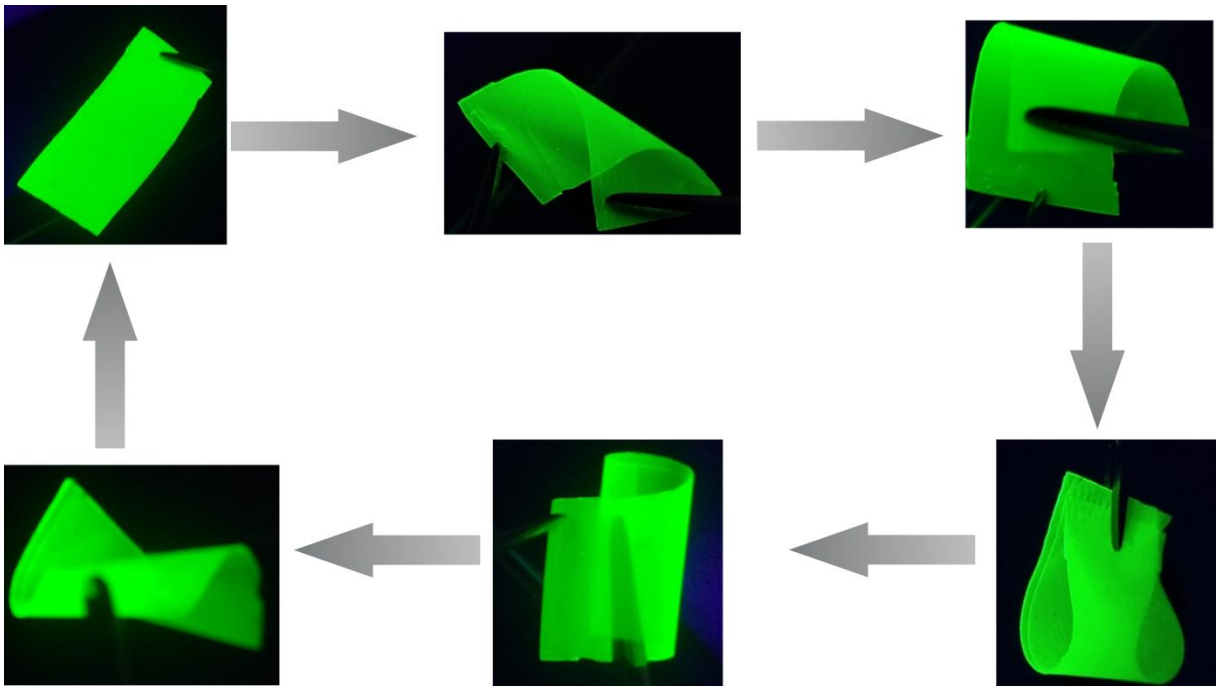

Appendix 5.24. Photographs shows the thin film flexibility of $MAPbBr_3$@MOG composite materials under UV light (365 nm).

Appendix Table 5.4. Comparison of this work with other current related investigations of intense blue (λ_{max} <440 nm) hybrid perovskites.

System	**PL Peak (nm)**	**PLQY (%)**	**FWHM (nm)**	**Air Stability**	**Photo Stability**	**Water Stability**	**Ref.**
$EAPbBr_3$@MOG	436	53	18.4	4 months	300 h	12 h	This work
$(C_6H_5CH_2NH_3)$. $2PbBr_4$ exfoliated crystals	411	63 (Average)	20	-	-	-	[13]
$MAPbCl_3$	404	5	15	-	-	-	[38]

$MA_3Bi_2Br_9$	423	12	62	7 days	25 h	-	[39]
Cl-$MA_3Bi_2Br_9$	422	54.1	41	-	-	-	[40]
$(C_6H_5CH_2NH_3)$. $2PbBr_4$ nanoplates	403	53	11	-	30 min	-	[41]
$(PEA)_2PbBr_4$	409	46.5	10.6	-	-	-	[42]
$EAPbBr_3$	432	5	19.8	-	-	-	[32]

Abbreviations: Phenylethylammonium (PEA).

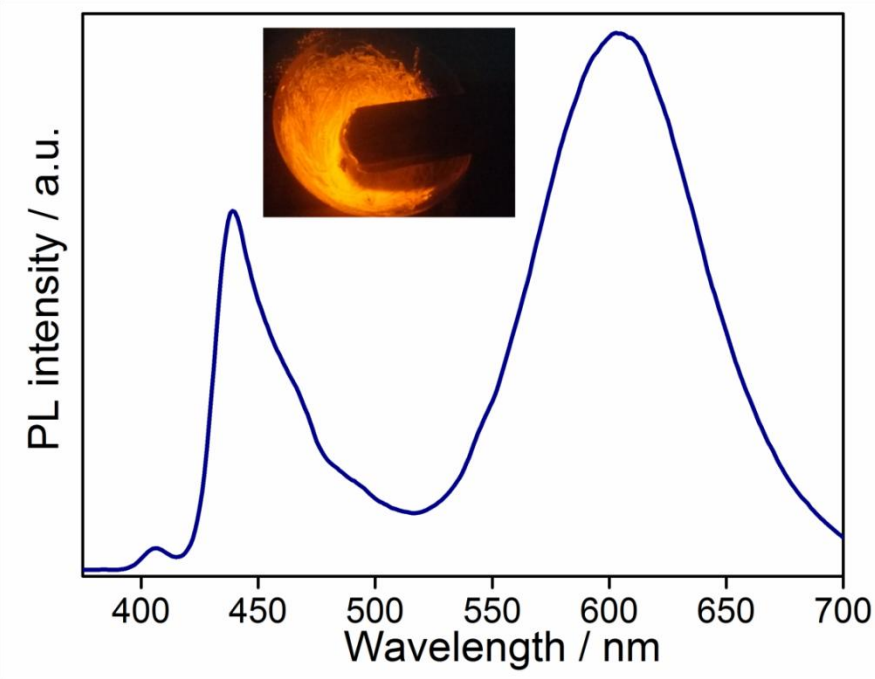

Appendix 5.25. Emission spectra of Mn doped $EAPbBr_3$. Inset photographs shows the color of Mn(II) doped $EAPbBr_3$ NCs under UV light (365 nm).

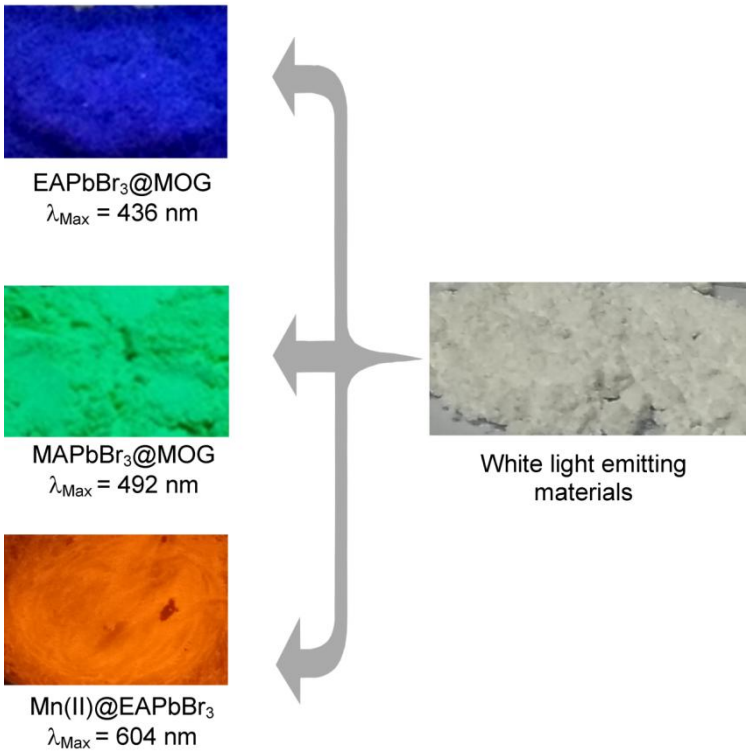

Appendix 5.26. Proper mixing of blue emitting $EAPbBr_3$@MOG, green emitting $MAPbBr_3$@MOG and red emitting Mn(II)@$EAPbBr_3$ produce white light emitting material. The photographs of diffrent colored perovskite materials and white light emitting mateials are taken under UV light (365 nm).

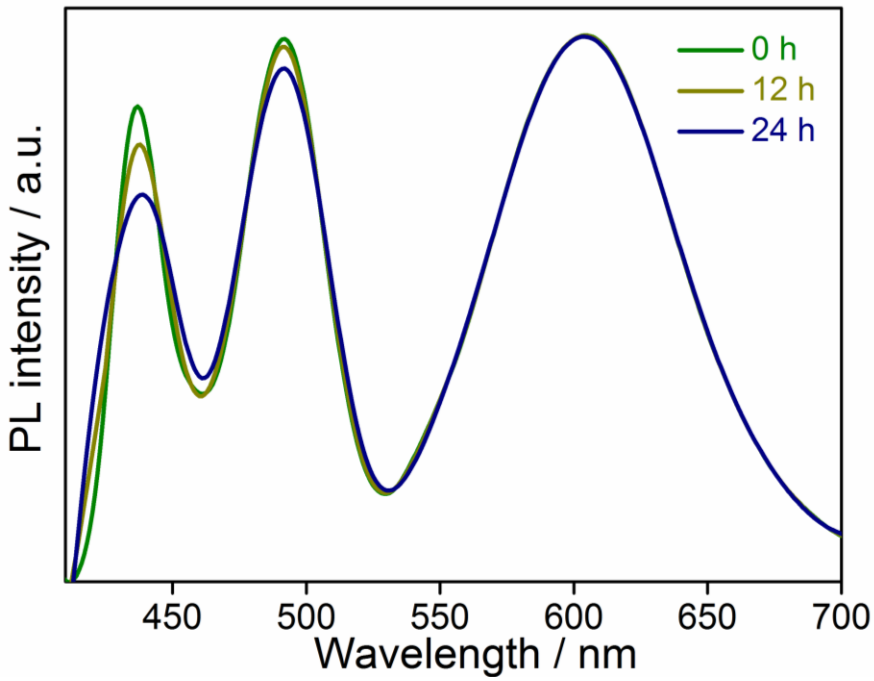

Appendix 5.27. Time dependent PL spectra of $EAPbBr_3$@MOG composite materials stored under open air**.**

5.6 References

[1] C. C. Stoumpos, M. G. Kanatzidis, *Acc. Chem. Res.* **2015**, *48*, 2791-2802.

[2] J. Heo, S. H. Im, J. H. Noh, T. N. Mandal, C.-S. Lim, J. A. Chang, Y. Lee, H.-J. Kim, A. Sarkar, M. K. Nazeeruddin, M. Grätzel, S. I. Seok, *Nat. Photonics* **2013**, *7*, 486-491.

[3] J. S. Manser, J. A. Christians, P. V. Kamat, *Chem. Rev*. **2016**, *116*, 12956-13008.

[4] M. M. Lee, J. Teuscher, T. Miyasaka, T. N. Murakami, H. J. Snaith, *Science* **2012**, *338*, 643-647.

[5] L. Protesescu, S. Yakunin, M. I. Bodnarchuk, F. Krieg, R. Caputo, C. H. Hendon, R. X. Yang, A. Walsh, M. V. Kovalenko, *Nano Lett*. **2015**, *15*, 3692-3696.

[6] Z.-K. Tan, R. S. Moghaddam, M. L. Lai, P. Docampo, R. Higler, F. Deschler, M. Price, A. Sadhanala, L. M. Pazos, D. Credgington, F. Hanusch, T. Bein, H. J. Snaith, R. H. Friend, *Nat. Nanotechnol.* **2014**, *9*, 687-692.

[7] X. Dai, Y. Deng, X. Peng, Y. Jin, *Adv. Mater*. **2017**, *29*, 1607022.

[8] M. V. Kovalenko, L. Protesescu, M. I. Bodnarchuk, *Science* **2017**, *358*, 745-750.

[9] B. S. Sutherland, *Joule* **2018**, *2*, 2199-2201.

[10] B. J. Bohn, Y. Tong, M. Gramlich, M. L. Lai, M. Doblinger, K. Wang, R. L. Z. Hoye, P. Muller-Buschbaum, S. D. Stranks, A. S. Urban, L. Polavarapu, J. Feldmann, *Nano Lett.* **2018**, *18*, 5231-5238.

[11] G. H. Ahmed, J. K. El-Demellawi, J. Yin, J. Pan, D. B. Velusamy, M. N. Medhili, E. Alarousu, O. M. Bakr, H. N. Alshareef, O. F. Mohammed, *ACS Energy Lett.* **2018**, *3*, 2301-2307.

[12] Y. Wu, C. Wei, X. Li, Y. Li, S. Qiu, W. Shen, B. Cai, Z. Sun, D. Yang, Z. Deng, H. Zeng, *ACS Energy Lett.* **2018**, *3*, 2030-2037.

[13] X. Gong, O. Voznyy, A. Jain, W. Liu, R. Sabatini, Z. Piontkowski, G. Walters, G. Bappi, S. Nokhrin; O. Bushuyev, M. Yuan, R. Comin, D. McCamant, S. O. Kelley, E. H. Sargent, *Nat. Mater.* **2018**, *17*, 550-556.

[14] T. M. Brenner, D. A. Egger, L. Kronik, G. Hodes, D. Cahen, *Nat. Rev. Mater.* **2016**, *1*, 15007.

[15] Y. Wu, X. Li, H. Zeng, *ACS Energy Lett.* **2019**, *4*, 673-681.

[16] J. Xing, Y. Zhao, M. Askerka, L. N. Quan, X. Gong, W. Zhao, J. Zhao, H. Tan, G. Long, L. Gao, Z. Yang, O. Voznyy, J. Tang, Z.-H. Lu, Q. Xiong and E. H. Sargent, *Nat. Commun*. **2018**, *9*, 3541.

[17] Y. Jiang, C. Qin, M. Cui, T. He, K. Liu, Y. Huang, M. Luo, L. Zhang, H. Xu, S. Li, J. Wei, Z. Liu, H. Wang, G.-H. Kim, M. Yuan, J. Chen, *Nat. Commun.* **2019**, *10*, 1868.

[18] N. K. Kumawat, X.-K. Liu, D. Kabra, F. Gao, *Nanoscale* **2019**, *11*, 2109-2120.

[19] M. K. Gangishetty, S. Hou, Q. Quan, D. N. Conreve, *Adv. mater*. **2018**, *30*, 1706226.

[20] S. Mollick, T. N. Mandal, A. Jana, S. Fajal, A. V. Desai, S. K. Ghosh, *ACS Appl. Nano Mater*. **2019**, *2*, 1333-1340.

[21] H. He, Y. Cui, B. Li, B. Wang, C. Jin, J. Yu, L. Yao, Y. Yang, B. Chen, G. Qian, *Adv. Mater*. **2019**, *31*, 1806897.

[22] Z. Chen, Z.-G. Gu, W.-Q. Fu, F. Wang, J. Zhang, *ACS Appl. Mater. Interfaces* **2016**, *8*, 28737-28742.

[23] V. Urbanova, K. Jayaramulu, A. Schneemann, S. Kment, R. A. Fischer, R. Zboril, *ACS Appl. Mater. Interfaces* **2018**, *10*, 41089-41097.

[24] X. Wang, X. Lian, Z. Zhang, H. Gao, *ACS Energy Lett.* **2019**, *4*, 1446-1454

[25] X. Yang, G. Zhang, D. Zhang, *J. Mater. Chem.* **2012**, *22*, 38-50.

[26] B. Luo, Y. Guo, X. Li, Y. Xiao, X. Huang, J. Z. Zhang, *J. Phys. Chem. C*, **2019**, *123*, 14239-14245.

[27] K. Jayaramulu, F. Geyer, M. Petr, R. Zboril, D. Vollmer, R. A. Fischer, *Adv. Mater.* **2017**, *29*, 1605307.

[28] F. Zhang, H. Zhong, C. Chen, X.-G. Wu, X. Hu, H. Huang, J. Han, B. Zou, Y. Dong, *ACS Nano* **2015**, *9*, 4533-4542.

[29] Q. Wang, J. Ren, X.-F. Peng, X.-X. Ji, X.-H. Yang, *ACS Appl. Mater. Inetrfaces* **2017**, *9*, 29901-29906.

[30] X. Gu, Z.-H. Lu, H.-L. Jiang, T. Akita, Q. Xu, *J. Am. Chem. Soc.* **2011**, *133*, 11822-11825.

[31] C. Zhang, B. Wang, W. Li, S. Huang, L. Kong, Z. Li, L. Li, *Nat. Commun.* **2017**, *8*, 1138.
[32] M. Mittal, A. Jana, S. Sarkar, P. Mahadevan, S. Sapra, *J. Phys. Chem. Lett.* **2016**, *7*, 3270-3277.

[33] Y. Wang, J. He, H. Chen, J. Chen, R. Zhu, P. Ma, A. Towers, Y. Lin, A. J. Gesquiere, S.-T Wu, Y. Dong, *Adv. Mater.* **2016**, *28*, 10710-10717.

[34] N. Mondal, A. De, A. Samanta, *ACS Energy Lett.* **2019**, *4*, 32-39.

[35] H. Sun, Z. Yang, M. Wei, W. Sun, X. Li, S. Ye, Y. Zhao, H. Tan, E. L. Kynaston, T. B. Schon, H. Yan, Z.-H. Lu, G. A. Ozin, E. H. Sargent, D. S. Seferos, *Adv. Mater.* **2017**, *29*, 1701153-1701162.

[36] D. Chen, J. Li, X. Chen, J. Chen, J. Zhong, *ACS Appl. Mater. Interfaces* **2019**, *11*, 10059-10067.

[37] M. Bidikoudi, E. Fresta, R. D. Costa, *Chem. Commun.* **2018**, *54*, 8150-8169.

[38] M. Imran, V. Caligiuri, M. Wang, L. Goldoni, M. Prato, R. Krahne, L. D. Trizio, L. Manna, *J. Am. Chem. Soc.* **2018**, *140*, 2656-2664.

[39] M. Leng, Z. Chen, Y. Yang, Z. Li, K. Zeng, K. Li, G. Niu, Y. He, Q. Zhou, J. Tang, *Angew. Chem. Int. Ed.* **2016**, *55*, 15012-15016.

[40] M. Leng, Y. Yang, Z. Chen, W. Gao, J. Zhang, G. Niu, D. Li, H. Song, J. Zhang, S. Jin, J. Tang, *Nano Lett*. **2018**, *18*, 6076-6083.

[41] D. Liang, Y. Peng, Y. Fu, M. J. Shearer, J. Zhang, J. Zhai, Y. Zhang, R. J. Hamers, T. L. Andrew, S. Jin, *ACS Nano* **2016**, *10*, 6897-6904.

[42] S. Yang, W. Niu, A.-L. Wang, Z. Fan, B. Chen, C. Tan, Q. Lu, H. Zhang, *Angew. Chem. Int. Ed.* **2017**, *56*, 4252-4255.

Chapter 6

Summary and Perspectives

6.1 Summary and Perspectives

APMs have received increased attention in the past few decades due to their broad multifarious applications. However, APMs have rarely been utilized as host matrix for stabilization of unstable functional guest molecules. The works carried out in this thesis demonstrates stabilization of various unstable functional materials through APMs, which can be further employed in different practical applications. However, one such APM viz., carboxylate MOP itself suffers from two major shortcomings, namely hydrolytic instability and aggregation-induced active sites blockage after guests removal. To overcome this issue the outer surface hydrophobic strategy is used for hydrolytic stability of MOPs while the cage molecules are hybridized with another APM i.e. COF matrix to prevent the aggregation problem. Furthermore, another extremely unstable functional material i.e. hybrid bromide perovskites were embedded into different APM matrices to protect them from various degradable environments. Owing to the easy synthesis and unique pore surface characters, ZIF-8 (well-known chemically stable MOF) have been used for hosting the photoactive semiconducting hybrid perovskite materials and the resulting composite material was further utilized for the degradation of toxic organic pollutants in water. Although the stability in various working conditions is an indispensable aspect for practical applications, the subsequent challenges include converting these materials into workable forms, as MOF based perovskite composite exhibits heterogeneous character. Therefore, to utilize the perovskite in device technologies, they were embedded inside a processable APM i.e. soft porous MOG matrix. The MOG encapsulated perovskite composite materials not only were stable in environmental conditions including water but also could be fabricated into different desirable architectures which is essential for flexible electronics. These works demonstrated that target-specific applications and exquisite control over the entire structure of APMs have facilitated their applicability as host matrix for the stabilization of various unstable functional materials. Although APMs have not been explored much for this type of applications, but such porous materials can be well suited for stabilization of various unstable materials as well as target specific applications in the near future.

JOHN WILEY AND SONS LICENSE
TERMS AND CONDITIONS

Jul 10, 2020

This Agreement between Mr. Samraj Mollick ("You") and John Wiley and Sons ("John Wiley and Sons") consists of your license details and the terms and conditions provided by John Wiley and Sons and Copyright Clearance Center.

License Number	4865211327871
License date	Jul 10, 2020
Licensed Content Publisher	John Wiley and Sons
Licensed Content Publication	Chemistry - An Asian Journal
Licensed Content Title	Stabilizing Metal–Organic Polyhedra (MOP): Issues and Strategies
Licensed Content Author	Sujit K. Ghosh, Soumya Mukherjee, Sahel Fajal, et al
Licensed Content Date	Aug 23, 2019
Licensed Content Volume	14
Licensed Content Issue	18
Licensed Content Pages	13
Type of use	Dissertation/Thesis
Requestor type	Author of this Wiley article

Format	Print and electronic
Portion	Full article
Will you be translating?	No
Title	Advanced Porous Materials(APMs) as Host to Develop Composite Materials: Stability and Functional Studies
Institution name	Indian Institute of Science Education and Research (IISER) Pune
Expected presentation date	Aug 2020
Requestor Location	Mr. Samraj Mollick IISER Pune, Dr. Homi Bhabha Road Pashan Pune, Maharashtra 411008 India Attn: Mr. Samraj Mollick
Publisher Tax ID	EU826007151
Total	0.00 USD

Terms and Conditions

TERMS AND CONDITIONS

This copyrighted material is owned by or exclusively licensed to John Wiley & Sons, Inc. or one of its group companies (each a"Wiley Company") or handled on behalf of a society with which a Wiley Company has exclusive publishing rights in relation to a particular work (collectively "WILEY"). By clicking "accept" in connection with completing this licensing transaction, you agree that the following terms and conditions apply to this transaction (along with the billing and payment terms and conditions established by the Copyright Clearance Center Inc., ("CCC's Billing and Payment terms and conditions"), at the time that you opened your RightsLink account (these are available at any time at http://myaccount.copyright.com).

Terms and Conditions

- The materials you have requested permission to reproduce or reuse (the "Wiley Materials") are protected by copyright.

- You are hereby granted a personal, non-exclusive, non-sub licensable (on a stand-alone basis), non-transferable, worldwide, limited license to reproduce the Wiley Materials for the purpose specified in the licensing process. This license, **and any CONTENT (PDF or image file) purchased as part of your order,** is for a one-time use only and limited to any maximum distribution number specified in the license. The first instance of republication or reuse granted by this license must be completed within two years of the date of the grant of this license (although copies prepared before the end date may be distributed thereafter). The Wiley Materials shall not be used in any other manner or for any other purpose, beyond what is granted in the license. Permission is granted subject to an appropriate acknowledgement given to the author, title of the material/book/journal and the publisher. You shall also duplicate the copyright notice that appears in the Wiley publication in your use of the Wiley Material. Permission is also granted on the understanding that nowhere in the text is a previously published source acknowledged for all or part of this Wiley Material. Any third party content is expressly excluded from this permission.

- With respect to the Wiley Materials, all rights are reserved. Except as expressly granted by the terms of the license, no part of the Wiley Materials may be copied, modified, adapted (except for minor reformatting required by the new Publication), translated, reproduced, transferred or distributed, in any form or by any means, and no derivative works may be made based on the Wiley Materials without the prior permission of the respective copyright owner.**For STM Signatory Publishers clearing permission under the terms of the STM Permissions Guidelines only, the terms of the license are extended to include subsequent editions and for editions in other languages, provided such editions are for the work as a whole in situ and does not involve the separate exploitation of the permitted figures or extracts,** You may not alter, remove or suppress in any manner any copyright, trademark or other notices displayed by the Wiley Materials. You may not license, rent, sell, loan, lease, pledge, offer as security, transfer or assign the Wiley Materials on a stand-alone basis, or any of the rights granted to you hereunder to any other person.

- The Wiley Materials and all of the intellectual property rights therein shall at all times remain the exclusive property of John Wiley & Sons Inc, the Wiley Companies, or their respective licensors, and your interest therein is only that of having possession of and the right to reproduce the Wiley Materials pursuant to Section 2 herein during the continuance of this Agreement. You agree that you own no right, title or interest in or to the Wiley Materials or any of the intellectual property rights therein. You shall have no rights hereunder other than the license as provided for above in Section 2. No right, license or interest to any trademark, trade name, service mark or other branding ("Marks") of WILEY or its licensors is granted hereunder, and you agree that you shall not assert any such right, license or interest with respect thereto

- NEITHER WILEY NOR ITS LICENSORS MAKES ANY WARRANTY OR REPRESENTATION OF ANY KIND TO YOU OR ANY THIRD PARTY, EXPRESS, IMPLIED OR STATUTORY, WITH RESPECT TO THE MATERIALS OR THE ACCURACY OF ANY INFORMATION CONTAINED IN THE MATERIALS, INCLUDING, WITHOUT LIMITATION, ANY IMPLIED WARRANTY OF MERCHANTABILITY, ACCURACY, SATISFACTORY QUALITY, FITNESS FOR A PARTICULAR PURPOSE, USABILITY, INTEGRATION OR NON-INFRINGEMENT AND ALL SUCH WARRANTIES ARE HEREBY EXCLUDED BY WILEY AND ITS LICENSORS AND WAIVED BY YOU.

- WILEY shall have the right to terminate this Agreement immediately upon breach of this Agreement by you.

- You shall indemnify, defend and hold harmless WILEY, its Licensors and their respective directors, officers, agents and employees, from and against any actual or

threatened claims, demands, causes of action or proceedings arising from any breach of this Agreement by you.

- IN NO EVENT SHALL WILEY OR ITS LICENSORS BE LIABLE TO YOU OR ANY OTHER PARTY OR ANY OTHER PERSON OR ENTITY FOR ANY SPECIAL, CONSEQUENTIAL, INCIDENTAL, INDIRECT, EXEMPLARY OR PUNITIVE DAMAGES, HOWEVER CAUSED, ARISING OUT OF OR IN CONNECTION WITH THE DOWNLOADING, PROVISIONING, VIEWING OR USE OF THE MATERIALS REGARDLESS OF THE FORM OF ACTION, WHETHER FOR BREACH OF CONTRACT, BREACH OF WARRANTY, TORT, NEGLIGENCE, INFRINGEMENT OR OTHERWISE (INCLUDING, WITHOUT LIMITATION, DAMAGES BASED ON LOSS OF PROFITS, DATA, FILES, USE, BUSINESS OPPORTUNITY OR CLAIMS OF THIRD PARTIES), AND WHETHER OR NOT THE PARTY HAS BEEN ADVISED OF THE POSSIBILITY OF SUCH DAMAGES. THIS LIMITATION SHALL APPLY NOTWITHSTANDING ANY FAILURE OF ESSENTIAL PURPOSE OF ANY LIMITED REMEDY PROVIDED HEREIN.

- Should any provision of this Agreement be held by a court of competent jurisdiction to be illegal, invalid, or unenforceable, that provision shall be deemed amended to achieve as nearly as possible the same economic effect as the original provision, and the legality, validity and enforceability of the remaining provisions of this Agreement shall not be affected or impaired thereby.

- The failure of either party to enforce any term or condition of this Agreement shall not constitute a waiver of either party's right to enforce each and every term and condition of this Agreement. No breach under this agreement shall be deemed waived or excused by either party unless such waiver or consent is in writing signed by the party granting such waiver or consent. The waiver by or consent of a party to a breach of any provision of this Agreement shall not operate or be construed as a waiver of or consent to any other or subsequent breach by such other party.

- This Agreement may not be assigned (including by operation of law or otherwise) by you without WILEY's prior written consent.

- Any fee required for this permission shall be non-refundable after thirty (30) days from receipt by the CCC.

- These terms and conditions together with CCC's Billing and Payment terms and conditions (which are incorporated herein) form the entire agreement between you and WILEY concerning this licensing transaction and (in the absence of fraud) supersedes all prior agreements and representations of the parties, oral or written. This Agreement may not be amended except in writing signed by both parties. This Agreement shall be binding upon and inure to the benefit of the parties' successors, legal representatives, and authorized assigns.

- In the event of any conflict between your obligations established by these terms and conditions and those established by CCC's Billing and Payment terms and conditions, these terms and conditions shall prevail.

- WILEY expressly reserves all rights not specifically granted in the combination of (i) the license details provided by you and accepted in the course of this licensing transaction, (ii) these terms and conditions and (iii) CCC's Billing and Payment terms and conditions.

- This Agreement will be void if the Type of Use, Format, Circulation, or Requestor Type was misrepresented during the licensing process.

- This Agreement shall be governed by and construed in accordance with the laws of the State of New York, USA, without regards to such state's conflict of law rules. Any legal action, suit or proceeding arising out of or relating to these Terms and Conditions or the breach thereof shall be instituted in a court of competent jurisdiction in New York County in the State of New York in the United States of America and each party hereby consents and submits to the personal jurisdiction of such court, waives any objection to venue in such court and consents to service of process by registered or certified mail, return receipt requested, at the last known address of such party.

WILEY OPEN ACCESS TERMS AND CONDITIONS

Wiley Publishes Open Access Articles in fully Open Access Journals and in Subscription journals offering Online Open. Although most of the fully Open Access journals publish open access articles under the terms of the Creative Commons Attribution (CC BY) License only, the subscription journals and a few of the Open Access Journals offer a choice of Creative Commons Licenses. The license type is clearly identified on the article.

The Creative Commons Attribution License

The Creative Commons Attribution License (CC-BY) allows users to copy, distribute and transmit an article, adapt the article and make commercial use of the article. The CC-BY license permits commercial and non-

Creative Commons Attribution Non-Commercial License

The Creative Commons Attribution Non-Commercial (CC-BY-NC)License permits use, distribution and reproduction in any medium, provided the original work is properly cited and is not used for commercial purposes.(see below)

Creative Commons Attribution-Non-Commercial-NoDerivs License

The Creative Commons Attribution Non-Commercial-NoDerivs License (CC-BY-NC-ND) permits use, distribution and reproduction in any medium, provided the original work is properly cited, is not used for commercial purposes and no modifications or adaptations are made. (see below)

Use by commercial "for-profit" organizations

Use of Wiley Open Access articles for commercial, promotional, or marketing purposes requires further explicit permission from Wiley and will be subject to a fee.

Further details can be found on Wiley Online Library
http://olabout.wiley.com/WileyCDA/Section/id-410895.html

Other Terms and Conditions:

v1.10 Last updated September 2015

Questions? customercare@copyright.com or +1-855-239-3415 (toll free in the US) or +1-978-646-2777.

JOHN WILEY AND SONS LICENSE
TERMS AND CONDITIONS

Jul 10, 2020

This Agreement between Mr. Samraj Mollick ("You") and John Wiley and Sons ("John Wiley and Sons") consists of your license details and the terms and conditions provided by John Wiley and Sons and Copyright Clearance Center.

License Number	4865211425858
License date	Jul 10, 2020
Licensed Content Publisher	John Wiley and Sons
Licensed Content Publication	Angewandte Chemie International Edition
Licensed Content Title	Hydrophobic Shielding of Outer Surface: Enhancing the Chemical Stability of Metal–Organic Polyhedra
Licensed Content Author	Sujit K. Ghosh, Myoung Soo Lah, Jianwen Jiang, et al
Licensed Content Date	Jan 2, 2019
Licensed Content Volume	58
Licensed Content Issue	4
Licensed Content Pages	5
Type of use	Dissertation/Thesis
Requestor type	Author of this Wiley article

Format	Print and electronic
Portion	Full article
Will you be translating?	No
Title	Advanced Porous Materials(APMs) as Host to Develop Composite Materials: Stability and Functional Studies
Institution name	Indian Institute of Science Education and Research (IISER) Pune
Expected presentation date	Aug 2020
Requestor Location	Mr. Samraj Mollick IISER Pune, Dr. Homi Bhabha Road Pashan Pune, Maharashtra 411008 India Attn: Mr. Samraj Mollick
Publisher Tax ID	EU826007151
Total	0.00 USD

Terms and Conditions

TERMS AND CONDITIONS

This copyrighted material is owned by or exclusively licensed to John Wiley & Sons, Inc. or one of its group companies (each a"Wiley Company") or handled on behalf of a society with which a Wiley Company has exclusive publishing rights in relation to a particular work (collectively "WILEY"). By clicking "accept" in connection with completing this licensing transaction, you agree that the following terms and conditions apply to this transaction (along with the billing and payment terms and conditions established by the Copyright Clearance Center Inc., ("CCC's Billing and Payment terms and conditions"), at the time that you opened your RightsLink account (these are available at any time at http://myaccount.copyright.com).

Terms and Conditions

- The materials you have requested permission to reproduce or reuse (the "Wiley Materials") are protected by copyright.

- You are hereby granted a personal, non-exclusive, non-sub licensable (on a stand-alone basis), non-transferable, worldwide, limited license to reproduce the Wiley Materials for the purpose specified in the licensing process. This license, **and any CONTENT (PDF or image file) purchased as part of your order,** is for a one-time use only and limited to any maximum distribution number specified in the license. The first instance of republication or reuse granted by this license must be completed within two years of the date of the grant of this license (although copies prepared before the end date may be distributed thereafter). The Wiley Materials shall not be used in any other manner or for any other purpose, beyond what is granted in the license. Permission is granted subject to an appropriate acknowledgement given to the author, title of the material/book/journal and the publisher. You shall also duplicate the copyright notice that appears in the Wiley publication in your use of the Wiley Material. Permission is also granted on the understanding that nowhere in the text is a previously published source acknowledged for all or part of this Wiley Material. Any third party content is expressly excluded from this permission.

- With respect to the Wiley Materials, all rights are reserved. Except as expressly granted by the terms of the license, no part of the Wiley Materials may be copied, modified, adapted (except for minor reformatting required by the new Publication), translated, reproduced, transferred or distributed, in any form or by any means, and no derivative works may be made based on the Wiley Materials without the prior permission of the respective copyright owner.**For STM Signatory Publishers clearing permission under the terms of the STM Permissions Guidelines only, the terms of the license are extended to include subsequent editions and for editions in other languages, provided such editions are for the work as a whole in situ and does not involve the separate exploitation of the permitted figures or extracts,** You may not alter, remove or suppress in any manner any copyright, trademark or other notices displayed by the Wiley Materials. You may not license, rent, sell, loan, lease, pledge, offer as security, transfer or assign the Wiley Materials on a stand-alone basis, or any of the rights granted to you hereunder to any other person.

- The Wiley Materials and all of the intellectual property rights therein shall at all times remain the exclusive property of John Wiley & Sons Inc, the Wiley Companies, or their respective licensors, and your interest therein is only that of having possession of and the right to reproduce the Wiley Materials pursuant to Section 2 herein during the continuance of this Agreement. You agree that you own no right, title or interest in or to the Wiley Materials or any of the intellectual property rights therein. You shall have no rights hereunder other than the license as provided for above in Section 2. No right, license or interest to any trademark, trade name, service mark or other branding ("Marks") of WILEY or its licensors is granted hereunder, and you agree that you shall not assert any such right, license or interest with respect thereto

- NEITHER WILEY NOR ITS LICENSORS MAKES ANY WARRANTY OR REPRESENTATION OF ANY KIND TO YOU OR ANY THIRD PARTY, EXPRESS, IMPLIED OR STATUTORY, WITH RESPECT TO THE MATERIALS OR THE ACCURACY OF ANY INFORMATION CONTAINED IN THE MATERIALS, INCLUDING, WITHOUT LIMITATION, ANY IMPLIED WARRANTY OF MERCHANTABILITY, ACCURACY, SATISFACTORY QUALITY, FITNESS FOR A PARTICULAR PURPOSE, USABILITY, INTEGRATION OR NON-INFRINGEMENT AND ALL SUCH WARRANTIES ARE HEREBY EXCLUDED BY WILEY AND ITS LICENSORS AND WAIVED BY YOU.

- WILEY shall have the right to terminate this Agreement immediately upon breach of this Agreement by you.

- You shall indemnify, defend and hold harmless WILEY, its Licensors and their respective directors, officers, agents and employees, from and against any actual or

threatened claims, demands, causes of action or proceedings arising from any breach of this Agreement by you.

- IN NO EVENT SHALL WILEY OR ITS LICENSORS BE LIABLE TO YOU OR ANY OTHER PARTY OR ANY OTHER PERSON OR ENTITY FOR ANY SPECIAL, CONSEQUENTIAL, INCIDENTAL, INDIRECT, EXEMPLARY OR PUNITIVE DAMAGES, HOWEVER CAUSED, ARISING OUT OF OR IN CONNECTION WITH THE DOWNLOADING, PROVISIONING, VIEWING OR USE OF THE MATERIALS REGARDLESS OF THE FORM OF ACTION, WHETHER FOR BREACH OF CONTRACT, BREACH OF WARRANTY, TORT, NEGLIGENCE, INFRINGEMENT OR OTHERWISE (INCLUDING, WITHOUT LIMITATION, DAMAGES BASED ON LOSS OF PROFITS, DATA, FILES, USE, BUSINESS OPPORTUNITY OR CLAIMS OF THIRD PARTIES), AND WHETHER OR NOT THE PARTY HAS BEEN ADVISED OF THE POSSIBILITY OF SUCH DAMAGES. THIS LIMITATION SHALL APPLY NOTWITHSTANDING ANY FAILURE OF ESSENTIAL PURPOSE OF ANY LIMITED REMEDY PROVIDED HEREIN.

- Should any provision of this Agreement be held by a court of competent jurisdiction to be illegal, invalid, or unenforceable, that provision shall be deemed amended to achieve as nearly as possible the same economic effect as the original provision, and the legality, validity and enforceability of the remaining provisions of this Agreement shall not be affected or impaired thereby.

- The failure of either party to enforce any term or condition of this Agreement shall not constitute a waiver of either party's right to enforce each and every term and condition of this Agreement. No breach under this agreement shall be deemed waived or excused by either party unless such waiver or consent is in writing signed by the party granting such waiver or consent. The waiver by or consent of a party to a breach of any provision of this Agreement shall not operate or be construed as a waiver of or consent to any other or subsequent breach by such other party.

- This Agreement may not be assigned (including by operation of law or otherwise) by you without WILEY's prior written consent.

- Any fee required for this permission shall be non-refundable after thirty (30) days from receipt by the CCC.

- These terms and conditions together with CCC's Billing and Payment terms and conditions (which are incorporated herein) form the entire agreement between you and WILEY concerning this licensing transaction and (in the absence of fraud) supersedes all prior agreements and representations of the parties, oral or written. This Agreement may not be amended except in writing signed by both parties. This Agreement shall be binding upon and inure to the benefit of the parties' successors, legal representatives, and authorized assigns.

- In the event of any conflict between your obligations established by these terms and conditions and those established by CCC's Billing and Payment terms and conditions, these terms and conditions shall prevail.

- WILEY expressly reserves all rights not specifically granted in the combination of (i) the license details provided by you and accepted in the course of this licensing transaction, (ii) these terms and conditions and (iii) CCC's Billing and Payment terms and conditions.

- This Agreement will be void if the Type of Use, Format, Circulation, or Requestor Type was misrepresented during the licensing process.

- This Agreement shall be governed by and construed in accordance with the laws of the State of New York, USA, without regards to such state's conflict of law rules. Any legal action, suit or proceeding arising out of or relating to these Terms and Conditions or the breach thereof shall be instituted in a court of competent jurisdiction in New York County in the State of New York in the United States of America and each party hereby consents and submits to the personal jurisdiction of such court, waives any objection to venue in such court and consents to service of process by registered or certified mail, return receipt requested, at the last known address of such party.

WILEY OPEN ACCESS TERMS AND CONDITIONS

Wiley Publishes Open Access Articles in fully Open Access Journals and in Subscription journals offering Online Open. Although most of the fully Open Access journals publish open access articles under the terms of the Creative Commons Attribution (CC BY) License only, the subscription journals and a few of the Open Access Journals offer a choice of Creative Commons Licenses. The license type is clearly identified on the article.

The Creative Commons Attribution License

The Creative Commons Attribution License (CC-BY) allows users to copy, distribute and transmit an article, adapt the article and make commercial use of the article. The CC-BY license permits commercial and non-

Creative Commons Attribution Non-Commercial License

The Creative Commons Attribution Non-Commercial (CC-BY-NC)License permits use, distribution and reproduction in any medium, provided the original work is properly cited and is not used for commercial purposes.(see below)

Creative Commons Attribution-Non-Commercial-NoDerivs License

The Creative Commons Attribution Non-Commercial-NoDerivs License (CC-BY-NC-ND) permits use, distribution and reproduction in any medium, provided the original work is properly cited, is not used for commercial purposes and no modifications or adaptations are made. (see below)

Use by commercial "for-profit" organizations

Use of Wiley Open Access articles for commercial, promotional, or marketing purposes requires further explicit permission from Wiley and will be subject to a fee.

Further details can be found on Wiley Online Library
http://olabout.wiley.com/WileyCDA/Section/id-410895.html

Other Terms and Conditions:

v1.10 Last updated September 2015

Questions? customercare@copyright.com or +1-855-239-3415 (toll free in the US) or +1-978-646-2777.

IISER PUNE

Mollick Samraj <mollick.samraj@students.iiserpune.ac.in>

Regarding Incident 3860545 Requesting for Reuse of Entire Article from my Recently Published Article in ACS Central Science for Doctoral Thesis

support@services.acs.org <support@services.acs.org> Tue, Oct 6, 2020 at 11:40 AM
To: mollick.samraj@students.iiserpune.ac.in

ACS Chemistry for Life®

Dear Mollick,

Thank you for contacting ACS Publications Support.

Your permission requested is granted and there is no fee for this reuse. In your planned reuse, you must cite the ACS article as the source, add this direct link https://pubs.acs.org/doi/10.1021/acscentsci.0c00533, and include a notice to readers that further permissions related to the material excerpted should be directed to the ACS.

If you need further assistance, please let me know.

Sincerely,

Keith Pearl

ACS Publications Support

Customer Services & Information

Website: https://help.acs.org/

Incident Information:

Incident #:	3860545
Date Created:	2020-10-06T11:36:13
Priority:	3
Customer:	Mollick Samraj
Title:	Requesting for Reuse of Entire Article from my Recently Published Article in ACS Central Science for Doctoral Thesis
Description:	Dear Sir/Ma'am, Myself Samraj Mollick, working in IISER Pune (India), recently published an article in ACS Central Science, here is the link https://pubs.acs.org/doi/10.1021/acscentsci.0c00533

As a first author of this article, I want to reuse the entire article as well as supporting information (SI) file for my doctoral thesis. For that, I want to take permission for the reuse of the whole article as well as SI file.

I will be grateful if you give me permission for these two figures.

Thank you for your cooperation.

Best,

Samraj

Department of Chemistry,

Main Academic Building (Lab-C213), IISER Pune

Dr. Homi Bhabha Road, Pashan

Pune-411008, Maharashtra, India

Ph. no.: 08918023703

{CMI: MCID1050580}

Ultrastable Luminescent Hybrid Bromide Perovskite@MOF Nanocomposites for the Degradation of Organic Pollutants in Water

Author: Samraj Mollick, Tarak Nath Mandal, Atanu Jana, et al

Publication: ACS Applied Nano Materials

Publisher: American Chemical Society

Date: Mar 1, 2019

PERMISSION/LICENSE IS GRANTED FOR YOUR ORDER AT NO CHARGE

This type of permission/license, instead of the standard Terms & Conditions, is sent to you because no fee is being charged for your order. Please note the following:

- Permission is granted for your request in both print and electronic formats, and translations.
- If figures and/or tables were requested, they may be adapted or used in part.
- Please print this page for your records and send a copy of it to your publisher/graduate school.
- Appropriate credit for the requested material should be given as follows: "Reprinted (adapted) with permission from (COMPLETE REFERENCE CITATION). Copyright (YEAR) American Chemical Society." Insert appropriate information in place of the capitalized words.
- One-time permission is granted only for the use specified in your request. No additional uses are granted (such as derivative works or other editions). For any other uses, please submit a new request.

BACK CLOSE WINDOW

C. Grovenor , M. B. Johnston , D. S. Ginger , R. J. Nicholas and H. J. Snaith , *Energy Environ. Sci.*, 2016, **9** , 2892 —2901 RSC .

50. T. Kyomen , R. Sakamoto , N. Sakamoto , S. Kunugi and M. Itoh , *Chem. Mater.*, 2005, **17** , 3200 —3204 CrossRef CAS .
51. D. Lu , Y. Zhang , M. Lai , A. Lee , C. Xie , T. Lei , Z. Lin , C. S. Kley , J. Huang , E. Rabani and P. Yang , *Nano Lett.*, 2018, **18** , 6967 —6973 CrossRef CAS PubMed .
52. Y. Tian , M. Peter , E. Unger , M. Abdellah , K. Zheng , T. Pullerits , A. Yartsev , V. Sundstron and I. G. Scheblykin , *Phys. Chem. Chem. Phys.*, 2015, **17** , 24978 —24987 RSC .
53. H. Sun , Z. Yang , M. Wei , W. Sun , X. Li , S. Ye , Y. Zhao , H. Tan , E. L. Kynaston , T. B. Schon , H. Yan , Z.-H. Lu , G. A. Ozin , E. H. Sargent and D. S. Seferos , *Adv. Mater.*, 2017, **29** , 1701153 —1701162 CrossRef PubMed .
54. D. Zhang , Y. Xu , Q. Liu and Z. Xia , *Inorg. Chem.*, 2018, **57** , 4613 —4619 CrossRef CAS PubMed .
55. D. Chen , J. Li , X. Chen , J. Chen and J. Zhong , *ACS Appl. Mater. Interfaces*, 2019, **11** , 10059 —10067 CrossRef CAS PubMed .
56. M. Bidikoudi , E. Fresta and R. D. Costa , *Chem. Commun.*, 2018, **54** , 8150 —8169 RSC .

Footnotes

† Electronic supplementary information (ESI) available: Details of characterization, stability test in detail, and photocatalysis graphs. See DOI: 10.1039/c9sc03829a

‡ These authors contributed equally.

A hybrid blue perovskite@metal–organic gel (MOG) nanocomposite: simultaneous improvement of luminescence and stability

S. Mollick, T. N. Mandal, A. Jana, S. Fajal and S. K. Ghosh, *Chem. Sci.*, 2019, **10**, 10524
DOI: 10.1039/C9SC03829A